Characterising Young Eclipsing Binaries and their Environments in NGC 2264

Edward Gillen
Oriel College
University of Oxford

A thesis submitted for the degree of
Doctor of Philosophy

Trinity 2015

For Mum and Dad, for everything.

Characterising Young Eclipsing Binaries and their Environments in NGC 2264

Edward Gillen

Oriel College, University of Oxford

A thesis submitted for the degree of Doctor of Philosophy

Trinity 2015

Stellar evolution models underpin much of astrophysics, yet they are severely under-constrained on the pre-main sequence. The masses, radii, temperatures and luminosities of detached double-lined eclipsing binaries (EBs) can be determined in a model-independent manner from the light and radial velocity curves of the system. When these reach a precision of a few percent or less, they provide one of the most powerful observational tests of stellar evolution theory. Furthermore, young binary star systems display significant photometric and spectroscopic variability over a range of timescales and wavelengths. EBs offer powerful test-beds for characterising such variability, as the stellar parameters and orbital geometry are known to high precision.

This thesis presents the characterisation of EBs discovered by the CoRoT and *Spitzer* space missions in the ∼3 Myr old NGC 2264 star forming region. A sample of EBs in a young open cluster such as this, constitutes a particularly strong test of stellar evolution models because the EBs share the same age and composition, yet span a wide range of masses.

We present the discovery of CoRoT 223992193, a detached, double-lined eclipsing binary, which comprises two pre-main sequence M-dwarfs and shows evidence of a circumbinary disk. We develop innovative approaches, based on Gaussian process regression, to determine the fundamental stellar parameters. At the time of discovery this was only the ninth pre-main sequence eclipsing binary (PMS EB) with component masses below $1.5\,M_{\odot}$ and provides a useful test of stellar evolution models.

CoRoT 223992193 is the first low-mass PMS EB to show evidence of a circumbinary disk and displays significant photometric and spectroscopic variability. The two stars are found to possess slightly different rotation periods: the primary is consistent with synchronisation while the secondary rotates slightly supersynchronously. The photometric and spectroscopic variations are consistent with the picture of two active stars possibly undergoing non-steady, low-level accretion; the system's very high inclination provides a new view of such variability.

The techniques developed in characterising CoRoT 223992193 are applied to the NGC 2264 EB sample. These work well for near equal-mass systems and two main sequence EBs are solved. However, primarily due to the one-dimensional nature of the radial velocity determination, the majority of the sample remains unsolved; more powerful methods are presented and are suggested for further work. Four low-mass EBs show evidence for youth, with three of these displaying low-to-extreme brightness (and hence mass) ratios. No such PMS systems have been reported in the literature. Once complete the full NGC 2264 sample will form one of the most stringent tests of PMS stellar evolution models to date.

Finally, we present a visual multiple containing three EBs spanning B–M spectral types. Two of these systems show evidence for youth and cluster membership; the third is more ambiguous. Further observations are required to confirm the nature of this multiple, but if all three EBs are constituent members, it would be the first triply-eclipsing multiple system discovered, and will provide a powerful test of star formation and stellar evolution models in dense cluster environments.

Declaration

I declare that no part of this thesis has been, or is being, submitted for any qualification other than the degree of Doctor of Philosophy at the University of Oxford.

Research presented in this thesis was carried out under the supervision of Professor Suzanne Aigrain between October 2011 and September 2015 at the University of Oxford. All work presented is my own, except where explicitly stated in the text.

Chapter 3 and part of Chapter 4 has been published in the following journal:

Gillen et al. (2014). *CoRoT 223992193: A new, low-mass, pre-main sequence eclipsing binary with evidence of a circumbinary disk.* A&A, 562 , A50.

Edward Gillen
28 September 2015

Acknowledgements

First and foremost, I would like to thank Suzanne Aigrain for being an excellent supervisor. Her friendly, helpful attitude when applying for PhDs was part of the reason I chose this project. Since then, her help, guidance, enthusiasm and humour have made the last four years far more enjoyable than I had could have hoped for. Time and again she went above and beyond the call of duty; I would like to formally acknowledge her invaluable contribution to this work.

I would like to thank Caroline Terquem for giving me so much of her time, as well as contributing her considerable insight into binaries and protoplanetary disks. I would also like to thank: Jonathan Irwin and John Southworth for helpful discussions on characterising EBs; Simon Hodgkin, Maria Morales-Calderón and Cecila Fariña for making observing so fun (and again to Cecilia for putting me up for the night when we were snowed off the mountain); Jerome Bouvier, Cathie Clarke and Stefano Facchini for insightful discussions on binaries and disks; Lynne Hillenbrand and Monika Lendl for many helpful observations; Davide Gandolfi for observing and help with spectra; and John Stauffer for being an excellent project lead, and for pointing out a new system that led to the formation of Chapter 6. Finally, I would like to thank Pierre Maxted and Pat Roche for agreeing to be my examiners.

I would also like to thank the members of the Oxford group, past and present: Neale, for getting me interested in Gaussian processes; Jo, for help at hand; Hannu, for Toulouse and computer problems; Amy, for friendship, endless chats and epic stories; and Tom and Ruth, for being great friends and for living opposite.

To Shravan, Thibaut, Ricarda, Ruth, Kiz, Eleanor and Yangjun, for making the office hours somehow as fun as the rest. And to Shravan and Paul, for the rest.

Finally, I would like to thank my family for their unwavering love and support; it means everything.

Contents

List of Figures

List of Tables

Thesis outline

This thesis presents the characterisation of eclipsing binaries (EBs) discovered by the CoRoT and *Spitzer* space missions in the ∼3 Myr old NGC 2264 star forming region.

- Chapter 1 presents an overview of star formation and pre-main sequence stellar evolution, discusses current discrepancies between observations and stellar evolution models, and presents the theory behind determining the fundamental parameters of EBs.
- Chapter 2 presents a literature review of the NGC 2264 star forming region, introduces the data used in this work and describes efforts made to improve the CoRoT background correction.
- Chapter 3 presents the fundamental parameters of CoRoT 223992193, a detached, double-lined eclipsing binary, comprising two pre-main sequence M dwarfs. Innovative methods, based on Gaussian process regression, are developed to determine the fundamental stellar parameters.
- Chapter 4 presents further characterisation of CoRoT 223992193 through analysis of the spectral energy distribution, and the photometric and spectroscopic variability.
- Chapter 5 presents the NGC 2264 EB sample, in which the techniques developed for CoRoT 223992193 are applied.
- Chapter 6 presents a visual multiple containing three EBs spanning B–M spectral types. One component is a previously known massive EB member of NGC 2264; the other two eclipsing components are characterised.

Chapter 1

Young eclipsing binary stars

In this chapter we provide a brief motivation for this work, detail the currently accepted paradigm for the formation and early evolution of low-mass stars, and discuss theoretical models seeking to explain pre-main sequence evolution. We then introduce the most powerful techniques for directly measuring fundamental stellar parameters and discuss the current discrepancies between observations and models on both the main and pre-main sequences. We argue that eclipsing binaries are the most powerful method of calibrating pre-main sequence stellar evolution models and present the theory behind determining their fundamental parameters from photometric and spectroscopic observations. We conclude with a brief discussion of stellar time-series photometry, specifically focussing on observations of young stars, which have led to a significant improvement in our understanding of star formation and pre-main sequence evolution, and promise further advances in the future.

1.1 Motivation for this work

The theory of how stars form and evolve underpins much of observational astrophysics, from the determination of initial mass functions and the subsequent evolution of star clusters and galaxies, to characterising exotic binary systems and extrasolar planets. However, significant uncertainties still remain for stars of all masses, from their formation in molecular clouds and contraction onto the main sequence to their evolution through the various giant branches to become compact remnants.

The evolutionary pathway of a star is governed primarily by its mass. One of the fundamental goals of stellar evolution theory is to accurately predict the observable

properties (radius, effective temperature and luminosity) for a star of given mass, age and metallicity. However, in general the masses of single stars are not observationally determinable. Furthermore, the radii, effective temperatures and luminosities are typically dependent on distance estimates, which are uncertain for all but the closest systems amenable to parallax measurements (although this will improve with GAIA; Lindegren et al. 2008).

Ideally therefore, we would calibrate stellar evolution models with stars of known mass, which have distance-independent measurements of radii, effective temperatures and luminosities. Dynamical mass determinations are generally only for possible for stars in binary (or higher order) systems. However, for the majority of binary stars the radii remain unknown, unless the stars eclipse. Eclipsing binaries (EBs) are standard binary stars that are simply orientated close to edge-on, such that we see one star periodically pass in front of the other giving drops in the amount of light observed. From spectroscopic observations, the projected orbits of the two stars can be determined. Combining the photometric and spectroscopic information allows the masses, radii, effective temperatures and luminosities of both stars to be precisely determined in a model- and distance-independent manner, ideal for testing stellar evolution theory (Andersen, 1991; Torres et al., 2010; Stassun et al., 2014).

The pre-main sequence is one of the most observationally under-constrained stages of stellar evolution. This is partially due to its short duration (especially for massive stars) but also because young stars are only found in large numbers in clusters, few of which are near us. This work seeks to determine the fundamental parameters of stars in pre-main sequence eclipsing binaries and to compare these to the predictions of stellar evolution models.

1.2 Star formation and stellar evolution

1.2.1 The star formation paradigm

The majority of stars are believed to form in clusters through the collapse of cold, interstellar gas clouds, which are composed predominantly of molecular hydrogen but also contain dust

and other molecules. Typically, these clouds are massive ($M \sim 10^6 M_\odot$), cold ($10 \lesssim T \lesssim 100$ K), relatively dense ($n \sim 10^2$ cm^{-3}) and quite large ($d \sim 30$ pc across) (Benacquista, 2013).

Star formation occurs through gravitational collapse of over dense regions within the molecular cloud. This occurs when the internal gas pressure is not strong enough to prevent the cloud collapsing under its own gravity. The stability of the cloud depends on its mass, size and temperature. The greater the mass (for a given radius and temperature) or the lower the temperature, the less stable the cloud will be to runaway gravitational collapse and eventual star formation. Jeans (1902) provided a derivation of the critical mass above which collapse will occur. An approximation of the Jeans mass, M_J, may be derived through the following simple argument.

Consider a spherical cloud of mass M and radius R, which is compressed slightly. The compression drives sound waves through the cloud which take time t_s to cross the region and exert a pressure to counter the contraction. This characteristic crossing time is governed by the speed of sound in the gas, C_s, and is therefore given by

$$t_\mathrm{s} \simeq \frac{R}{C_\mathrm{s}} \ . \tag{1.1}$$

During this time, the self-gravity of the cloud will attempt to further the contraction. This free-fall time is given by

$$t_\mathrm{ff} \simeq \left(\frac{GM}{R^3}\right)^{-1/2} = \frac{1}{\sqrt{G\rho}} \tag{1.2}$$

where G is the gravitational constant and $\rho = M/R^3$ is the mean density.

If the free-fall time is shorter than the sound-crossing time, i.e. $t_\mathrm{ff} < t_\mathrm{s}$, self-gravity overcomes the countering pressure forces and collapse ensues,

$$\frac{1}{\sqrt{G\rho}} < \frac{R}{C_\mathrm{s}} \ . \tag{1.3}$$

The Jeans length, R_J[1], is found from the limit of equation 1.3, i.e.

$$R_\mathrm{J} = \frac{C_\mathrm{s}}{\sqrt{G\rho}} \ . \tag{1.4}$$

[1]This is typically denoted λ_J in the literature.

As we defined $\rho = M/R^3$, we can rewrite this as

$$M_{\rm J} = \frac{C_{\rm s}^3}{G^{3/2}\rho^{1/2}} \tag{1.5}$$

where $M_{\rm J}$ is the Jeans mass. It is worth noting that the growth rate of such a gravitational instability will be slower than Jeans presented as the surrounding cloud is also unstable to collapse, whereas Jeans assumed it to be constant. The Jeans mass depends on temperature, density and composition of the cloud, and is typically given values ranging from $\sim 100\,M_\odot$ for cold, dense clouds to as high as $10^4 - 10^5\,M_\odot$ for warmer, sparser clouds. Even the lower end of the range is significantly larger than typical stellar masses. This is because as collapse progresses, the density increases and the Jeans mass correspondingly decreases[2], meaning that smaller regions within the collapsing cloud that were initially slightly overdense compared to their surroundings are able to themselves collapse; this process is known as fragmentation. Fragmented cores can have $M_{\rm J}$ as low as $\sim 0.01\,M_\odot$ (Benacquista, 2013).

1.2.1.1 Protostellar and pre-main sequence evolution

The collapsing fragmented cores, often called 'pre-stellar cores', become hotter and denser as the gravitational energy is converted into thermal kinetic energy. As the density increases, so does the opacity, eventually becoming opaque in the central regions, which causes the temperature to rise further until pressure halts the contraction. Hydrostatic equilibrium is achieved and a protostar (Class 0 source) is formed. At this stage the mass in the surrounding envelope of material is significantly greater than the mass of the protostar, $M_{\rm env} \gg M_\star$ (Andre et al., 1993). Material in the envelope settles into the plane of the mean angular momentum vector of the gas supply, as residual motion in other directions is damped out on a free-fall timescale by shocks between colliding fluid elements. Once the gas has settled into a circular orbit, centrifugal support prevents further radial collapse (on a free-fall timescale) (Clarke & Carswell, 2014). The protostar accretes material from both the disk and envelope, which increases its luminosity, making it observable at long

[2]There is also a strong dependence on temperature but at these temperatures the cloud is transparent to the microwave (blackbody) radiation and hence the collapse can be considered isothermal.

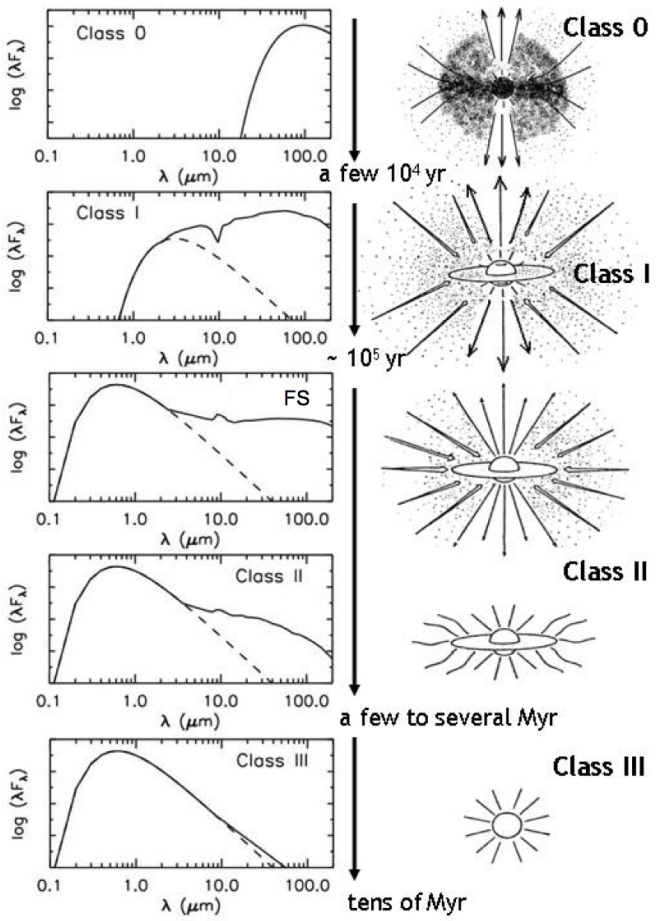

Figure 1.1: Evolutionary phases of protostellar and pre-main sequence evolution (right column, top to bottom), along with their corresponding spectral energy distributions (SEDs; left column). The Class boundaries are defined by the IR slope of the SED; see Table 1.1 for details. [Adapted from a schematic obtained from elisefurlan.com which, in turn, is adapted from Wilking (1989)]

wavelengths (see Figure 1.1, top row). The majority of the mass is accreted in these first few 10^4 Myr.

As the accretion process continues the majority of the envelope mass transfers to the star ($M_\star > M_{\rm env} \sim M_{\rm disk}$) and the source becomes visible in the mid-IR: a Class I source (see Figure 1.1, second row). Accretion and contraction continue until the source is no longer embedded, becoming optically-visible; this defines the stellar birth line and begins the pre-main sequence phase of evolution.

The object is now a Class II source (see Figure 1.1, third & fourth rows) comprising a pre-main sequence (PMS) star and a circumstellar disk ($M_{\rm disk}/M_\star \sim 1\%$). Accretion continues from the disk, which drives significant photometric and spectroscopic variability. Solar-type PMS stars ($M < 2\,M_\odot$) are called T Tauri stars after their prototype T Tauri.

Those that actively accrete are termed classical T Tauri stars (CTTS). Accretion is assessed based on the strength of (primarily) optical emission lines, such as Hα, either through measuring their equivalent widths (EW) or full-widths at 10% maximum (FW10M). Systems displaying Hα EW > 10 Å or FW10M > 270 km s^{-1} are generally considered to be actively accreting (Basri et al., 1997; White & Basri, 2003). T Tauri stars that do not show obvious signs of accretion are denoted weak-lined T Tauri stars (WTTS) and typically display only stellar activity. These systems are generally thought to represent CTTS after the accretion process has finished, which is commonly interpreted as the beginning of the circumstellar disk dispersal by high energy stellar photons (far and extreme UV, and X-ray). PMS stars which have dispersed, or are in the process of dispersing, their protoplanetary disks are termed Class III objects (see Figure 1.1, bottom row).

The Class system is determined from the slopes of spectral energy distributions (SEDs) between 2–25 μm (see Table 1.1) but the broad correlation between SED class and evolutionary phase is widely accepted (Alexander, 2008). We note, however, that inclination can confuse the physical interpretation of the SED. The two classifications are complimentary: CTTS accrete from a disk and therefore typically show Class II SEDs, while WTTS do not show signs of accretion usually due to a lack of circumstellar material close to the star and hence typically display Class III SEDs. The median lifetime of protoplanetary disks is 2-3 Myr (Williams & Cieza, 2011), although there is substantial dispersion. Nonetheless, the fraction of WTTS/CTTS in clusters increases with age throughout the first 10 Myr with essentially no active accretion remaining after this time. It is important to note that while there is broad overlap between the two classification schemes, there is not a one-to-one correspondence: disks can still be present without active accretion, i.e. WTTS can show Class II SEDs, and a few CTTS display Class III SEDs (e.g. Strom et al., 1993; Kaas et al., 2004).

Throughout the PMS stage of evolution, T Tauri stars show significant variability; it is one of the defining characteristics of the class. A detailed discussion of the photometric and spectroscopic variability is given in Chapter 4.

Table 1.1: Classification of young stellar objects. [Table adapted from Williams & Cieza (2011)]

Class	SED slope*	Physical properties	Observational characteristics
0	–	$M_{\rm env} > M_\star > M_{\rm disk}$	No optical or near-IR emission
I	$\alpha > 0.3$	$M_\star > M_{\rm env} \sim M_{\rm disk}$	Generally optically obscured
FS	$-0.3 < \alpha < 0.3$		Intermediate between Class I and II
II	$-1.6 < \alpha < -0.3$	$M_{\rm disk}/M_\star \sim 1\%$. $M_{\rm env} \sim 0$	Accreting disk; strong Hα and UV
III	$\alpha < -1.6$	$M_{\rm disk}/M_\star \ll 1\%$	Passive disk; no or very weak accretion

* SED slope defined as $\alpha = \frac{d \log \lambda F_\lambda}{d \log \lambda}$ and typically measured between 2 and 25 μm. The numerical boundaries follow Greene et al. (1994).

1.2.1.2 PMS evolution and Li depletion

PMS stars are powered by the gravitational potential energy released from their contraction; they do not yet have core temperatures sufficient to fuse hydrogen nuclei. However, the temperatures required to burn Lithium (Li) are much lower ($2.5 - 3.0 \times 10^6$ K; Bildsten et al. 1997; Jeffries 2004). For masses $M < 1.2\,M_\odot$, convective mixing is able to rapidly bring Li-depleted material to the observable photosphere. Measuring Li depletion therefore offers a window into the stellar interior and provides a sensitive test of stellar evolution models.

Li depletion in stars with masses $M < 0.35\,M_\odot$, which remain fully convective throughout the PMS phase, is relatively straightforward. Li burning begins when the core reaches the required temperaure and full depletion is rapid (see Figure 1.2, right panel). Age determination from observed luminosities at the Li depletion boundary (LDB) vary by only 10% between the different models (Burke et al., 2004).

However, for masses between $0.35 < M < 1.2\,M_\odot$, a radiative core develops before Li burning is complete. As the radiative core expands to fill increasing fractions of the stellar interior, the temperature at the base of the receding convective zone decreases until Li burning is no longer possible in the convective envelope (further depletion in the radiative core goes unobserved). The interplay between the rate of Li burning and radiative core expansion can be seen in the left panel of Figure 1.2. For stars below $0.6\,M_\odot$, Li is fully depleted before the radiative core forms. For a $0.8\,M_\odot$ star the radiative core forms early in the Li depletion phase but the convective envelope maintains sufficient temperature at

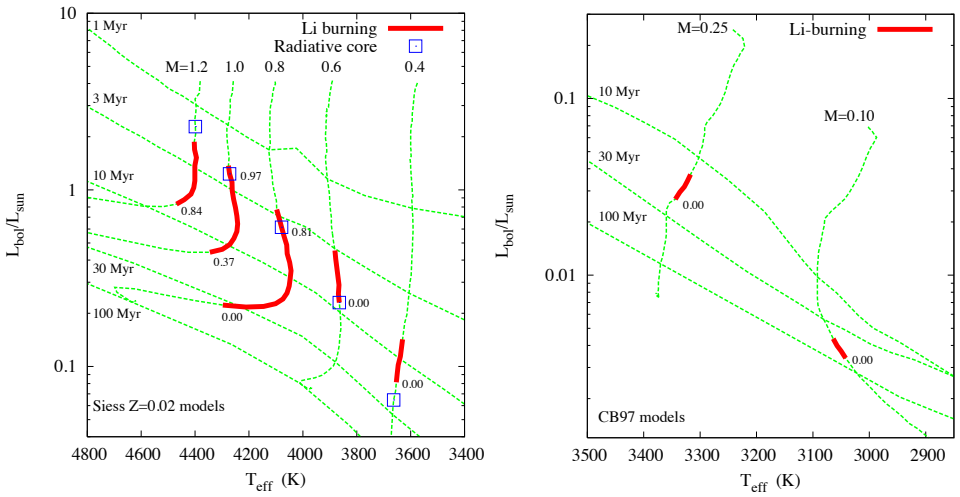

Figure 1.2: Li burning for low-mass stars on the pre-main sequence. Evolutionary tracks for stars with masses $0.1 < M < 1.2\,M_{\odot}$, with isochrones indicated. The left and right panels show the models of Siess et al. (2000) and Chabrier & Baraffe (1997), respectively. In both plots epochs of Li burning are shown in red with the development of a radiative core indicated by blue squares. The numbers to the right of the mass tracks indicate the fraction of photospheric Li remaining at the point where the radiative core develops (top or only number) and at the end of Li burning (bottom number). [Taken from Jeffries (2004)]

its base that full Li depletion is observed. At higher masses, Li depletion is halted due to larger radiative cores. The presence of Li in low-mass stars (c.f. the optical 6708 Å doublet) is a strong indicator of youth.

1.2.1.3 Zero age main sequence (ZAMS)

Temperature increases steadily throughout the PMS phase as the star contracts. When the core reaches a sufficient temperature and density, energy generation through hydrogen fusion begins and the star stops contracting once hydrostatic equilibrium is achieved. This defines the zero age main sequence (ZAMS) and ends the PMS phase. The age of stars on the ZAMS is a strong function of stellar mass, with more massive stars reaching the ZAMS more quickly. Stars of mass $M = 1.5$, 1.0, 0.5 and 0.2 $M_{\odot}$ reach the ZAMS at ages of ∼15, 30, 100 and 180 Myr, respectively, according to the predictions of Siess et al. (2000)[3].

1.2.2 Formation of multiple star systems

The high degree of multiplicity in star forming regions implies it is inherent in the star formation process (Mathieu, 1994). The leading theory for binary formation is through

[3]In these models, the ZAMS is defined as the time, after deuterium burning, when $L_{\rm nucl} > 0.99\,L_{\star}$ (i.e. $L_{\rm grav} < 0.01\,L_{\star}$).

fragmentation; there are two main ways in which this can occur. The first is known as prompt fragmentation and occurs because over-dense regions within the cloud collapse faster resulting in more than one protostar being formed in a bound system (Boss & Bodenheimer, 1979; Boss, 1986). The process of fragmentation depends on the balance between pressure and gravitational forces in the collapsing core: rotation and turbulence promote it, while magnetic fields and radiative feedback act to inhibit it (Offner et al., 2009; Commerçon et al., 2010). The second method is disk fragmentation; if a massive disk around a single protostar becomes cool enough it can become dynamically gravitationally unstable, although it is unclear how much mass can be assembled into new protostars within the disk (Duchêne & Kraus, 2013; Bate, 2015).

The majority of stars form in clusters and associations (e.g. Bressert et al., 2010). Numerical simulations of the collapse of large turbulent clouds point towards a highly dynamic process, in which fragmentation commonly results in multiple systems wider than a few AU (the typical resolution of simulations). The formation of close binaries (separation < 10 AU) is an ongoing issue. Such systems must form either through fragmentation at a later stage (although this has been questioned; Bate 1998, 2011) or via orbital decay induced by accretion or interaction with third bodies (other stars or the remaining cloud and disk material; e.g. Bate et al. 2002; Tokovinin et al. 2006; Fabrycky & Tremaine 2007; Tokovinin 2014a,b). As a prominent formation mechanism of close binaries is thought to require interaction with a third star, we might expect most young spectroscopic and eclipsing binaries to have a tertiary companion.

The search for close PMS binaries in clusters remains challenging as stellar activity inhibits radial velocity analyses (Duchêne & Kraus, 2013), although (notably incomplete) systematic surveys find companion frequencies typically of several percent, similar to the field (e.g. Nguyen et al., 2012). Visual PMS binaries are far better studied. In loose T Tauri associations, such as Taurus and Upper Scorpius, only one-quarter to one-third of all systems comprise a single star. In comparison, the multiplicity frequency in young dense clusters, such as the Orion Nebula Cluster (ONC), is much lower suggesting that the

prevalence of wide multiple systems is a declining function of stellar density. Observations of intermediate regions are required to determine whether the decline is smooth or if there is a sharp dichotomy (Duchêne & Kraus, 2013).

1.2.3 Stellar evolution models for pre-main sequence stars

For a star of given mass and composition, the ultimate goal of stellar models is to accurately predict the evolution of its radius, effective temperature and observable colours throughout its lifetime. While a relatively straightforward aim, stellar evolution is somewhat complicated, with many physical processes and complex interplays.

Models for solar and higher mass main sequence (MS) stars are generally in good agreement with observations, however for lower mass M dwarfs there are notable discrepancies (see section 1.3.5). The pre-main sequence (PMS) introduces additional complications with rapid evolution and many competing physical effects. Furthermore, for up to at least the first ∼10 Myr the models can still be sensitive to their initial conditions, which are somewhat arbitrary, as opposed to being defined from e.g. a stellar birth line (Baraffe et al., 2002). The models are in need of observational constraints on the PMS.

A good stellar evolution model requires: a) an accurate equation of state, b) correct treatment of nuclear reaction rates, c) accurate atmosphere models and d) correct treatment of the surface boundary conditions between the interior and atmosphere profiles. There are numerous stellar evolution models, which have developed along many lines and include different descriptions for the relevant physical processes. Individual stellar models are discussed in Chapter 3. In the following subsections, we discuss the key physics in these models.

1.2.3.1 Equation of State

Central to determining stellar structure is the equation of state (EOS), which relates the pressure to the temperature, density and composition. Low-mass stars have typical central densities and temperatures of order $100 - 1000\ \mathrm{g\,cm^{-3}}$ and $T < 10^7$ K, respectively. The correct EOS for the description of their inner structure must include contributions from

strong interactions between particles, which results in important departures from perfect gas EOS (Chabrier & Baraffe, 1997).

1.2.3.2 Opacity

Elemental and molecular species within a star inhibit the flow of energy from core to surface, either through scattering or absorption and re-emission, which introduces radiation pressure. The chemical composition of the star plays an important role: the higher the metallicity, the higher the opacity and the less transparent the atmosphere. In low-mass stars, with temperatures decreasing below ∼5000 K, molecular opacity comes to dominate the absorption (Alexander & Ferguson, 1994). In the optical, the major absorbers are metal oxides and hydrides (TiO, VO, FeH, CaH, MgH), whereas the IR is dominated by CO and H_2O. These molecules introduce non-grey effects and significant departures from black body emission, as clearly seen in spectral energy distributions of cool stars (Mathieu et al., 2007). For the lowest mass stars and brown dwarfs (BDs) dust condensation can act as an additional source of opacity (Allard et al., 2011). Missing sources of opacity can introduce colour offsets in the models: e.g. the Baraffe et al. (1998) $V - I$ colours for $T_{\rm eff} \lesssim 3700$ K are too blue by 0.5 mag for a given magnitude.

1.2.3.3 Nuclear reaction rates

The thermonuclear processes relevant for the central temperature and densities are given by the pp chain, which converts hydrogen (H) into Helium (He). As mentioned in section 1.2.1.2 Li is also converted into He, as are Beryllium (Be) and Boron (B).

1.2.3.4 Surface boundary conditions

Accurate surface boundary conditions between the internal and atmospheric descriptions are required to solve the set of internal structure equations. Surface boundary conditions defined by grey atmospheres, i.e. assuming opacity is independent of wavelength, are considered valid for $M > 0.9\,M_{\odot}$. However, below this range the presence of molecules introduces a strong wavelength-dependence to the opacity. In such atmospheres, both convection and radiation play important roles in the transport of flux through the stellar

atmosphere, which means that non-grey boundary conditions are required. In fact, non-grey boundary conditions are valid from the sub-stellar regime up to stars of late-B spectral type (Stassun et al., 2014).

1.2.3.5 Energy transport: radiative diffusion and convective motion

The dominant method of energy transport within a given layer of a star depends primarily on the local temperature gradient. Radiative diffusion (random motion of electrons and photons) dominates up to a certain critical gradient, above which it cannot transport energy efficiently enough; this gives rise to convective motions. Energy transport by convection is more difficult to model than radiative diffusion, but it is important in low-mass stars, especially above ∼4000 K where the choice of surface boundary condition becomes less important (Mathieu et al., 2007).

As the details of convective flows are difficult to model exactly, convection is usually treated within the framework of "mixing length theory" (MLT). In MLT, a rising parcel of gas is assumed to transfer its excess heat to the surrounding material over a characteristic length scale $l = \alpha_{\mathrm{MLT}} H_p$, where H_p is the scale height of pressure variation and α_{MLT} an empirically-determined constant. The convective flux is then given by the rate at which this heat is transferred (Benacquista, 2013). The choice of α_{MLT} in the models typically varies in the range 1.5–2.0. Some models calibrate α_{MLT} on the Sun, i.e. a $1\,M_\odot$ star has radius and luminosity equal to the Sun at 4.5 Gyr.

The choice of α_{MLT} has noticeable effect on stellar parameters: decreasing the efficiency of convection (i.e. towards smaller values of α_{MLT}) increases the radius at which the star achieves hydrostatic equilibrium and correspondingly decreases its effective temperature.

1.2.4 Current sources of uncertainty

There are still many sources of uncertainty in the models. Some of the main ones arguably arise from the treatment of opacity and convective efficiency, especially as a function of age and mass. For example, the mass and age at which a radiative core develops depends on the temperature gradient and hence on opacities, which is why different models make

slightly different predictions. Magnetic fields and accretion are also known sources of uncertainty; these are discussed in the context of rectifying observational discrepancies in sections 1.3.5 and 1.3.6.

1.3 Measuring fundamental stellar parameters

For the vast majority of stars, direct probes of the stellar fundamental parameters are unattainable. Stellar properties are typically inferred by comparing observables, such as photometric colours or spectral features, to the predictions of stellar atmosphere and evolution models. It is vital therefore, that these models are accurate, which necessitates the need for robust testing and calibration with multiple methods able to span a wide range of stellar parameter space. In this section we briefly detail the most common methods of directly measuring fundamental stellar parameters, compare their strengths and weaknesses, and discuss the present constraints on both the main and pre-main sequences.

1.3.1 Interferometry

Astronomical interferometry uses multiple mirrors (or telescopes) to combine electromagnetic waves using the principle of superposition. The technique achieves high angular resolution, close to that of a single mirror encompassing all the individual mirrors in the interferometric array. Interferometry can measure the angular diameters of nearby stars which, combining with observed bolometric fluxes and distance estimates from parallaxes, allows the determination of radii, luminosities and effective temperatures for single stars. With current facilities, e.g. CHARA, interferometry is able to resolve stars with angular diameters of order a few tenths of a milli arcsecond and has determined radii to $< 5\%$ for several tens of nearby main-sequence stars ($d \lesssim 50$ pc), including transiting planet host stars (Boyajian et al., 2012a, 2013, 2015; von Braun et al., 2011, 2014).

1.3.2 Asteroseismology

Asteroseismology is the study of stellar oscillations. Solar-like oscillations are acoustic standing waves excited by near-surface convection (e.g. Samadi et al., 2007). These can be used to probe the sound travel time across the stellar diameter, which directly yields

information on the mean stellar density. In addition, the frequency at which the oscillations contain maximum power can also be related to fundamental stellar properties, most notably the surface gravity[4], which gives a good indicator of the evolutionary state (Huber et al., 2013). Oscillations are classified by their mode of restoration: pressure modes (p-modes) where the restoring force arises from the pressure gradient, and gravity modes (g-modes) where the restoring force is gravity. p-mode oscillations are seen in the Sun and solar-like pulsators, and g-modes most notably in white dwarfs, γ-Dor stars and slowly pulsating B stars. Some stars oscillate in mixed modes, which possess p-mode character in the envelope and g-mode character in the core (Pallé & Esteban, 2014).

1.3.3 Binary stars

Binary stars are the primary source of our knowledge of fundamental stellar parameters. The direct determination of the mass of any astronomical object requires measurable gravitational interaction between (at least) two objects. That binary stars are numerous and span a wide rage of stellar parameter space is an added benefit (Kallrath & Milone, 2009)[5]. The two components of a given binary can generally be assumed to share the same age and metallicity, which adds to the tightness of the constraints.

1.3.3.1 Visual binaries

If the two components of a binary system can be individually resolved, their relative orbits can be determined. By converting angular size to true size with parallax measurements, the masses can be determined from Kepler's third law (equation 1.11) and the moment equation ($m_1 a_1 = m_2 a_2$, where m denotes mass and a the semi-major axis). By determining the luminosities from bolometric fluxes (given the parallax distance), such systems provide a calibration for the mass-luminosity relation.

[4] Although there is some dependence on effective temperature.

[5] For star-planet systems typically only the stellar motion can be determined, and hence the stellar properties (and planet properties) are derived from model predictions.

1.3.3.2 Spectroscopic binaries

The radial component of the motion of binary stars about their common centre of mass can be detected through the Doppler shift of spectroscopic lines; such systems are called spectroscopic binaries. Spectra yield the light and mass ratios: the former from the spectra and the latter from the motion of the two stars (the derivation is presented in section 1.4.2). For double-lined systems (where the spectral features of both stars are detected), the individual projected masses and semi-major axes can be determined which, unless the inclination is known, provide lower limits on these quantities (again, the derivation is presented in section 1.4.2). As the individual components of binary systems are typically unresolved (i.e. not visual binaries), spectroscopic projected mass determinations are very valuable, especially if the inclination can be determined, such as if the two stars eclipse.

1.3.3.3 Eclipsing binaries

Detached, double-lined eclipsing binaries (EBs) are extremely valuable objects because their masses, radii, effective temperatures and luminosities can be determined in a model-independent manner from the light and radial velocity curves of the system (see sections 1.4.2 and 1.5.2). When these reach a precision of a few percent or less, they provide one of the most powerful tests of stellar evolution models available (Andersen, 1991; Torres et al., 2010; Stassun et al., 2014). However, the vast majority of EBs have short orbital periods so it is possible that interactions between the two stars affect their evolution.

1.3.4 Comparison of the different methods

Focussing on close binary stars, e.g. spectroscopic and eclipsing binaries, for model evaluation makes it difficult to distinguish between the effects of binarity and other physics which may be missing in the models. Interferometry and asteroseismolgy do not suffer from this limitation but have other issues. Interferometry is feasible only for very nearby, bright stars, and their mass remains unknown (unless the target is a member of a visual binary with a well characterised orbit). While asteroseismology is an exquisite probe of stellar interiors, able to provide model-independent density estimates, it only gives

model-dependent masses and radii. Therefore, binary stars and specifically detached, double-lined EBs remain an important observational test of stellar evolution models, and significant resources are dedicated to discovering and characterising them across as wide a range of mass, age and metallicity as possible.

1.3.5 Constraints and discrepancies on the main sequence

The predictive power of stellar evolution theory can be assessed using both colour-magnitude diagrams of clusters and touchstone stars, i.e. where stellar parameters have been established by direct observations. While the former is very useful, the latter is a more fundamental test and we focus on it here. Sufficiently accurate determinations of stellar fundamental parameters can reveal deficiencies in the physical descriptions of stellar models. Ideally, the masses, radii and effective temperatures of both stars, as well as their chemical composition (e.g. [Fe/H]), would be known to high precision ($< 2\%$). The (preferably unequal) masses and composition fix the basic parameters of the model for each star (assuming an He abundance Y and mixing length parameter α_{MLT}): requiring these models to then reproduce the observed radii and effective temperatures of both stars at the same age is a non-trivial test (Torres et al., 2010).

In practice, very few systems have robust constraints on all the above observables. For most systems, only the masses and radii are known to high precision. A subset of these have precise constraints on the temperatures and rotational velocities, and even fewer possess [Fe/H] determinations (although it is sometimes possible to indirectly infer the composition for members of clusters). However, even systems with only masses and radii can provide useful constraints on the models: fixing the system age from the mass and radius of one star and requiring the model to accurately predict the observed radii for the other star (given its mass) at the same age is still a significant and valuable test.

Torres et al. (2010), building on the work of Andersen (1991), compiled all known stars with masses and radii determined to a precision of $\leqslant 3\%$. With the sole exception of α Centuri, these 95 systems were all detached, double-lined EBs. Figure 1.3 shows the

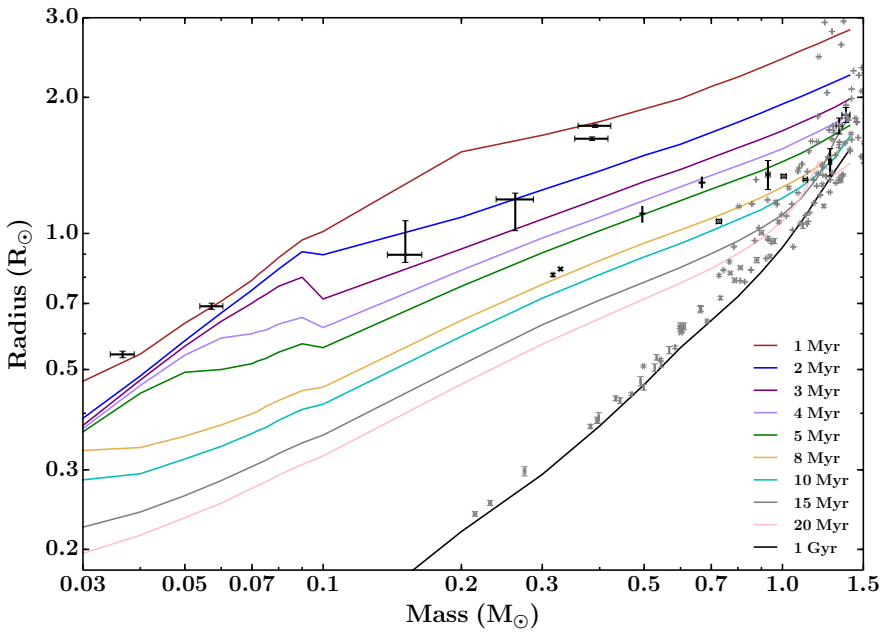

Figure 1.3: Mass-radius relation for low-mass EBs. The grey points show measurements for main sequence stars with masses $< 1.5\,M_{\odot}$ in detached EBs[7], and black points show measurements for pre-main sequence stars (see Table 1.2). The lines show, from top to bottom, the theoretical isochrones of Baraffe et al. (2015, BHAC15) for 1, 2, 3, 4, 5, 8, 10, 15, 20 Myr and 1 Gyr (brown, blue, purple, lilac, green, grey, ochre, cyan, grey, pink and black, respectively. $Y = 0.28$, [M/H] = 0, mixing length $\alpha = 1.6$).

existing mass and radius measurements for low-mass, detached EBs[6]. Perhaps the most important discrepancy between current observations and models is the fact that low-mass stars are observed to be larger and cooler than predicted by the models: theoretical models under-predict radii by up to 10% (see Fig 1.4; Torres & Ribas, 2002; Ribas, 2003, 2006; López-Morales & Ribas, 2005; Coughlin et al., 2011) and over-predict temperatures by up to ∼400 K (Torres et al., 2010). The radii and effective temperature discrepancies combine to essentially yield similar luminosities as single stars, suggesting that this is a surface phenomenon. The radius and temperature discrepancies have been attributed primarily to magnetic activity, but also to rotation, albeit with arguably less success (López-Morales, 2007; Feiden & Chaboyer, 2012a; Feiden, 2015a). Magnetic activity inhibits convection, which means the radius must increase to allow the star to cool and maintain hydrostatic equilibrium; therefore, larger, cooler stars are observed (Chabrier et al., 2007; Morales et al., 2010; Macdonald & Mullan, 2010).

Testing stellar evolution models with EBs assumes that the stars can be considered

[6]Data from John Southworth's catalogue, `http://www.astro.keele.ac.uk/~jkt/debdata/debs.html`.

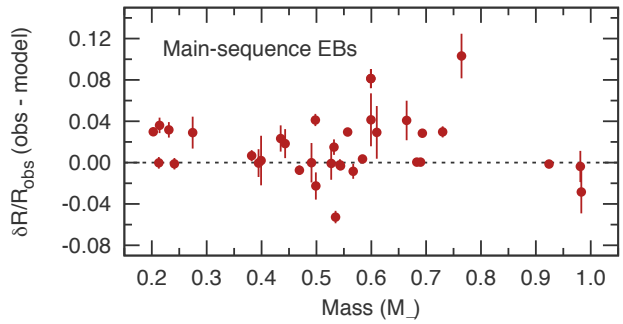

Figure 1.4: Radius discrepancy for low-mass, main-sequence EBs. Difference between observed and model-predicted radii of stars in detached-EBs below 1 $M_{\odot}$. [Taken from Feiden (2015a); adapted from Feiden & Chaboyer (2012a)]

to evolve independently. This has been questioned for close-separation binaries, which are spun up by tidal interactions, and are more magnetically active than single stars of comparable masses and ages. Coughlin et al. (2011) find that the radius excess seen in members of EBs decreases as the orbital period increases, suggesting that the radius excess may be a by-product of interactions between the two components of a close binary system. Indeed, long period main sequence EBs, with component masses $M \gtrsim 0.7\,M_{\odot}$, appear not to exhibit a radius excess (e.g. Lacy et al., 2005; Bass et al., 2012; Southworth, 2013). However, it is worth noting that: a) at lower masses a radius excess is observed in some main sequence systems, even at long periods (e.g. Irwin et al., 2011), and b) a radius excess is also observed in single low-mass stars (e.g. Hoxie, 1973) including those measured using interferometry (e.g. Boyajian et al., 2012b).

Mullan & MacDonald (2001), Chabrier et al. (2007) and Feiden & Chaboyer (2012b) studied the impact of this enhanced magnetic field on convective processes within low-mass stars possessing radiative cores, finding that it could explain the observed cool temperatures and large radii. The required magnetic field strengths are consistent with both direct (Reiners, 2012) and indirect observational determinations (Feiden & Chaboyer, 2013; MacDonald & Mullan, 2014). However, the situation is more complex for fully convective stars: to explain the observations requires internal magnetic field strengths in excess of $\sim$1 MG, which is questionable (Feiden, 2015a).

In terms of the observed radii of active stars in EBs, starspots and the magnetic field

structures that give rise to them, are arguably more important than global magnetic field strengths. Starspots that are unaccounted for in light curve modelling efforts can bias the radius determination, predominately affecting the relative radius sum. Morales et al. (2010) and Windmiller et al. (2010) showed that the radius sum can be biased by up to 6%, depending on the spot coverage, properties and locations. Although this is unlikely to explain the inflated radii in all systems, it is nevertheless worth noting.

While magnetic activity is a promising solution to the observed radius discrepancies in low-mass stars with radiative cores, the situation is more complex for fully convective stars. It is also possible that mass-dependent convective efficiency, heavy element composition, Helium abundance and differences in the internal structure could also contribute to rectifying the current radius and temperature discrepancies in all low-mass stars (Feiden, 2015a).

1.3.6 Constraints and discrepancies on the pre-main sequence

PMS stars represent a significant challenge for stellar evolution models due to their additional complexity. Young stars typically exhibit strong magnetic activity in the form of starspot modulation, as well as strong Hα and X-ray emission (Stassun et al., 2004; Gillen et al., 2014; Kraus et al., 2015). In addition, they are faster rotators than their MS counterparts, which have begun to spin down, losing angular momentum through a magnetised stellar wind (Irwin & Bouvier, 2009). Furthermore, for up to the first ∼few Myr, systems undergo significant accretion, which is either ongoing or recent enough to still be potentially important. Finally, as PMS binary stars are contracting under their own gravity, the tidal forces observed could be lower than throughout the majority of their history. To compound the above issues, stars that will eventually develop a radiative core are expected to be fully convective during the early stages of PMS contraction; fully convective MS stars are among the most discrepant with models and hardest to resolve (Feiden, 2015a).

However, given the above difficulties, the PMS is an important region of parameter space because it corresponds to a period of very rapid evolution, when the models are still sensitive to their initial conditions. Fundamentally, the absolute ages provided by

PMS stellar evolution models describe the formation and thermal evolution of stars, inform the evolution of magnetic activity and angular momentum, and determine protoplanetary disk lifetimes, which directly constrains gas giant planet formation theory; these motivate significant effort to discover and characterise more PMS touchstone stars. Despite this, there are very few observational constraints on the PMS (see Figure 1.3): to the best of our knowledge at the time of writing, there are only eight published low-mass EBs, where both components are PMS objects with masses below $1.5\,M_{\odot}$ and have known radii (see Table 1.2 for details). Six of the eight are located in Orion.

Dynamical mass constraints, being arguably *the* fundamental parameter, have been compiled and compared to model predictions over the last decade. Hillenbrand & White (2004) considered 27 pre-main sequence stars (predominantly astrometric binaries and those with measured disk kinematics, but also including the known PMS EBs). They find good agreement between predicted and dynamical masses above $1.2\,M_{\odot}$ but below this value most models systematically underpredict the observed masses by 10–30% (the greater discrepancy corresponding to lower masses).

Mathieu et al. (2007) also find that stellar evolution models underpredict dynamical mass measurements for their sample of 23 PMS stars younger than 10 Myr (10 stars in EBs, 9 with either solely disk kinematics or including a spectroscopic orbit, and 4 astrometric binaries). They also highlight limitations in the mass comparison arising from systematic errors in the determined effective temperatures and luminosities.

Stassun et al. (2014) compared the 13 known PMS EBs[7] with masses below $4\,M_{\odot}$ to a suite of PMS stellar evolution models. No set of model isochrones is able to reproduce the measured properties of all EBs (masses, radii and effective temperatures). From observed radii and effective temperature estimates, the model-predicted masses are consistent with observations to within 10% above $1\,M_{\odot}$ but at lower masses they are discrepant by 50–100% (see Figure 1.5, left six panels). This is perhaps unsurprising given the observed properties of some low-mass members of the sample: the one BD-BD EB shows a temperature reversal, with the less luminous secondary being hotter (2MJ0535-05; Stassun et al. 2007)

[7] at the time.

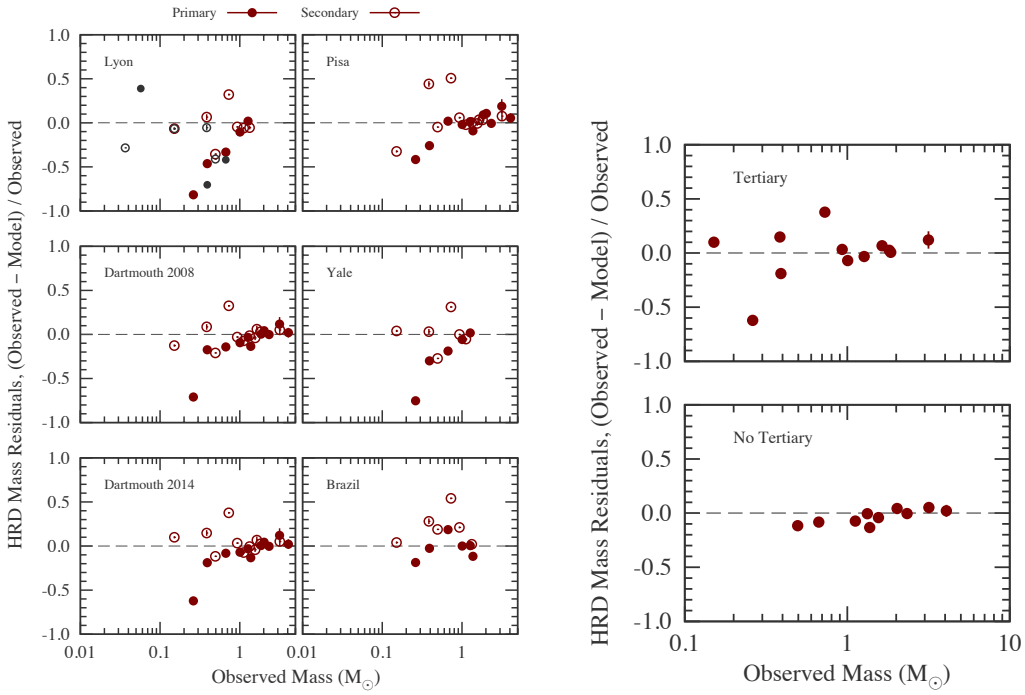

Figure 1.5: *Left*: discrepancy between observed and model-predicted masses from fitting PMS EBs in the H-R diagram. Each panel shows the results for a different set of models, with primary and secondary stars depicted with filled and open circles, respectively. For the 'Lyon' (BCAH98) models both $\alpha_{\rm MLT} = 1.0$ and 1.9 models were used below 0.6 $M_{\odot}$ (only the $\alpha_{\rm MLT} = 1.0$ models extend down to 0.02 $M_{\odot}$ to fit the brown dwarf EB). *Right*: Comparison of the mass residuals between systems with and without tertiary companions (top and bottom, respectively). The mass residuals are shown relative to the predictions of the Dartmouth 2014 models (i.e. the binary and tertiary systems from the bottom left subplot in the left hand panels have been separated). [Adapted from Stassun et al. (2014)]

and another system, comprising two equal-mass stars shows significant temperature and radius differences (Par 1802; Gómez Maqueo Chew et al. 2012). Generally, the models overpredict the masses of primaries but underpredict the masses of secondaries. Correcting for magnetic activity helps rectify the observed discrepancies in some systems but fails as a general solution. Interestingly, systems containing a tertiary companion (half of the sample) show the largest deviations from model predictions (see Figure 1.5, right hand panels). Focussing on systems without third stars, the model-predicted masses are consistent with observations to within 10% down to 0.5 $M_{\odot}$ (below which the sample is comprised exclusively of triples). Reipurth & Mikkola (2012) suggest that triple systems are born compact but can develop extreme hierarchical architectures over Myr timescales as the tertiary component is scattered into a wide orbit. In such a scenario, energy is transferred from the tertiary orbit into both the binary orbit and the individual components: the binary orbit shrinks and heat is deposited into one or both stars (most likely through successive

periastron passages). For the latter, the deposited energy must be rapidly dissipated within the stars from large-to-small scales so as to quickly provide support against gravity, e.g. via convective turbulence. Initial analysis suggests that the energy contained in tertiary orbits could be sufficient to explain the scatter in EB properties through the injection of heat. In addition, if the binary orbit is shrunk at a young enough age, when the two stellar radii are large, increased tidal interaction between the binary components can also inject heat (Stassun et al., 2014). As the Li abundances of stars in both binaries and triples are broadly in agreement with model predictions for their ages, the effect of a tertiary companion appears to be mainly restricted to the surface layers.

It is important to note that using binary stars to calibrate models of single star evolution on the PMS is more dubious than for the MS. In our current understanding, young binary stars are subject to strong tidal interactions during their first few Myr; these can slow stellar contraction rates by pumping energy into the stars. Given that PMS EBs in triple systems are more discrepant with models than their binary counterparts, tidal heating might play an important role in the evolution of stellar structure during the PMS phase (Feiden, 2015b). On the other hand, studies of single PMS stars with well-determined effective temperatures and luminosities also find discrepancies with models, which predict systematically younger ages for decreasing effective temperature (Malo et al., 2014).

Given the high levels of observed activity in PMS stars, the theoretical effort to reconcile the current discrepancies has focussed predominantly on magnetic fields and starspots, and on accretion.

Magnetic fields: PMS stars are powered through the release of gravitational potential energy from their contraction. Magnetic fields inhibit convection, reducing the outward energy flow and hence both decreasing the surface temperature and slowing the contraction. Magnetic young stars are therefore larger and cooler than non-active stars of the same mass and age. It is important to note that young, low-mass magnetic stars are not 'inflated' like their MS counterparts, but rather they simply undergo a more gradual contraction. Magnetic inhibition of convection is a promising avenue for reconciling

Table 1.2: Known low-mass, pre-main sequence eclipsing binary systems below $M \leqslant 1.5\,M_{\odot}$.

Name	$M_{\rm pri}$ ($M_{\odot}$)	$M_{\rm sec}$ ($M_{\odot}$)	$R_{\rm pri}$ ($R_{\odot}$)	$R_{\rm sec}$ ($R_{\odot}$)	Cluster *	Age (Myr)	Reference(s)
2MJ0535-05	0.06	0.04	0.68	0.49	ONC	~ 1	Stassun et al. (2006, 2007)
JW 380	0.26	0.15	1.19	0.90	ONC	~ 1	Irwin et al. (2007)
UScoCTIO 5	0.33	0.32	0.83	0.81	Up Sco	~ 5–11	Kraus et al. (2015)
Par 1802	0.39	0.39	1.73	1.62	ONC	~ 1	Cargile et al. (2008); Stassun et al. (2008) Gómez Maqueo Chew et al. (2012)
CoRoT 223992193	0.67	0.50	1.30	1.11	NGC 2264	~ 3	Gillen et al. (2014)
ISOY J0535-0447	0.83[a]	0.05[a]			ONC	~ 1	Morales-Calderón et al. (2012)
V1174 Ori	1.00	0.73	1.34	1.07	Ori OB 1c	~ 5–10	Stassun et al. (2004)
RXJ 0529.4+0041A	1.27	0.93	1.44	1.35	Ori OB 1a	~ 7–13	Covino et al. (2000, 2001, 2004)
ASAS J0528+03	1.38	1.33	1.83	1.73	Ori OB 1a	~ 7–13	Stempels et al. (2008)
MML 53	0.99	0.86	2.20[b]		UCL	~ 15	Hebb et al. (2010, 2011); Stassun et al. (2014)

* ONC = Orion Nebula Cluster, UCL = Upper Centaurus Lupus and Up Sco = Upper Scorpius.

[a] preliminary estimates.

[b] radius sum: $(R_{\rm pri} + R_{\rm sec})/a$.

models with observations: for example, introducing magnetic fields has reconciled the apparent age discrepancy between the low and higher mass populations of the β-Pic moving group (Macdonald & Mullan, 2010; Malo et al., 2014). Although encouraging, a better understanding of magnetic field strengths in young stars, specifically as a function of age and effective temperature, is required to test the predicted fields in magnetic models (Feiden, 2015b).

Starspots: Starspots inhibit outgoing flux and hence slow the contraction in much the same way as magnetic inhibition of convection (Jackson & Jeffries, 2014). However, as the stellar surface is comprised of different temperature regions, they can affect stars differently depending on their exact properties, and hence could provide an explanation for the observed spreads in PMS colour-magnitude diagrams (Feiden, 2015b).

Accretion: Accretion is an obvious process to include given that in standard models the star is supposed to evolve from the early PMS as an already formed object. Baraffe et al. (2012) showed significant differences between accreting and non-accreting models. Importantly, they predict that, if most of the accreted energy is radiated away (which is expected for the modest initial core masses that will eventually become low-mass stars),

accreting stars should have smaller radii than non-accreting stars of the same age and mass. However, Tognelli et al. (2013) show that for high accretion rates the star cannot radiate away enough energy to contract and in fact achieve similar radii and luminosities to non-accreting stars by the end of the total convective phase.

1.4 Modelling eclipsing binary data I. Radial velocity determination

As previously mentioned, eclipsing binaries are typical binary systems that are simply orientated close to edge on, such that we observe eclipses. The probability of an eclipse occurring for a given inclination angle depends on the sizes of the two stars relative to their separation, and the frequency of eclipses depends on the orbital period. Given these constraints it is easy to see why known eclipsing binaries are unresolved. As we cannot observe each star individually we cannot determine its orbit in three dimensional space. However, due to the close proximity of the stars, and therefore typically high orbital velocities, EBs are well-suited to spectroscopic characterisation. This allows us to determine some orbital properties relevant to the derivation of the stellar masses and separations.

A full derivation of the two body problem and the orbital elements of a binary system is beyond the scope of this work and is readily available in the literature. The reader is referred to, for example, *Celestial Mechanics* by J. B. Tatum and *An Introduction to the Evolution of Single and Binary Stars* by Matthew Benacquista for fuller discussions. The former details a primarily geometric derivation of the orbital parameters and the latter focusses on conservation of energy and angular momentum. Here, we restrict ourselves to a discussion of spectroscopic orbits but first detail certain properties of elliptical orbits as needed to place the spectroscopic derivation into context. We begin by presenting a geometric discussion of ellipse properties as it is intuitive and sufficient for the present purpose, although we note that conservation of energy and angular momentum considerations are perhaps more physically insightful.

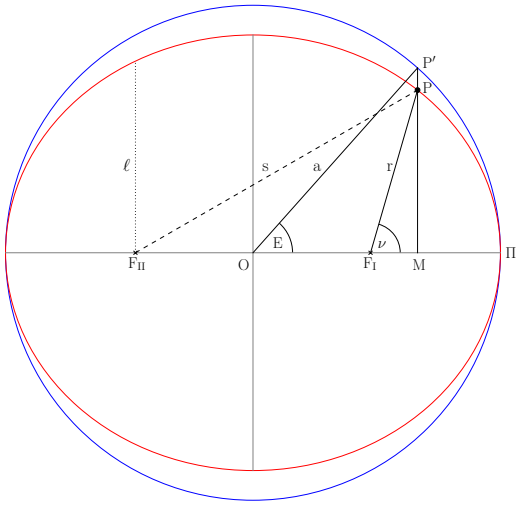

Figure 1.6: Properties of an ellipse. The star lies at position P (black point) on the ellipse (red) and orbits the focus F_{I} (the other focus of the ellipse is denoted F_{II}). The angle ν (the true anomaly) represents the angle swept out by the star from the focus F_{I} relative to the reference direction (Π). Similarly, angle E (the eccentric anomaly) represents the angle swept out by the star from the centre of the ellipse O relative to the reference direction (Π). The auxiliary circle to the ellipse is shown in blue. a represents the semi-major axis of the ellipse (and, by definition, the radius of the auxiliary circle) and r the distance from the star to the focus F_{I}. ℓ is the *semi latus rectum* which is the vertical distance from a focus to the ellipse edge.

1.4.1 Elliptical geometry

Any two gravitationally bound bodies travel on elliptical orbits around their common centre of mass[8]. An ellipse can be defined as the locus of a point that moves such that the sum of its distances from two fixed points called the foci is constant (see Figure 1.6). The equation of an ellipse is given by

$$\frac{x^2}{a^2} + \frac{y^2}{b^2} = 1 \tag{1.6}$$

where $b^2 = a^2(1 - e^2)$ and defines the eccentricity of the ellipse. A line drawn parallel to the minor axis and passing through the focus is called a *latus rectum*. The length of the semi latus rectum is commonly denoted as l and can be determined by setting $x = ae$ in equation 1.6 to give

$$l = a(1 - e^2) \ . \tag{1.7}$$

From our definition of the ellipse, i.e. that the sum of the distances from any point on

[8]Strictly speaking this is true only for point masses, as the mass distribution within celestial bodies, as well as relativistic effects, give rise to apsidal motion.

the ellipse to the two foci is equal to twice the semi-major axis, we can write

$$s = 2a - r \tag{1.8}$$

and, using the cosine formula on the triangle $F_{\rm I}PF_{\rm II}$, we can also define s as

$$s = \left(4a^2e^2 + r^2 + 4aer\cos\nu\right)^{1/2} \tag{1.9}$$

which, equating the two and using equation 1.7, gives

$$r = \frac{l}{1 + e\cos\nu}\ . \tag{1.10}$$

Ideally, as our observations are typically conducted as a time-series, we want to relate the true anomaly ν to time t. This process is conducted in three steps: first, we define the average angular speed of a star over its orbit (and hence average angle) and relate it to time; second, we relate the eccentric anomaly E to this average angle; and third, we relate the true anomaly ν to the eccentric anomaly E, thereby defining the true anomaly ν as a function of time. Let us begin by defining the time of periastron passage (i.e. when the star is located at Π) as $t = T$. The period of the orbit is given by Kepler's third law

$$P^2 = \frac{4\pi^2}{GM}a^3 \tag{1.11}$$

where $M = m_1 + m_2$ and G is the gravitational constant. The radius vector from star to focus $F_{\rm I}$ sweeps out equal areas in equal time intervals (Kepler's second law) but, over a full orbit, possesses an *average* angular speed of $2\pi/P$. We can therefore define this average angle as

$$\mathcal{M} = \frac{2\pi}{P}(t - T) \tag{1.12}$$

where $\mathcal{M}$ is termed the mean anomaly.

The second step is to relate the mean anomaly to the eccentric anomaly E. In time $t-T$, the motion of the star sweeps out the area $\rm F_IP\Pi$, which is equal to $(t-T)\pi ab/P$. This has a corresponding area in the auxiliary circle of $\rm F_IP'\Pi$, which is equal to $(t-T)\pi a^2/P$ (every ordinate on the two surfaces are related by the multiplicative factor b/a). We note that $\rm F_IP'\Pi$ = OP'Π – OP'$\rm F_I$, and that OP'$\Pi = \frac{E}{2\pi} \times \pi a^2 = \frac{1}{2}Ea^2$ and OP'$\rm F_I$ =

$\frac{1}{2}ae \times a\sin E = \frac{1}{2}a^2 e\sin E$. Equating the two expressions for the area swept out by the star gives

$$\frac{(t-T)\pi a^2}{P} = \frac{1}{2}Ea^2 - \frac{1}{2}a^2 e\sin E \tag{1.13}$$

which immediately yields the relation between the mean and eccentric anomalies

$$\mathcal{M} = E - e\sin E\ . \tag{1.14}$$

This is *Kepler's equation.* Finally, we wish to relate the true anomaly to the eccentric anomaly. The radius vector r can be written as

$$r^2 = (PM)^2 + (F_1M)^2 = b^2\sin^2 E + a^2(\cos E - e)^2 \tag{1.15}$$

Substituting $\sin^2 E = 1 - \cos^2 E$ and $b = a(1-e)$ gives

$$r = a(1 - e\cos E)\ . \tag{1.16}$$

Considering the right angle triangle F_1PM, it now becomes possible to write

$$\cos\nu = \frac{\cos E - e}{1 - e\cos E}\ . \tag{1.17}$$

This then defines the true anomaly ν as a function of time through equations 1.14 and 1.12. We now have all the required information to characterise the orbits of stars based on their doppler signals.

1.4.2 Spectroscopic orbits

The frequency of spectral lines shift due to the observed motion of the two stars around their common centre of mass. From these shifts we can determine the total radial velocity of each star, which is a combination of the system's recessional velocity from the Sun and the individual velocities of the stars

$$V_{\rm rad} = \dot{z} + V_{\rm sys} \tag{1.18}$$

where $\dot{z}$ is the velocity in the z-direction (towards/away from the observer) and $V_{\rm sys}$ is the systemic (or recessional) velocity. Following the notation in Figure 1.7, we see that the

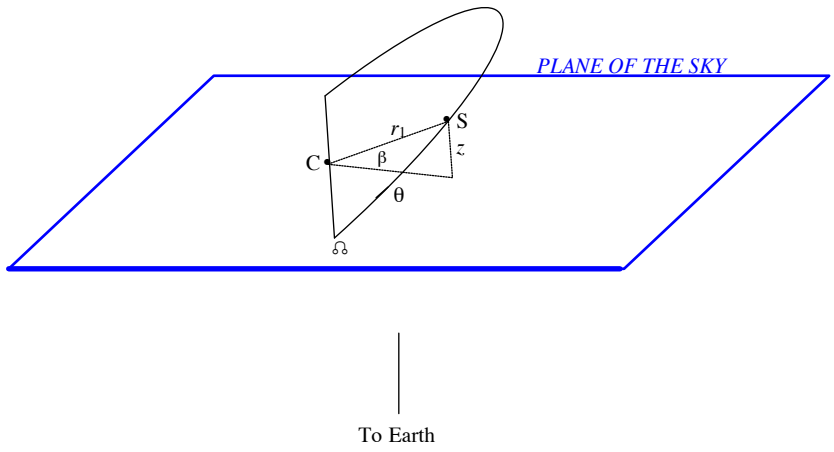

Figure 1.7: Orbital elements of an elliptical orbit. Star 1 is located at S, a distance r_1 from its focus C. The argument of latitude $\theta = \nu + \omega$ subtends the angle between star 1 and the ascending node Ω. z denotes the distance of the star away from the plane of the sky, which is subtended by the angle β. [Taken from Celestial Mechanics by J. B. Tatum]

z-component of the star (which we denote as star 1) in its orbit is

$$z_1 = r_1 \sin\beta \tag{1.19}$$

$$= r_1 \sin(\nu + \omega) \sin i \ . \tag{1.20}$$

where we have substituted $\theta = \nu + \omega$. In section 1.4.1, we assumed the ellipse major axis was aligned with the reference direction, whereas in practice orbits are randomly aligned; introducing the longitude of periastron, ω, as the angle between the ellipse major axis and the reference direction (ascending node) allows us to consider all orientations. Equation 1.20 implies an observed radial velocity of

$$\dot{z}_1 = \sin i \, [\, \dot{r}_1 \sin(\nu + \omega) + r_1 \dot{\nu} \cos(\nu + \omega) \,] \tag{1.21}$$

Ideally, we wish to express $\dot{z}_1$ in terms of the orbital elements. Remembering equation 1.10 we can obtain

$$\dot{r}_1 = \frac{e r_1 \dot{\nu} \sin\nu}{(1 + e\cos\nu)} \ . \tag{1.22}$$

To relate $r_1\dot{\nu}$ to the orbital elements requires consideration of the angular momentum, which can be written as

$$r_1^2 \dot{\nu} = L_1 = \frac{m_2^2}{M^2} L = \frac{m_2^2}{M^2} \sqrt{GMa(1-e^2)} \tag{1.23}$$

where $L = J/\mu$ is the specific angular momentum of the system, J is the angular momentum and μ the reduced mass. Using Kepler's third law (equation 1.11) and substituting $a = a_1 M/m_2$ we obtain

$$r_1^2 \dot{\nu} = \frac{2\pi}{P} a_1^2 \sqrt{(1-e^2)} \ . \tag{1.24}$$

which yields the required relation

$$r_1 \dot{\nu} = \frac{2\pi a_1^2 \sqrt{1-e^2}}{r_1 P} = \frac{2\pi a_1 (1 + e\cos\nu)}{P\sqrt{1-e^2}} \ . \tag{1.25}$$

Substituting equations 1.22 and 1.25 into 1.21, and applying the sine and cosine sum identities[9], gives

$$\dot{z}_1 = \frac{2\pi a_1 \sin i}{P\sqrt{1-e^2}} \left[\cos(\nu+\omega) + e\cos(\omega) \right] \ . \tag{1.26}$$

Equation 1.18 can now be written as

$$V_{\mathrm{rad},1} = K_1 \left[\cos(\nu+\omega) + e\cos(\omega) \right] \ + \ V_{\mathrm{sys}} \tag{1.27}$$

where $K_1 = 2\pi a_1 \sin i/(P\sqrt{1-e^2})$ is the *semi-amplitude of the velocity.* It is clear from equation 1.27 that the extrema of $V_{\mathrm{rad},1}$ occur when $\nu + \omega = 0$ and π (maximum and minimum, respectively), i.e. the extrema are at the line of nodes. Therefore,

$$V_{\mathrm{max},1} = K_1 \left[e\cos(\omega) + 1 \right] \ + \ V_{\mathrm{sys}} \tag{1.28}$$

$$V_{\mathrm{min},1} = K_1 \left[e\cos(\omega) - 1 \right] \ + \ V_{\mathrm{sys}} \tag{1.29}$$

and subtracting one from the other gives

$$K_1 = \frac{1}{2} \left(V_{\mathrm{max},1} - V_{\mathrm{min},1} \right) \ . \tag{1.30}$$

By considering the first terms on the right hand side of equations 1.28 and 1.29 we also see that

$$e\cos\omega = \frac{\dot{z}_{\mathrm{max},1} + \dot{z}_{\mathrm{min},1}}{2K_1} \ . \tag{1.31}$$

$e\cos\omega$ is also related to the relative timings the primary and secondary eclipses and is typically better constrained from the light curve.

[9] $\sin(\nu+\omega) = \sin\nu\cos\omega + \cos\nu\sin\omega$ and $\cos(\nu+\omega) = \cos\nu\cos\omega - \sin\nu\sin\omega$

Equation 1.27 gives the radial velocity as a function of the true anomaly, whereas it is more convenient to define it as a function of time. This is relatively straightforward as we already have the means to relate the true anomaly to time. Equations 1.12, 1.14 and 1.17 relate the mean anomaly to time, the mean anomaly to the eccentric anomaly and the eccentric anomaly to the true anomaly, respectively, thereby allowing us to calculate the radial velocity as a function of time. Equation 1.14 is a transcendental equation in E, which is typically solved using e.g. the Newton-Raphson method.

Fitting equation 1.27 to the observed radial velocities yields estimates of K_1, e, ω and $V_{\rm sys}$. If we have a double-lined system where we can trace the orbits of both stars we can write down expressions for the two semi-major axes. Remembering that $K_1 = 2\pi a_1 \sin i/(P\sqrt{1-e^2})$, we can write

$$a_1 \sin i = \frac{\sqrt{1-e^2}}{2\pi} K_1 P \tag{1.32}$$

$$a_2 \sin i = \frac{\sqrt{1-e^2}}{2\pi} K_2 P \ . \tag{1.33}$$

Given that we know $m_1 a_1 = m_2 a_2$, we can use equations 1.32 and 1.33 to write

$$m_2 = m_1(a_1/a_2) = m_1 \left(\frac{a_1 \sin i}{a_2 \sin i} \right) = m_1 (K_1/K_2) \ . \tag{1.34}$$

Next, we apply this to Kepler's third law $GM = 4\pi^2 a^3/P^2$ to give

$$G m_1 \left(1 + \frac{K_1}{K_2} \right) \sin^3 i = \frac{4\pi^2 (a_1 \sin i + a_2 \sin i)^3}{P^2} \tag{1.35}$$

where we have expanded $a = a_1 + a_2$ and multiplied both sides by $\sin^3 i$. This allows us to directly substitute equations 1.32 and 1.33 into equation 1.35 to give

$$\begin{aligned} m_1 \sin^3 i &= \frac{4\pi^2}{P^2} \frac{(K_1 + K_2)^3}{G\left(1 + \frac{K_1}{K_2}\right)} \left(\frac{\sqrt{1-e^2}}{2\pi} P \right)^3 \\ &= \frac{P}{2\pi G} \left(1 - e^2\right)^{3/2} (K_1 + K_2)^2 K_2 \ . \end{aligned} \tag{1.36}$$

Similarly, m_2 can be determined by interchanging the subscripts 1 and 2 in equation 1.36,

$$m_2 \sin^3 i = \frac{P}{2\pi G} \left(1 - e^2\right)^{3/2} (K_1 + K_2)^2 K_1 \ . \tag{1.37}$$

These two equations allow us to determine the *projected* masses of both stars, as we do not know i. However, for EBs we can determine i from the eclipse shapes, which allows us to directly solve for the individual masses and semi-major axes in double-lined systems.

1.4.2.1 Mass function

For single-lined systems, where only the spectroscopic variations of one star are observed, we cannot solve for the individual masses and radii. However, using equation 1.34, we can write K_2 in terms of m_1, m_2 and K_1. Substituting for K_2 in equation 1.37 then gives

$$m_2 \sin^3 i = \frac{PK_1^3}{2\pi G} \left(1 - e^2\right)^{3/2} \left(\frac{m_1 + m_2}{m_2}\right)^2 \tag{1.38}$$

which can be rearranged to give

$$f(m) = \frac{m_2^3 \sin^3 i}{(m_1 + m_2)^2} = \frac{PK_1^3}{2\pi G} \left(1 - e^2\right)^{3/2} \tag{1.39}$$

where $f(m)$ is known as the mass function and can be used to determine m_2 for a given m_1.

1.4.3 Methods of radial velocity determination

To extract radial velocities from observed stellar spectra requires fitting the spectral line profiles with a representative model. Ideally, one would obtain high-resolution, high signal to noise spectra and model these directly with a suite of theoretical model spectra to determine the relevant RV information, rotational broadening, stellar temperatures, surface gravities and chemical composition. However, telescope time (as well as the use of high-resolution spectrographs) is at a premium and researchers often observe at medium resolution, achieving a signal-to-noise $S/N \gtrsim 30$. In addition, the use of theoretical model atmospheres is often complicated, especially at the low-mass end, by incomplete line lists and abundance ratios, e.g. it is well known that most theoretical models do not contain the correct prescription for molecules such as titanium oxide (TiO), which dominate the optical continuum in cool stars (although recently this has begun to improve; e.g. Husser et al. 2013).

In practice, therefore, directly fitting an observed spectrum with theoretical models has not been widely adopted. A simple variant on such a method would be to select one or more well-defined spectral lines and fit these with e.g. a double Gaussian model. The error on the RV measurement decreases with the number of lines N as $1/\sqrt{N}$. As each chosen

line must be both detectable and resolved above the noise, it is difficult to automate such a procedure (unless the spectra are high-resolution, high S/N) and hence, we do not use this approach for the majority of the work presented here. The one exception is a system discussed in Chapter 6 where very few lines were available. The most common method of extracting radial velocities is via cross-correlation, which is an alternative to direct-fitting approaches.

1.4.3.1 One dimensional cross-correlation

The cross-correlation technique measures the 'similarity' between the object spectrum and a template spectrum at different relative velocity shifts. The method, first presented in Simkin (1974) and further developed by Tonry & Davis (1979), is able to determine RVs for single stars as well as individual components of multiple star systems, provided these are well-matched by a single template spectrum. The cross-correlation function for an observed spectrum $f(n)$ and a template spectrum $g(n)$ is given by

$$C_{f,g}(s) = \frac{1}{N\sigma_f\sigma_g}\sum_n f(n)g(n-s) \tag{1.40}$$

where s is the velocity shift applied to the template spectrum, N is the number of bins in the spectra, and σ_f and σ_g are the root mean square (r.m.s.) of the spectra and template, respectively. The r.m.s. of the spectra is given by

$$\sigma_f^2 = \frac{1}{N}\sum_n f(n)^2 \tag{1.41}$$

where the same is true for the template spectrum simply replacing f with g. The summation in equation 1.40 is typically computed with a fast Fourier transform (FFT) for efficiency[10]. This allows us to re-write equation 1.40 as

$$C(k) = \frac{1}{N\sigma_f\sigma_g}F(k)G^*(k) \tag{1.42}$$

where $F(k)$ and $G(k)$ denote the discrete Fourier transforms (DFT) of $f(n)$ and $g(n)$ respectively, and * representes the complex conjugate.

[10]It transform the calculation from an $\mathcal{O}(N^2)$ to a $\mathcal{O}(N\log N)$ process.

Although widely used, the cross-correlation technique suffers from some drawbacks. Arguably, the most serious of these is that there is no principled way of determining errors directly from the cross-correlation function (CCF); this is discussed in detail in Chapter 3.

Another drawback is that the width of the CCF peaks are not the line profile of the object spectrum but are rather the quadrature sum of the widths of both the target spectrum and the template spectrum. For rapidly rotating stars or low spectral resolutions the CCF peaks can be blended for large fractions of the orbital phase, inhibiting extraction of the RVs and subsequent determination of the orbits. A similar method to cross-correlation, which does not suffer from this is the broadening function method introduced by Rucinski (2002), which solves directly for the line profile and which has been used in the analyses of EBs (Kraus et al., 2015).

It is important to note that one-dimensional cross-correlation is limited to cases where the spectral features of both stars can be extracted by correlation with a single template, i.e. a stellar spectrum of single temperature and surface gravity[11]. In cases where the spectral types of the binary components are significantly different the method generally fails to extract both components simultaneously. To extend the use of cross-correlation to systems with extreme brightness ratios, the cross-correlation technique has been extended to two and three dimensions (the latter to include triple systems). The limitations of 1D cross-correlation are shown and discussed in detail in Chapter 5 along with alternatives to the technique, namely 2D correlation and direct spectral modelling, where an implementation of the latter is also presented.

1.5 Modelling eclipsing binary data II. Light curve analysis

For a system to be designated an eclipsing binary requires photometry[12]. The apparent brightness of an EB over time is a function of the observed orbital geometry, variations in stellar brightness and shape, and additional sources of contaminating light. Stellar

[11] And also chemical composition but this is not generally considered an issue as the de facto assumption is that the binary components formed from the same natal cloud.

[12] In theory, if one possesses very high S/N spectroscopy at orbital phases corresponding to eclipses, it should be possible to measure the Rossiter–McLaughlin effect in the RV measurements. However, we are not aware of this detection method being used to date.

brightness variations and shape distortions can arise from e.g. limb darkening, magnetically active starspot regions, deformation of the stellar surfaces due to the gravitational pull of the other star (ellipsoidal variability), and oblateness caused by high rotational velocities (the rotational velocity at the equatorial regions is higher than at the pole). Contaminating light is usually due to a third star, either gravitationally bound in the case of a hierarchical triple or from an unassociated foreground / background star, which is aligned along the line of sight. Interacting stellar winds in massive binaries and accretion-related processes in young systems can also cause brightness variations. Given the multiple and complex origins, a physical interpretation of the apparent photometric brightness variations of an EB is a challenging task.

1.5.1 Eclipsing binary models

The analysis of EBs spans more than a century, with the first promising method presented in a two-part paper by Russell (1912a,b), which was subsequently applied to the EBs Z Draconis and RT Persei (Russell & Shapley, 1914), and was widely used for many years. It was eventually surpassed by computer-based methods such as the Wilson-Devinney (WD) model (Wilson & Devinney, 1971), WINK (Wood, 1973) and EBOP (Eclipsing Binary Orbit Program; e.g. Popper & Etzel, 1981; Etzel, 1981; Nelson & Davis, 1972). WD is based on the Roche equipotential model, which is computationally very expensive but gives it the required flexibility to model contact binaries (where both stars fill their Roche lobes), semi-detached binaries (where one star fills its Roche lobe) and detached binary stars (where both stars lie within their Roche lobes). The EBOP model approximates the stars as spheres for the eclipse shapes and as biaxial ellipsoids for the calculation of the reflection and ellipsoidal effects. It is therefore restricted to well-detached systems with only modest distortion. Intermediate in flexibility and computational expense to the WD and EBOP models is WINK, which approximates the surface of each star with a triaxial ellipsoid. WD-based and EBOP-based models remain very popular, arguably more so than WINK and its successors (Vaz, 1984, 1986; Vaz & Nordlund, 1985; Nordlund & Vaz, 1990) and we therefore focus on these two model structures in the following discussion.

1.5.1.1 WD-based models

The Wilson-Devinney series of EB models (WD, WD93, WD98, WD2003; e.g. Wilson & Devinney 1971; Wilson 1993) employ the Roche prescription of equipotential surfaces to directly compute the observed light through numerical integration over the stellar surfaces at each point in a grid of orbital phase. A major advantage of this approach is that much of the underlying physics affecting the observed light curve, such as tidal distortion, reflection, limb and gravity darkening, and starspots, are easily integrated into the model. Orosz & Hauschildt (2000) presented a similar model that directly incorporates model atmosphere specific intensities giving a better prescription of limb darkening. More recently, the WD model has been extended under PHOEBE (Physics Of Eclipsing BinariEs; Prša & Zwitter 2005), which includes a Nelder-Mead optimiser (rather than the differential corrections method employed in WD) and graphical user interface, as well as being able to model multiple light curves and incorporate radial velocity data.

1.5.1.2 EBOP-based models

The original EBOP model (Popper & Etzel, 1981; Etzel, 1981) is based on the Nelson-Davis-Etzel (NDE) model (Nelson & Davis, 1972; Etzel, 1980) and approximates the stars as biaxial spheroids. However, proximity effects (reflection and asphericity) are not included in the calculation of occulted light during eclipse and so the eclipse shapes are determined using spherical stars. Light curves are computed through numerical integration of concentric circles over each star and differential corrections performed to find the best fit. P and $T_{\rm prim}$ must be held fixed when performing differential corrections and only formal uncertainties are calculated. This latter point is particularly important as the parameters of EB models are generally correlated meaning that formal uncertainties tend to be overly-optimistic.

The above limitations motivated the development of JKTEBOP (Southworth et al., 2004, 2007), an extension of the EBOP code, which models single-band light curves. JKTEBOP employs a Levenberg-Marquardt optimisation algorithm in finding the best fit and contains Monte Carlo and residual-permutation algorithms for robust estimation of the uncertainties

in the derived light curve parameters. Recently, the ability to model RVs simultaneously with the light curve has been implemented (Southworth, 2013).

Another successor to the EBOP model was presented in Irwin et al. (2011, hereafter referred to as the Irwin model), who modified the light curve generator of EBOP/JKTEBOP and incorporated the analytic method of Mandel & Agol (2002) for the quadratic limb darkening law. An important step forward for the EBOP-based framework is the inclusion of a prescription to account for the effects of occulted and unocculted starspots[13]. As the light curve generator is a standalone piece of software it enables researchers to wrap their own preferred software tools, e.g. Markov chain Monte Carlo (MCMC), around the core module for robust determination of parameter uncertainties.

1.5.1.3 Consistency between the different light curve models

Numerous analyses have compared the results of the WD, WINK and EBOP frameworks on detached systems (e.g. Etzel 1980; Andersen et al. 1984, 1990, 1993; Clausen et al. 2008) and the results have been essentially identical in all parameters. However, the inclination can be susceptible to the different geometrical treatments of the stars, and has occasionally been found to be slightly discrepant (e.g. Popper & Etzel 1981; Andersen et al. 1993; Clausen et al. 2008). For rapidly-rotating (and hence oblate) stars that partially-eclipse, the inclination can be underestimated by EBOP due to the spherical approximation of the stars when computing the light in eclipse. For stars well-suited to a spherical approximation, inclination differences could also arise from uncorrected starspot effects or incorrect limb-darkening coefficients, as seen by Clausen et al. (2008) between all three WD, WINK and EBOP frameworks.

1.5.1.4 Models used in this work

As we are interested in testing models of stellar evolution we require well-detached EBs in which the stars can be assumed to have evolved relatively independently, i.e. they do not interact, except perhaps through stellar winds or large scale magnetic fields. All of

[13] Although we note this is not automated in the fitting procedure, rather the tools are simply available to re-run the analysis and observe the effects of different spot configurations.

the aforementioned light curve treatments are able to model such systems. We favour the EBOP framework and present analysis with both the JKTEBOP and Irwin models (primarily the former but, once it became publicly available, also the latter due to additional control available to the user). Below, we discuss the main properties of EBOP-based models and present simple geometric analyses of eclipses.

1.5.2 Properties of EBOP-based models

At the heart of any eclipsing binary model is the light curve generator, and at its heart is the treatment of eclipses. It is possible to write down the projected, i.e. plane-of-sky, separation of the two stars as a function of their orbital phase. To do so requires a transformation of the co-ordinate system typically used for binary systems (defined in the plane of the binary) into one defined relative to the plane-of-sky. It is relatively lengthy and arduous[14] and so here we simply quote its useful result, namely that the projected separation between the centres of the two stars is given by

$$\delta^2 = d^2 \left(\cos^2 i + \sin^2 i \sin^2 \Phi\right) \tag{1.43}$$

where $\Phi = \nu + \omega - 90$ and

$$d = d(\Phi) = \frac{1 - e^2}{1 + e\cos\nu} = 1 - e\cos E \ . \tag{1.44}$$

Therefore, the eclipsed area at any phase angle is dependent on the two stellar radii, $R_{\rm pri}$ and $R_{\rm sec}$ (as δ is the projected separation between the *centres* of the two stars), and on i, e and ω. This geometry is shown in Figure 1.8.

The area under the eclipse chord can then be analytically calculated, with expressions suited to the specific type of eclipse. In the following, subscripts f and b stand for the foreground and background stars, respectively, i.e. the eclipsing star and the eclipsed star. There are two main regimes for a given eclipse: when the two stars slightly overlap ($\delta^2 \geqslant |R_{\rm f}^2 - R_{\rm b}^2|$) and when they largely overlap ($\delta^2 < |R_{\rm f}^2 - R_{\rm b}^2|$). For the latter a further distinction is made if the larger component is being eclipsed (i.e. if $R_{\rm b} > R_{\rm f}$) and the eclipse is therefore annular.

[14]The interested reader is referred to e.g. Chapter 3 of Eclipsing Binary Stars: Modelling and Analysis by Josef Kallrath and Eugene F. Milone.

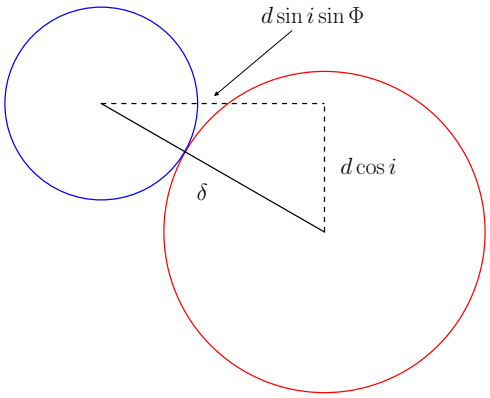

Figure 1.8: Projected plane-of-sky distance δ between the centres of the two stars (red and blue). δ is used to test whether an eclipse can occur, as a function of orbital phase. Represented here is the point of first contact.

1.5.2.1 Eclipse shapes

Assuming uniformly bright spheres, the lost light during eclipse can be calculated analytically. However, including the effects of limb darkening requires the stars to be divided into concentric rings and numerically integrated over. In the original EBOP model this was done using a simple linear limb darkening law (Russell, 1912b), in JKTEBOP it is possible to use the original linear law as well as the quadratic, square-root and logarithmic laws (Kopal, 1950; Diaz-Cordoves & Gimenez, 1992; Klinglesmith & Sobieski, 1970, respectively) and in the Irwin model the analytic method of Mandel & Agol (2002) is applied for the quadratic law.

We now consider, as an example, a partial eclipse. Here, for simplicity, we neglect limb darkening in order to obtain the following analytic relations, although we note that the method generalises to the full case. Figure 1.9 shows the geometry of the two stars during a partial eclipse. The lost light during eclipse is related to the area under the eclipse chord through the surface brightness of the eclipsed star. The area A is given by summing the sectors of each star and subtracting from these the non-eclipsed parts of each sector, i.e. the area of the kite. This can be written, equivalently, in the following two ways:

$$A = 2R_1^2\alpha + 2R_2^2\beta - \delta R_1 \sin\alpha \tag{1.45}$$

$$A = 2R_1^2\alpha + 2R_2^2\beta - \delta R_2 \sin\beta \tag{1.46}$$

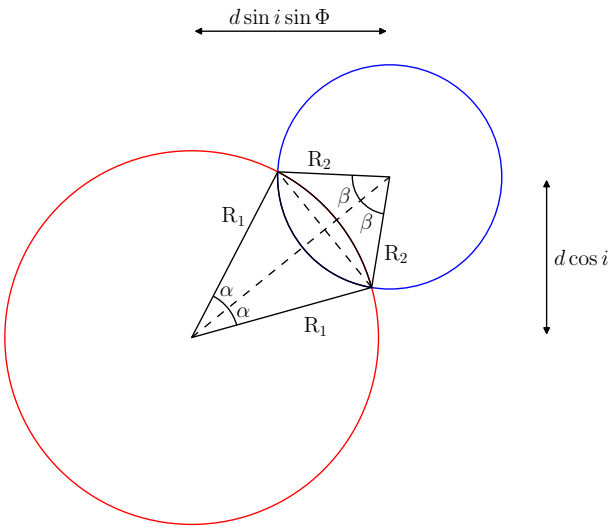

Figure 1.9: Geometry of a partial eclipse. The two stars are shown in red and blue (star 1 and 2, respectively) and the eclipse sectors in black. The sector half angles α and β are indicated along with the two stellar radii R_1 and R_2. The vertical and horizontal projected distances between the centres of the two stars are also shown (as defined in equation 1.43 and depicted in Figure 1.8). [Adapted from Irwin (2007)]

where the last term can be defined with with respect to R_1 and α or to R_2 and β. As above, δ represents the projected separation between the centres of the two stars (equation 1.43). The angles α and β are given through applying the cosine rule on the triangles comprising the kite,

$$\cos \alpha = \frac{\delta^2 + R_1^2 - R_2^2}{2\delta R_1} \tag{1.47}$$

$$\cos \beta = \frac{\delta^2 + R_2^2 - R_1^2}{2\delta R_2} \ . \tag{1.48}$$

These are equivalent to the corresponding set of equations in the original Nelson & Davis (1972) paper but presented in a slightly more intuitive manner (Nelson & Davis subtract off the non-overlapping part of the sector for each star individually rather than considering both stars together).

1.5.2.2 Eclipse durations

It is clear that the duration of an eclipse is given by the length of time where $\delta < |R_1 + R_2|$ is continuously satisfied. From Figure 1.9 we see that the projected distance from the beginning of ingress to mid-eclipse is given by

$$d \sin i \sin \Phi = \sqrt{(R_1 + R_2)^2 - d^2 \cos^2 i} \ . \tag{1.49}$$

which is related to time through the angle Φ. The duration of eclipse is simply the time taken for the star to travel twice this projected distance. We can divide equation 1.49 through by a to give an expression for the eclipse duration dependent on the ratio $(R_1 + R_2)/a$. We note that for circular orbits the distance between the two stars d is fixed to the semi-major axis a and hence the eclipse duration depends only on $(R_1 + R_2)/a$. As a depends on the RV semi-amplitudes (equations 1.32 and 1.33) this allows us to decouple the light curve solution from its dependence on the RV orbit; for circular systems the light curve and RV analyses can be performed independently, which is not possible for eccentric systems.

1.5.2.3 Eclipse depths

Consideration of the eclipse depths can provide useful insight into the binary properties. Following Irwin (2007), first, let us define the bolometric luminosity of each star as

$$L_1 = 4\pi R_1^2 \sigma T_1^4 \tag{1.50}$$

$$L_2 = 4\pi R_2^2 \sigma T_2^4 \tag{1.51}$$

where σ is the Stefan-Boltzmann constant and T denotes the effective temperature of the star. The total luminosity of the system outside of eclipse is simply given by

$$L_{\rm tot} = L_1 + L_2 \tag{1.52}$$

and at the centres of primary and secondary eclipse the light from the eclipsed star is decreased by the fraction under the eclipse chord, i.e.

$$L_{\rm pe} = (1 - f_1)L_1 + L_2 \tag{1.53}$$

$$L_{\rm se} = L_1 + (1 - f_2)L_2 \tag{1.54}$$

where f represents the fraction of the star occulted at the centre of eclipse and where we have designated star 1 as the brighter component, and hence as the primary star (primary eclipse *pe* occurs *by definition* when the brighter star is eclipsed). The fractional drop in brightness at the centre of each eclipse can then be written as

$$\zeta_{\rm pri} = \frac{L_{\rm tot} - L_{\rm pe}}{L_{\rm tot}} = 1 - \frac{L_{\rm pe}}{L_{\rm tot}} \tag{1.55}$$

$$\zeta_{\rm sec} = \frac{L_{\rm tot} - L_{\rm se}}{L_{\rm tot}} = 1 - \frac{L_{\rm se}}{L_{\rm tot}} \ . \tag{1.56}$$

The ratio of the secondary to primary eclipse depths is given by

$$\frac{\zeta_{\rm sec}}{\zeta_{\rm pri}} = \frac{L_{\rm tot} - L_{\rm se}}{L_{\rm tot} - L_{\rm pe}} \tag{1.57}$$

$$= \frac{f_2 L_2}{f_1 L_1} \ . \tag{1.58}$$

The ratio of eclipse depths therefore depends on the intrinsic luminosity of both stars as well as the area under the eclipse chord during each eclipse. For eccentric systems the area under the eclipse chord is not necessarily the same for primary and secondary eclipses. However, for non-eccentric systems ($e = 0$) the areas must be equal for both eclipses due to the circular nature of the orbits, i.e.

$$\pi f_1 R_1^2 = \pi f_2 R_2^2 \ . \tag{1.59}$$

This allows us to take a further step and relate the eclipse depths directly to the stellar effective temperatures. Substituting $f_2 = f_1 R_1^2 / R_2^2$ into equation 1.58 and making a further substitution for the luminosities from equations 1.50 and 1.51 gives

$$\frac{\zeta_{\rm sec}}{\zeta_{\rm pri}} = \frac{R_1^2 L_2}{R_2^2 L_1} \tag{1.60}$$

$$= \frac{R_1^2}{R_2^2} \frac{4\pi R_2^2 \sigma T_2^4}{4\pi R_1^2 \sigma T_1^4} \tag{1.61}$$

$$= \left(\frac{T_2}{T_1} \right)^4 \ . \tag{1.62}$$

It is clear from equation 1.60 that the ratio of eclipse depths is the ratio of the luminosities per unit area L/R^2, i.e. *the surface brightness*, of the two stars. For circular systems, therefore, the ratio of the stellar surface brightnesses J is given by the ratio of the eclipse depths, i.e.

$$J = \frac{\zeta_{\rm sec}}{\zeta_{\rm pri}} = \left(\frac{T_2}{T_1} \right)^4 \ . \tag{1.63}$$

It is important to note that this result refers to the bolometric surface brightness ratio as it is derived from the definition of bolometric luminosity. As EBs are observed in finite (albeit typically broad) bandpasses the observed eclipse depth ratio does not directly yield the effective temperature ratio; we need to apply a bolometric correction to equation

1.63. In this thesis we primarily analyse CoRoT photometry, whose bandpass extends from 300–1000 nm and therefore the observed eclipse depth ratio gives a relatively good approximation of the true stellar effective temperature ratio for solar-type stars, but not for significantly hotter or cooler objects.

1.5.2.4 Eccentricity and longitude of periastron

The eccentricity and orientation of the orbits (specifically, the longitude of periastron, ω) affect the relative timings and durations of eclipses. In EBOP-based models, e and ω are incorporated through the combination terms $e\cos\omega$ and $e\sin\omega$, as these tend to be less correlated and are also better determined when the orbit is only slightly eccentric (Etzel, 1993). To first approximation[15], $e\cos\omega$ depends on the phase of secondary eclipse relative to primary and $e\sin\omega$ depends on the relative durations:

$$e\cos\omega \approx \frac{\pi}{2}\left(\frac{t_{\rm sec}-t_{\rm pri}}{P}-0.5\right) \tag{1.64}$$

and

$$e\sin\omega \approx \frac{\delta_{\rm sec}-\delta_{\rm pri}}{\delta_{\rm sec}+\delta_{\rm pri}} \tag{1.65}$$

where $t_{\rm pri}$ and $t_{\rm sec}$, and $\delta_{\rm pri}$ and $\delta_{\rm sec}$ are the times and durations of primary and secondary eclipses, respectively (Southworth, 2012).

1.5.3 Additional effects in light curve analyses

So far we have neglected effects which are not easily incorporated into the above analytic considerations. We now discuss two of these: limb darkening and gravity brightening, and also discuss the effects of third light.

1.5.3.1 Limb darkening

Limb darkening is an optical effect that that causes the limb of a star to appear darker than its centre. It arises because, as the line of sight moves from the centre to the limb, a star is observed at increasing angle θ to the local surface normal. The observed flux can be approximated as the sum of that emitted from an optical depth of $\tau = 1$ to the surface

[15]Ignoring quadratic and higher order terms in e and assuming $i \approx 90^\circ$.

(at $\tau = 0$). The $\tau = 1$ surface corresponds to a physical depth $d_{\rm los}$ along the line-of-sight. Assuming uniform density in the stellar photosphere, the radial depth $d_{\rm r}$ inside the star is related to the line-of-sight depth $d_{\rm los}$ and angle θ via

$$d_{\rm r} = d_{\rm los} \cos\theta \tag{1.66}$$

i.e. the maximum physical depth from which flux is observed from inside the star decreases with increasing angle from centre to limb. As temperature increases with depth inside the photosphere, the line-of-sight averaged temperature observed decreases towards the limb, and therefore a lower surface brightness is measured.

In practice, the limb darkening is empirically parameterised using an analytic approximation. Several limb darkening laws exist, the simplest is the 'linear' approximation, which simply accounts for the $\cos\theta$ projection of the emergent flux

$$\frac{I_\lambda(\mu)}{I_\lambda(1)} = 1 - u_\lambda(1-\mu) \tag{1.67}$$

where $I_\lambda(1)$ is the specific intensity at the centre of the disc, u_λ is the wavelength-dependent linear limb darkening coefficient, which depends on the stellar effective temperature, surface gravity and chemical composition, and $\mu = \cos\theta$. The linear approximation is usually acceptable for low-mass dwarfs, especially for the typical precision of historic ground-based data. More complicated two-parameter laws have been proposed to better approximate the limb darkening profile, e.g. quadratic, logarithmic and square root laws, and more recently a four-parameter law (e.g. Claret, 2000; Sing, 2010; Claret et al., 2012, 2013). It is worth noting that very high precision observations of exoplanet transits, which are more sensitive to limb darkening, especially in the ultraviolet, require 3D atmospheres and four-parameter laws to obtain good fits. However, this is usually not required for EB studies. In this work we use the quadratic limb darkening law as it is widely tabulated, is available in both the JKTEBOP and Irwin models, and provides an acceptable approximation for EB light curves with the precision of CoRoT. The quadratic law is given by

$$\frac{I_\lambda(\mu)}{I_\lambda(1)} = 1 - a_\lambda(1-\mu) - b_\lambda(1-\mu)^2 \tag{1.68}$$

where a and b are the limb darkening coefficients for the linear and quadratic terms.

It is important to note that theoretical limb darkening coefficients are calculated from model atmospheres of isolated single stars. In close binaries the stellar atmospheres will be modified by the incident flux from the other star. The effect of external irradiation has been investigated by Claret & Gimenez (1990) and Claret (2004, 2007) for close binaries where a cool secondary star is strongly irradiated by a significantly hotter primary. They find that the specific intensity across the stellar face is significantly modified and can even lead to limb brightening. It is difficult to generalise the effect of external radiation on the limb darkening coefficients as it depends on many system parameters (e.g. both stellar temperatures, the radii of both stars relative to their separation and the angle of incidence), which inhibits its uptake into light curve synthesis codes. For the stars under consideration in this thesis, i.e. low-mass, well-detached systems, the effect of irradiation on limb darkening is not significant given the precision of the light curves and the limitations inherent in the modelling.

1.5.3.2 Gravity brightening

The equatorial surface regions of a rotating star move more rapidly than the polar regions and hence achieve hydrostatic equilibrium at larger radii, i.e. a rotating star is oblate with a larger radius at the equator than the pole. As the emergent flux is dependent on the local surface gravity, which is lower at the equator than the pole, the polar regions appear brighter; this is known as gravity brightening. A similar effect can also be seen in systems where tidal distortion from a companion object deforms the stellar surface preferentially at the equatorial regions (assuming spin-orbit alignment). Gravity brightening is usually parameterised as

$$F \propto g^{\beta} \ , \quad \beta = \begin{cases} 1.0 & \text{Radiative stars; von Zeipel (1924)} \\ \approx 0.32 & \text{Convective stars; Lucy (1967)} \end{cases} \tag{1.69}$$

where F is the local emergent flux, g the local surface gravity and β is the gravity brightening exponent. Alencar & Vaz (1997) investigate the form of β for temperatures $3700 \leqslant T \leqslant 7000$ K finding that the exponent values range between 0.2 and 0.4 (the 0.32

average result of Lucy (1967) best describes stars with $T = 6500$ K). For low-mass stars with convective envelopes, the effect of gravity brightening is typically small.

1.5.3.3 Third light

Third light refers to the presence of a third component, in addition to the two stars comprising the EB. This third star can either be an unassociated object aligned along the line of sight or be an associated third star in a hierarchical triple system, typically on a long orbit.

The RVs of the third star are generally non- or slowly-varying, which usually allows them to be distinguished from the binary components. They do not strongly effect the binary orbits and are typically neglected in RV analyses. The effect of a third star on the light curve, however, is more serious: essentially, the eclipses are diluted without changing their shape. To easily show this we can reconsider our derivation of the eclipse depths in section 1.5.2.3. By adding the luminosity of the third star L_3 to equations 1.52, 1.53 and 1.54 and performing the same derivation (equations 1.55–1.58) we see that the fractional drop in brightness during eclipse is reduced by a factor $\frac{L_1+L_2}{L_1+L_2+L_3}$ but that the ratio of the eclipses depths $\zeta_{\rm sec}/\zeta_{\rm pri}$ is unchanged.

The presence of third light in the light curve, if not well-constrained, complicates the analysis because it is strongly correlated with the orbital inclination i and the radius ratio $R_{\rm sec}/R_{\rm pri}$, which inhibits precise determination of the masses and radii. We note that certain eccentric alignments can break the degeneracy between orbital inclination and third light as a change in inclination will effect each eclipse differently but not a change a third light (Popper, 1984; Nelson & Davis, 1972).

1.5.3.4 Parameters of EBOP-based models

Now that we have taken an general look at the information contained within a typical light curve, we can see how this relates to the parameters determined from light curve modelling. The parameters in EBOP-based models are chosen to be closely related to the

eclipse shapes and to be as uncorrelated with each other as possible. The main parameters to compute light curves of spherical stars with EBOP-based models are:

- central surface brightness ratio, J
- sum of the radii relative to their separation, $(R_{\rm pri} + R_{\rm sec})/a$.
- ratio of the radii, $R_{\rm sec}/R_{\rm pri}$
- inclination[16], i
- eccentricity e and longitude of periastron ω, which are incorporated through the combination terms $e\cos\omega$ and $e\sin\omega$
- limb darkening coefficients $\mu^x_{\rm pri}$ and $\mu^x_{\rm sec}$ for various laws.
- third light, $L_3 = L_{\rm total} - L_{\rm pri} - L_{\rm sec}$

It is also possible to specify a phase correction for the centre of primary eclipse, a normalisation for the light curve if not given in relative flux/magnitude units and the size of the integration rings.

1.5.3.5 Solving for the fundamental parameters

In this section we briefly detail the process by which fundamental stellar parameters can be determined. From the light and radial velocity curves we can obtain[17],

Light curve: P, $(R_1 + R_2)/a$, R_2/R_1, i and $e\cos\omega$

RV curve: K_1, K_2 and $e\sin\omega$

Combining $e\cos\omega$ and $e\sin\omega$	$\Rightarrow$	e and ω
Combining K_1, K_2, i and e	$\Rightarrow$	M_1, M_2 and a (see equations 1.32–1.37)
Combining $(R_1 + R_2)/a$, R_2/R_1 and a	$\Rightarrow$	R_1 and R_2

Thus, the masses and radii of both stars in a detached, double lined eclipsing binary can be determined. These further yield surface gravities and mean densities. In addition, if we have a constraint on the effective temperature of one star then the other can be determined from the eclipse depth ratio. It is also possible to estimate the temperatures from the

[16] In the Irwin model $\cos i$ rather than i is used as it is less correlated with other parameters than i itself.
[17] We note that the period can also be found from the RV orbit and $e\sin\omega$ can be determined from the light curve, but generally they are better constrained as listed.

Table 1.3: Fiducial values of light curve parameters for investigating the effect of individual parameters on the eclipse shapes. The limb darkening coefficients chosen (for both stars) correspond to the theoretical predictions of Claret et al. (2012) for a star with $T = 4000$ K and $\log g = 4.0$ observed in the CoRoT bandpass. Note that all other parameters, e.g. those for gravity darkening and reflection, are set to zero.

Parameter	Symbol	Unit	Value
Central surface brightness ratio	J		0.6
Sum of radii	$(R_{\rm pri} + R_{\rm sec})/a$		0.3
Radius ratio	$R_{\rm sec}/R_{\rm pri}$		0.6
Orbital inclination	i	(°)	85
Orbital eccentricity	e		0
Longitude of periastron	ω	(°)	90
Linear LD coefficient	$u_{\rm pri}$ and $u_{\rm sec}$		0.6564
Non-linear LD coefficient	$u'_{\rm pri}$ and $u'_{\rm sec}$		0.0929
Third light	L_3		0

* LD = limb darkening

relative eclipse depths across multiple bands, but this is model dependent. Nonetheless, if we have constraints on the effective temperatures of the two stars then:

Combining $T_{\rm eff,1}$ and $T_{\rm eff,2}$, and R_1 and R_2 $\Rightarrow$ luminosities L_1 and L_2 (see equations 1.50 and 1.51) and distance (equation 1.72).

1.5.4 Effect of parameters on eclipse shapes

While some physical intuition can be derived from the mathematics, greater insight can generally be garnered from graphical representations. In this section we examine the effect of selected parameters on the shape of the eclipses. In an illustrative rather than exhaustive manner, we restrict ourselves to the following: the radius ratio, R_2/R_1; the surface brightness ratio, $J = {\rm SB}_2/{\rm SB}_1$; the inclination, i; the limb darkening parameters, u_1, u'_1, u_2 and u'_2; the effect of eccentricity and longitude of periastron, e and ω; and third light, L_3. Table 1.3 shows the fiducial parameter values used for all plots in this section, except where that specific parameter is being varied (in which case the parameter values used are specified in the figure captions and legends).

Radius ratio (Figure 1.10, top left): smaller radius ratios give shallower eclipses. For primary eclipse this is because relatively less of the primary light is occulted and for secondary eclipse it is because the secondary star contributes less of the total system light. In addition, eclipses are 'flatter' for smaller radius ratios as, for a given inclination

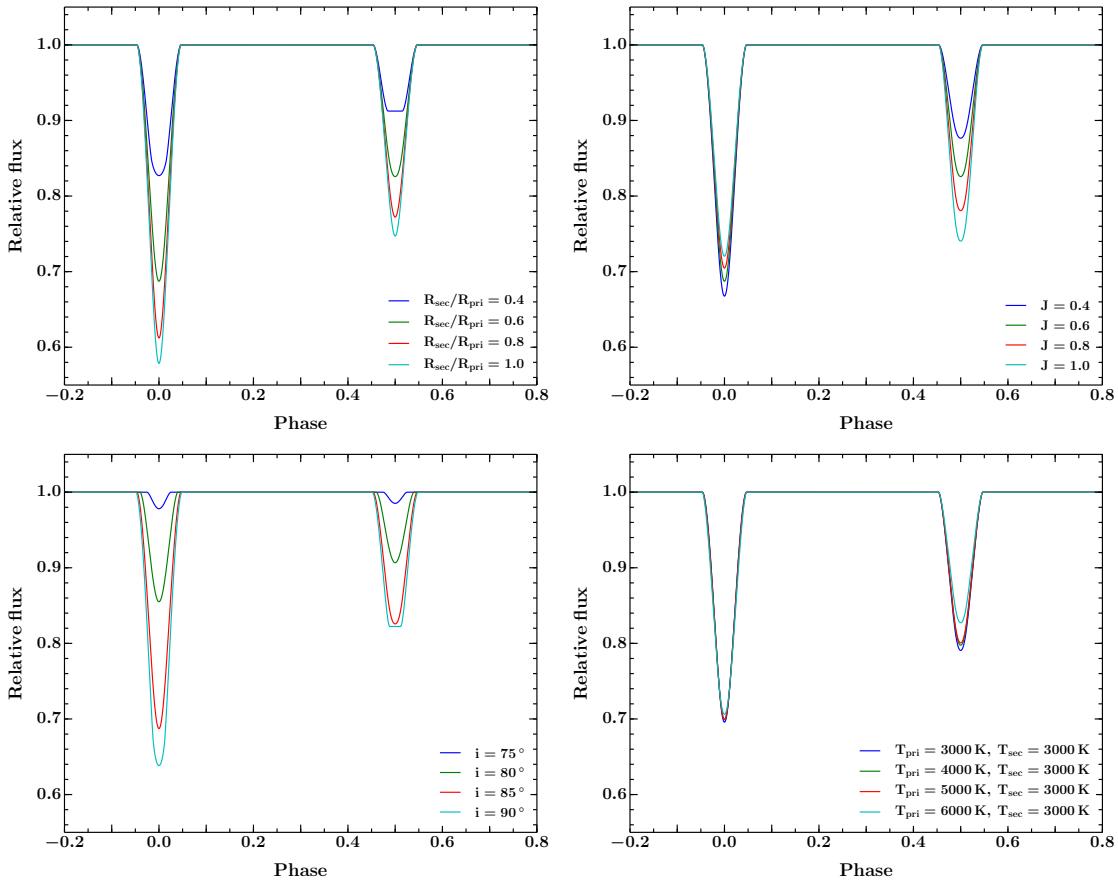

Figure 1.10: Effect of varying the radius ratio, surface brightness ratio, inclination and limb darkening parameters on the eclipses. The *top left* panel shows the effect of varying the radius ratio $R_{\rm sec}/R_{\rm pri}$ between 0.4 and 1.0, while fixing all other parameters to those given in Table 1.3. The *top right* panel shows the same but varying the surface brightness ratio J between 0.4 and 1.0. The *bottom left* panel shows the effect of varying the inclination i between 75 and 90°. The *bottom right* panel shows the effect of varying the limb darkening coefficients: the primary temperature is varied between $T = 3000$ and 6000 K, while keeping the secondary temperature fixed at $T = 3000$ K. J is also fixed as our aim is to isolate the effect of limb darkening. We use the quadratic limb darkening law, selecting the coefficients of Claret et al. (2012) for stars with $\log g = 4.0$ in the CoRoT bandpass. All plots in this section share common axes.

and separation, the fraction of the secondary star occulting the primary and itself being occulted is higher.

Central surface brightness ratio (Figure 1.10, top right): the primary effect of decreasing the surface brightness ratio is a reduced secondary eclipse depth, while the primary eclipse depth remains relatively constant. It is important to note that over a limited range when the eclipse depth ratio is high, varying J gives a similar effect on the eclipses as varying $R_{\rm sec}/R_{\rm pri}$; this highlights the well-known surface brightness – radius ratio degeneracy, which is commonly seen in near equal-mass systems.

Orbital inclination (Figure 1.10, bottom left): smaller inclinations give shallower eclipses,

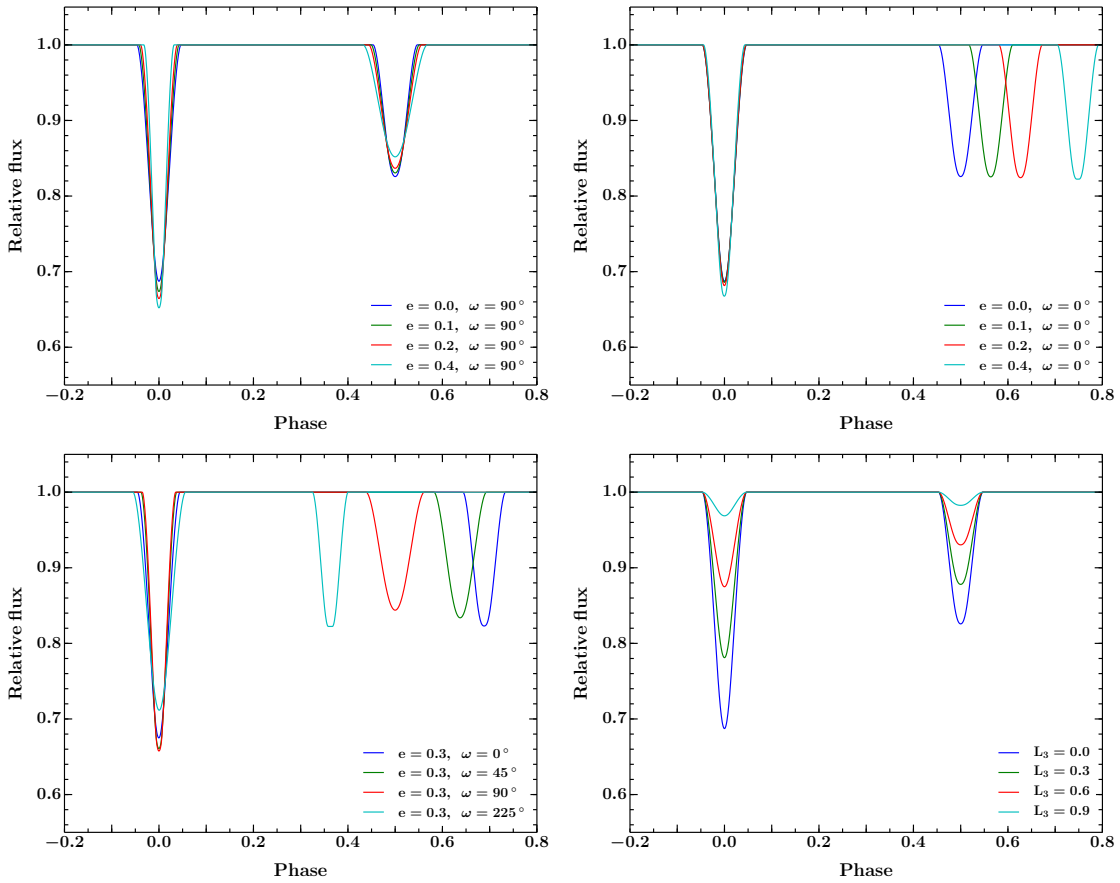

Figure 1.11: Effect of varying the eccentricity and longitude of periastron on the eclipses. The *top left* panel shows the effect of varying the eccentricity e between 0.0 and 0.4, while fixing all other parameters to those given in Table 1.3. Fixing the longitude of periastron ω to 90° essentially hides the eccentricity as periastron passage is aligned with the line of sight. The *top right* panel shows the same but fixing the longitude of periastron ω to 0°, which reveals the eccentricity. The *bottom left* panel shows the effect of varying ω but fixing $e = 0.3$; again the eccentricity is visible. The *bottom right* panel shows the effect of varying the level of third light between 0.0 and 0.9. All plots in this section share common axes.

shorter durations, increased ratio of secondary-to-primary eclipse depths, and shallower ingress and egress.

Limb darkening (Figure 1.10, bottom right): limb darkening parameters have only a small effect on the eclipse shapes over a wide range of temperature ratios. In the figure, the limb darkening parameters correspond to primary temperatures varying over 3000 K while the secondary parameters are kept fixed; the effect on the eclipses is small. Given that typical uncertainties on temperature estimates in the literature are of order 250 – 500 K (e.g. Stassun et al., 2014), limb darkening coefficients are often fixed in EB analyses, especially for grazing eclipses. For edge-on inclinations and flat-bottomed eclipses, limb darkening has a slightly larger effect, but it is still relatively modest.

The eccentricity e is closely tied to the longitude of periastron ω. If the binary major axis is aligned with the line-of-sight (i.e. $\omega = 90$) then eccentricity can be hidden in the light curve (Figure 1.11, top left). The top right panel shows the same plot but for $\omega = 0$ and the eccentricity is revealed in the relative timing of secondary eclipse. Both the relative timings and durations of eclipses are affected for eccentric orbits with different alignments (bottom left panel). The key point is that for eccentric systems, both light and radial velocity curves are needed for accurate characterisation of the stellar parameters.

Third light (Figure 1.11, bottom left): increasing the fraction of third light decreases both primary and secondary eclipse depths, yet maintains their ratio (as we noted in section 1.5.3.3).

1.5.5 Distance determination for eclipsing binaries

The radii and effective temperatures of detached, double-lined eclipsing binaries can be determined directly from photometric and spectroscopic observations, which allows the distance to the system to be estimated. Although distances can be determined from spectral energy distributions (SEDs) and surface brightness relations (e.g. Maxted et al., 2015), the most common method of distance determination relies on the following procedure: 1) determine the system's bolometric luminosity, 2) convert the bolometric luminosity to bolometric absolute magnitude, 3) convert bolometric absolute magnitude to absolute magnitude in the passband of interest via a bolometric correction (BC), and 4) compare absolute and apparent bandpass magnitudes to estimate the distance. We now show this process: first we determine the bolometric luminosity for the two stars using equations 1.50 and 1.51. Next we convert the bolometric luminosities L to bolometric absolute magnitudes M using

$$M_{1,2}^{\rm bol} = -2.5 \log_{10} \left(\frac{L_{1,2}}{L_\odot} \right) + M_\odot^{\rm bol} \tag{1.70}$$

where the subscripts 1 and 2 refer to the two stars, and we define the luminosity and absolute bolometric magnitude of the Sun as $L_\odot = 3.855 \times 10^{33}$ erg s^{-1} and $M_\odot^{\rm bol} = 4.74$. To compare to observations we need to transform the absolute bolometric magnitudes into the absolute magnitudes in the passband of interest, which requires a bolometric correction

(BC) of the form $M^{\lambda}_{1,2} = M^{\rm bol}_{1,2} - BC^{\lambda}_{1,2}$. These absolute magnitudes are then combined to give the passband-specific absolute magnitude of the system

$$M^{\lambda}_{\rm sys} = -2.5 \log_{10} \left(10^{-\frac{M^{\lambda}_1}{2.5}} + 10^{-\frac{M^{\lambda}_2}{2.5}} \right) \ . \tag{1.71}$$

The distance can now be determined by comparing the absolute magnitude to the (de-reddened) apparent magnitude in the passband of interest

$$d = 10^{\frac{m^{\lambda} - A^{\lambda} - M^{\lambda}_{\rm sys} + 5}{5}} \ \ {\rm pc} \tag{1.72}$$

where A^{λ} is the total line-of-sight extinction in the passband λ. It is important to note that, as we have used a bolometric correction, the determined distance is model-dependent. Nonetheless, typical distance uncertainties for well-characterised EBs are only $\sim$5%, although this is sensitive to any systematic uncertainty in the stellar effective temperatures as $d \propto T^2_{\rm eff}$ (Torres et al., 2010).

As noted above, an alternative approach is to use relations between (bandpass-specific) surface brightness and effective temperature; empirical relations have been derived by e.g. Kervella et al. (2004) using interferometric observations. Southworth et al. (2005) show that BCs and surface brightness – $T_{\rm eff}$ relations yield consistent distances of comparable precision. Both methods achieve smaller uncertainties using IR wavelengths: BCs are smaller and less model-dependent, and IR surface brightness – $T_{\rm eff}$ relations have smaller scatter than their optical counterparts and are also less affected by interstellar reddening. As a further point, $T_{\rm eff}$ estimates based on optical measurements are more sensitive to the unspotted photospheric regions of low-mass stars and hence will slightly overestimate the true $T_{\rm eff}$ and resulting distance.

1.5.6 Sources of out-of-eclipse variability

There are many potential causes of brightness variations in binary systems that are unrelated to eclipses. In well-behaved systems it is possible to include physically motivated models for e.g. ellipsoidal variability, reflection or static starspots[18]. However, in systems displaying

[18] Although the treatment of spots tends to be relatively basic as a small number of large spots are typically chosen to match the observed modulation patterns as opposed to a large number of small spots, which is arguably more likely.

complex and evolving variability, standard models are unable to accurately present a physical interpretation of the variations. Given that we are interested in young systems, which tend to be active, not necessarily synchronised, and which can display variability arising from accretion processes and local dust obscuration, it is not always possible to write down a physically motivated model for the observed brightness variations. In the majority of cases therefore, bar as discussed in Chapter 6, we model the out-of-eclipse variations with Gaussian processes (GPs), which offer a motivated means of modelling variations based on their covariance properties rather than a detailed physical understanding of their origin; GPs are introduced and discussed in Chapter 3.

We note that in the past researchers typically did not have continuous photometry, i.e. did not have the tools available to robustly investigate the out-of-eclipse (OOE) variations, and usually attempted to remove their contribution with splines or sinusoids. However, unlike GPs (and as discussed in Chapter 3), this does not provide a motivated means of propagating uncertainties into the residual light curves, upon which the eclipses are modelled.

1.6 Stellar time-series photometry

We conclude this introduction with a brief historical, current and future overview of photometric time-series observations which, as previously discussed, are the fundamental driving force behind the discovery and characterisation of EBs, and by extension the calibration of stellar evolution models.

The evolutionary timescales associated with astrophysical objects, such as stars or galaxies, are typically too long to observe in the time domain. However, distinct events (e.g. supernovae, gamma-ray bursts (GRBs) and other transients), phenomena such as pulsations, or celestial mechanics (the motions of stars and planets) are readily observable. Indeed, our understanding of the universe and our place in it has been driven by time-domain observations, such as those of the solar systems planets and their orbits around the Sun.

However, until only a couple of decades ago, the time-domain was restricted to targeted observations of single objects. With the advent of large-format charge couple devices (CCDs) it has been possible to conduct simultaneous high-cadence observations of a large number of targets. With this advance, numerous avenues of astrophysical research opened up, specifically those that rely on detecting low-probability events, such as eclipsing binaries, microlensing and transiting planets. The radial velocity detection of the first extrasolar planet, 51 Peg b, (hereafter exoplanet) by Mayor & Queloz (1995) and the subsequent detection of the first transiting exoplanet, HD 209458 b, by Charbonneau et al. (2000) paved the way for dedicated transiting planet surveys. First, from the ground, e.g. Hat-NET, SuperWASP and MEarth (Bakos et al., 2004; Pollacco et al., 2006; Irwin et al., 2009), and subsequently also space-based missions, e.g. CoRoT and *Kepler* (Baglin, 2003; Borucki et al., 2010). As these surveys conduct continuous high-precision, high-cadence photometric observations of a large number of stars they are ideally suited to the discovery of eclipsing binaries[19], and many other stellar phenomenon, including flares, pulsations, rotation and stellar activity.

1.6.1 Ground-based transit surveys

A detailed discussion of the numerous photometric surveys is beyond the scope of this work; here, we briefly introduce the three that have specifically targeted star forming regions and young open clusters:

- The Monitor project (Aigrain et al., 2007) performed photometric monitoring of nine young (∼1–200 Myr) nearby clusters with 2–4 m telescopes. The science goals included detecting stellar and brown dwarf eclipses, planetary transits, and characterising rotation and activity throughout the pre-main sequence. The main results came from rotation studies, as characterising PMS EBs proved harder than anticipated.
- The Palomar Transient Factory Orion project (PTF Orion; van Eyken et al., 2011) was a 40-night designated survey of the young (7–10 Myr) 25 Ori association with

[19] In fact, EBs are the primary source of false planet detections in these surveys, with 'blended' EB signals being roughly an order of magnitude more prevalent.

the Palomar 48-inch telescope in December 2009 – January 2010. Its main science goal is the detection of transiting planets, with one possible detection to date (van Eyken et al., 2012; Barnes et al., 2013), but also discovered nine good EB candidate members of the 25 Ori or Orion OB1a associations; spectroscopic orbits are not yet published.

- The Young Exoplanet Transit Initiative (YETI; Neuhäuser et al., 2011) uses a global network of 0.2 to 2.6-m telescopes to continuously monitor 10 young, nearby stellar clusters ($\leqslant 100$ Myr and $\leqslant 1$ kpc) for up to two weeks, repeating the runs three times per year per cluster. Again, the main science driver is the detection and characterisation of young planets with a view to constraining planet formation and early evolution scenarios. Three transiting candidates (two in Trumpler 37 and one in 25 Ori) have thus far been reported with follow-up ongoing (Errmann et al., 2014).

1.6.2 Space-based transit surveys

1.6.2.1 CoRoT and *Kepler*

With their wide field of view, excellent photometric precision and continuous monitoring capability over weeks or even years, the CoRoT and Kepler space missions are extremely efficient at detecting EBs (see e.g. Prša et al. 2011), but they normally target main sequence field stars. Fortunately, the young open cluster NGC 2264 falls within the visibility zone of CoRoT, which enabled it to be observed in March 2008 and again in December 2011–January 2012; these observations form the basis of this thesis and are discussed in detail in Chapter 2.

While the nominal *Kepler* mission focussed on a fixed region of sky in Cygnus (RA=19h 22m 40s, Dec=+44° 30' 00") that did not contain young clusters, the failure of two of its four reactions wheels gave rise to the *Kepler*/K2 mission (Howell et al., 2014). K2 is targeting a number of star forming regions and young open clusters for ∼80 days each over a 2.5-year period[20]. 99 newly-discovered field EBs were reported in the first field (LaCourse et al., 2015) and eclipses have been detected on a previously known PMS spectroscopic

[20]With a possible extension to the mission subject to funding.

binary in the third field (Kraus et al., 2015). More PMS EB discoveries are forthcoming (e.g. David et al., in prep.).

1.6.2.2 *Spitzer*

The 5.2'×5.2' FoV of the *Spitzer* satellite is significantly smaller than either CoRoT or *Kepler* (2.7 × 3.05 and 16.1 × 16.1 degrees, respectively), which means it is typically used in more targeted observations, either staring at a small region within a cluster or mapping a larger area at the loss of continuous photometry. Nonetheless, it is relatively efficient at detecting PMS EBs: six candidate members of the Orion Nebula cluster were reported in Morales-Calderón et al. (2011), which are in various stages of follow-up, and a number of PMS EB candidate members were also discovered in observations of NGC 2264, which form part of this thesis.

1.6.3 Discovery of low-mass PMS EBs

All characterised low-mass PMS EBs discovered until 2011 were detected from ground-based observations, either from targeted surveys of star forming regions, e.g. JW380 (Monitor) and 2MJ0535-05, Par1082, V1174 Ori and RXJ 0529.4+0041A (various individual efforts on ∼1-m class telescopes), or from wide-field all-sky transiting surveys, e.g. ASAS J0528+03 and MML 53 (the All-Sky Automated Survey and SuperWASP, respectively). In 2011, the first space-based detections of low-mass PMS EBs by *Spitzer* were reported (Morales-Calderón et al., 2011), followed by the first PMS EB discovered by CoRoT (Gillen et al., 2014) and subsequently the first PMS EB discovered by the *Kepler*/K2 mission (Kraus et al., 2015). Since 2011, all characterised low-mass PMS EBs reported in the literature have been detected by space-based photometric monitoring programs.

Chapter 2

Observations of NGC 2264

In this chapter we give a brief literature overview of the NGC 2264 star forming region and introduce the datasets used in this thesis (namely, observations of NGC 2264 conducted in March 2008 and December 2011 – March 2012). We then compare the 2008 and 2011/2012 observations obtained with the CoRoT space mission, note differences in the photometric behaviour resulting from incomplete background correction, and detail our attempts to improve the background correction to rectify the observed discrepancies. Finally, we detail the follow-up spectroscopic observations obtained to determine radial velocities of candidate eclipsing binary members of the cluster.

2.1 NGC 2264 literature review

NGC 2264 is a very well-studied young star forming region due to its relative proximity, well-defined membership list and low foreground extinction (Dahm, 2008). The ∼few Myr old young open cluster is the dominant component of the Mon OB1 association in the Monoceros constellation and is situated in the local Orion–Cygnus spiral arm. It lies in the direction away from the Galactic centre at a distance of ∼700–900 pc (e.g. Sung et al., 1997; Park et al., 2000; Rebull et al., 2002; Dahm, 2008; Baxter et al., 2009; Sung & Bessell, 2010).

2.1.1 Environment

NGC 2264 was discovered by Friedrich Wilhelm Herschel in 1784 and lies on the eastern edge of a ring-like structure, roughly 3° in diameter, which links the Mon OB1 and Mon

R1 associations (Schwartz, 1987). The former comprises 20 molecular cloud cores, ranging from $\sim 10^2 - 10^4 M_\odot$ (Crutcher et al., 1978) and the latter includes the reflection nebulae NGC 2245 and NGC 2247, which lie on the western edge of the ring. It is thought that Mon OB1 and Mon R1 lie at similar distances and are likely related. 5° southwest of NGC 2264 lies the Rosette Nebula, NGC 2237-9, along with its embedded young cluster, NGC 2244. These are not considered to be associated with the Mon OB1 or Mon R1 associations but rather belong the outer Perseus arm, 1.7 kpc distant (Román-Zúñiga & Lada, 2008). The region surrounding NGC 2264, including the Rosette Nebula, is shown in the left panel of Figure 2.1.

The cluster of stars in NGC 2264 are seen projected on an extensive molecular cloud complex that extends more than 2° from the cluster to the north and west. Within NGC 2264, the dominant stellar member is the massive multiple O7 V star, S Monocerotis (S Mon; Skiff 2013), which lies in the northern part of the cluster. Ionising flux from S Mon and the OB population illuminate the cluster and the Cone Nebula, which is a triangular projection of molecular gas that lies approximately 40' (∼6 pc) south of S Mon (Schwartz et al., 1985; Dahm, 2008). A false-colour composite image of NGC 2264 is shown in the right panel of Figure 2.1.

2.1.2 Morphology

The cluster is hierarchically structured with significant sub-clusterings. There are three main regions of star formation: one centred around S Mon and two sub-clusters to the south known as the "Cone" and "Spokes" (Teixeira et al., 2006). These latter two are centred on two strong infrared sources, IRS 1 and IRS 2, respectively. IRS 1, also known as Allen's source (Allen, 1972), is a deeply-embedded B2-B5 star, and IRS 2 is a star forming core and associated protostellar cluster. Young et al. (2006) suggest that a dense group of low-mass protostars just south of IRS 2 may represent a fragmenting, collapsing core based on a dynamical age of a few 10^4 yr, composition of Class 0/I objects and proximity of molecular hydrogen. The remainder of the Spokes sub-cluster, as well as the Cone sub-cluster contain predominately Class I objects. In comparison, the star forming region

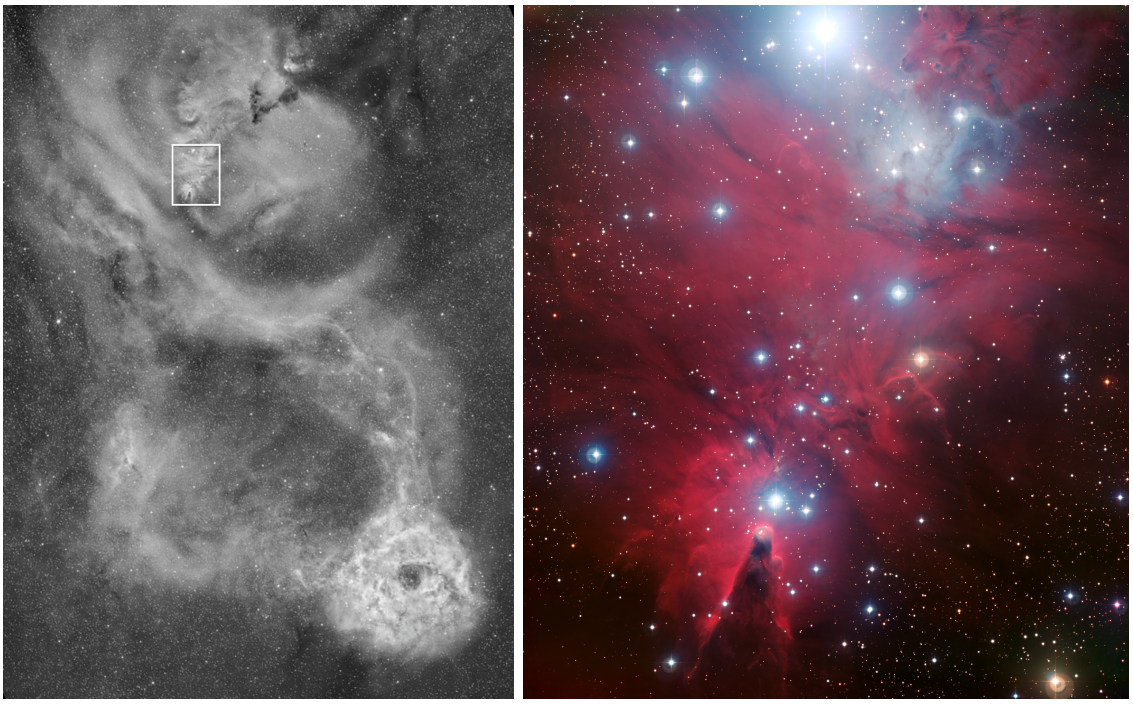

Figure 2.1: *Left*: A narrow-band Hα image of NGC 2264 (upper left; central regions boxed), and the Rosette Nebula and its central dark molecular cloud NGC 2244 (bottom right). Wind-blown shells and supernova remnants are visible throughout the image, possibly associated with either the Mon OB1 or OB2 associations. The image is orientated with North up and East left. [Taken from Dahm 2008] *Right*: A composite B, V, R and Hα image of the NGC 2264 star forming region taken with the Wide Field Imager on the 2.2-m MPG/ESO telescope at La Silla, Chile. The image shows the region of the left panel inside the white box (again, the image is orientated North up and East left). The brightest star to the north is S Mon, and the rest of the OB population are clearly seen throughout the cluster. The dark pillar of gas and dust towards the south is the Cone nebula, which has a vertical extent of $\sim$10 arcmin. Immediately above this is the Cone sub-cluster, and above that (in the middle of the cluster) is the Spokes sub-cluster (these are difficult to discern in this optical image but are clearly visible in the IR). NGC 2264 also contains a reflection/emisson nebula, which lies towards the north-west of the cluster (but south-west of S Mon). [Credit: ESO].

surrounding S Mon comprises mainly Class II sources, which are more dispersed than in the Spokes or Cone (Sung et al., 2009). In addition to these three star forming regions, there exists a "halo" population of young stars distributed throughout the cluster (Sung et al., 2008; Feigelson et al., 2013).

2.1.3 Distance

NGC 2264 is well-suited to precise distance determination due to its abundant early-type population and lack of foreground extinction. Early distance estimates in the literature primarily focussed on comparing apparent to (expected) absolute magnitudes for the early-type population; these typically find distances of 700–800 pc (e.g. Walker, 1956; Sung et al., 1997). More recently, Baxter et al. (2009) obtained a somewhat larger estimate of

$913 \pm 40 \pm 110$ pc (sampling and systematic errors respectively) by comparing projected rotational velocities and rotational periods, assuming an isotropic inclination distribution. As part of their study on the initial mass function (IMF) of NGC 2264, Sung & Bessell (2010) computed a distance to the cluster of 815 ± 95 pc from spectral energy distribution (SED) fitting of suspected members using the SED fitter of Robitaille et al. (2007). We note a recent, anomalous determination of the distance to the cluster by Dzib et al. (2014), who inferred a distance of ∼400 pc from the proper motions of sources in the HH 124 IRS Radio Cluster, which is thought to be associated with NGC 2264. Furthermore, they argue that reanalysed Hipparcos parallaxes for members of NGC 2264, a convergent point approach, as well as a kinematic analysis all argue in favour of their smaller distance. While we consider this an intriguing possibility, we focus on the more commonly accepted distances repeatedly found in the literature; we formally consider a distance range of ∼700–900 pc (e.g. Sung et al., 1997; Baxter et al., 2009; Sung & Bessell, 2010). We note that the cluster extends ∼28 pc perpendicular to the line of sight which, assuming a similar line-of-sight depth, would introduce an intrinsic uncertainty of ∼3–4 % into any distance determination.

2.1.4 Extinction

As mentioned above, the foreground extinction towards the cluster is believed to be low. Using early-type cluster members, literature estimates typically range from ∼0.06 – 0.08 (Walker, 1956; Perez et al., 1987; Sung et al., 1997), which give $A_V = 0.18 - 0.25$, assuming a standard ratio of total-to-selective absorption, $R = 3.08$. Extinctions determined for low-mass membership typically yield higher estimates: Rebull et al. (2002) use a spectroscopically selected sample of over 400 predominantly K and M stars to derive a mean $E(B-V) = 0.146 \pm 0.03$ ($A_V = 0.45$). Further, Dahm & Simon (2005) derive a higher A_V of 0.71 mag from low-mass Hα emitters, although they note that some of these may well have dustier environments or lie in embedded regions of the cluster. The extinction values derived for the OB population should yield more accurate distance-induced interstellar reddening as these systems are believed to lie on the main sequence and posses well-characterised intrinsic colours (Dahm, 2008). However, the extinction values derived

from the low-mass population may well be more applicable to the majority of cluster members given that cluster-induced extinction effects could also contribute to the observed stellar colours. We therefore consider the range of reddening values in the literature as $A_V = 0.18 - 0.71$ mag (Walker, 1956; Perez et al., 1987; Park et al., 2000; Rebull et al., 2002; Sung et al., 2004; Dahm & Simon, 2005; Mayne & Naylor, 2008).

2.1.5 Age

Walker (1956) estimated NGC 2264 to be ∼3 Myr old based on the contraction time for an A0 star, which is the latest spectral type believed to be on the main sequence. Most Galactic OB associations extend over ∼100 pc; it is difficult to imagine star formation occurring as a single widespread event over such large scales. Indeed, investigations of young clusters usually infer an apparent age dispersion from luminosity spreads in CMDs. However, it is important to note that these are strongly dependent on the pre-main sequence (PMS) stellar evolution models used. By comparison with two sets of PMS models, Sung et al. (1997) find most suspected cluster members have ages between ∼1 – 16 Myr (0.8–8 Myr for the PMS and 1.4 – 16 Myr for MS sources). Park et al. (2000) compare to four sets of PMS isochrones and determine median ages and dispersions of 2.1 ± 8.0, 0.9 ± 5.5, 4.3 ± 15.3 and 2.7 ± 10 Myr for Swenson et al. (1994), D'Antona & Mazzitelli (1998) and Baraffe et al. (1998) with mixing lengths of $\alpha = 1.0\,H_\mathrm{p}$ and $\alpha = 1.9\,H_\mathrm{p}$, respectively. Furthermore, Rebull et al. (2002) found systematic differences in model-derived ages of up to half an order in magnitude for their spectroscopically classified sample of variable stars. Sequential star formation has also been suggested (Adams et al., 1983), with the peak rate of low-mass ($M < 0.5 M_\odot$) star formation preceding that of the higher mass population. Sequential star formation is an appealing explanation given the number of late-B dwarf members and the presence of young sub-clusters (e.g. Spokes) and numerous embedded protostars, which together imply an intrinsic age dispersion of at least 3–5 Myr within the cluster membership (Young et al., 2006; Dahm, 2008; Sung & Bessell, 2010). Speculation over the star formation history and intrinsic vs. apparent age dispersion of

NGC 2264 endures but the commonly accepted median age is ∼3 Myr with an apparent dispersion of ∼5 Myr.

2.1.6 Stellar population

The stellar population of NGC 2264 is dominated by S Mon and the OB population, which totals at least two dozen stars (Walker, 1956; Morgan et al., 1965; Dahm, 2008). Six of these are known binaries, with one system, HD 47755, showing eclipses (we will return to this system in Chapter 6). There are two main clusterings of early type stars: one near S Mon and the other in the rosette-shaped emission/reflection nebulae to the southwest (Dahm, 2008). The intermediate and low mass populations have been extensively studied from X-ray to millimetre wavelengths with studies focussing on Hα emission (e.g. Reipurth et al., 2004; Dahm & Simon, 2005), X-ray emission (e.g. Flaccomio et al., 2000; Ramírez et al., 2004; Dahm et al., 2007), photometric variability (e.g. Koch & Perry, 1974; Lamm et al., 2004; Cody et al., 2014) and spectroscopic surveys (e.g. Young, 1978; Rebull et al., 2002; Makidon et al., 2004). Recent observations of the cluster with the CoRoT and *Spitzer* space missions, as well as deep *ugr* imaging with the Canada France Hawaii Telescope (CFHT), have identified many new members bringing the total number of members to at least 1500 (Cody et al. 2014; Venuti et al. 2014; A. Cody & E. Flaccomio, priv. comm.).

2.1.7 Radial velocity distribution

The radial velocity (RV) distribution of the cluster has been extensively studied. Fűrész et al. (2006) analysed high-resolution spectra of 990 stars, confirming 471 as members based on their Hα profiles and/or RVs. They find the RV distribution to be 22 ± 3.5 $\mathrm{km\,s^{-1}}$ with a significantly non-Gaussian dispersion and consider potential membership for stars within 4σ ($8 - 36$ $\mathrm{km\,s^{-1}}$). Following on from this work, Tobin et al. (2015) report RVs for an additional 407 confirmed or likely members and investigate the kinematic relationship between the stellar population and the associated molecular gas. They find the northern region of the cluster around S Mon to be more redshifted than the central regions containing the Cone and Spokes sub-clusters. They also find a population of stars

spread throughout the cluster that are blue-shifted with respect to the molecular gas. The differences between the observed stellar and gas kinematics are tentatively attributed to a combination of optical bias against stars moving away from us into the gas and dispersal of molecular gas on the nearside of the cluster by the ionising radiation from S Mon. It may be that NGC 2264 is more easily understood as a loose collection of star-forming clumps rather than a single, well-defined cluster.

In March 2008, the CoRoT space mission observed NGC 2264 for 23 days. Almost four years later the cluster was the subject of a co-ordinated synoptic campaign with CoRoT, *Spitzer*, CFHT, VLT (Very Large Telescope) and a host of other ground- and space-based observatories spanning November 2011 – March 2012. The work presented in this thesis is based on observations of eclipsing binaries obtained in these two campaigns, as well as directed spectroscopic follow-up observations. Section 2.2 below details the 2008 CoRoT observations and section 2.3 details the 2011–2012 campaign.

2.2 The 2008 CoRoT observation

The CoRoT space mission (COnvection ROtation et Transits planétaires[1]) was the first space mission designed for exoplanetary research. It was led by the French Space Agency (Centre National d'Études Spatiales; CNES) in coordination with the European Space Agency (ESA), Austria, Belgium, Germany, Spain and Brazil. Launched on 27 December 2006 CoRoT completed its nominal 2.5 year mission, which was subsequently extended until the spacecraft suffered a computer failure on 2 Novemeber 2012 that made it impossible to retrieve observational data. Unsuccessful repair attempts followed until, on 24 June 2013, the spacecraft was retired. A short time into the extended mission phase one of the two exoplanet CCDs failed. While operational, CoRoT flew in a low-Earth polar orbit at a height of ∼900 km with a period of 1.7 hours.

[1] In English: Convection, Rotation and planetary Transits.

The CoRoT payload was built around a PROTEUS spacecraft bus and comprised a 27 cm-diameter afocal telescope with a 4-CCD wide-field camera. The four 2048×2048 pixel CCDs have a pixel scale of 13.5 μm (corresponding to 2.32 arcsec on the sky) and are arranged in a square pattern. Two CCDs are dedicated to exoplanet detection and two to asteroseismology. The combined field of view (FoV) of 2.7×3.05 degrees, with 2.7×1.5 degrees for each program (Aigrain et al., 2008; Auvergne et al., 2009).

The exoplanet CCDs are able to monitor up to 6000 stars between $11.5 < V < 16$. Prisms in front of the exoplanet CCDs disperse the observed 300–1000 nm broadband flux from each observed source onto the detector giving a small spectrum. Each CoRoT aperture consists of three individual apertures that extract the red, green and blue light separately. These three 'colour' light curves are combined onboard the spacecraft to produce 'white' light curves with a cadence of 512 s, which are then downloaded (32 s sampling is available for up to 500 stars per CCD). For stars brighter than $R < 15$ the individual 'colour' light curves are downloaded along with the combined 'white' light curve (Aigrain et al., 2008; Auvergne et al., 2009).

CoRoT observed in two regions of the sky, known as the CoRoT "eyes", and changed between these every 6 months to avoid the Sun entering the field of view. In the Northern hemisphere's summer CoRoT observed an area around Serpens Cauda, towards the Galactic centre, and during the winter months observed in Monoceros, in the Galactic anticentre direction. CoRoT observed perpendicular to its orbit which allowed for up to $\sim$150 days of continuous observation; these runs are known as 'Long Runs' and are typically denoted as, e.g. LRc01, which stands for the first Long Run in the direction of the Galactic centre. Between Long Runs, CoRoT conducted 'Short Runs' of typically a few weeks in length, which are similarly denoted as, e.g. SRa02 (the second Short Run in the direction of the Galactic anticentre).

As discussed in Chapter 1, the lack of pre-main sequence eclipsing binaries (PMS EBs) is widely recognised, and numerous observational programs have been set up to detect and characterise more systems; see for example the Monitor and YSOVAR projects,

and the *Kepler*/K2 mission (Aigrain et al., 2007; Morales-Calderón et al., 2011; Howell et al., 2014). With their wide field of view, excellent photometric precision and continuous monitoring capability over weeks or even years, the CoRoT (Baglin, 2003) and Kepler (Borucki et al., 2010) space missions are extremely efficient at detecting EBs (see e.g. Prša et al. 2011), but they normally target main sequence field stars. Fortunately, the young open cluster NGC 2264 falls within the visibility zone of CoRoT, which enabled it to be observed continuously for over three weeks in March 2008. The resulting dataset offers an unprecedented insight into the variability of PMS stars, and was used to study accretion (Alencar et al., 2010), rotation (Favata et al., 2010; Affer et al., 2013) and PMS pulsations (Zwintz et al., 2011), as well as to search for eclipsing binaries (Gillen et al., 2014).

CoRoT observed NCG 2264 continuously for 23.4 days between 7 and 31 March 2008 (run SRa01; see Table 2.1). CoRoT observations are conducted in a broad $300 - 1000\,\mathrm{nm}$ bandpass with a standard cadence of 512 s, giving 3936 photometric data points for this run. A total of 8150 stars with magnitudes $9.5 < R < 17$ were monitored in the 1.3×2.6 degrees field-of-view of CoRoT's exoplanet channel. About 1000 of these were previously known or suspected members of NGC 2264. These observations[2] represent an unprecedented photometric dataset for a young cluster, both in terms of sampling and precision. Basic aperture photometry is carried out on board the satellite, and the data were further processed by the CoRoT pipeline (Samadi et al., 2006; Auvergne et al., 2009) to correct them for known instrumental effects (including gain and zero offset, electromagnetic interference, pointing jitter and background subtraction).

2.2.1 Eclipse detection

The work detailed in this subsection was completed by S. Aigrain before I began my PhD.

To search for eclipses, a short-baseline running median filter was applied to exclude outlying data points followed by a 1 day baseline iterative non-linear filter (see Aigrain & Irwin, 2004) to remove long-term variations such as stellar activity. An automated, least-squares search for trapezoidal eclipses was then performed in the light curves of all targets,

[2]The data are publicly available from the IAS CoRoT archive: `http://idoc-corot.ias.u-psud.fr/`.

Table 2.1: Observations of NGC 2264 conducted in 2008 and 2011/2012 relevant to this work.

Telescope	Instrument	Band	Dates	Cadence / epochs
		2008		
CoRoT	E1 CCD	3 700 – 10 000 Å	7 – 31 March 2008	512 s [a]
		2011/2012		
CoRoT	E2 CCD	3 700 – 10 000 Å	1 Dec 2011 – 9 Jan 2012	512 s [a]
Spitzer	IRAC	3.6 & 4.5 μm	3 Dec 2011 – 1 Jan 2012	101 mins
CFHT	MegaCam	u & r	14 – 28 Feb 2012	30 epochs
VLT [b]	FLAMES	6440 – 6820 Å	4 Dec 2011 – 29 Feb 2012	20 – 22 epochs
USNO 40-inch	CCD	Cousins I	22 Nov 2011 – 9 Mar 2012	912 – 1026 epochs

[a] 32 s at high cadence. [b] Spectroscopy.

followed by visual examination of all candidates with an eclipse signal-to-noise ratio above 30. Systems with only one detected eclipse were discarded, along with spurious detections induced by hot pixels (identified from the shape of the 'eclipses', and the three-colour light curves, which are available for stars with $R < 15$). This led to the detection of 103 eclipsing systems (see Chapter 5).

2.3 The 2011/2012 dataset: the Coordinated Synoptic investigation of NGC 2264 (CSI 2264)

Almost 4 years after the 2008 CoRoT observations, NGC 2264 was the subject of a co-ordinated photometric and spectroscopic campaign: the Co-ordinated Synoptic Investigation of NGC 2264 (CSI 2264; Cody et al. 2014), which comprised multi-wavelength observations by 15 ground- and space-based telescopes during November 2011 – March 2012. The broad science goals focussed on the time-domain behaviour of young stellar objects, ranging from star-disk interaction and accretion variability to stellar activity and rotation. Here we focus on those observations relevant to the characterisation of eclipsing binaries. Table 2.1 gives an overview of the 2011/2012 dataset, which is briefly detailed below.

CoRoT: The CSI 2264 CoRoT observations spanned 38.7 days (1 December 2011 – 9 January 2012; PI Micela) and comprised the fifth CoRoT short run in the Galactic anticentre direction (SRa05). CoRoT monitored 4235 stars (489 known members, 1617

candidates and 2129 field stars[3]) in a 1.3° × 1.3° field in NGC 2264 centred on RA = 06h 40m 18.0s and Dec = +09° 41' 46.24". CoRoT observations are conducted in a broad 300 – 1000 nm bandpass with a standard cadence of 512 s, giving ∼6500 photometric data points for this run[4]. Photometry is extracted and light curves produced as described in section 2.2.

Spitzer: The CSI 2264 *Spitzer*/IRAC observations (program 80040; PI Stauffer) were conducted in both staring and mapping modes with the 3.6 and 4.5 μm Warm Mission bands and spanned 3 Dec 2011 – 1 Jan 2012. The stare-mode observations comprised four observing blocks of ∼20 hours each towards the beginning of the run. These focussed on a central 0.8° × 0.8° field centred on RA = 06h 40m 45.0s and Dec = +09° 40' 40", which encompassed the Cone and Christmas Tree Cluster regions. *Spitzer* also conducted mapping-mode observations as its 5.2' × 5.2' FoV is significantly smaller than the cluster. Mapping-mode targets typically have almost simultaneous 3.6 and 4.5 μm observations with a cadence of 101 mins, except at the edges of the composite *Spitzer* field, where targets have only one or other band (Cody et al., 2014). Most *Spitzer* targets were observed in mapping-mode only and therefore have gaps early on in their light curves corresponding to when stare-mode observations were being carried out.

CFHT: The CSI 2264 CFHT/Megacam observations (PI Bouvier) consisted of deep *ugri* mapping as well as u and r-band monitoring of the entire NGC 2264 region over a 14 night period (14 – 28 February 2012). On each monitoring night, the region was repeatedly imaged with a temporal cadence ranging from 20 mins to 1.5 hours. Each typical observing block consisted of 5 r-band exposures followed by 5 u-band exposures, each utilising a 5-step dithering pattern, with individual exposure times of 3 and 60s, respectively. Observations conducted in non-photometric conditions were discarded giving ∼40 u and r-band epochs spread over 11 nights within the two week period. The reader is referred to Venuti et al. (2014) for a detailed description of the reduction process.

[3]The field stars were selected for CoRoT's transiting planet program.

[4]Note that roughly half way through the run the onboard software automatically changed to high cadence mode (32s) for a number of the EBs; for this work, these data were binned to the standard cadence.

VLT/FLAMES: 20–22 medium resolution optical spectra were obtained with the FLAMES instrument on the Very Large Telescope (VLT) at Paranal, Chile, as part of a multi-object monitoring program primarily designed to study accretion (GO program 088.C-0239(A), PI Alencar). Spectra of two fields in the cluster were obtained over a ∼3 month period (4 December 2011 – 29 February 2012), with both sparsely and densely sampled time intervals. Telescope pointing issues on one of the fields resulted in significant loss of flux through the fibres during 6 epochs, so that only ∼15 spectra could be used for the fainter sources in that field. Observations were taken using the standard setting HR15N, yielding a resolving power $R \sim 17000$ over the wavelength range ∼6440–6820 Å, which includes Hα and Li 6707.8 Å. In this work, the FLAMES spectra were used primarily to derive radial velocities, but they contain a wealth of additional information, particularly in the Hα profile, which we analysed for one system, CoRoT 223992193 (see section 4.4). The FLAMES spectra were reduced, extracted and wavelength-calibrated using the standard ESO pipeline[5] by S. Alencar.

USNO: Near-IR Cousins I band monitoring of NGC 2264 was obtained with the USNO 40-inch telescope between 23 November 2011 – 8 March 2012 (PI Vrba). These data were used to investigate the long term photometric variability of only one system, CoRoT 223992193. Data were not obtained on all nights, but typically 5–20 images were acquired on each observation night. Four fields were observed, each 23×23 arcmin, with the one including CoRoT 223992193 centred at RA = 6:41:31.7 and Dec = +09:31:53. Exposure times were typically 300 seconds (although they ranged between 30–900 seconds) and seeing ranged from 1.5 to 8 arcsec. The data were reduced using standard bias subtraction and flatfielding techniques (using dome flatfield images). Differential photometry was then produced relative to seven bright, photometrically non-variable, cluster non-members[6]. This process was performed by A. Cody and yielded 859 differential photometric data points for CoRoT 223992193.

[5] http://www.eso.org/sci/software/pipelines/giraffe/giraf-pipe-recipes.html

[6] These targets displayed light curves constant to 1% or better and lacked any evidence for cluster membership.

2.3.1 Comparing the CoRoT SRa01 and SRa05 datasets

The SRa01 observations were conducted near the start of the CoRoT mission in March 2008 whereas the SRa05 observations took place towards the end of the mission in December 2011 – January 2012, almost four years later. During this time the CoRoT detector performance has degraded appreciably due to effects which are not fully understood, but are presumably related to the hostile radiation environment associated with CoRoT's orbit. This degradation manifests itself as an increased and more spatially variable background, which is not fully accounted for by the standard, globally-averaged CoRoT background correction (see section 2.4). The resulting effect can be seen in the apparent eclipse depths of EBs observed in both runs (see Fig. 2.2); eclipses are shallower in SRa05 than in SRa01.

We therefore sought to model the background in the SRa01 and SRa05 fields and apply a spatially dependent background correction to the photometry in the two runs. Our aims were:

1. Correct for the spatially-dependent nebulosity to improve the background correction for each run individually.

2. Correct for the effects of detector degradation, allowing for direct comparison of the two runs (and hence more precise measurements of eclipsing binary parameters).

The following section details our attempts to achieve both aims.

2.4 Improving the CoRoT background correction to incorporate the 2011/2012 data

CoRoT was originally designed to stare at main sequence field stars, both to search for planetary transits and to study stellar interiors through asteroseismology. The standard background correction was therefore designed with these science goals in mind. Four different approaches to the background correction were tested by Drummond et al. (2008), which utilised: a) the closest background window, b) three surrounding windows, c) a polynomial fit to all windows (which are spread across the detector) and d) the median of all windows. They found that the closest window correction was sensitive to bright pixels

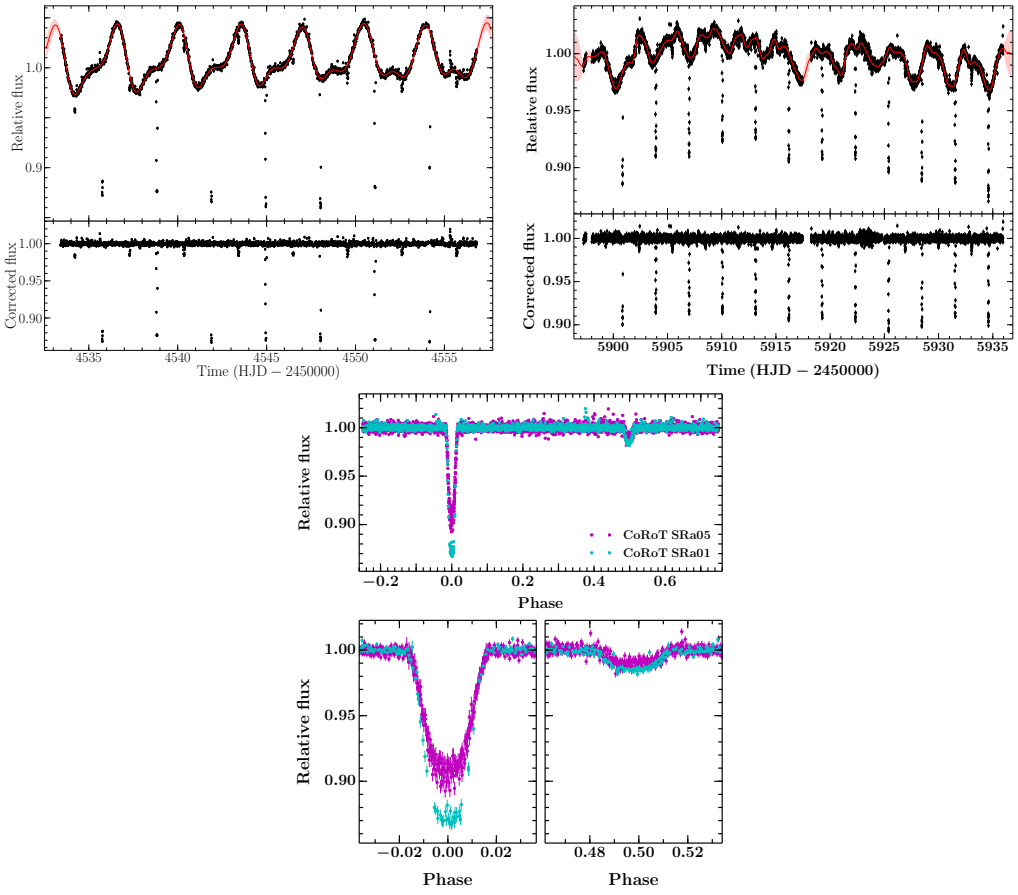

Figure 2.2: Comparison of eclipse depths in SRa01 and SRa05 for a selected eclipsing binary, CoRoT 616780604. *Top left*: 2008 CoRoT SRa01 light curve (top panel) with the mean and 95% confidence interval of the predictive distribution of the Gaussian Process used to model the out-of-eclipse variations (red and pink shaded region, respectively). The bottom panel show the detrended light curve. *Top right*: same but for the 2011/2012 CoRoT SRa05 light curve. *Bottom*: top panel shows the phase folded, detrended SRa01 and SRa05 light curves (cyan and magenta, respectively) and highlights the difference in eclipse depths between the two runs. The bottom panels show zooms on the primary and secondary eclipses (left and right, respectively).

arising in the background window, caused by e.g. energetic particles creating defects in the silicon lattice of the affected pixel(s). This increases the dark current, which subsequently decreases when/if the defects switch to a more stable state (Hopkinson et al., 1996; Srour et al., 2003). Usually this occurs immediately but it can take hours or even days to randomly drop through different configurations back to the nominal level. In some cases it remains a permanent problem. The sharp rise and fall in dark current (if the additional charge is quickly dispersed) can mimic a planetary transit, introducing a systematic into the background correction. Using three background windows increases the probability of the bright pixel effect (although with a lower amplitude) and does not significantly

improve performance. Both the polynomial fit and median methods were found to give good corrections in most cases, but the median behaved best overall and was therefore implemented in the CoRoT pipeline to correct science data.

While the globally averaged median background correction behaves well for studies of stars in the field, i.e. where there are relatively constant background levels, it is less suitable for fields containing spatially variable background emission, such as arises from nebulosity in star forming regions. This was noted in the first CoRoT observations of NGC 2264 (SRa01), although the magnitude of the effect was small over most of the CCD and hence the globally averaged background method was still used.

Over the course of the mission, the CoRoT system aged due to the effects of radiation. This ageing caused a gradual loss in the overall transmission of the dioptric chain ($\sim$10% for the full 6 year mission) and degradation of the detector, e.g. increased numbers of hot pixels and reduced quantum efficiency. In addition, the dark current, which was negligible at CoRoT's launch, increased with time (and radiation exposure). The effect of dark current is not uniform across the detector but displays a gradient along the y-axis due to the readout process. The CCD data is transferred along the x-axis to the memory zone (over $\sim$0.2 s) and read out along the y-axis (over $\sim$23 s from top to bottom), which causes higher dark current levels at the bottom of the detector than at the top.

Therefore, when CoRoT re-observed NGC 2264 in SRa05 (almost 4 years after SRa01), degradation of the detector meant that the problem of the spatially variable nebula was significantly compounded by the dark-current-induced gradient. The simple CoRoT median background correction was found to be insufficient to properly account for the varying background level across the detector in SRa05[7].

2.4.1 Background model: spatial and temporal variations

The background level in the SRa01 and SRa05 runs is a function of both location and time. Before each run, CoRoT takes three full-frame images of the field to be observed, with the first designed to locate areas free of faint stars[8] in which to place the 400 10×10

[7] By extension, this is probably the case for all the later CoRoT runs, even those targeting field stars.
[8] assessed via convolution with a constant kernel; windows are located at minima in the resulting function.

pixel background windows (∼100 are designated for 32 s sampling and ∼300 for 512 s). Therefore, given the full-frame images and background window time series, we sought to model the background as

$$\mathrm{BG}\,(\mathrm{x},\mathrm{y},\mathrm{t}) = \mathrm{f}_{\mathrm{smooth}}(\mathrm{x},\mathrm{y}) + \mathrm{g}\,(\mathrm{t}) \tag{2.1}$$

where f_{smooth} denotes the smoothly varying static background (nebula + dark current) and g denotes temporal variations arising from e.g. cosmic rays, the satellite passing through the South Atlantic Anomaly (SAA), temperature variations and variable scattered light. We note that, ideally, we would implement a more sophisticated model where the brightness of the nebula would be allowed to vary throughout the runs and where temperature variations and scattered light would possess a location dependence in addition to a temporal one. However, given the available tools (three full frame images obtained before the run and background flux time-series during the run) such a model is not possible. Instead, we adopted the proposed model, which is reasonable to first order for our science goals, i.e. a correction to the absolute background level to rectify the difference in eclipse depths between the SRa01 and SRa05 runs. We also note that were we not interested in eclipses we could use the EBs themselves as a correction tool on the assumption that the eclipse depths should be the same in the two runs.

Fig. 2.3 shows full-frame images taken before the SRa01 run (left) and SRa05 run (right), plotted on the same colour axis. Both images are obtained from stacking 64 32-second exposures on board the spacecraft giving a total exposure time of 2048 s (∼34 mins). The images shown have been converted from e^{-} pix^{-1} to counts pix^{-1} via the gain and renormalised to a 512 s cadence to facilitate comparison between the images (Figures 2.3, 2.4 and 2.5) and the 512 s background time-series (Figures 2.6, 2.7 and 2.8; see section 2.4.2.3).

The two fields are rotationally offset with respect to each other: SRa01 is oriented 2.31° east of north and SRa05 is oriented 18.61° west of north, giving a relative offset of 20.92°. The field centres are also slightly offset but this is difficult to quantify as the reported

values correspond to the centre of the focal plane (centre of the four CCDs) and the two runs were observed with different CCDs[9].

In SRa01 the background level is fairly uniform across the detector (bar the regions of strong nebulosity near the centre) with an average value of ∼500–550 counts. In SRa05 the background is higher and there is also a gradient, predominantly in the y-direction, ranging from ∼550 to ∼680 counts (top to bottom). We also note a significantly higher number of bright pixels in SRa05 and return to this point in section 2.4.2.2.

In constructing our background model, we first sought to estimate the smoothly varying background component using the full-frame images before applying a temporal correction to the time series.

2.4.2 Modelling the smoothly varying background

2.4.2.1 Common approaches to background estimation

Most common methods for background estimation in photometric surveys involve splitting an image into coarse grids of, e.g. 100×100 pixels, estimating a clipped average background value for each grid, and then interpolating back at the original pixel sampling to create a background image. As with CoRoT's globally averaged correction, such approaches work well on fields with well-behaved backgrounds but are insufficient in regions of spatially variable nebulosity and/or systematics.

A more sophisticated approach is known as unsharp masking, which works by subtracting a smoothed version of an image from itself (the smoothing is usually achieved via convolution with e.g. a Gaussian kernel). This smoothed image suppresses the high spatial frequency information (the objects of interest), which means that the low spatial frequency information (the large scale variations) are suppressed when the smoothed image is subtracted from the original. This process achieves a very flat background but also introduces magnitude-dependent dark halos around each object. A similar issue is seen when filtering in Fourier space because the lower spatial frequency components of objects of interest also get affected.

[9]The SRa01 field is nominally centred on RA = 06h 44m 09.00s and Dec = 9° 01' 22.73" and the SRa05 field is centred on RA = 06h 44m 29.91s and Dec = 10° 04' 12.00". Although there is a 1° 3' 2.3" offset between the two telescope pointings, the offset between the two field centres is actually much smaller (of order $\lesssim$1 arcmin).

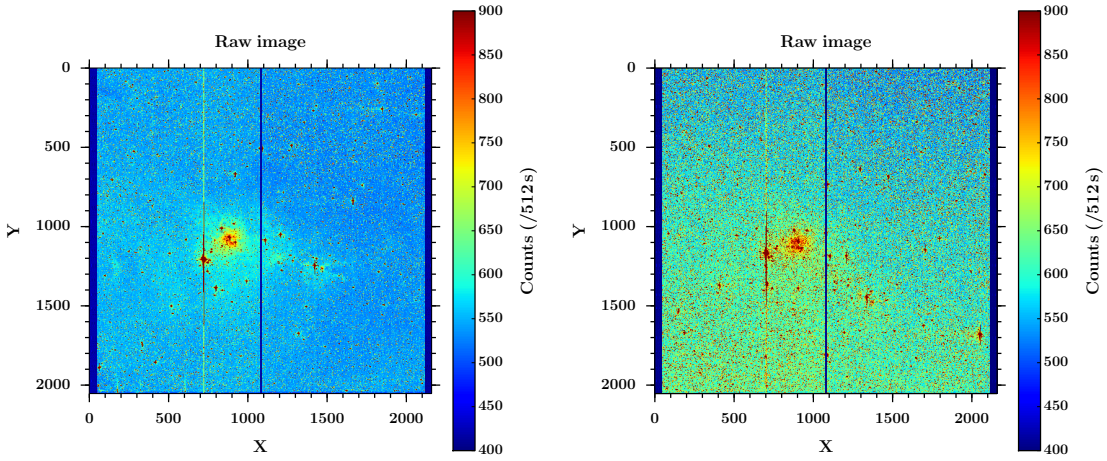

Figure 2.3: Raw CoRoT images of the SRa01 (left) and SRa05 (right) fields. The image exposure times were originally 2048 s (∼34 mins), which were obtained from stacking 64 32-second exposures on board the spacecraft. They have been converted to a 512 s cadence to allow ease of comparison with Figures 2.6, 2.7 and 2.8. All plots on this page share common colour axes.

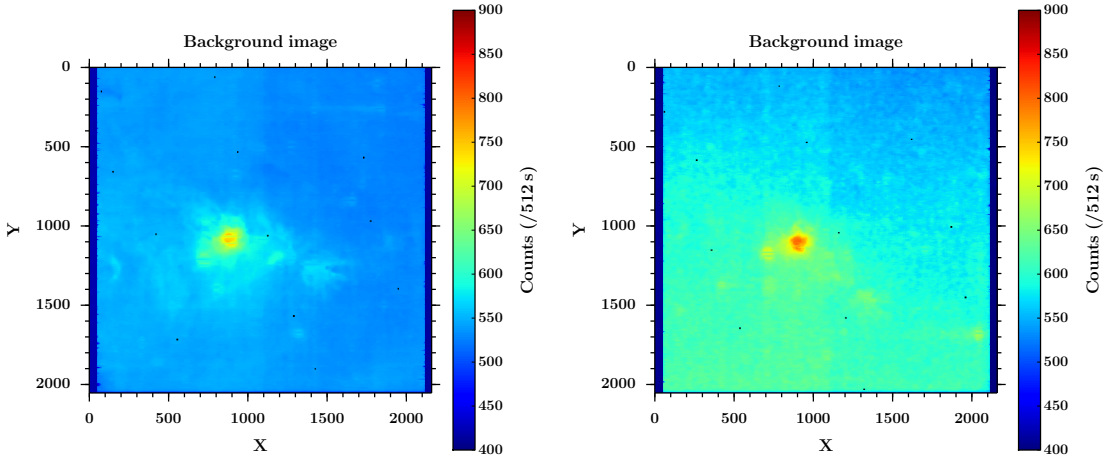

Figure 2.4: Model representations of the background in the SRa01 and SRa05 fields as computed with Nebuliser. The model background has been computed by iterating over the background estimation procedure 3 times using a median filter size of 24 pixels, a linear filter size of 3 pixels. The locations of selected background windows, whose time-series are shown in Figures 2.6, 2.7 and 2.8, are indicated with black squares, which reflect their true size (10×10 pixels).

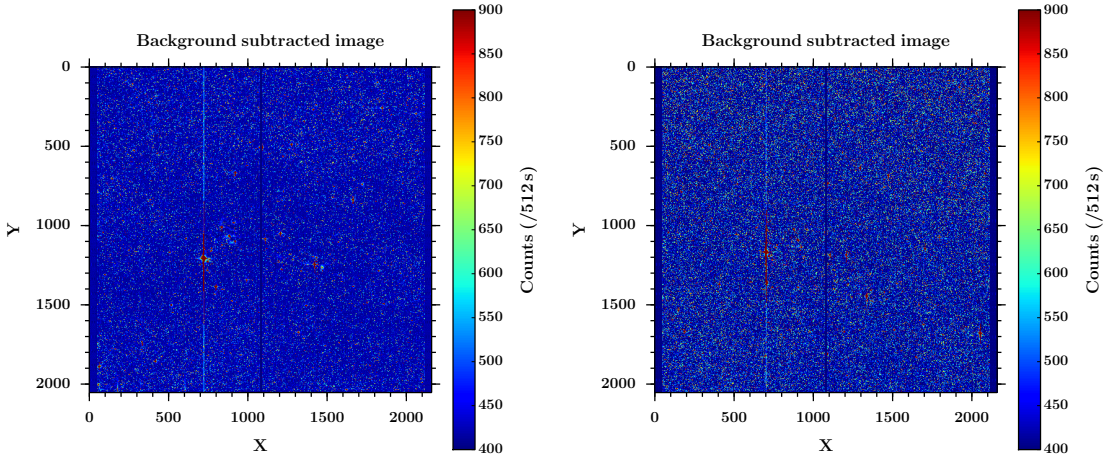

Figure 2.5: Background-corrected images of the SRa01 and SRa05 fields. In each case, the Nebuliser model background has been subtracted from the raw image.

A simple improvement to the linear smoothing applied in unsharp masking is to replace the Gaussian kernel convolution with a non-parametric approach, which more effectively decouples the components of the image that are varying on different scales; this results in significantly reduced dark halos around stars. The Nebuliser[10] software, produced by the Cambridge Astronomy Survey Unit (CASU), applies a series of iterative sliding median and mean filters to separate out the different components of the image. First, a bi-linear median filter (a cross-shape) is applied followed by a simple linear box-car filter (also a cross-shape). k-sigma clipping is then applied to the background subtracted image to mask objects of interest, and the filtering operation repeated.

2.4.2.2 Application to the SRa01 and SRa05 fields

We performed a background correction on the SRa01 and SRa05 images shown in Fig. 2.3 using the Nebuliser software. Figs. 2.4 and 2.5 show the background estimations and background subtracted images, respectively, for both the SRa01 and SRa05 runs (left and right, respectively, in each plot). In decoupling the smoothly varying background from the stars, we opted for a median filter size of 24 pixels and a mean filter size of 3 pixels, and repeated the filtering process 3 times. These values were optimised through trial and error from initial guesses determined through visual inspection of small sections of the images to estimate characteristic length scales for the background variations across the detector in both runs.

As previously noted, the background in SRa01 (Fig. 2.4, left panel) appears fairly uniform around ∼500 – 550 counts, with increased emission in the central regions of the nebula, as expected (shown in green and yellow). In SRa05 (Fig. 2.4, right panel), the background level is higher and displays a gradient, predominantly in the y-direction, ranging from ∼550 – 680 (top to bottom). The cause of this gradient is primarily due to increased dark current. During pre-launch testing the dark current was estimated at $D \sim 0.1$ $\mathrm{e^-\,pix^{-1}\,s^{-1}}$ and was expected to increase at a rate of $1 - 3$ $\mathrm{e^-\,pix^{-1}\,s^{-1}\,yr^{-1}}$ giving $D \sim 3 - 10$ $\mathrm{e^-\,pix^{-1}\,s^{-1}}$ by the end of the nominal mission (Lapeyrere et al.,

[10] http://casu.ast.cam.ac.uk/surveys-projects/software-release/background-filtering

2006). Extrapolating this to the time of the SRa05 observation (observed ∼5 years after launch during the extended mission) gives $D \sim 5 - 15$ e$^-$ pix^{-1} s^{-1}, which corresponds to $D \sim 160 - 480$ e$^-$ pix^{-1} in a 512 s observation[11]. Comparing the background levels between the two runs suggests that the increase in dark current is actually at the lower end of this estimate. However, while the magnitude of the increase was expected, the gradient was not; it is primarily due to the readout time (∼23 s) but could be compounded by non-uniform radiation exposure across the detector.

Fig. 2.5 shows the background subtracted images for SRa01 and SRa05 (left and right, respectively), which both display a uniform background level. This indicates that the smooth variations in the background, resulting from the nebula emission and dark-current-induced gradient, have been adequately corrected for. The remaining objects in the images are stars and bright pixels[12]. Comparison of the SRa01 and SRa05 images shows a significant increase in the number of bright pixels in SRa05. With the current analysis, it is not clear what percentage of these are transient features as opposed to permenant artefacts.

Nonetheless, we now have a model for the smoothly varying background, which enables us to predict its contribution to the observed flux at any given location on the detector.

2.4.2.3 Correcting the background window time series for smooth spatial variations in the background

We test our background model on the background window time series under the assumption that the background windows, as they are located in regions devoid of detectable astrophysical sources, should reflect the true value of the background at their locations. Both 32 s and 512 s background windows are available; we opt to use the 512 s time series as most CoRoT light curves are binned to this cadence. Fig. 2.6 shows example background window time series from windows located throughout the detector during the SRa01 and SRa05 runs (left and right, respectively; these windows are shown in Figure 2.4).

[11] Note that the 512 s observations are the *mean* of the 16 individual 32 s exposures that comprise them and not their sum.

[12] or any other sources that have high spatial frequencies and hence were not removed in the background filtering.

The SRa01 time-series display an upwards trend throughout the run due to increased scattered light, with a spread of $\sim 200\ e^-\ \text{pixel}^{-1}$. Orbital stray light oscillations with a period of 1.7 hours and typical amplitudes of $10 - 15\ e^-\ \text{pix}^{-1}$ are also seen. The red and pink time series show the bright pixel effect, the latter sharply rising at CoRoT Date = 2997, before relaxing in increments back to a stable level, albeit higher than before the jump. The time series are mainly closely grouped and follow the same trend; subtracting the same value across the detector therefore appears validated (i.e. the global CoRoT background correction).

The SRa05 background time series are less well behaved: they display a larger spread (as expected), greater diversity between the individual time series and a global downwards jump at CoRoT Date = 4380, that is non-uniform in magnitude. This jump is due to the temperature of the detector straying outside its allowed range and being reset. The orbital stray light oscillations are again present with the same period and similar amplitude to SRa01.

To test our model, we predict the background level at the locations of the background windows and subtract it off. We then correct for temporal variations using a normalised version of the globally averaged background correction (i.e. we divide our spatially-corrected background time series by a normalised version of the nominal CoRoT background correction.

The results of this process for SRa01 are shown in Fig. 2.7 (right panel) where we compare to the results of applying the standard, globally-averaged background correction (left panel). As the same temporal correction has been applied to both sets of time series, this allows direct comparison of the nominal globally-averaged correction to our spatially dependent one. Both panels are plotted on the same axes, with y-values plotted relative to the median of the global correction over time. The median-corrected background time series display a spread of $\sim 200\, e^-\ \text{pixel}^{-1}$, the same as before the correction, because this correction simply subtracts the median of the background time series at each observation time. In comparison, the spatially-corrected time series should have a smaller spread in the

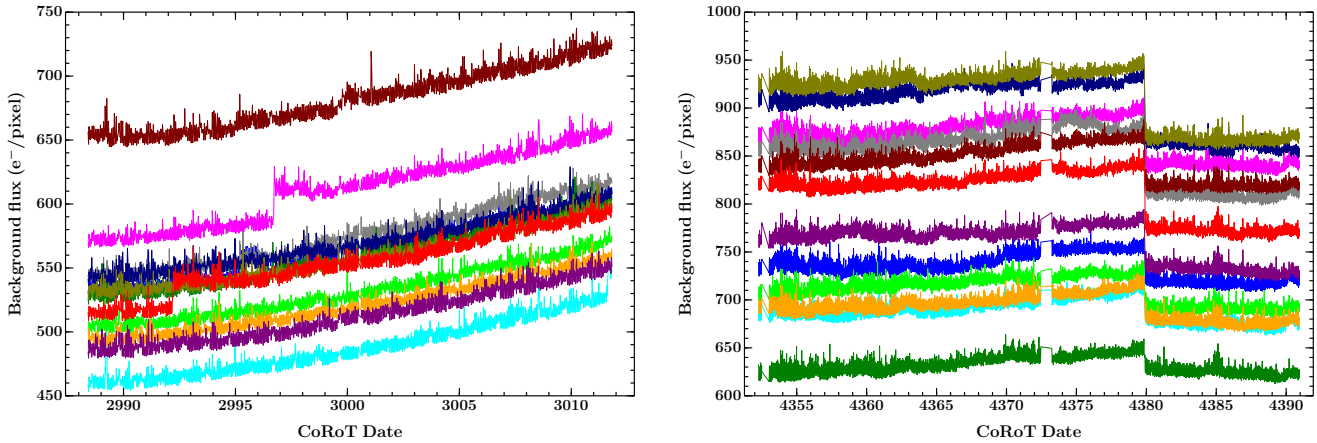

Figure 2.6: Selected background window time series for SRa01 and SRa05 (left and right, respectively).

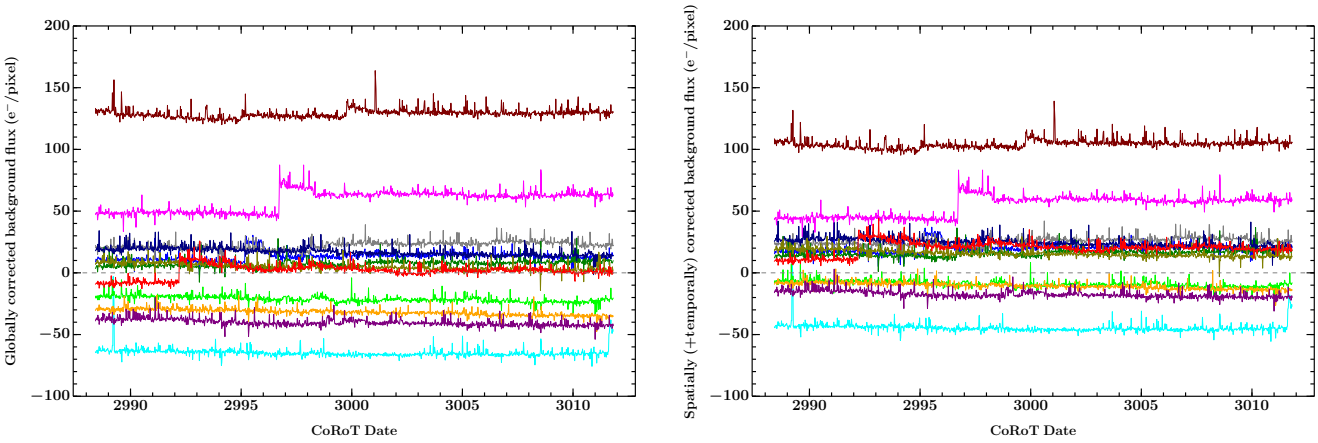

Figure 2.7: Selected background window time series for SRa01 with the old, CoRoT median correction and new spatially-dependant correction (left and right, respectively).

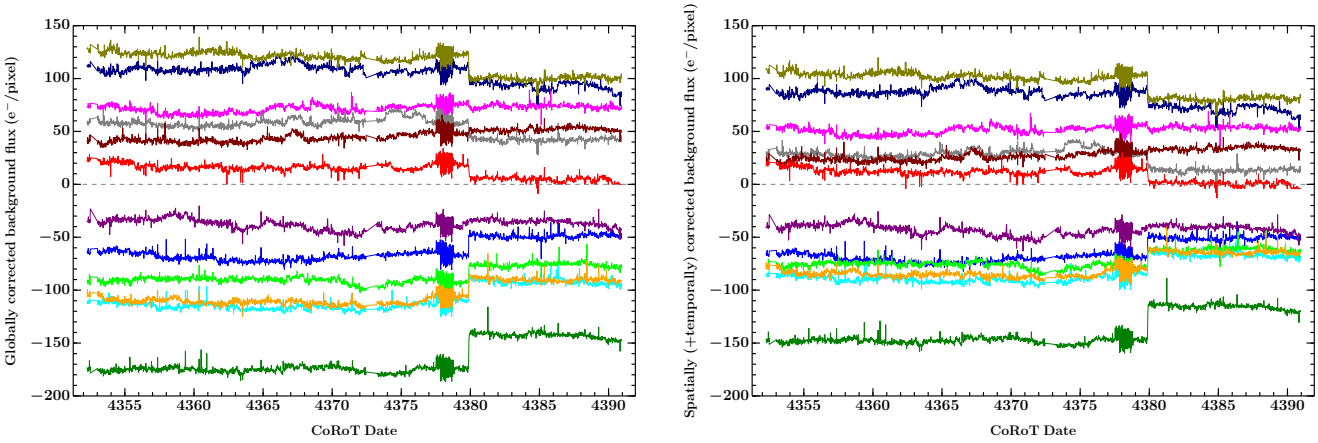

Figure 2.8: Selected background window time series for SRa05 with the old, CoRoT median correction and new spatially-dependant correction (left and right, respectively).

y-direction as they have been corrected for the background level at their location, not simply the median across the detector. These time series display a spread of $\sim 150\,e^-$ pixel^{-1}, which is only a modest improvement on the globally-averaged median correction. Encouragingly however, larger relative improvements are seen in time series with larger initial deviations from the median, suggesting that the spatial correction is working. The remaining spread could be due to sharp variations, e.g. bright pixels, which would not be decoupled from the stars in the background filtering process and hence do not contribute to our smooth background model.

Fig. 2.8 shows the same as Fig. 2.7 but for SRa05. The median-subtracted time series show a spread of $\sim 300\,e^-$ pixel^{-1}, again the same as before the correction. For $\sim$1.5 days around a CoRoT Date = 4378 the background correction rapidly oscillates around the expected background levels; the cause of these oscillations is not known. At CoRoT Date = 4380, the magnitude dependent flux drop manifests as a shift closer to the median value, i.e. time series with a larger initial drop are under-corrected and those with a small initial drop are over-corrected. The spatial and normalised-globally corrected time series (right panel) show a spread of $\sim 250\,e^-$ pixel^{-1}, which is an improvement on the global correction but again a modest one. We note that the time series are more closely bunched after applying the spatial correction. As with SRa01, the remaining spread could be due to bright pixels, of which there is a significantly increased number across the detector.

2.4.2.4 Conclusions from the background modelling

Attempts to improve the background correction, and hence rectify the difference in eclipse depths between the SRa01 and SRa05 runs was not successful. Presumably, this is because the applied model, i.e. that the background can be approximated by a smoothly varying spatial function with a global temporal correction, is insufficient.

Given the significant spread remaining in the SRa05 time series, which is $\sim$70% greater than that observed in SRa01, and the fact that this could be due to temporally-variable contributions from bright pixels, we opted not to include the SRa05 data when determining fundamental parameters for the sample of EBs. We instead focus on the SRa01 dataset,

using the SRa05 data to constrain the system ephemerides only (the period, P, and the reference time for primary eclipse minimum, $T_{\rm prim}$).

2.5 Spectroscopic follow-up and data reduction

As previously discussed, the masses and radii of detached, double-lined eclipsing binaries can be determined directly from photometric and spectroscopic observations. In addition, assessment of whether a system is a member of NGC 2264, and hence young, partially relies on its kinematic relationship with the cluster. We therefore conducted an intensive programme of ground-based spectroscopic follow-up to confirm membership and determine fundamental parameters.

Initial follow-up was performed by S. Aigrain, L. Affer and A. McQuillan before I began my PhD; this work is detailed in section 2.5.1 below. Three further spectroscopic follow-up runs were conducted to obtain medium resolution spectra of the EB sample; this work is detailed in sections 2.5.2 and 2.5.3. For these runs, I prepared the observations, observed (independently for the last two), reduced the data with my custom-written pipeline, and analysed the spectra. In addition, I wrote the final proposal, which was awarded 6 nights on WHT.

2.5.1 Initial follow-up based on the 2008 CoRoT data

The eclipse detection process (section 2.2.1) performed by S. Aigrain yielded 103 eclipsing systems, which were cross-matched with 2MASS and other published data on NGC 2264, covering: X-rays (Flaccomio et al., 1997, 2006; Ramírez et al., 2004); disks (Rebull et al., 2002); optical and infrared variability (Makidon et al., 2004; Lamm et al., 2004) and spectroscopic and proper motion studies (Walker, 1956). A 2MASS J vs. J–K colour-magnitude diagram (CMD; Fig. 2.9) was then used in conjunction with other membership information (where available), the spatial distribution of the targets, and a magnitude limit of $R = 15.5$, to select 12 possible cluster member systems for spectroscopic follow-up.

These 12 systems were observed with the SARG spectrograph on the 3.58 m Telescopio Nazionale Galileo (TNG) at Roque de Los Muchachos observatory on La Palma, Spain (see

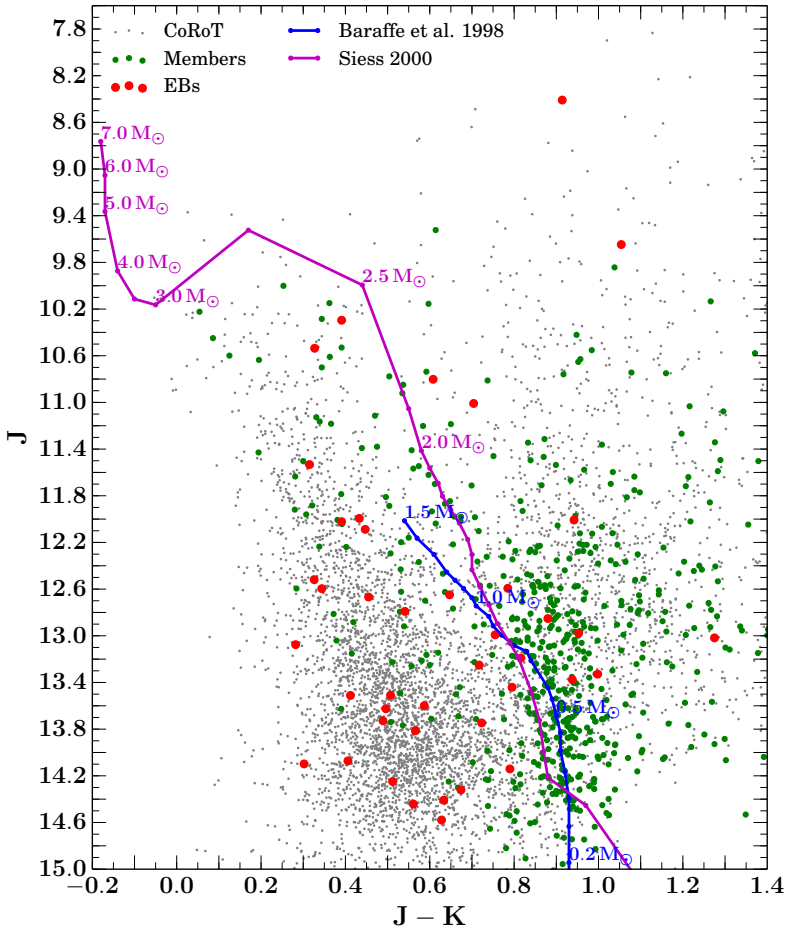

Figure 2.9: J vs. J–K colour magnitude diagram for stars observed in the 2008 CoRoT field. Field stars are shown in grey, cluster members in green and EBs in red. Over-plotted are the 3 Myr isochrones for the Baraffe et al. (1998) and Siess et al. (2000) models (blue and magenta, respectively).

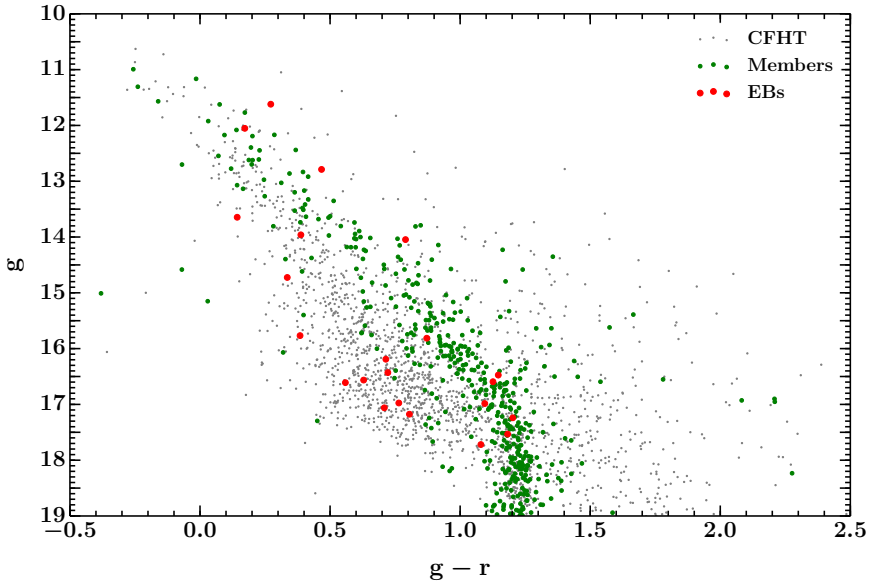

Figure 2.10: g vs. g–r colour magnitude diagram for stars observed in the CFHT field (2011/2012). Field stars are shown in grey, cluster members in green and EBs in red.

Table 2.2: Spectroscopic follow-up of eclipsing binaries discovered in the NGC 2264 field.

Telescope	Instrument	Dates	Resolution	λ range (Å)	No. of EBs	No. of nights
		Data used in this thesis				
INT	IDS	7–12 Mar 2009	$R \sim$ 9 300	$\sim 7650 - 9300$	18	6
WHT	ISIS	21 Dec 2012 – 1 Jan 2013	$R \sim 12\,000$	$\sim 7950 - 9000$	20	4
WHT	ISIS	8 – 16 Feb 2014	$R \sim 12\,000$	$\sim 7950 - 9000$	8	6
VLT [b]	FLAMES	4 Dec 2011 – 29 Feb 2012	$R \sim 17\,000$	$\sim 6440 - 6820$	2	15
		Data discussed in this thesis but not directly used				
TNG	SARG	9–16 Feb 2009	$R \sim 46\,000$	$\sim 5000 - 8000$	9	6
Gemini	GNIRS	2013–2015	$R \sim 18\,000$	$\sim 15\,260 - 15\,740$	2	6
Keck	HIRES	2014–2015	$R \sim 66\,400$	$\sim 4780 - 9060$	6	4
Euler	CORALIE	2011 & 2013	$R \sim 48\,400$	$\sim 3880 - 6900$	5	32

[b] Obtained as part of CSI 2264, rather than designated follow-up, but included for completeness.

Table 2.2 for details). The spectra were reduced by L. Affer (Palermo) and A. McQuillan (Oxford). The reduction suffered from two problems: the presence of cosmic rays and the form of the échelle orders, which disappear into the noise at different CCD rows; these made the spectral tracing a non-trivial procedure. Although recent improvements to the pipeline have been implemented, these spectra do not form part of this thesis.

While not yielding precise constraints on the RV orbits, the spectra did indicate the single or double-lined nature of the systems observed and highlighted potential blends. This information was used in conjunction with other criteria to prioritise the remainder of the sample for spectroscopic follow-up.

2.5.2 Spectroscopic follow-up with INT/IDS

In March 2012, we obtained medium resolution spectra of 18 candidate-member EBs with the Intermediate Dispersion Spectrograph (IDS) on the 2.5 m Isaac Newton Telescope (INT) on La Palma. The aims of these observations were to a) ascertain the spectral types and single/double-lined natures of each system, b) search for signs of youth (via Hα emission and Li 6707.8 Å absorption) and c) obtain preliminary orbits for high-priority systems. Due to the weather conditions during the run, we were only able to complete a) and b) for some candidates; c) was not possible for any.

The IDS spectra were obtained on 7 and 9–12 March 2012 with the R1200R setting giving a resolution of $R \sim 9300$ over the wavelength range ∼7650–9300 Å (see Table 2.2). On 8 March we observed between $\sim 5700 - 7300$ Å to asses signs of youth. 13 EBs were observed in the former wavelength range and 14 in the latter, with 9 systems observed in both. The spectra were processed with IRAF, using the CCDPROC packages to perform the standard CCD reduction steps (trimming and overscan subtraction, bias subtraction and flat fielding) and SPECRED.DOSLIT to extract and wavelength calibrate the spectra using the arc lamp spectra. Individual exposures taken at a given epoch were then combined to maximise the signal-to-noise ratio (S/N) and perform cosmic ray rejection.

2.5.3 Spectroscopic follow-up with WHT/ISIS

The INT/IDS spectra enabled us to refine our priority list in terms of membership likelihood (by comparison of the inferred spectral type and apparent magnitude) and solvability (i.e. single vs. doubled-lined in the near-IR). At this stage, we also incorporated the light curve morphology into the priority weighting for each system, with those displaying larger amplitude flux variations holding a higher priority (younger systems are typically more active). While the 2.5 m INT was suitable for characterising the brighter members of our sample we required a larger collecting area for the fainter candidates. We therefore obtained moderate resolution, near-IR spectra from the Intermediate dispersion Spectrograph and Imaging System (ISIS) on the 4 m William Herschel Telescope (WHT), again at the Roque de Los Muchachos observatory on La Palma. Two observing runs were conducted: the first in December 2012 – January 2013 and the second in February 2014; overviews are given in Table 2.2) and further detailed below. In preparation for these runs we also used a g vs. g–r CMD from the CSI 2264 CFHT observations (Figure 2.10) to refine our priority list.

December 2012 – January 2013: We obtained 4 nights of $R \sim 12000$ spectra using the R1200R grating, covering a wavelength range of ∼8100–9000 Å during 21 December 2012 – 1 January 2013. 20 EBs were observed with 1–8 epochs each. At each epoch we took 2–4 successive spectra, with exposure times of 300–900 s, bracketed by CuAr and CuNe arc

lamp spectra. The spectra were reduced as described for the IDS spectra (section 2.5.2) except that the two arc spectra for a given telescope pointing (epoch for a given target) were combined to minimise any systematics arising from instrument flex during the observations affecting the wavelength calibration. In addition, the reduction process was incorporated into a custom-written PYTHON pipeline, which was automated where possible.

February 2014: We obtained 6 further nights on ISIS during 8–16 Feb 2014 with the same setup as above. Eight high-priority EBs were observed with 1–18 epochs each (5 EBs $\geqslant$ 7 epochs). Again, the spectra were reduced with the same pipeline.

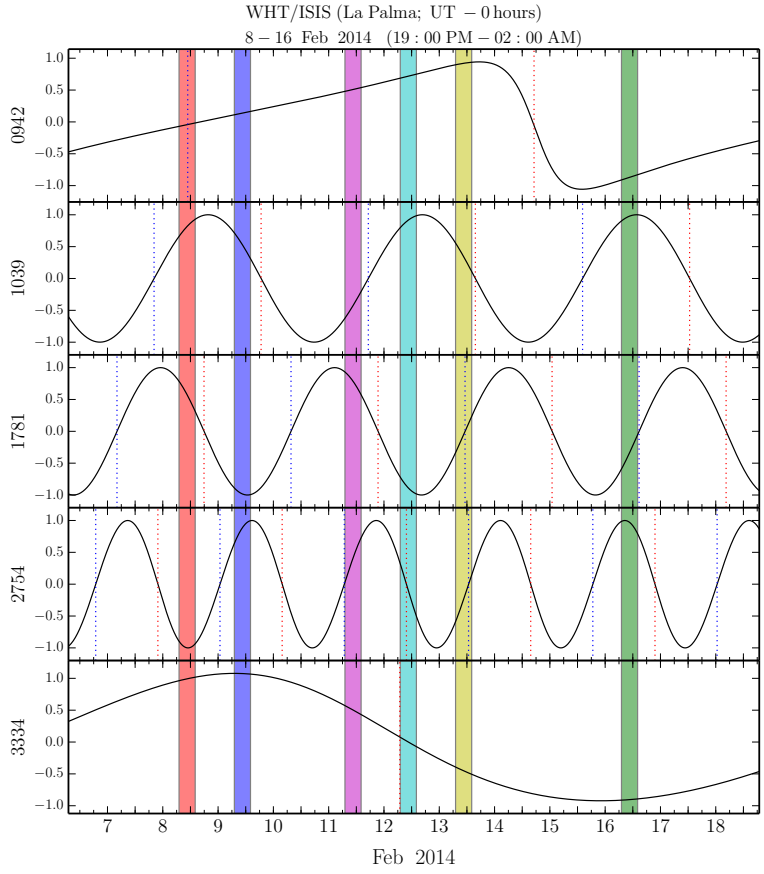

Figure 2.11: Phase curves of selected high-priority EBs observed during a spectroscopic follow-up run with WHT/ISIS from 8–16 Feb 2014. The black curve in each subplot shows the phase as a function of time for a different EB (the EB is denoted via its four digit CoRoT window identifier located in place of the y-axis label). The vertical dotted red and blue lines indicate times of primary and secondary eclipse, respectively, and the the different coloured shaded regions indicate the times during which the systems are visible on the observing nights. Note that for this run, conducted in February, the cluster was only visible for the first half of the night and hence the coloured regions span 19:00 - 02:00 local time. Such plots are used to determine when to observe each EB so as to obtain the most useful phase coverage.

2.5.4 Observing strategy

The ephemeris and eccentricity of an EB can be determined from the light curve[13], which allows us to create phase curves to facilitate efficient RV follow-up. Figure 2.11 shows example phase curves for selected EBs observed with WHT/ISIS in February 2014. Each plot shows the phase of the EB as a function of time (black curve) with the vertical dotted red and blue lines indicating times of primary and secondary eclipse, respectively. The EB is denoted by its four digit CoRoT SRa01 aperture window identifier on the left of the plot. The coloured regions indicate the times during which the systems are visible on observing nights.

These plots enable us to prioritise EBs on a given night, and throughout an observing run, based on the phase coverage that would ultimately be achieved when incorporating all observations. For example, observing EB 3334 on the first, second and last nights (red, blue and green) would give RVs around quadrature, whereas the third, fourth and fifth nights (magenta, cyan and yellow) would sample around primary eclipse. Comparing different systems on e.g. the third night (cyan), we see that EBs 2754 and 3334 are close to primary eclipse, whereas EBs 0942, 1039 and 1781 are close to quadrature and hence would typically carry a higher priority.

2.6 Conclusions

This chapter presented a literature review of the NGC 2264 star forming, and detailed the 2008 and 2011/2012 observations, along with the dedicated spectroscopic follow-up. Eclipses in the SRa05 CoRoT run were found to be shallower than in SRa01 due to a higher and more spatially variable background. Attempts to improve the background correction by applying a spatially variable model had limited success and failed to rectify the difference in eclipse depths. In the following work therefore, we focus on the SRa01 light curves for determining the eclipse parameters, using the SRa05 data to constrain the system ephemerides only.

[13]Note, however, that eccentricity can be 'hidden' in the light curve if the binary major axis is aligned with the line of sight.

Chapter 3

Fundamental parameters of CoRoT 223992193

The work presented in this Chatper is based on:

Gillen et al. (2014). ***CoRoT 223992193: A new, low-mass, pre-main sequence eclipsing binary with evidence of a circumbinary disk.*** **A&A, 562, A50.**

In this Chapter we present the initial characterisation of CoRoT 223992193, a detached, double-lined eclipsing binary, comprising two pre-main sequence M dwarfs, discovered by CoRoT during the 2008 observations of NGC 2264. Using multi-epoch optical and near-IR follow-up spectroscopy with FLAMES on the Very Large Telescope and ISIS on the William Herschel Telescope we obtain a full orbital solution and derive the fundamental parameters of both stars by modelling the light curve and radial velocity data. The orbit is circular and has a period of 3.8745745 ± 0.0000014 *days. The masses and radii of the two stars are* 0.67 ± 0.01 *and* 0.495 ± 0.007 $M_{\odot}$ *and* 1.30 ± 0.04 *and* $1.11\ ^{+0.04}_{-0.05}$ $R_{\odot}$*, respectively. This system is a useful test of evolutionary models of young low-mass stars, as it lies in a region of parameter space where observational constraints are scarce; comparison with these models indicates an apparent age of ∼3.5–6 Myr. The systemic velocity is within* 1σ *of the cluster value which, along with the presence of lithium absorption, strongly indicates cluster membership.*

All work presented in this chapter is my own except for: a) obtaining and analysing the low resolution CAFOS spectrum to infer the combined spectral type, which was performed by

J. Bouvier and is included for completeness; and b) obtaining and reducing the WHT/ISIS and VLT/FLAMES spectra, which were performed by S. Hodgkin and S. Alencar, respectively (the latter is described in section 2.3).

3.1 Introduction

The 2008 CoRoT observation of NGC 2264 revealed several tens of new EBs, half a dozen of which may be cluster members. These are described in more detail in Chapter 5; here we present the discovery and characterisation of one particular system, CoRoT 223992193. This system is also referred to as 2MASS J06414422+0925024, W6712 (Sung et al., 2008) and has a CSI 2264 identifier of Mon-000256. Its light curve displays deep (∼30%) eclipses with a period of 3.87 days, as well as significant (∼15% peak-to-peak) irregular out-of-eclipse (OOE) variability. Its optical and near-infrared colours are compatible with cluster membership, and preliminary light curve modelling and follow-up radial velocity measurements showed it to be a double-lined, near-equal mass system with a total mass of $\sim 1.2\,M_{\odot}$ and individual radii $> 1\,R_{\odot}$, as expected for a PMS system. This motivated additional follow-up spectroscopy and modelling, enabling us to refine the fundamental parameters of both stars and to confirm that the systemic velocity is compatible with that of the cluster.

The system also shows indirect evidence for a proto-planetary disk, most likely circumbinary. If confirmed, it will be the first PMS EB system found to harbour such a disk. This is particularly interesting in light of the recent discovery of a number of circumbinary exoplanets (e.g. Kepler-16, Doyle et al. 2011; Kepler-34 and 35, Welsh et al. 2012; Kepler-38, Orosz et al. 2012a; Kepler-47, Orosz et al. 2012b; and Kepler-64, Schwamb et al. 2013). In all of these systems, the orbital angular momentum of the planets are closely aligned with that of the host binary, strongly suggesting in situ formation within a circumbinary disk. In comparison to CoRoT 223992193's 3.87-day orbit, all these systems host EBs with orbital periods $P > 7$ days. It is possible that closer binaries more strongly torque the inner regions of their circumbinary disks during the PMS phase, and hence drive stronger spiral density waves through the disk, disrupting potential planet formation. However, given

the low-number statistics available, conclusive statements are difficult. Initial theoretical modelling suggests that circumbinary planets around close separation binaries should be a common occurrence (Alexander, 2012). We present the evidence for the circumbinary disk hypothesis in Chapter 4 along with a study of the interaction of the stars with their environment using additional, multi-band photometry and spectroscopy.

CoRoT 223992193 is a very rich system. This chapter focuses on the first step in its characterisation, namely the determination of the parameters of the two stars based on the 2008 CoRoT data and follow-up radial velocities. In Section 3.2, we briefly recap the CoRoT observations and follow up spectroscopy. In Section 3.3 we model the light curve and radial velocity data, deriving fundamental parameters. We discuss the properties of the stars in Section 3.4 and compare to stellar evolution models, before concluding in Section 3.5.

3.2 Observations

3.2.1 Photometry

As described in section 2.5.1, initial selection of EB targets included a magnitude limit of $R = 15.5$. CoRoT 223992193 was selected, despite being fainter than our nominal cut-off ($R = 15.74$), because it fulfilled all the other criteria, and its light curve shows interesting OOE variations. The photometric properties of the system are shown in Table 3.1. Its magnitude and colours are consistent with a fairly low mass member of the cluster. Its light curve is shown in Figure 3.1. The large-amplitude, rapidly evolving variability seen outside the eclipses is discussed in detail in Chapter 4 and is found to be consistent with a combination of constructive and destructive interference of starspots at two slightly different periods, plus additional short-timescale variability arising from variable dust emission and obscuration. In this chapter, we simply note the variations and account for them to extract precise constraints on the stars from the stellar eclipses. The 2011/2012 CoRoT light curve is shown in Figure 3.2 (as previously discussed, due to incomplete background correction this data is used only to refine the ephemeris of the system; see Section 3.3.1.2).

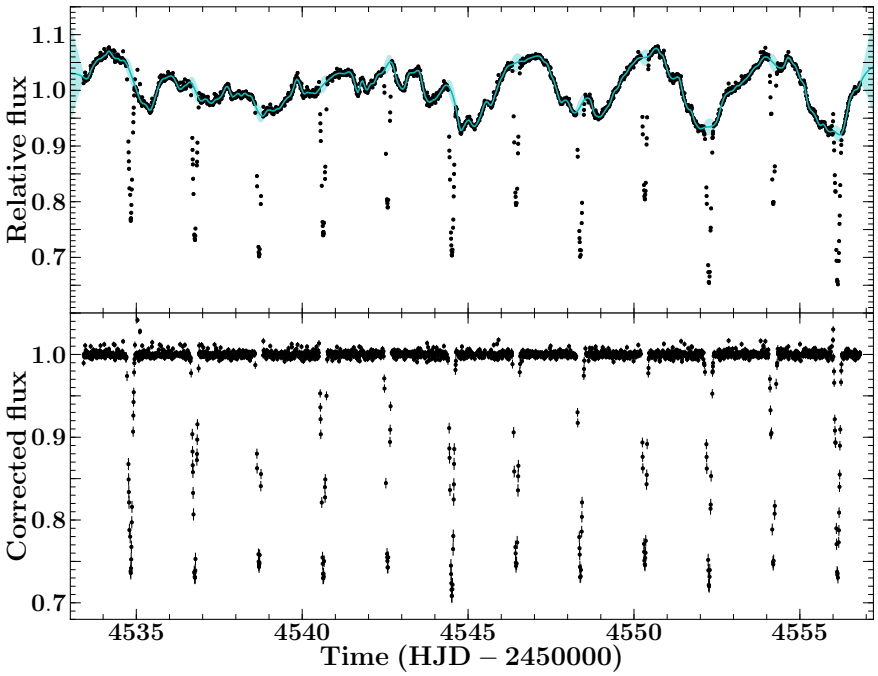

Figure 3.1: Light curve of CoRoT 223992193 obtained by CoRoT in 2008. The original light curve is shown in black in the top panel. The cyan line and light cyan shaded area show the mean and 95% confidence interval of the predictive distribution of the Gaussian Process used to model the out-of-eclipse variations. The bottom panel shows the light curve after subtracting the mean of the predictive distribution and re-normalising to unity. The detrended light curve, which was used to model the eclipses, has a typical photometric precision of $\sim 0.26\%$ per 512 s exposure.

3.2.2 Spectroscopy

We performed low resolution spectroscopy to infer the combined spectral type (credit: J. Bouvier) and medium resolution spectroscopy to extract radial velocities.

A low-resolution ($\sim$7 Å) optical spectrum of CoRoT 223992193 was obtained on 13 April 2011 (JD 2455665.3334) using the CAFOS focal reducer (Meisenheimer, 1994) on the 2.2 m Calar Alto telescope equipped with the G-100 grism and the SITe#1d_15 CCD camera, over the 4600–7700 Å wavelength range. The spectrum was acquired at an airmass of 1.4 using a slit width of 1.5 arcsec, and an exposure time of 1800 s. A spectrum of the spectrophotometric standard, Feige 34, was obtained immediately after, at an airmass of 1.0, with the same set-up. The spectra of the two objects were reduced in the same way, namely: the 2D images were bias and flat-field corrected, and the stellar and neighbouring sky spectra were extracted using the IRAF/TWODSPEC package [1] (Tody, 1993). The wavelength

[1] IRAF is distributed by the National Optical Astronomy Observatories, which are operated by the Association of Universities for Research in Astronomy, Inc., under cooperative agreement with the National Science Foundation.

Table 3.1: Coordinates and photometric properties of CoRoT 223992193. Note that the photometric uncertainties listed here are the formal measurement errors; they do not account for the intrinsic variability of the system.

RA		Dec
06 41 44.22		+09 25 02.398
Passband	(ref.)	Magnitude
u	[a]	20.021 ± 0.048
g	[a]	17.543 ± 0.005
r	[a]	16.090 ± 0.004
i	[a]	15.069 ± 0.004
z	[a]	14.479 ± 0.004
J	[b]	13.329 ± 0.029
H	[b]	12.614 ± 0.022
K	[b]	12.331 ± 0.029
[3.6]	[c]	11.731 ± 0.031
[4.5]	[c]	11.533 ± 0.049
[5.8]	[c]	11.336 ± 0.065
[8.0]	[c]	10.951 ± 0.034

[a] SDSS (Abazajian et al., 2009; Adelman-McCarthy & et al., 2009), AB magnitudes

[b] 2MASS (Cutri et al., 2003), Vega magnitudes

[c] *Spitzer*/IRAC (Sung et al., 2009), Vega magnitudes

scale was calibrated using the HgHeRb spectral lamp, and owing to the small number of lines available in the arc spectrum over the observed wavelength range, the wavelength calibration is accurate to only about 20 Å. Finally, the response of the instrument was corrected for in the target spectrum using that of the spectrophotometric standard. The resulting spectrum is shown in Figure 3.3. It exhibits clear emission at Hβ and Hα, with equivalent widths of 3.2 and 5.6 Å, respectively. The strong TiO absorption bands are indicative of a late spectral type. Comparing CoRoT 223992193's photospheric spectrum with a grid of young spectral standards from Alves de Oliveira et al. (2012) yielded a spectral type estimate of M2 with negligible visual extinction ($A_V \simeq 0$).

Moderate resolution, near-IR spectra from WHT/ISIS were also obtained. The target was observed at seven epochs between 3 and 5 December 2011, covering the wavelength range, ∼7850–8900 Å, with a spectral resolution of R ∼12000 and using the R1200R grating. Six observations were at quadrature and one close to eclipse. Three successive spectra were taken at each epoch, with exposure times of 300 or 600 s, directly followed by CuAr

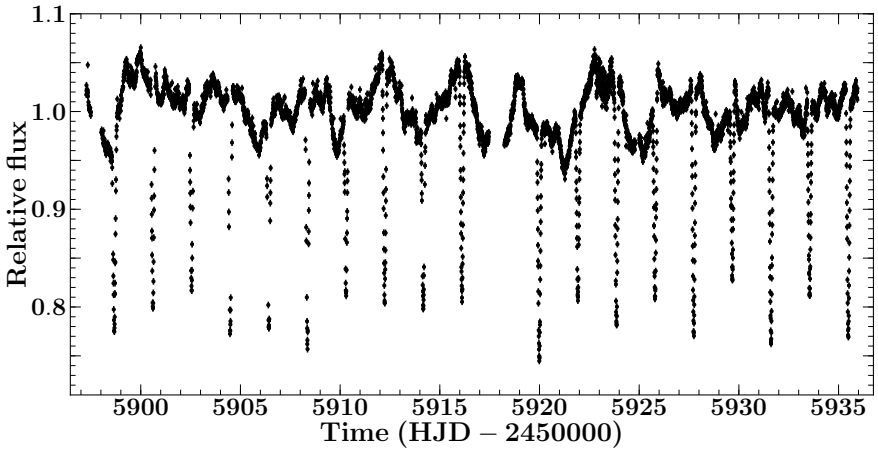

Figure 3.2: Light curve of CoRoT 223992193 obtained by CoRoT in December 2011/ January 2012.

and CuNe arc lamp spectra. An example ISIS spectrum is shown in the top panel of Figure 3.4. The ISIS spectra were processed with IRAF, using the CCDPROC packages to perform the standard CCD reduction steps (trimming and overscan subtraction, bias subtraction and flat fielding) and SPECRED.DOSLIT to extract and wavelength calibrate the spectra using the arc lamp spectra. The three exposures taken at a given epoch were then combined to maximise the signal-to-noise ratio (S/N) and perform cosmic ray rejection. The resulting spectra typically have S/N ∼20 per pixel (∼25 per spectral resolution element; see Table 3.2).

A further 21 medium resolution optical spectra were obtained with VLT/FLAMES (see section 2.3 for details). Telescope pointing issues resulted in significant loss of flux through the fibre during 6 of the 21 epochs, so that only 15 spectra could be used in the present analysis, but the phase coverage of the orbit is nonetheless fairly complete. An example FLAMES spectrum is shown in the bottom panel of Figure 3.4. The most prominent absorption feature is Li 6707.8 Å, which is consistent with the youth of the system. In this chapter, the FLAMES spectra are used only to derive radial velocities, but they contain a wealth of additional information, particularly in the broad, resolved and highly variable Hα emission line, which we analyse in Chapter 4.

Finally we also obtained three spectra with INT/IDS (see section 2.5.2 for details). As the ISIS and FLAMES spectra already gave good phase coverage of the orbit, we obtained one spectrum at quadrature and one during each eclipse in the hope of disentangling the

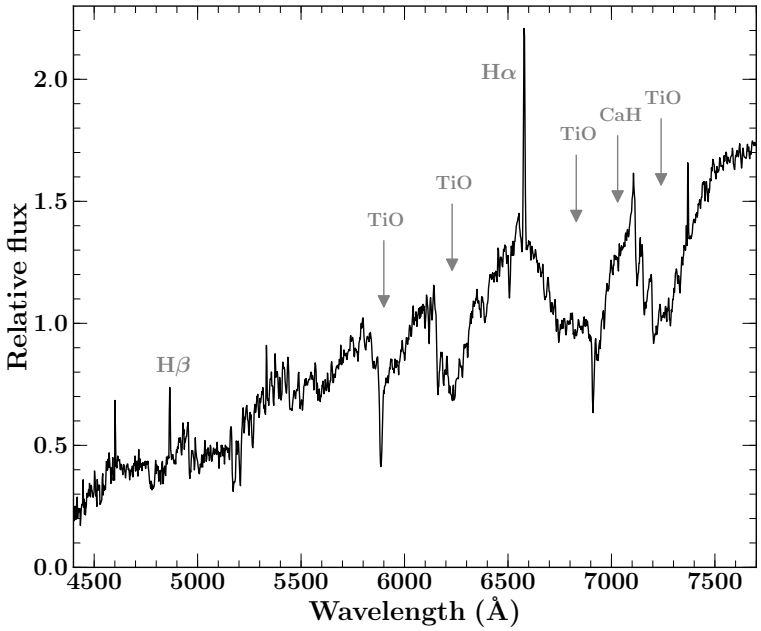

Figure 3.3: Low-resolution optical spectrum of CoRoT 223992193 taken with the 2.2 m CAHA telescope. Note the strong molecular bandheads (from TiO) characteristic of the early-M combined spectral type of the target, as well as Hα and Hβ emission.

spectra of the two components. However, the signal-to-noise ratio of the IDS spectra turned out to be insufficient for this purpose, so we did not include them in the rest of the analysis.

3.3 Analysis

3.3.1 Light Curve Modelling

3.3.1.1 Out of eclipse variability removal

The target displays significant out-of-eclipse (OOE) flux variations, which must be accounted for when modelling the CoRoT light curve to determine the fundamental parameters of the two stars. Given the complex nature of the OOE variations, it is not practical to model them at the same time as the eclipses. We therefore opted to remove the OOE variations before modelling the residuals with standard eclipse modelling software. We first tried fitting cubic splines to the OOE data (masking the in-eclipse regions) and interpolating across the eclipses. This gives fairly satisfactory results, but there is no principled way to propagate uncertainties arising from the OOE removal process through to the residuals. We therefore implemented a second approach, based on Gaussian Process (GP) regression,

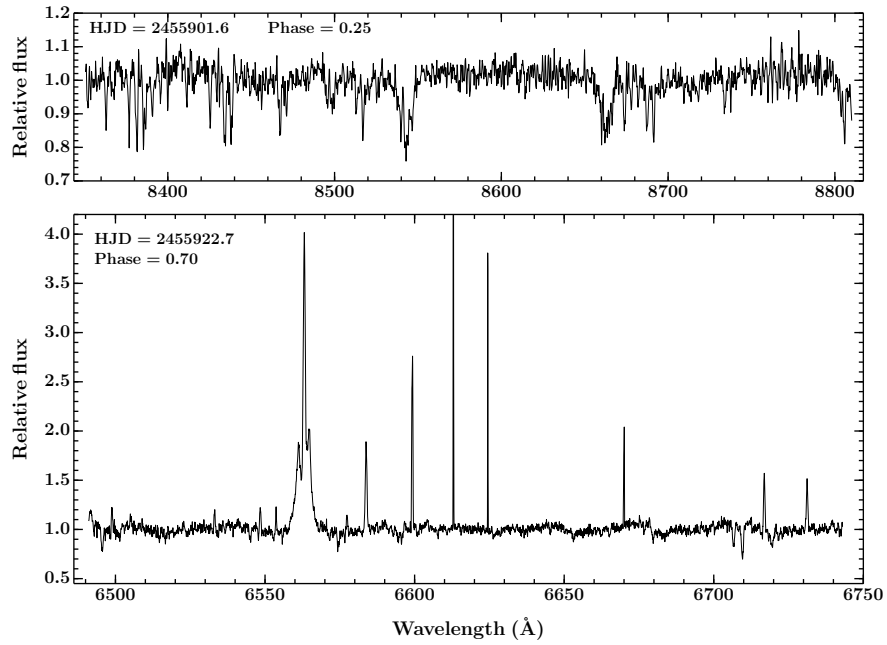

Figure 3.4: Example continuum-corrected spectra from ISIS (top), and FLAMES (bottom). Note that some of the emission lines visible in the FLAMES spectra are caused by the background nebula.

which provides both a better fit to the OOE data, and a more robust means of interpolating across the eclipses.

A detailed description of GP regression is beyond the scope of this thesis; we refer the interested reader to Rasmussen & Williams (2006) for a textbook-level introduction, Gibson et al. (2012) for a relatively detailed description in the context of astrophysical time-series data, and Aigrain et al. (2012) for specific examples of GP regression applied to stellar light curves. For the present purpose, it is sufficient to think of GPs as a means of modelling the light curve by parameterising the covariance between pairs of flux measurements, rather than specifying an explicit expression for the fluxes themselves. The joint distribution of the observed fluxes is then taken to be a multi-variate Gaussian, with a covariance matrix whose elements depend on the observation times through a covariance function. After experimenting with a range of widely-used covariance functions, we opted for a member of the Matérn family with smoothness parameter $\nu = 3/2$. This is appropriate for data displaying a relatively rough behaviour (Rasmussen & Williams, 2006), such as we observe in the OOE light curve (see Figure 3.1). The covariance k between the fluxes observed at

times t and t' is modelled as:

$$k_{3/2}(r) = A^2 \left(1 + \frac{\sqrt{3}r}{l}\right) \exp\left(-\frac{\sqrt{3}r}{l}\right) + \sigma^2 \delta(r) \tag{3.1}$$

where $r = |t - t'|$ is the time-interval between the observations and $\delta(x)$ is the Kronecker delta function. The first term represents the OOE variations, with amplitude A and characteristic time scale l, and the second term represents white noise with standard deviation σ. For a given set of parameters, the likelihood of the model, marginalised over all the possible flux vectors which share the same covariance matrix, can be estimated analytically. It requires an inversion of the covariance matrix, which is computationally expensive, but nonetheless feasible for up to a few thousand data points. In this analysis, we opt to subsample the data to speed up this inversion. We bin sets of $\sim$8 measurements, i.e. retaining information on much shorter timescales than the OOE variations, and take the median and mean values for the flux and time respectively. Starting with an initial guess for the OOE and white noise parameters (obtained from visual inspection of the light curve, and from photon counting statistics, respectively), we use a Nelder-Mead optimiser to find the values which maximise the likelihood. These are $A = 11.6\,\%$, $l = 1.25$ days and $\sigma = 1.5\,\mathrm{mmag}$. We note that the white noise estimate is comparable to the estimated photon noise of $\sigma = 1.1\,\mathrm{mmag}$ for the residuals (subsampled to the same frequency as used in the OOE modelling). Once the parameters are fixed to these values, we can then compute a predictive distribution for the fluxes at any given set of times. We do this for the times of all observations (both in and out of eclipse), and obtain a light curve corrected for the OOE variations by subtracting the mean of that distribution from the observed values (Figure 3.1, bottom panel). The standard deviation of the predictive distribution provides an estimate of the uncertainty on the corrected flux.

Once we have a satisfactory model for the OOE variations, we must decide whether to subtract it from the original, or divide the original by the OOE model, before fitting the eclipses. The appropriate course of action depends on how the OOE variability affects an eclipse. For example, spots on the background star will tend to have a multiplicative effect across an eclipse, while those on the foreground star will have an additive effect. With

eclipses on both stars, and with both stars likely to be spotted, the effect across all eclipses will not be the same. In addition, if some of the OOE variability arises from obscuration of one or both stars by material located outside the binary orbit (see Chapter 4), then this complicates matters further. Neither simply subtracting nor dividing will fully account for all the effects caused by the OOE variations. It may be feasible to disentangle the different effects using simultaneous light curves in widely separated bandpasses, but this is not possible using the CoRoT light curve alone. We therefore simply tested both approaches to remove the OOE variability. Subtracting gives slightly better results, in the sense that the depths of both primary and secondary eclipses are more consistent from one orbit to the next. We use the OOE-subtracted light curve when subsequently fitting the eclipses.

3.3.1.2 JKTEBOP

Analysis of eclipsing binary light curves yields a wealth of physical information, from orbital geometry to relative stellar parameters. Light curve modelling was performed with JKTEBOP (Southworth et al., 2004, 2007), an extension of the EBOP code (Eclipsing Binary Orbit Program; e.g. Popper & Etzel, 1981; Etzel, 1981; Nelson & Davis, 1972). As discussed in Chapter 1, JKTEBOP models each star as a sphere and computes light curves through numerical integration of concentric circles over each star, employing a Levenberg-Marquardt optimisation algorithm in finding the best fit. The approximation of modelling each star as a sphere is valid in the case of well-detached systems with modest tidal distortion.

The parameters adjusted during modelling are: J, $(R_{\rm pri} + R_{\rm sec})/a$, $R_{\rm sec}/R_{\rm pri}$, i, P, $T_{\rm prim}$, $e\cos\omega$ and $e\sin\omega$. The initial guesses for these parameters were derived from the output of the eclipse search, from visual estimates of the ratio of eclipse depths, their durations and relative phases, and from blackbody approximations relating radius, effective temperature, luminosity and surface brightness. We checked that the final results were not sensitive to the initial guesses (provided these were sufficiently close to the final values for JKTEBOP to converge). Our GP treatment of the OOE variability removes reflection and

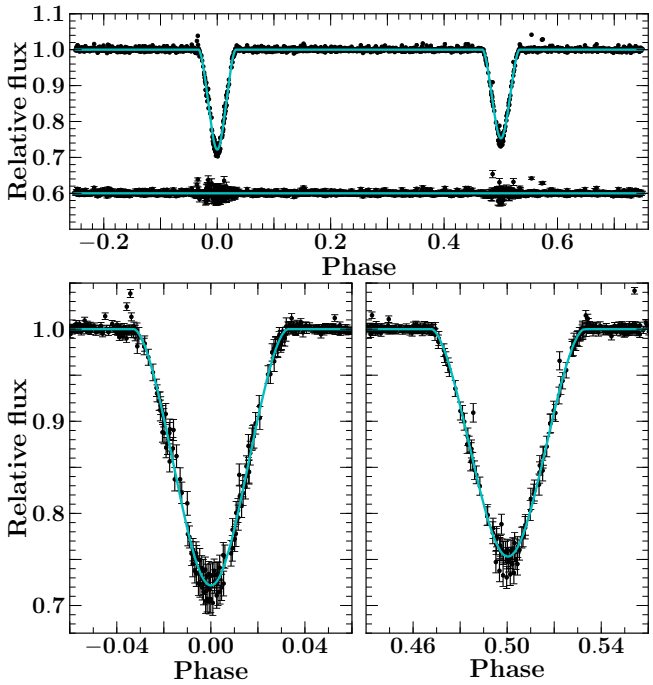

Figure 3.5: Top: Phase folded, detrended CoRoT light curve (black points, 2008 observation) with the JKTEBOP best-fit model shown in cyan. The residuals of the best-fit model are also shown, with a vertical offset for clarity. Phase zero marks the centre of the primary eclipse. The bottom panels show zooms on the primary and secondary eclipses (left and right, respectively).

gravity darkening effects from the light curve, and we therefore do not incorporate these into our modelling.

JKTEBOP models single-band light curves and unlike other techniques to determine eclipsing binary parameters, e.g WD-based models such as PHOEBE, does not require the use of model atmospheres. Effective temperatures and surface gravities therefore are only introduced in the determination of the limb darkening coefficients. We used a quadratic limb-darkening law with coefficients from ATLAS model spectra for the CoRoT bandpass (Sing, 2010). The coefficients were specified from estimates of $T_{\rm eff}$, $\log g$ and [M/H]: effective temperatures were estimated from template spectra giving the highest stellar peaks in cross-correlation (see section 3.3.2), $\log g$ was set at 4.0 (cgs) for both stars (reasonable for low-mass PMS stars) and metallicity was taken to be [M/H]$= -0.1$, the closest value available to the cluster metallicity (King et al., 2000). We initially allowed the limb darkening parameters to vary but found that this yielded unphysical values for these parameters, while it did not significantly change the results for the other parameters. This is because the eclipses are grazing and the light curve simply does not contain enough

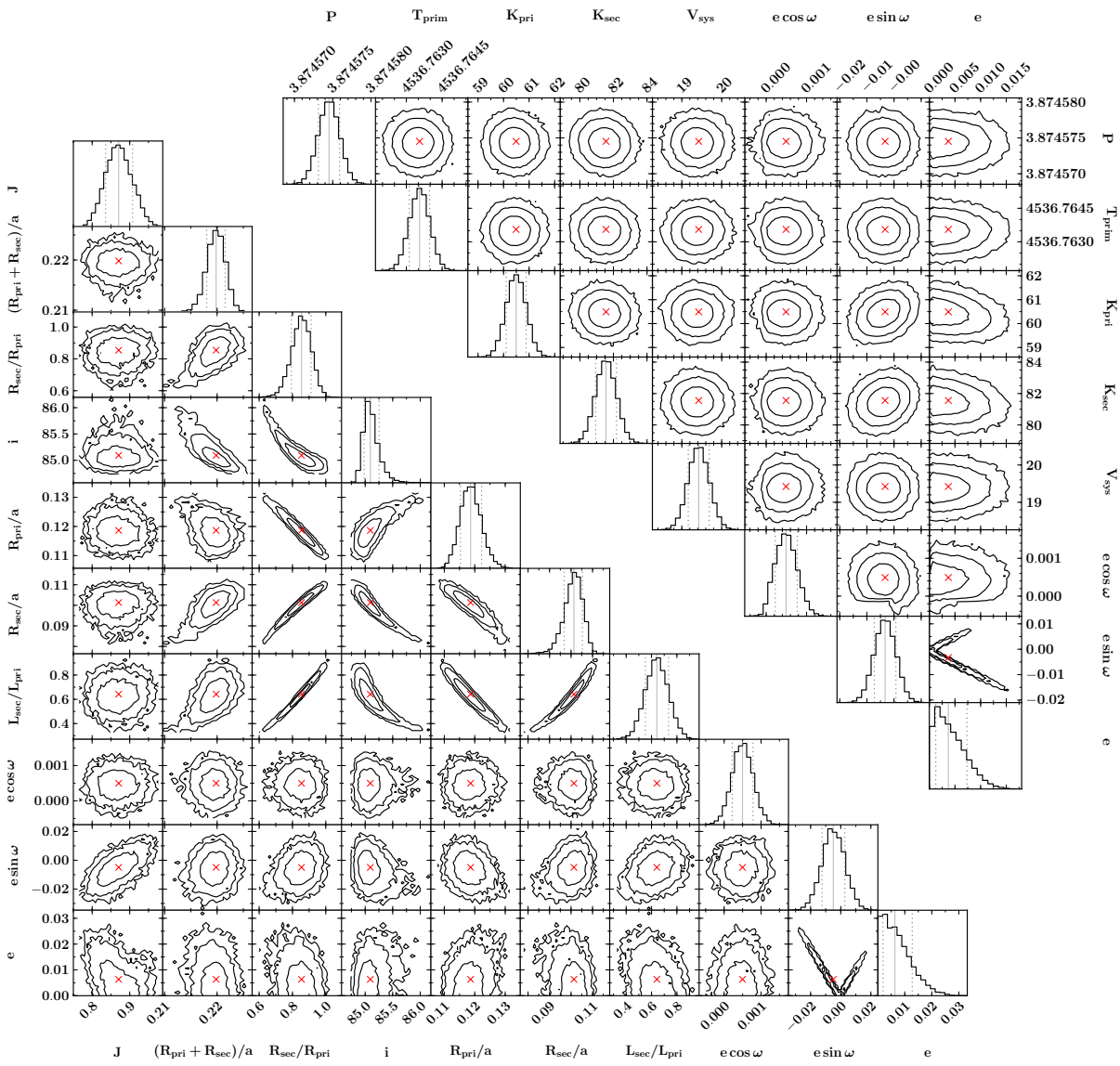

Figure 3.6: 2-D contours and 1-D histograms of the Monte Carlo chains for selected JKTEBOP parameters (bottom left) and of the MCMC chains for the photometrically constrained radial velocity solution (top right; see Section 3.3.2). On the 2-D plots, red crosses show the median values and black contours represent 1, 2 and 3 σ confidence intervals. On the histograms, solid and dotted grey vertical lines show the median and $\pm 1\sigma$ intervals, respectively.

information to constrain the limb darkening parameters. We therefore fixed them to the theoretical values in the final fit.

The fact that the eclipses are grazing also gives rise to a degeneracy between the surface brightness ratio and the radius ratio. To break this degeneracy, we added an additional constraint in the form of a light ratio, estimated from the relative cross-correlation function (CCF) peak heights. We used a FLAMES spectrum for this purpose, because the wavelength coverage of FLAMES is more similar to that of CoRoT than either ISIS or IDS, and so the

relative CCF peak heights are expected to be more representative of the light ratio of the two stars in the CoRoT bandpass. We chose a single CCF (HJD = 2455940.64, see Figure 3.7, left panel) with strong, well-separated, stellar peaks, and obtained a peak height ratio of 0.641 (see section 3.3.2 for details of the CCF fitting procedure).

As explained in Chapter 2, we rely primarily on the 2008 light curve to model the eclipses, because the spatially dependent background in the 2011/2012 observation affects the eclipse depths (the differences between the 2008 and the 2011/2012 depths is significantly larger than the small variation in the apparent eclipse depths during either run). However, we obtain the best-fit period and time of primary eclipse centre ($T_{\rm prim}$) from a combined fit to both light curves (after removing the OOE variations in the second run, in same way as for the first). The background correction error should not affect these parameters and the extended time coverage gives significantly improved accuracy.

Figure 3.5 shows the phase folded light curve along with the best-fit JKTEBOP model. The scatter of the residuals is significantly larger in eclipse than out of eclipse. This is partly due to occultation by the foreground star of starspots on the background star, as seen in numerous EB and transiting planet systems. In the present case, it is also due to increased uncertainty in the GP prediction across the eclipses, and to the residual variations in the depths of individual eclipses, already noted in Section 3.3.1.1, and which could be caused by changes in the global (or simply observable) spot coverage of either star between one eclipse and the next. To account for this increased in-eclipse scatter, we performed a preliminary JKTEBOP run on the detrended, 2008 light curve (Figure 3.1, bottom panel), and used the resulting fit to compute the reduced χ^2 for the primary, secondary and out-of eclipse data separately. The photometric uncertainties on the fluxes were then rescaled so as to give a reduced χ^2 of unity in each subset; the rescaling factors were 1.55 (primary), 2.68 (secondary) and 1.07 (out-of eclipse). JKTEBOP was then re-run (with the same initial guesses), using the scaled photometric errors.

The resulting best-fit parameters are given in Table 3.3, along with uncertainties derived from a Monte Carlo analysis. This involves generating a model light curve from the best-fit

parameters, adding Gaussian white noise (matching the observational errors), fitting the result, and repeating the procedure 10 000 times to obtain distributions for each parameter, which are shown in Figure 3.6. This procedure highlights the degeneracies between some parameters, most notably the radii, luminosity ratio and inclination, as expected for a grazing system, and ensures they are accounted for in the reported uncertainties. Interestingly, the use of the light ratio constraint from the FLAMES spectra enables us to break the usual degeneracy between the radius and surface brightness ratios, which is often the limiting factor in the final radius estimates for near equal-mass EBs (see e.g. the case of JW 380, Irwin et al. 2007). We note that the sum of the radii is roughly a fifth of the orbital separation and that the expected oblateness of each star is 0.0025 (primary) and 0.0016 (secondary), well within the allowable range for JKTEBOP (the EBOP model breaks down around an oblateness of 0.04, Popper & Etzel 1981). This validates our initial assumption that the stars are well-detached and can be treated as spherical. The best-fit model has an eccentricity consistent with zero at $< 1.5\sigma$ level. Finally, we note that there is no evidence for a change in the orbital period between the two runs, which could suggest the presence of a tertiary companion: the periods derived from modelling the SRa01 and SRa05 runs separately and together are all consistent.

3.3.2 Radial Velocities

We measured radial velocities by cross-correlating the spectra described in Section 3.2.2 with MARCS theoretical model spectra (Gustafsson et al., 2008).

Before performing the cross-correlation, we masked out regions contaminated by emission lines. There were many emission lines present in the FLAMES spectra, not only from the system but also the nebula. These emission lines were not present in the model spectra and inhibited clean cross-correlation. We therefore clipped and interpolated a few data points before and after each emission line to try and fully remove their effect[2]. After experimenting with a range of parameters for the MARCS model spectra, we opted to use $T = 4000\,\mathrm{K}$ and $\log g = 4$, which gave the best CCF contrast. We did not broaden

[2]In the rest of the thesis we use specific regions of the WHT/ISIS spectra but this does not make a significant difference for this system.

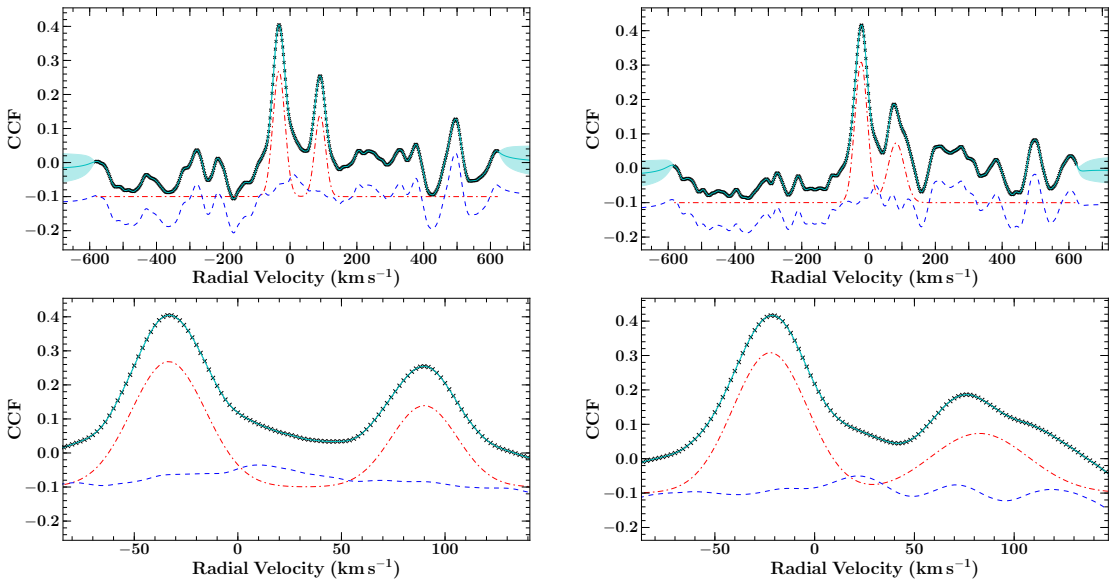

Figure 3.7: Example CCFs (black crosses) obtained from FLAMES spectra taken at HJD = 2455940.6 (left) and 2455979.6 (right), showing the best-fit model (cyan) together with the associated 68.5% confidence interval (light cyan shaded region). The Gaussian and GP terms are also shown separately by the red dot-dashed and blue dashed lines respectively, with a vertical offset added for clarity. The top panel in each case shows the full range used in the fit and the bottom panel a zoom on the region around the peaks.

the template, as that results in broader CCF features which makes it more difficult to separate the peaks corresponding to the two stars. The CCFs were computed and fitted using purpose written PYTHON code.

We initially performed a simple least-squares fit to the largest peak(s) in the CCFs, using a model consisting of either one or two Gaussians plus a constant offset. However, we found that the resulting RVs were significantly affected by the pronounced correlated noise in the CCFs (examples of which are shown in Figure 3.7). This is a major issue when measuring RVs via cross-correlation, particularly for late-type stars. This correlated noise arises in part from noise in the object spectrum and spurious matches between spectral features (Zucker & Mazeh, 1994), but also – more critically – from mismatch between the object and template spectra. A number of approaches have been developed to account for it when evaluating the uncertainties. For example, Tonry & Davis (1979) decompose the CCF into components which are symmetric and anti-symmetric with respect to the peak, and use the root mean square (RMS) scatter of the antisymmetric component to estimate the CCF noise, on the basis that any 'real' CCF signal should be symmetric about the peak. This is the most widely used approach, and it is implemented in the IRAF cross-correlation

Table 3.2: Radial velocities derived from the WHT/ISIS and VLT/FLAMES spectra. RV values in brackets were not used in deriving the orbital solution, for reasons detailed in the text. C and W are the height and full-width at half-maximum of each peak, respectively.

HJD	Orbital phase	S/N (/pixel)	Primary			Secondary		
			C	W ($\mathrm{km\,s^{-1}}$)	RV ($\mathrm{km\,s^{-1}}$)	C	W ($\mathrm{km\,s^{-1}}$)	RV ($\mathrm{km\,s^{-1}}$)
				ISIS				
2455899.51482	0.716	~ 14	0.36	33.3 ± 1.8	$+73.6 \pm 1.9$	0.28	35.4 ± 2.5	-68.7 ± 2.7
2455899.73483	0.773	~ 13	0.25	$36.9^{+2.5}_{-3.9}$	$(+83.4 \pm 3.9)$	0.08	94^{+537}_{-78}	(-57^{+73}_{-236})
2455900.55487 *	0.985	~ 19				0.69	30.9 ± 1.0	$(+16.5 \pm 1.0)$
2455901.50491	0.230	~ 18	0.37	32.7 ± 1.2	(-40.6 ± 1.4)	0.28	31.2 ± 1.6	$(+96.2 \pm 1.8)$
2455901.57491	0.248	~ 25	0.60	32.7 ± 1.1	-50.0 ± 1.1	0.42	35.0 ± 2.0	$+95.0 \pm 1.8$
2455901.69492	0.279	~ 24	0.56	32.8 ± 1.3	-49.2 ± 1.2	0.42	33.3 ± 1.7	$+93.2 \pm 1.6$
2455901.77492	0.300	~ 21	0.51	34.8 ± 1.3	-49.0 ± 1.2	0.43	34.8 ± 1.6	$+88.7 \pm 1.4$
				FLAMES				
2455915.65584	0.882	~ 26	0.36	20.8 ± 1.8	$+60.5 \pm 1.6$	0.21	16.1 ± 1.7	-38.1 ± 1.7
2455917.70423	0.411	~ 22	0.37	19.9 ± 1.3	-13.2 ± 1.3	0.17	$34.2^{+6.4}_{-5.4}$	$+66.5 \pm 5.3$
2455918.68222	0.663	~ 22	0.38	17.6 ± 1.1	$+74.9 \pm 1.2$	0.15	$16.1^{+2.1}_{-2.8}$	-46.4 ± 2.7
2455922.69870	0.700	~ 22	0.40	18.2 ± 1.1	$+75.3 \pm 1.2$	0.20	$17.9^{+2.1}_{-2.5}$	-53.1 ± 2.4
2455939.65778	0.077	~ 22	0.37	19.0 ± 1.6	-8.1 ± 1.2	0.18	16.7 ± 1.6	$(+52.6 \pm 2.2)$
2455940.64342	0.331	~ 34	0.38	17.6 ± 1.1	-33.2 ± 1.1	0.24	16.1 ± 1.4	$+89.9 \pm 1.5$
2455940.67976	0.341	~ 34	0.41	18.4 ± 1.1	-31.1 ± 1.1	0.27	16.2 ± 1.2	$+88.2 \pm 1.4$
2455941.66163	0.594	~ 35	0.38	18.4 ± 1.2	$+50.9 \pm 1.0$	0.22	24.2 ± 3.0	(-19.4 ± 2.6)
2455943.68750	0.117	~ 23	0.38	18.5 ± 1.3	-21.6 ± 1.2	0.19	21.4 ± 4.0	$+76.3 \pm 3.0$
2455944.63515	0.362	~ 32	0.36	19.4 ± 1.8	-24.9 ± 1.5	0.22	17.1 ± 1.9	$+84.4 \pm 2.1$
2455945.66720	0.628	~ 36	0.34	16.7 ± 1.2	$+62.0 \pm 1.2$	0.18	16.8 ± 1.9	-39.8 ± 2.2
2455946.68154	0.890	~ 22	0.36	20.7 ± 1.6	$+56.9 \pm 1.4$	0.23	19.3 ± 2.3	-29.1 ± 1.9
2455977.63971	0.880	~ 30	0.33	19.4 ± 1.8	$+62.1 \pm 1.4$	0.19	$20.4^{+3.8}_{-6.0}$	$-34.7^{+3.1}_{-4.2}$
2455979.57946	0.380	~ 31	0.40	18.7 ± 1.0	-21.9 ± 1.0	0.17	$26.0^{+6.0}_{-4.8}$	$(+81.4 \pm 4.8)$
2455981.61509	0.906	~ 28	0.40	18.1 ± 1.0	$+50.5 \pm 1.0$	0.24	24.2 ± 2.6	-21.1 ± 2.5

* Only one stellar peak was resolved in the CCF because the spectra were taken close to primary eclipse.

package FXCOR. Working with VLT/FLAMES spectra of moderately faint stars from the OGLE survey, Bouchy et al. (2005) used the relation $\sigma_{\mathrm{RV}} = 3\sqrt{\mathrm{FWHM}}/S\,C$, where σ_{RV} is the RV uncertainty, C and FWHM are the height and full-width at half-maximum of the CCF peak, respectively, and S is the signal-to-noise of the object spectrum. The form of this relation was deduced from photon-noise considerations, and it was calibrated on multiple observations of a large sample of stars, most of which were presumed to be non-variable. In practice, both of these methods give good results for the objects they were initially designed for, but they tend to systematically under-predict the uncertainties for late-type, rapidly rotating stars.

We therefore decided to model the CCF noise at the same time as fitting for the CCF peaks. Each CCF was modelled as the sum of two Gaussians[3] plus a stochastic noise term, which is described by a GP. The choice of GP kernel was based on a careful examination of the CCFs such as those shown in Figure 3.7. Away from the main peak(s), the CCFs display variations on both moderate velocity scales (few tens of $\mathrm{m\,s^{-1}}$) and long velocity scales (few 100 $\mathrm{m\,s^{-1}}$). These cannot be adequately described by a single squared exponential covariance function, which only allows for variations on a single characteristic length scale:

$$k_{\mathrm{SE}}(r) = A^2 \exp\left(-\frac{r^2}{2l^2}\right). \tag{3.2}$$

Instead, we use the rational quadratic:

$$k_{\mathrm{RQ}}(r) = A^2 \left(1 + \frac{r^2}{2\alpha l^2}\right)^{-\alpha}. \tag{3.3}$$

This can be seen as a squared exponential with a certain amount of additional covariance on large scales, controlled by the parameter α (when α is $\gg 1$, it reduces to the squared exponential), or alternatively as a scale mixture of squared exponential covariance functions with different characteristic length-scales (Rasmussen & Williams, 2006). We also incorporate a very small white noise term on the diagonal of the covariance matrix to aid convergence. For the sake of computational efficiency, we model the CCFs only in the range $-580 \leq v \leq 620\,\mathrm{km\,s^{-1}}$, and use only every other data point in the fit. We used a Metropolis-Hastings Markov Chain Monte Carlo (MCMC) with Gaussian proposal distributions to marginalise over the parameters of the Gaussian terms and of the covariance function. We performed five relatively short-chains of 15000 steps, which were sufficient to achieve convergence in all cases; the first 5000 steps were discarded to minimise sensitivity to the initial guesses, and the parameter distributions were derived from the remaining 10000 steps. Figure 3.7 shows example CCFs with the best-fit model obtained in this way.

Not all the CCFs contain well-defined peaks that clearly stand out above the noise. To avoid inferring erroneous RV measurements, we visually inspected every CCF and fit, and discarded any epochs where the contrast of stellar peaks was below $\sim$0.1, or where

[3]No evidence for a third stellar peak was detected in the CCFs.

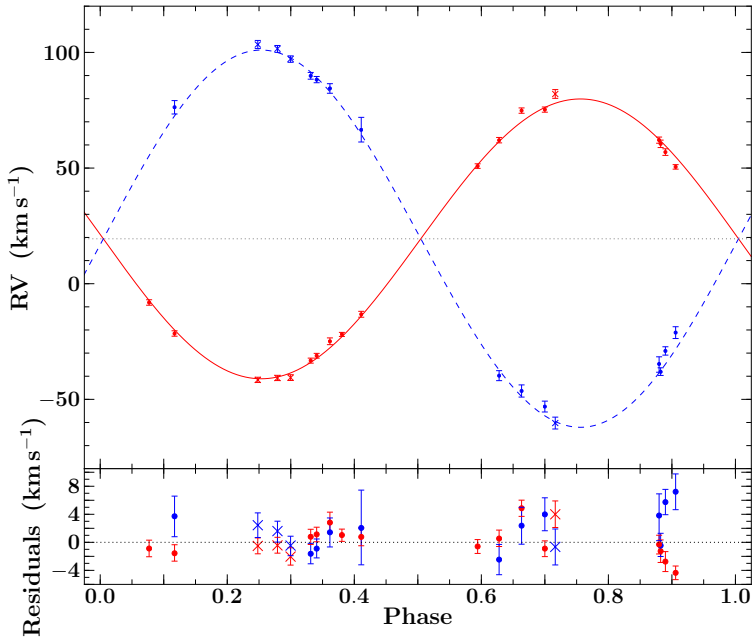

Figure 3.8: Top: Phase-folded RV data (points with error bars) and best-fit orbital solution for the primary (red solid line) and secondary (blue dashed line). Crosses and circles represent RVs derived from ISIS and FLAMES spectra, respectively. The grey horizontal dotted line shows the systemic velocity. Bottom: residuals of the best-fit model.

the properties of the GP component of the fit appeared to change markedly in the region containing the stellar peaks. In a few cases, the best fit to the secondary peak is low compared to the noise, has an unusually large width, and has an RV slightly offset from the expected value (given a preliminary orbital solution based on the rest of the observations). An example of such a case is shown in the right panel of Figure 3.7. In such cases, we discarded the secondary measurement, but retained the primary RV. We note that it might be possible to obtain RV measurements from a larger fraction of our spectra by fixing the widths of the two stellar peaks, but we opted not to do this, as we already have enough useful RVs for a good orbital solution, and this would only add data points with large error bars.

3.3.2.1 Orbital solution

We fit the RV measurements using Keplerian orbits, as described in section 1.4.2. The parameters of the fit were $K_{\rm pri}$ and $K_{\rm sec}$ (the semi-amplitudes of the primary and secondary), $V_{\rm sys}$ (the systemic velocity), as well as P, $T_{\rm prim}$, $e\cos\omega$ and $e\sin\omega$. The values and uncertainties obtained from the light curve modelling for the last four of these parameters

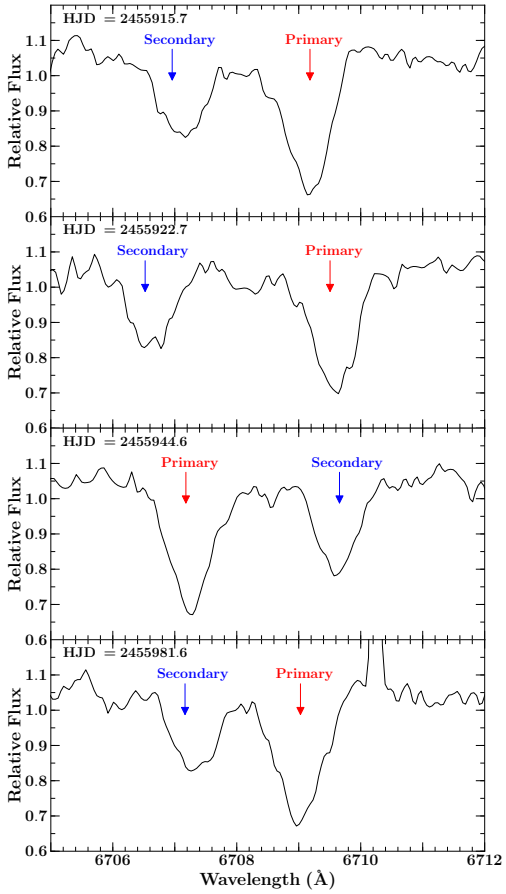

Figure 3.9: Examples of the lithium 6707.8 Å absorption feature for both primary and secondary stars from FLAMES spectra. From top to bottom, HJD = 2455915.7, 2455922.7, 2455944.6 and 2455981.6. In each case the predicted positions of the two stars are indicated.

were used as priors in the RV fit. We used a Metropolis-Hastings MCMC with Gaussian proposal distributions to estimate the uncertainties on the parameters of the RV fit and performed 5 chains of 10^5 steps each to ensure convergence. Figure 3.8 shows the resulting orbital fit, whose parameters are listed in Table 3.3. The distributions from the MCMC are shown in Figure 3.6 and display negligible degeneracy.

We find that our systemic velocity of $V_{\rm sys} = 19.42 \pm 0.26$ km s^{-1} is consistent with the literature value of the cluster's recessional velocity, $V = 22 \pm 3.5$ km s^{-1} (Fűrész et al., 2006), suggesting that the system is kinematically associated with the cluster.

3.3.3 Lithium absorption

The presence of lithium (6707.8 Å) absorption in both stars (Figure 3.9) indicates youth and therefore membership. We determine equivalent widths of both lines by first fitting a cubic

spline through the continuum data (masking out all absorption and emission features) and interpolating across each lithium line. We then determine relative flux contributions from each star (using the CCF peak heights for that spectrum) and scale both the data and the spline, before calculating the equivalent widths. We select three spectra in which the lines are well separated and calculate approximate equivalent widths of 0.56 and 0.55 Å for the primary and secondary, respectively (each individual measurement is mutually consistent with these values to within 0.01 and 0.02 Å, respectively). The equivalent widths are very similar, tentatively suggesting that there has not been significant lithium depletion, as the rate of depletion is expected to be faster in the less massive secondary. They are also consistent with other cluster members (e.g. Sergison et al., 2013), including early/mid-K spectral types, which are expected to still have their initial abundances at this age.

3.3.4 Fundamental Parameters

From our photometric and radial velocity analysis, we can calculate masses and radii. We propagate our distributions for the period, semi-amplitudes of the velocities, radius sum, radius ratio and inclination to derive masses and radii (using equations 1.36 and 1.37). These are presented in the bottom part of Table 3.3, along with the surface gravities and orbital separations. The masses of $0.668^{+0.012}_{-0.011}$ and $0.4953^{+0.0073}_{-0.0072}\,M_{\odot}$ are consistent with the combined spectral type derived from the CAHA spectrum. The large radii ($1.295^{+0.040}_{-0.037}$ and $1.107^{+0.044}_{-0.050}\,R_{\odot}$) are what we would expect for a PMS system.

3.4 Discussion

3.4.1 Comparison to pre-main sequence stellar evolution models

We are now in a position to place the components of CoRoT 223992193 on the mass-radius diagram (Figure 3.10, red diamonds). We note that it lies in a very sparsely populated region of the diagram, highlighting its value in testing and constraining PMS stellar evolution models. In Figure 3.11, we compare the masses and radii of both stars to six sets of widely used pre-main sequence (PMS) isochrones: BCAH98 (Baraffe et al., 1998), DM98 (D'Antona & Mazzitelli, 1998), SDF00 (Siess et al., 2000), Dartmouth (Dotter et al.,

Table 3.3: Fitted and derived parameters of the system.

Parameter	Symbol	Unit	Value
	JKTEBOP light curve fit		
Central surface brightness ratio	J		$0.871^{+0.037}_{-0.035}$
Sum of radii	$(R_{\rm pri}+R_{\rm sec})/a$		$0.2198^{+0.0017}_{-0.0018}$
Radius ratio	$R_{\rm sec}/R_{\rm pri}$		$0.854^{+0.058}_{-0.061}$
Fractional primary radius	$R_{\rm pri}/a$		$0.1186^{+0.0036}_{-0.0033}$
Fractional secondary radius	$R_{\rm sec}/a$		$0.1013\ ^{+0.0039}_{-0.0045}$
Orbital inclination	i	(°)	$85.09\ ^{+0.16}_{-0.11}$
Orbital period	P	(days)	3.8745746 ± 0.0000014
Time of primary eclipse centre	$T_{\rm prim}$	(HJD)	$2454536.76357 \pm 0.00043$
	$e\cos\omega$		$0.00050^{+0.00029}_{-0.00028}$
	$e\sin\omega$		$-0.0049^{+0.0077}_{-0.0075}$
	Photometrically constrained RV fit		
Primary semi-amplitude	$K_{\rm pri}$	($\mathrm{km\,s^{-1}}$)	60.49 ± 0.39
Secondary semi-amplitude	$K_{\rm sec}$	($\mathrm{km\,s^{-1}}$)	81.56 ± 0.62
Systemic velocity	$V_{\rm sys}$	($\mathrm{km\,s^{-1}}$)	19.42 ± 0.26
Orbital period	P	(days)	3.8745745 ± 0.0000014
Time of primary eclipse centre	$T_{\rm prim}$	(HJD)	$2454536.76355^{+0.00042}_{-0.00043}$
	$e\cos\omega$		$0.00049^{+0.00028}_{-0.00027}$
	$e\sin\omega$		-0.0033 ± 0.0040
	Derived parameters		
Luminosity ratio [a]	$L_{\rm sec}/L_{\rm pri}$		$0.642^{+0.092}_{-0.091}$
Orbital eccentricity	e		$0.0037^{+0.0036}_{-0.0025}$
Semi-major axis	a	($R_\odot$)	10.921 ± 0.056
Primary mass	$M_{\rm pri}$	($M_\odot$)	$0.668^{+0.012}_{-0.011}$
Secondary mass	$M_{\rm sec}$	($M_\odot$)	$0.4953^{+0.0073}_{-0.0072}$
Primary radius	$R_{\rm pri}$	($R_\odot$)	$1.295^{+0.040}_{-0.037}$
Secondary radius	$R_{\rm sec}$	($R_\odot$)	$1.107^{+0.044}_{-0.050}$
Primary surface gravity	$(\log g)_{\rm pri}$	($\mathrm{cm\,s^{-2}}$)	$4.038^{+0.025}_{-0.026}$
Secondary surface gravity	$(\log g)_{\rm sec}$	($\mathrm{cm\,s^{-2}}$)	$4.045^{+0.040}_{-0.033}$
Primary semi-major axis [b]	$a_{\rm pri}$	($R_\odot$)	4.651 ± 0.030
Secondary semi-major axis [b]	$a_{\rm sec}$	($R_\odot$)	$6.270^{+0.047}_{-0.048}$

[a] in the CoRoT bandpass.

[b] relative to centre of mass.

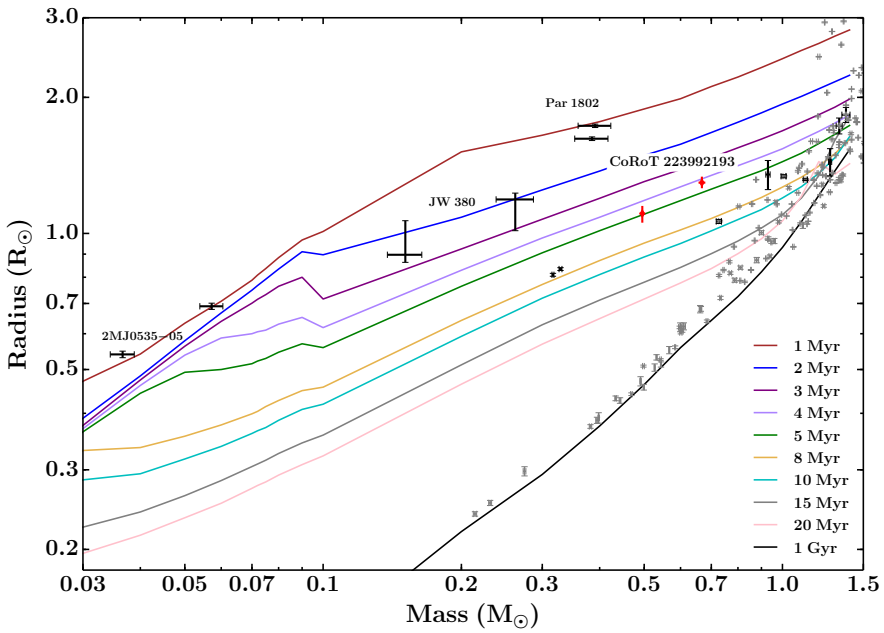

Figure 3.10: Mass-radius relation for low-mass EBs. The grey and black points show measurements for stars with masses $< 1.5\,M_\odot$ in detached EBs[1] (for main and pre-main sequence systems).The lines show, from top to bottom, the theoretical isochrones of Baraffe et al. (2015, BHAC15) for 1, 2, 3, 4, 5, 8, 10, 15, 20 Myr and 1 Gyr (brown, blue, purple, lilac, green, ochre, cyan, grey, pink and black, respectively. $Y = 0.28$, [M/H] = 0, mixing length $\alpha = 1.6$). The components of CoRoT 223992193 are shown by red diamonds. Note that the system lies in a very sparsely populated region of the diagram, making it a valuable test of PMS stellar evolution models. For comparison, we have also labelled the three youngest, lowest mass systems known in the Orion Nebula Cluster (see Table 1.2 for details. For clarity, the higher mass systems are not labelled).

2008), Pisa (Tognelli et al., 2011) and BHAC15 (Baraffe et al., 2015); the model parameters are given in Table 3.4. These were chosen to match the metallicity of NGC 2264. For BCAH98 we selected models with a solar-calibrated mixing length $\alpha_{\rm ML} = 1.9$, which have been extended down to $0.1\,M_\odot$ (I. Baraffe, priv. comm[4]). For the Pisa models we chose $\alpha_{\rm ML} = 1.2$, as models with lower convective efficiency are known to be more consistent with existing observations of low-mass PMS objects (e.g. Stassun et al., 2004; Mathieu et al., 2007).

BCAH98, SDF00, Dartmouth, Pisa and BHAC15, which contain non-grey surface boundary conditions, all manage to fit both components of CoRoT 223992193 simultaneously. In contrast, DM98, which uses grey surface boundary conditions, is unable to fit both components with a single isochrone. All models under-predict the radius of the primary slightly, compared to that of the secondary. This is a feature which is also seen in other close

[4]The extended models are available at http://perso.ens-lyon.fr/isabelle.baraffe/

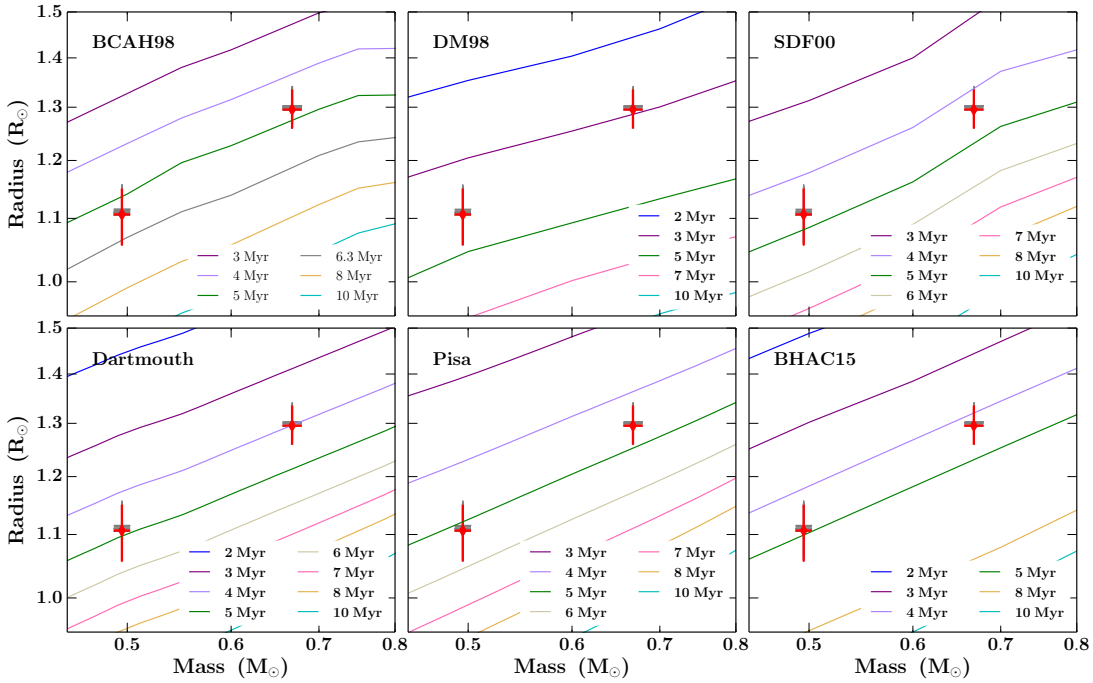

Figure 3.11: Comparison of measured masses and radii for the two components of CoRoT 223992193 to the predictions of six sets of theoretical PMS models (see text for details). In each subplot the ages of the isochrones increase from top to bottom. The isochrone colour scheme is consistent between subplots; the apparent differences are due to the different temporal sampling in the models. The different values obtained when varying the limb-darkening coefficients (see Section 3.4.2) are shown in grey and the final, adopted values by red diamonds.

binaries, and Chabrier et al. (2007) proposed that it could be due to enhanced magnetic activity on the primary. However, in the present case the discrepancy is not statistically significant ($< 1.5\,\sigma$). More precise masses and radii for this system are needed to distinguish between the different models containing non-grey surface boundary conditions.

The best match to the BCAH98, SDF00, Dartmouth, Pisa and BHAC15 isochrones is obtained for ages ∼3.5–6 Myr. Ages from all isochrones are consistent with the literature estimates of the age of NGC 2264, given the wide dispersion of the latter. For example, Dahm (2008) report a median age of 3 Myr, but infer an apparent age spread of 5 Myr from the broadened sequence of cluster members, and Naylor (2009) determine a slightly older age of 5.5 Myr. Baraffe et al. (2009, 2012) showed that the broadened cluster sequences observed in a number of star forming regions, which are usually interpreted as arising from an age spread, could also be caused by episodic accretion early on in the star formation process. Importantly, they predict that, if most of the accreted energy is radiated away (which is expected for the modest initial core masses that will eventually become low-mass

Table 3.4: Parameters of the stellar evolution models shown in Figure 3.11. Information on the parameters is given below the Table.

Model	Y	Z	$\alpha_{\rm ML}$	$X_{\rm D}$ ($\times 10^{-5}$)	Reference
BCAH98	0.282	0.019	1.9	2.0	Baraffe et al. (1998)
DM98	0.28	0.02	1.5	2.0	D'Antona & Mazzitelli (1998)
SDF00	0.277	0.02	1.605	2.0	Siess et al. (2000)
Dartmouth	0.274	0.0189 *	1.938	0.0	Dotter et al. (2008)
Pisa	0.268	0.01	1.2	2.0	Tognelli et al. (2011)
BHAC15	0.28	0.019	1.6	2.0	Baraffe et al. (2015)

Y = He mass fraction, Z = metal mass fraction, $\alpha_{\rm ML}$ = mixing length parameter, $X_{\rm D}$ = deuterium abundance.

* [Fe/H] = [α/Fe] = 0

stars), accreting stars should have *smaller* radii than non-accreting stars of the same age and mass. Differential accretion history could therefore contribute not only to the apparent age spread within star forming regions such as NGC 2264, but also to the discrepancies between the parameters of individual components of binary systems such as CoRoT 223992193.

However, it is worth noting that a non-steady accretion history is also expected to cause enhanced lithium depletion, due to higher temperatures at the base of the convective envelope (Baraffe & Chabrier, 2010) and this is not seen in the present case. In addition, other well-characterised PMS EBs, e.g. JW 380 in the ONC and UScoCTIO 5 in Upper Scorpius, posses internally coeval components. Kraus & Hillenbrand (2009) investigate the coevality of young visual binary systems in the Taurus-Auriga association and find $\sim 2/3$ appear coeval to within $\Delta \log \tau < 0.16$ dex or $< 40\%$. They attribute the discrepancies in the remainder to unrecognised hierarchical multiples, or stars seen in scattered light or which have disk contamination. This implies that $\leq 20\%$ of all stars have apparent ages that differ substantially from the true age (Kraus et al., 2015).

3.4.2 Stellar temperatures and the effect of limb darkening

When modelling the eclipses, we fixed the limb darkening (LD) coefficients to theoretical values from Sing (2010), given an estimate of the effective temperature of each star. We initially chose temperatures of 4000 and 3750 K, which maximised the peak of the CCF for

the primary and secondary respectively. However, our best-fit masses and radii correspond to somewhat lower effective temperatures, of 3670 and 3570 K respectively, according to the BCAH98 isochrones. To check whether this has a significant effect on our analysis, we repeated the eclipse modelling using every combination of temperatures for which Sing (2010) tabulated LD coefficients, such that the $4250\,\mathrm{K} \geq T_{\mathrm{eff,pri}} \geq T_{\mathrm{eff,sec}}$ (LD coefficients were available for 3500, 3750, 4000 and 4250 K). The results are shown in Figure 3.11: the values obtained using different combinations of temperatures are shown by the grey symbols, while the adopted values are shown by red diamonds. These correspond to effective temperatures of 3750 K and 3500 K for the primary and secondary respectively, and provide the best internal consistency between the effective temperatures used to fix the LD coefficients and those derived from the measured masses and radii according to the BCAH98 isochrones. We note, however, that the masses and radii themselves are essentially insensitive to the choice of LD coefficients, within the range we examined.

3.4.3 Distance to CoRoT 223992193

Having measured radii and obtained approximate effective temperatures for the two stars, we can evaluate their luminosities and hence the distance to the system. This can then be compared to published estimates of the distance to NGC 2264, as a further consistency check. We performed this check using both the V and K band magnitudes of the system. The V-band magnitude was obtained by averaging the *ugriz* magnitudes' approximation (according to the prescription of Jester et al. 2005), and the quoted V-band magnitude from Dahm et al. (2007, V = 16.81). This gives $V = 16.74 \pm 0.1$, where the uncertainty has been inflated to account for the system's variability.

To derive distances to the system, we used the theoretical bolometric corrections (BCs) of Bessell et al. (1998), as they provide the best sampling in our region of the T_{eff}–$\log g$ parameter space. Empirical BCs are also available in the literature, but these have been shown to give comparable results to the theoretical BCs (e.g. Southworth et al., 2005). We adopt the values tabulated for solar metallicity, the closest match available to the metallicity of the cluster, and for $\log g = 4.0$, which again provides the best match to our

Table 3.5: Estimates of the distance to CoRoT 223992193 using V and K-band magnitudes, bolometric corrections (BCs; Bessell et al., 1998) for different effective temperature estimates, and a range of extinction estimates (from both the literature and as indicated from the CAHA spectrum, Figure 3.3).

Extinction (mag)	$T_{\rm eff}$ (K) (pri)	(sec)	Distance (pc)
$A_V = 0.71$	3500	3500	561 ± 61
(Dahm & Simon, 2005)	3750	3500	627 ± 71
	3750	3750	668 ± 73
$A_V = 0.45$	3500	3500	633 ± 69
(Rebull et al., 2002)	3750	3500	707 ± 80
	3750	3750	754 ± 83
$A_V = 0.25$	3500	3500	694 ± 76
(Sung et al., 1997)	3750	3500	775 ± 88
	3750	3750	826 ± 91
$A_V = 0.0$	3500	3500	776 ± 85
(CAHA spectrum)	3750	3500	868 ± 98
	3750	3750	924 ± 101
$A_K = 0.073$	3500	3500	766 ± 85
(Rebull et al., 2002)	3750	3500	743 ± 82
	3750	3750	728 ± 81
$A_K = 0.0$	3500	3500	791 ± 87
(CAHA spectrum)	3750	3500	768 ± 84
	3750	3750	751 ± 83

estimate of the surface gravities of both stars. The BCs are tabulated for $T_{\rm eff} = 3500$ and 3750 K, and are very sensitive to temperature, particularly in the V-band, so we computed a combined bolometric magnitude for the system using either value for each star (always ensuring $T_{\rm eff,pri} \geq T_{\rm eff,sec}$). Finally, we carried out the calculation for different amounts of extinction along the line of sight, both to the cluster, corresponding to the different determinations available in the literature (Sung et al., 1997; Rebull et al., 2002; Dahm & Simon, 2005), and for CoRoT 223992193, from the CAHA spectrum (Figure 3.3). The results are reported in Table 3.5. Note that although we have matched $T_{\rm eff}$ and $\log g$ to our estimates for the system, giant stars with the same values would posses different photospheres and so a systematic uncertainty will be present, the effect of which is not well understood.

The V-band extinction estimates in the literature vary widely, mainly because of the different samples of stars used to measure them: the lowest value of $A_V = 0.25$ was obtained by Sung et al. (1997) using O and B main sequence stars, and the highest ($A_V = 0.71$)

by Dahm & Simon (2005) using lower mass Hα emitters which may well have dustier environments. Rebull et al. (2002) measured an intermediate value of $A_V = 0.45$, as well as $A_K = 0.073$, using a spectroscopically selected sample of K and M stars. As the K-band distance estimates are less sensitive to reddening, and the BCs in that band less temperature-dependent, we consider the distance estimates we obtain using the K-band magnitude of the system and effective temperatures of 3750 K for the primary and 3500 K for the secondary, to be the most reliable. We consider the full distance range given by the Rebull et al. (2002) determination of A_K and that inferred from the CAHA spectrum.

This places the system at a distance of 756 ± 96 pc, in good agreement with the distances reported for the cluster by Sung et al. (1997) (760 ± 90 pc from isochrone fitting to main sequence B stars) and Sung & Bessell (2010) (815 ± 95 pc, from fitting the spectral energy distribution of individual members using the models of Robitaille et al. 2007). Baxter et al. (2009) obtained a somewhat larger estimate of $913 \pm 40 \pm 110$ pc (sampling and systematic errors respectively) by comparing projected rotational velocities and rotational periods, assuming an isotropic inclination distribution. This estimate relies heavily on $v \sin i$ measurements which are notoriously difficult using low signal-to-noise spectra, but is still within 2σ of our value for CoRoT 223992193. Thus we can confirm that the system's magnitude and fundamental parameters are consistent with cluster membership. Finally, we note that the determined distance to CoRoT 223992193 is not consistent with the anomalous, smaller distance estimate of ∼400 pc for NGC 2264, as suggested by Dzib et al. (2014). As noted in Chapter 1, optical measurements of low-mass stars are more sensitive to the unspotted regions and hence can yield a slight over-estimate for $T_{\rm eff}$. It is therefore possible that our derived distance is also a slight over-estimate. However, we do not believe this can reconcile the Dzib et al. (2014) distance.

3.5 Conclusions and future work

This chapter reports a new double-lined, detached eclipsing binary, comprising two pre-main sequence M-dwarfs, discovered by the CoRoT space mission in the NGC 2264 star forming region. We have measured the fundamental parameters of both stars using the continuous

23.4 day light curve obtained by CoRoT in March 2008, as well as 22-epochs of radial velocity data obtained almost four years later with VLT/FLAMES and WHT/ISIS. The orbit is consistent with circular ($e = 0.0037^{+0.0036}_{-0.0025}$) and has a period of 3.8745745 ± 0.0000014 days and a separation of $10.921 \pm 0.056\,R_{\odot}$. The primary and secondary stars have masses of $0.668^{+0.012}_{-0.011}$ and $0.4953^{+0.0073}_{-0.0072}\,M_{\odot}$, and radii of $1.295^{+0.040}_{-0.037}$ and $1.107^{+0.044}_{-0.050}\,R_{\odot}$, respectively. The systemic velocity is within 1σ of the cluster median which, along with the presence of lithium absorption, strongly indicates cluster membership.

At the time of discovery this was only the ninth PMS EB system with component masses below $1.5\,M_{\odot}$ (there are now 10), and it lies in a region of the mass-radius plane where existing observational constraints are very scarce. Within the current uncertainties, the parameters of the two stars are essentially consistent with the predictions of PMS stellar evolution models for ages of ∼3.5–6 Myr. Although we have broken the degeneracy between the radius and surface brightness ratios, which can be a severe limitation in grazing EB systems, the final uncertainties on the component masses and radii are still a few percent. As highlighted by Torres et al. (2010), sub-percent accuracies are needed to place truly significant constraints on evolutionary models.

We hope to improve the constraints on this system in the future, by refining the treatment of the out-of-eclipse variability and improving the radial velocity determination (see section 5.6). In addition, obtaining simultaneous light curves in different bandpasses and performing spectral disentangling on high resolution, high S/N spectra would yield precise temperature constraints, as well as refining the light curve parameters and RV orbit; precise mass, radius and temperature constraints would provide a powerful test of PMS stellar evolution models.

The work presented in this chapter represents the first step in the characterisation of CoRoT 223992193. In Chapter 4 we analyse the spectral energy distribution and investigate the physical origins of the observed photometric and spectroscopic variability.

Chapter 4

Variability in CoRoT 223992193: an active eclipsing binary with evidence of a circumbinary disk?

The SED analysis presented in this Chatper is based on:
Gillen et al. (2014). ***CoRoT 223992193: A new, low-mass, pre-main sequence eclipsing binary with evidence of a circumbinary disk.*** **A&A, 562, A50.**

In this chapter we present evidence for a circumbinary disk in CoRoT 223992193 through analysis of the spectral energy distribution (SED). We then analyse the photometric and spectroscopic variability in the CoRoT and Spitzer *light curves, and VLT/FLAMES Hα profiles, before presenting a model of the inner regions of the binary.*

The SED reveals a mid-infrared excess, which we model as thermal emission from a small amount of dust located in the inner cavity of a circumbinary disk. The presence of dust in the cavity at ∼4–5 Myr implies the presence of a circumbinary disk as the most natural means of replenishment.

The system displays complex photometric and spectroscopic variability over a range of timescales and wavelengths. We model the out-of-eclipse light curves (2008 CoRoT, and 2011/2012 CoRoT and Spitzer 3.6 and 4.5 μm), finding that the large scale structure in both CoRoT light curves is consistent with the constructive and destructive interference of starspot signals at two slightly different periods. Using the $v \sin i$ of both stars, we interpret this as the two stars having slightly different rotation periods; the primary is consistent with

synchronisation and the secondary rotates slightly supersynchronously. Comparison of the raw 2011/2012 light curve data to the residuals of our spot model in colour-magnitude space indicates additional contributions consistent with a combination of variable dust emission and obscuration. For the latter, we identify short-duration flux dips preceding secondary eclipse in all three CoRoT and Spitzer bands. A model of the inner regions of the binary is constructed and we propose that these dips could be caused by partial occultation of the central binary by the accretion stream onto the primary star.

Analysis of the 15 VLT/FLAMES Hα profiles reveal an emission profile associated with each star. The majority of this is consistent with chromospheric emission but additional higher velocity emission is also seen, which could be due to prominences. However, half of the secondary star's emission profiles display full widths at 10% intensity that could also be interpreted as having an accretion-related origin. In addition, the simultaneous u and r-band CFHT/MegaCam observations reveal a short-lived u-band excess consistent with either an accretion hot spot or stellar flare.

The photometric and spectroscopic variations are consistent with the picture of two active stars possibly undergoing non-steady, low-level accretion; the system's very high inclination provides a new view of such variability.

All work presented in this chapter is my own except for a) obtaining, reducing and determining $v \sin i$ *s from the NOT/FIES spectra, which was performed by D. Gandolfi, and b) modelling the inner regions of the binary, which was performed by C. Terquem.*

4.1 Spectral energy distribution

As a likely member of NGC 2264, CoRoT 223992193 is presumably no more than a few Myr old. It is therefore natural to ask whether there is any evidence for circumstellar or circumbinary material in the spectral energy distribution (SED) of the system. This material could conceivably contribute to the large-amplitude, rapidly evolving, out-of-eclipse variability in the CoRoT light curves, particularly as we will see in Section 4.3 that it is difficult to explain this variability using starspots alone. Indeed, the OOE variability

of CoRoT 223992193 is similar to that of classical T Tauri stars in the same region (Alencar et al., 2010). It is also, to a certain extent, reminiscent of the quasi-periodic flux variations seen of AA Tau (e.g. Bouvier et al., 1999, 2003, 2007), which are attributed to occultations of the central star by a warped circumstellar disk. We therefore constructed an SED for CoRoT 223992193 using the magnitudes listed in Table 3.1. We also sought evidence of emission at longer wavelengths from archival data, namely *Spitzer*/MIPS 24 μm [1] and *Herschel*/PACS 70 and 160 μm [2]. The nebula is prominent at these wavelengths (increasing with wavelength) and displays significant structure. Unfortunately, this system lies on the edge of a nebula filament making detection and analysis more difficult. We performed aperture photometry with Aperture Photometry Tool (APT)[3] and found no clear evidence of emission associated with this system. At the PACS wavelengths, the nebula is very bright, and while there is emission above the sky level at CoRoT 223992193's location, its profile is not Gaussian, it is not centred on the system and its structure largely follows the nebula. At MIPS 24 μm, the nebula is less prominent but the emission observed follows the structure of the nebula, and while there is a hint of a slightly larger flux at the system's location, it is not statistically significant given the scatter in the sky flux. A more detailed analysis, accounting for the structured nebula emission would be necessary to determine whether this small excess is real. We therefore attribute the emission at the system's location to the nebula in all cases and compute an upper limit for the flux of CoRoT 223992193 at each wavelength by taking the 'nebula' emission (above that of the median sky level) and quoting the 3σ upper limit on this value. These upper limits are: 4.7, 35.2 and 1916.3 mJy at 24, 70 and 160 μm respectively. The resulting SED is shown in Figure 4.1.

A preliminary inspection of the SED suggests that there is a moderate amount of excess flux in the mid-IR. We confirmed this by fitting a stellar photosphere model to the Sloan and 2MASS fluxes, and comparing the best fit model to the observed *Spitzer* fluxes. To do this we constructed a grid of two-photosphere models from pairs of MARCS spectra with

[1] Spitzer Heritage Archive, http://sha.ipac.caltech.edu/applications/Spitzer/SHA/
[2] Herschel Science Archive, http://herschel.esac.esa.int/Science_Archive.shtml
[3] http://www.aperturephotometry.org/

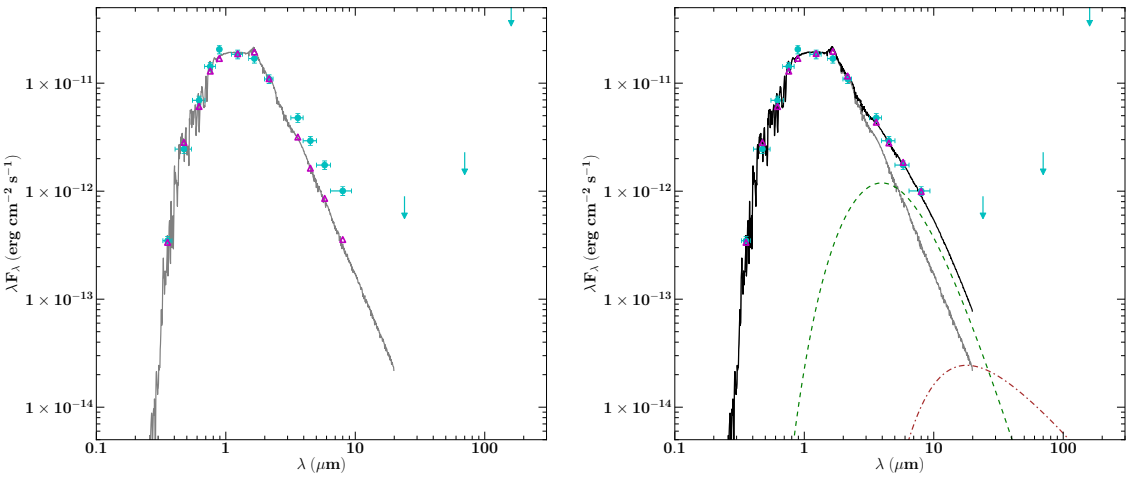

Figure 4.1: Spectral energy distribution of CoRoT 223992193 (cyan points) based on the magnitudes listed in Table 3.1, plus upper limits in the far-infrared (cyan arrows). Left: the grey line and magenta triangles show the best-fit two naked photospheres model. Right: the black line and magenta triangles show the best-fit two naked photospheres model with a small amount of hot dust in the inner cavity of the circumbinary disk (see text for details). The stellar and hot dust terms are shown separately as the grey solid and dashed green lines, respectively. Also shown for completeness, but not used in the fit, is the expected emission from a razor-thin circumbinary disk extending down to 22 $R_\odot$ (brown dot-dashed line), which is illuminated by the central star and heated by the gravitational potential energy released from accretion with $\dot{M} = 10^{-11} M_\odot\,\mathrm{yr}^{-1}$.

$2500 \leq T_{\rm eff} < 8000\,\mathrm{K}$, $\log g = 4.0$ and solar metallicity, ensuring that $T_{\rm eff,pri} \geq T_{\rm eff,sec}$, and that the radii of the two stars were within 5σ of the measured values. We then convolved the model spectra with the bandpass of each filter and optimised the χ^2 of the fit with respect to the temperatures and radii of the two stars, and the distance and amount of extinction to the system. We constrain the temperatures such that $T \geq 3300\,\mathrm{K}$ to be consistent with the combined spectral type and temperature ratio from JKTEBOP. The best fit parameters are: $T_{\rm pri} = 3700\,\mathrm{K}$, $T_{\rm sec} = 3600\,\mathrm{K}$, $R_{\rm pri} = 1.42\,R_\odot$ ($+\,3\,\sigma$), $R_{\rm sec} = 1.15\,R_\odot$ ($+\,1\,\sigma$), distance = 830 pc and $A_V = 0.1$. The results are shown in the left panel of Figure 4.1, showing that there is clear excess emission in the mid-IR compared to any reasonable combination of naked stellar photospheres. We also investigated the effect of starspots on the primary star covering up to 20% of the stellar surface but could still not match the mid-IR magnitudes.

We therefore tested whether this excess could be due to extended dust emission in the vicinity of the two stars. To do this, we must first set out the basic geometry of the system. As the system is young, each star could be surrounded by a circumstellar disk, and both by a circumbinary disk. Tidal truncation of the circumstellar disks by the other star

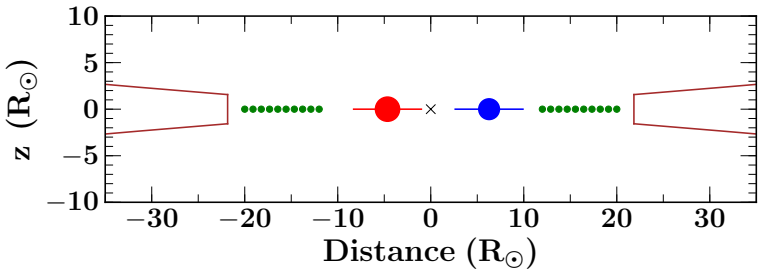

Figure 4.2: Schematic representation of the proposed system geometry, showing distance from the centre of mass against height above the system plane (z). The primary and secondary stars, along with their circumstellar disks (truncated to a third of the binary separation), are shown in red and blue respectively (the circumstellar disks are shown for completeness but there is no direct evidence for their presence). The sizes and separations of the two stars are to scale. The circumbinary disk (brown) has its inner radius truncated at twice the binary separation. The green dots indicate the general location of dust lying within the inner cavity of the circumbinary disk, such as one could expect to find in accretions streams.

would limit their outer radii to about one third of the binary separation (Paczynski, 1977; Papaloizou & Pringle, 1977, i.e. $\sim$0.017 AU or 3.6 $R_\odot$). The circumbinary disk would be centred on the centre of mass of the binary, and its inner radius is expected to be roughly twice the binary separation, i.e. $\sim$0.1 AU or 22 $R_\odot$, because the tidal torque exerted by the binary prevents the disk from extending further in (Lin & Papaloizou, 1979). However, material may stream through the inner cavity to be accreted onto the circumstellar disks (Artymowicz & Lubow, 1996). A schematic representation of this geometry is shown in Figure 4.2.

There is no evidence for excess emission in the near-IR, which is where we would expect any emission from material in the circumstellar disks to peak. If the primary were a single star, its sublimation radius, i.e. the distance beyond which amorphous dust grains typically survive ($T_{\mathrm{dust\ grain}} \leqslant 1500$ K), would be 3.9 $R_\odot$. This assumes that the temperature of a dust grain at a distance r from a star of luminosity L is given by $T_{\mathrm{dust}} = \left[L/(16\pi\sigma r^2)\right]^{1/4}$, i.e. that the grains are spherical blackbodies, and are located in an optically thin environment. This close to the primary star, the effect of the secondary's flux on the dust temperature is not significant. Similarly, if the secondary star were single, its sublimation radius would be 3.2 $R_\odot$, at which distance the flux of the primary star has a negligible effect. Therefore, the circumprimary disk would not be expected to contain dust and the circumsecondary disk would only be expected to contain a small amount of very hot dust near the sublimation temperature. Added to this, the CCF peaks are not

obviously rotationally broadened, which given the resolution of the FLAMES spectrograph, implies that the two stars have rotational velocities of order 17 $\mathrm{km\,s^{-1}}$ or less. Taking this limiting value gives corotation radii (the radii in the circumstellar disks where the Keplerian period is equal to the stellar rotation period) of $\gtrsim 8.2\,R_\odot$ and $\gtrsim 7.4\,R_\odot$ for the primary and secondary stars, respectively. The strong magnetic fields of young, low-mass stars are usually assumed to lead to truncation of the inner disk at or near the corotation radius, which makes it less likely that circumstellar disks exist in this system. Note that the allowed rotational velocities of both stars are consistent with synchronisation; the corresponding rotation periods are $\gtrsim 3.87$ and $\gtrsim 3.31$ days for the primary and secondary respectively.

We therefore attempted to model the mid-IR excess (essentially the residuals of the photosphere-only model shown in the left panel of Figure 4.1 but with the radii of the two stars constrained to within $1\,\sigma$) as emission from dust in a circumbinary disk. As the inner edge of the circumbinary disk is $> 20\,R_\odot$ from the centre of mass of the system, we can approximate the incident flux by that of a single star with luminosity $L_\star = L_1 + L_2$, temperature $T_\star$ such that $\sigma T_\star^4 = L_1/(4\pi R_1^2) + L_2/(4\pi R_2^2)$ and radius $R_\star$ such that $\sigma T_\star^4 = L_\star/(4\pi R_\star^2)$.

We consider a razor thin disk that is aligned with the plane of the binary's orbit and which radiates away energy from both incident stellar flux and the gravitational potential energy released by the accretion of gas. An order of magnitude estimate of the accretion rate $\dot{M} = 10^{-11} M_\odot\,\mathrm{yr}^{-1}$ was determined from the multicomponent Hα emission, using the relation described in Fang et al. (2009) (J. Bouvier & L. Venuti, priv. comm.). This is also consistent with the UV excess upper limit derived from fitting the SED models of Robitaille et al. (2007). We compute the disk temperature as

$$T_{\mathrm{disk}} = \left(T_{\mathrm{irr}}^4 + T_{\mathrm{acc}}^4\right)^{1/4} \tag{4.1}$$

where, following Armitage (2010), T_{irr} and T_{acc} are the temperatures arising from stellar

irradiation and accretion respectively, and are given by

$$T_{\rm irr}^4 = \frac{T_\star^4}{\pi}\left(\sin^{-1}\left(\frac{R_\star}{r}\right) - \frac{R_\star}{r}\sqrt{1-\left(\frac{R_\star}{r}\right)^2}\right) \tag{4.2}$$

$$T_{\rm acc}^4 = \frac{3GM_\star\dot{M}}{8\pi\sigma r^3}\left(1-\sqrt{\frac{R_\star}{r}}\right) \tag{4.3}$$

The disk SED is shown by the brown dot-dashed line in the right panel of Figure 4.1, which is two orders of magnitude smaller than that observed between 3.6 and 8 μm. We need an accretion rate of $\sim 10^{-7}\,M_\odot\,{\rm yr}^{-1}$ to reproduce the observed fluxes. Such a high accretion rate would lead to much stronger Hα emission, and a large UV excess, three orders of magnitude larger than observed (from the u-band magnitude of the system). We conclude that the mid-IR excess cannot be explained by emission from a circumbinary disk.

We now consider the possibility that the mid-IR excess is due to optically thin dust located in the inner cavity of the circumbinary disk, following Jensen & Mathieu (1997), who found evidence for this in the SEDs of a number of young spectroscopic binaries. This could arise from ongoing low-level accretion from the circumbinary disk onto the two stars, as predicted by recent numerical simulations (Shi et al., 2012). The geometry and kinematics of any dust located within the cavity would, of course, be complex. However, for the purpose of estimating the approximate temperature of the dust and the amount of it needed to reproduce the observed SED, a very simplified toy model is sufficient. We assume that the dust surface mass density varies as $r^{-1/2}$, and that the gas-to-dust ratio is 100. Again, we approximate the incident radiation field by using a single star with the parameters given above. We are now considering dust located much closer to the two stars, so the validity of this approximation is more doubtful, but it is acceptable for a simple order of magnitude calculation. We model the line-of-sight optical depth through the disk as $\tau_\lambda(r) = \kappa_\lambda\Sigma(r)/\cos i$, where Σ is the gas surface density, i is the angle between the normal to the disk plane and the line of sight, and $\kappa_\lambda = 0.1(\lambda/250\,\mu{\rm m})^{-1}\,{\rm cm}^2\,{\rm g}^{-1}$ is the

opacity (Jensen & Mathieu, 1997). The emitted flux is then given by:

$$\lambda F_\lambda = \frac{\cos i}{D^2} \int_{r_{\rm in}}^{r_{\rm out}} \lambda B_\lambda[T_{\rm dust}(r)] \left(1 - e^{-\tau_\lambda(r)}\right) 2\pi r \, dr. \tag{4.4}$$

where the inner and outer radii of the cavity, $r_{\rm in}$ and $r_{\rm out}$, should be larger than the sublimation radius of the single star we consider ($5\,R_\odot$) and similar to the circumbinary disk's inner radius, respectively. The flux received from the cavity increases with the mass of dust as long as $\tau_\lambda < 1$ and becomes insensitive to this mass when the optical depth reaches unity[4]. We find that we can explain the observed mid-IR excess with as little as $\sim 1 \times 10^{-13}\,M_\odot$ of dust, which gives $\tau_\lambda \sim 1$ at the outer edge of the cavity for λ between 3.6 and 8 μm. In this model, the cavity extends from ~ 5 to $32\,R_\odot$ with corresponding dust temperatures of ~ 1450 to 600 K. The resulting fit to the SED is shown in the right panel of Figure 4.1. Although the outer radius of the dust model is slightly larger than the expected inner edge of the circumbinary disk, they are of the same order of magnitude, which is sufficient given the very simplified nature of our model. Note that the mass of dust required and the extent of the cavity are insensitive to interstellar reddening (up to $A_V = 1.0$). As a consistency check, we compared the mass of dust we calculate to that required to reproduce the estimated mass accretion rate, and find them in agreement to within an order of magnitude.

Our model is very crude, but it does demonstrate that the observed SED can be reproduced by invoking a very small amount of dust within the inner cavity of a circumbinary disk, such as one could expect to find in accretion streams. Unfortunately, the flux measurements beyond 10 μm are only rather weak upper limits, because of emission by interstellar dust filaments (nebulosity) superimposed on the target, so we cannot place any constraints on the circumbinary disk itself. However, the presence of such a disk would certainly be required to replenish the dust in the cavity. This is because when dust grains enter the inner cavity, their motion is essentially ballistic; the accretion timescale is therefore close to the free fall time.

[4]Even if the dust is optically thin when considering light from the star incident on a particle within the cavity, it could be optically thick when viewed (near) edge-on, i.e. from the point of view of an observer on Earth.

4.2 Variability in T Tauri stars

Classical T Tauri stars (CTTS) are young solar-type stars ($M < 2M_{\odot}$), which accrete material from their circumstellar disks. They display both photometric and spectroscopic variability over a range of timescales (from hours to years) and wavelengths (from ultraviolet to infrared). This variability is inferred to result from processes at and near the stellar surface and can be categorised into intrinsically stellar and accretion-related processes (e.g. Bouvier et al., 2007; Cody et al., 2014). Weak-lined T Tauri stars (WTTS) are commonly thought to represent young systems after the accretion process has finished and display only stellar variability (e.g. Grankin et al., 2008).

Intrinsic stellar variations are caused by surface inhomogeneities arising from cool, magnetically active starspots, which cause photometric and spectroscopic modulation due to the star's rotation. Accretion-related variations arise from the infall of material from the circumstellar disk onto the star which, in the most commonly accepted paradigm, is mediated by the stellar magnetic field. Zeeman measurements indicate typical surface field strengths of order a few kilogauss (e.g. Symington et al., 2005; Donati et al., 2008), which is strong enough to disrupt the inner disk flow at a few stellar radii, truncating the disk and funnelling material towards the star along the magnetospheric field lines. The structure and evolution of these accretion columns are governed by the field configuration, the inclination between the stellar rotation and magnetic axes, and the mass accretion rate (Romanova et al., 2003, 2008; Long et al., 2007, 2008). As material approaches the stellar surface it reaches near free-fall velocities, dissipating its kinetic energy in a shock at the stellar surface and heating the immediate area.

In this context, an actively accreting TTS could display photometric variability arising from cool and hot spot modulation, changing mass accretion rates and variable extinction (e.g. Venuti et al., 2015). Extinction can result from obscuration of the central star by the inner disk wall, either due to a warp, as in AA Tau-like objects (e.g. Bouvier et al., 1999; Fonseca et al., 2014), or possibly due to changing disk height (e.g. Flaherty & Muzerolle, 2010; Espaillat et al., 2011). Spectroscopically, such a star would display variable permitted

emission lines whose profiles might show evidence of hot spots, accretion columns and disk winds, and in a less well-ordered accretion framework, emission from material in the stellar magnetosphere (Alencar et al., 2012). High mass accretion rates can also drive stellar winds and jets, which can be investigated through forbidden emission line profiles (Shang et al., 2002).

TTS variability is ubiquitous and has been studied since their discovery by Joy (1945). In recent decades, most ground-based studies have focussed on optical and near-infrared (near-IR) photometry (e.g. Bouvier et al., 1993; Herbst et al., 1994; Makidon et al., 2004; Grankin et al., 2007; Parks et al., 2014). Recent observations with the *Spitzer Space Telescope* and *Herschel* detected flux variations in disk-bearing stars in the mid and far-IR (e.g. Morales-Calderón et al., 2011; Espaillat et al., 2011; Billot et al., 2012). Combining the available data with advances in modelling of the star-disk interaction and inner disk dynamics has furthered our understanding of the underlying physics but has yet to unambiguously distinguish between plausible physical scenarios, in part due to the sparseness and non-simultaneity of the data (Flaherty & Muzerolle, 2010; Romanova et al., 2011, 2013).

Further progress may come from the ongoing YSOVAR project (Young Stellar Object Variability; Morales-Calderón et al., 2011; Rebull et al., 2014), which monitors a dozen young clusters at high cadence with *Spitzer*/IRAC at 3.6 and 4.5 μm. In addition, the recent Coordinated Synoptic Investigation of NGC 2264 (CSI 2264) comprises the most extensive continuous simultaneous multi-band photometric and spectroscopic dataset ever compiled for a young star forming region. It is introduced in detail in Cody et al. (2014) who analyse simultaneous optical CoRoT and IR *Spitzer* photometry of 162 disk bearing stars to classify their variability into seven morphological variability classes, which they argue represent different physical mechanisms and geometric effects. Surprisingly, they also find that optical and IR variability is not correlated in the majority of cases. Additional insights have come from analysing AA Tau analogs and their cousins with deep, aperiodic flux dips (McGinnis et al., 2015), as well as a similar, but distinct, class of CTTS that

displays narrow, periodic flux dips (Stauffer et al., 2015). Furthermore, a new morphological class of CTTS was reported by Stauffer et al. (2014) whose light curves are dominated by short-duration accretion bursts.

The vast majority of variability studies to date have focussed on single T Tauri stars in clusters. As a significant fraction of stars form in binaries or higher order systems (Duchêne & Kraus, 2013) it is important to understand both the physical processes at play and their effect on the system's formation and early evolution. In well-separated, accreting binary systems one might expect individual circumstellar disks around each star, as well as a circumbinary disk around both, separated by a region of very low density, which arises from the transfer of angular momentum from the binary to the circumbinary disk (Artymowicz & Lubow, 1994). Material streams through this central cavity from the circumbinary disk onto the circumstellar disks, which in turn accrete onto the stars (Artymowicz & Lubow, 1996; Günther & Kley, 2002). One might therefore expect any of the aforementioned variability to be present for each star as well as additional contributions from the accretion streams and the inner regions of the circumbinary disk. In close-separation binaries substantial circumstellar disks may be prohibited due to tidal truncation by the other star (Paczynski, 1977; Papaloizou & Pringle, 1977) but accretion can still take place via the accretion streams. Due to the greater geometric complexity of binary systems, characterising the physical origins of their variability is more challenging than for single stars, and hence one needs well-characterised, benchmark systems to use as test-beds.

CoRoT 223992193 is an ideal candidate for studying variability in a young, close-separation binary for two reasons: a) the stellar properties and system geometry are known to a precision unattainable for non-eclipsing systems, and b) we have obtained continuous simultaneous multi-band photometric and spectroscopic observations (as part of CSI 2264), which allow us to probe the variability over a range of timescales and wavelengths.

In the remainder of the chapter we address the following question: *what are the physical origins of both the photometric and spectroscopic variability seen in CoRoT 223992193.* In section 4.3 we model the 2008 and 2011/2012 photometric observations and discuss

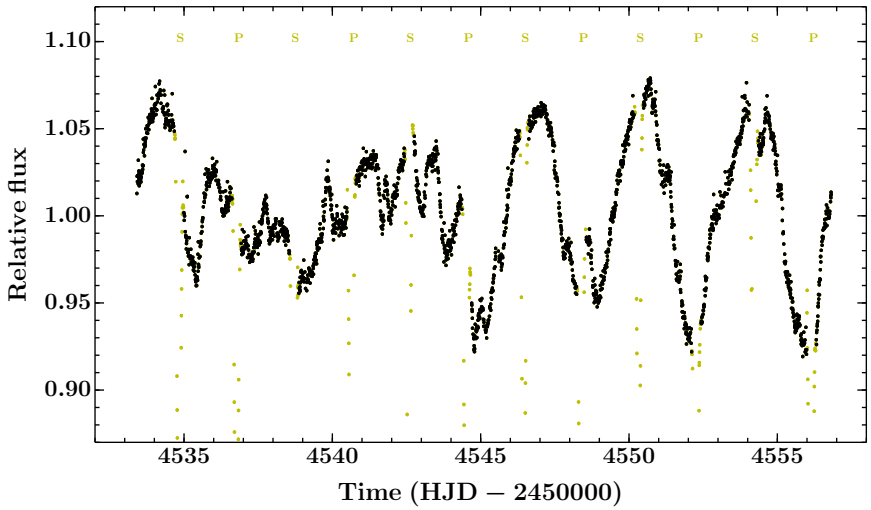

Figure 4.3: CoRoT light curve from the 2008 observations. The out-of-eclipse data is shown in black and the stellar eclipses in yellow (P and S indicate primary and secondary eclipses, respectively).

plausible physical origins for the different types of variability. In section 4.4 we model the Hα profiles and search for other emission lines, and in section 4.5 we perform consistency checks between the photometric and spectroscopic data. Finally, we present a model of the inner regions of the binary and propose a possible scenario to explain the observed short-duration flux dips in section 4.6, before concluding in section 4.7.

4.3 Photometric variability

4.3.1 Overall light curve morphology

4.3.1.1 2008 CoRoT light curve

The 2008 CoRoT light curve is shown in Fig. 4.3 with the out-of-eclipse (OOE) data in black and stellar eclipses in yellow. There are two apparent 'regimes' in the OOE variability: one where small amplitude, short-timescale variations (SAVs) dominate the structure (cf. rHJD[5] ∼4536–4543), and one where large amplitude, quasi-periodic variations (LAVs) dominate (cf. rHJD ∼4545–4557), but where the SAVs are still present.

4.3.1.2 Simultaneous 2011/2012 CoRoT and *Spitzer* light curves

The simultaneous optical and IR light curves obtained by CoRoT and *Spitzer* during the 2011/2012 campaign confirm the long-lived nature of the intriguing out-of-eclipse (OOE)

[5]reduced heliocentric julian date = HJD - 2450000

variability seen in 2008 (Fig. 4.3) and can help us investigate its physical origin(s). The top three plots of Fig. 4.4 show the CoRoT and *Spitzer* 3.6 and 4.5 μm light curves with the OOE data in black and stellar eclipses in yellow. The CoRoT light curve displays a similar morphology to that seen in 2008: small amplitude, short-timescale variations (SAVs) dominate the structure between rHJD ∼5900–5910 and between 5930–5936, and large amplitude, quasi-periodic variations (LAVs) dominate between rHJD ∼5910-5925, but again the SAVs are still present. The light curve morphologies of the two IR *Spitzer* bands appear to be dominated by the SAVs; the LAVs seen in the CoRoT light curves have a reduced amplitude indicating a relatively warm origin. The most striking common feature in all three bands of the 2011/2012 dataset are short, sharp flux dips, e.g. at rHJD $\sim$ 5910 and 5925, which occur just before secondary eclipse (i.e. at multiples of the binary orbital period) and display different colour signatures throughout the light curves. There are also differences in behaviour, e.g. at rHJD $\sim$ 5926 the CoRoT flux falls whereas both *Spitzer* fluxes rise. The complexity of the observed variations suggests multiple origins.

4.3.1.3 CFHT light curves

Simultaneous u and r-band light curves obtained with CFHT/Megacam the month after the 2011/2012 CoRoT/*Spitzer* run (Fig. 4.5) show a short-lived u-band excess at rHJD $\sim$ 5974. Perhaps the simplest interpretation of this is a stellar flare (e.g. Fernández et al., 2004). However, given that we require dust in the central cavity of the circumbinary disk to explain the SED it is plausible that some of this material accretes onto one or both stars. The u-band excess could therefore be explained as a short-lived accretion hot spot resulting from accreting material heating the stellar surface upon impact. Due to the sparsely sampled CFHT data it is difficult to differentiate between these two options from the shape of the u-band excess or to place meaningful constraints on the frequency of such events, as we are insensitive to many periods. Nonetheless, this opens up the possibility that some of the variations in the CoRoT and *Spitzer* light curves could be due to short-lived, and potentially recurring, hot spot emission or to stellar flares. We recall that the system's average colours do not show a significant u-band excess (section

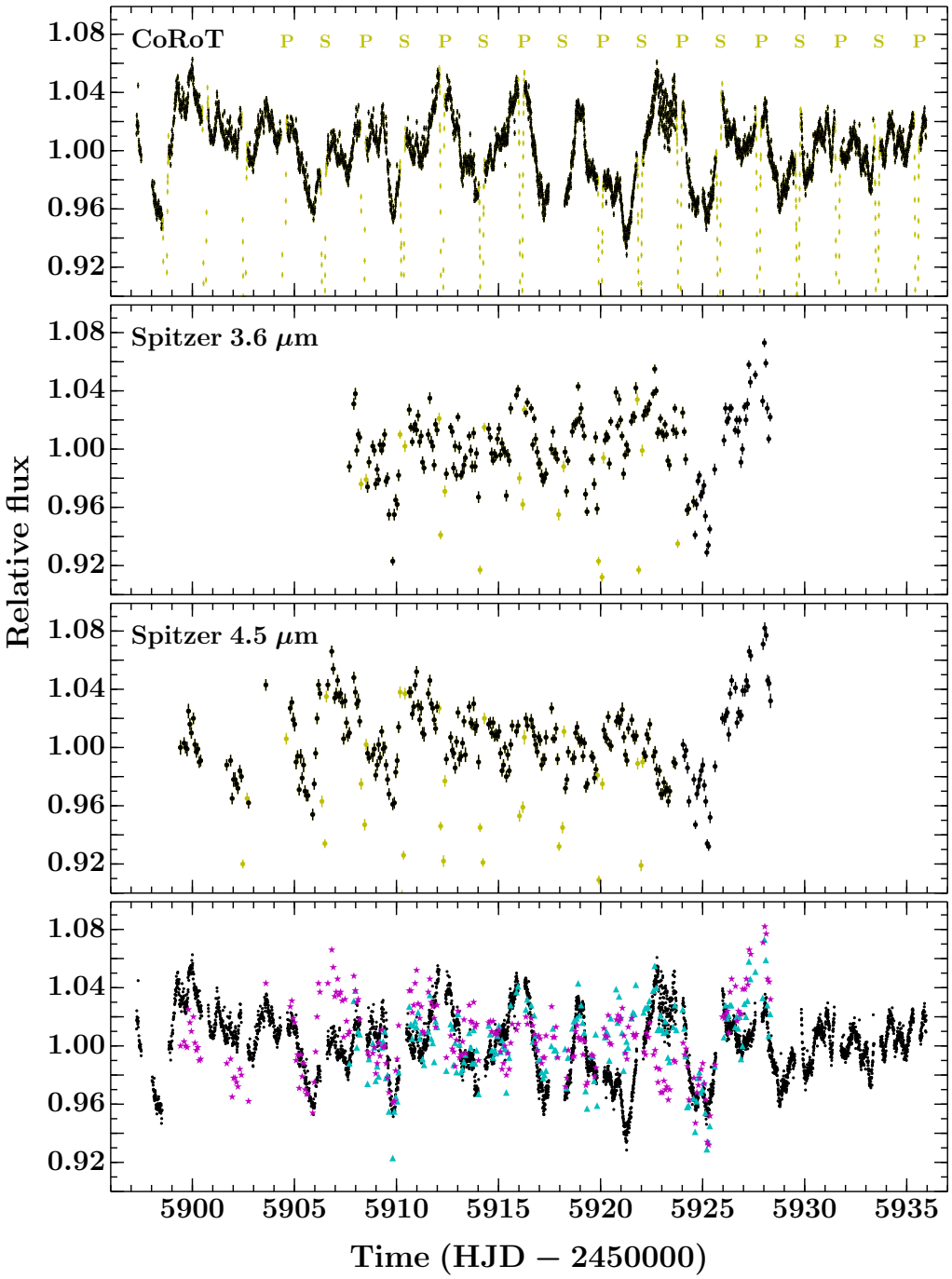

Figure 4.4: CoRoT and *Spitzer* light curves from the CSI 2264 campaign. *Top three plots*: optical CoRoT, IR *Spitzer* 3.6 μm and *Spitzer* 4.5 μm light curves. The out-of-eclipse data is shown in black and the stellar eclipses in yellow (P and S indicate primary and secondary eclipses, respectively). *Bottom*: CoRoT, 3.6 and 4.5 μm out-of-eclipse light curves (without errors) over-plotted (black points, cyan triangles and magenta stars, respectively). All plots share common axes.

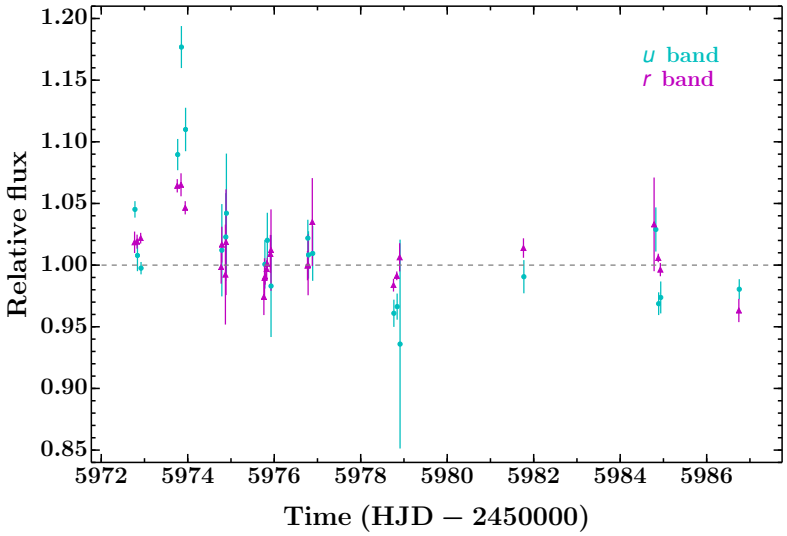

Figure 4.5: CFHT u and r-band out-of-eclipse light curves (cyan circles and magenta triangles, respectively). A short-lived u-band excess at rHJD $\sim$ 5974 can clearly be seen, which could be due to either an accretion hot spot or a stellar flare.

4.1), implying a low-to-negligible average accretion rate consistent with the majority of the CFHT light curve.

It is important to note that the raw CFHT light curves consist of short runs of 5 consecutive observations and these have been binned using a weighted average to give each data point seen in the figure. Hence, the three points indicating a u-band excess are derived from 15 independent observations conducted in photometric conditions.

4.3.2 Spot model

Young, low-mass stars tend to be heavily spotted (e.g. Donati et al., 2000) and can display photometric modulations not unlike the LAV-dominated parts of the CoRoT light curves. However, changes in such modulations from starspot evolution tend to occur smoothly on timescales of many days to weeks (e.g. Roettenbacher et al., 2013), rather than the sudden morphological changes we see at rHJD $\sim$ 4544 in the 2008 CoRoT light curve (when the LAVs appear) and at rHJDs $\sim$ 5910 and 5930 in the 2011/2012 CoRoT light curve (when the LAVs appear and disappear, respectively).

Given that there are two stars in this system, both of which are likely spotted, an appealing solution could be constructive and destructive interference of starspots where different active regions have slightly different periods. This could arise due to either

different stellar rotation periods (the system is young and not necessarily synchronised) or, even if the stars are synchronised, different latitudes (differential rotation)[6]. We therefore sought to understand how much of the large scale structure in the CoRoT and *Spitzer* OOE light curves could be attributed to the constructive and destructive interference of starspots.

We set up a simple two-spot model following the formalism of Dorren (1987). Due to the well known degeneracy of spot models we allow only two starspots and opt for a single spot on each star rather than two spots on one star[7]. Before modelling the data we need to *a)* determine the flux contributions of each star in each band, *b)* determine the flux ratios between the spotted and unspotted stellar photospheres and *c)* mask variations that are clearly not due to spot modulation:

a) the observed flux in each band is the sum of the stellar and dust components. Our SED modelling indicated that the dust contributes negligible flux in the CoRoT band but makes up a significant fraction at 3.6 and 4.5 μm. The stellar flux fractions are 0.62, 0.41 and 0.34 for the primary star in the CoRoT, *Spitzer* 3.6 and 4.5 μm bands respectively, and 0.38, 0.25 and 0.21 in turn for the secondary.

b) we determine flux ratios using MARCS model spectra (Gustafsson et al., 2008) with a surface gravity of $\log g = 4.0$ and assuming unspotted stellar temperatures of $T_{\rm pri} = 3700\,{\rm K}$ and $T_{\rm sec} = 3600\,{\rm K}$. Limb darkening (LD) coefficients were taken from Sing (2010) assuming the above parameters and [M/H] = -0.1 (the closest available to the cluster metallicity; King et al., 2000).

c) visual examination of the light curves revealed variations which clearly could not be explained by starspot modulation, based on the sharpness and amplitude of their features and/or their colour signatures; these data were masked when fitting the light curves. It was difficult to unambiguously identify such variations in the 2008 CoRoT light curve but was much easier in the 2011/2012 light curves due to the three colour bands. We note that the regions of the light curves satisfying these criteria in the 2011/2012 dataset occur just

[6]For the latter case, starspots on the same star would be indistinguishable from spots on two stars.

[7]Note that these spots should more realistically be seen as a group of many small spots covering a large fraction of the stellar surface around the specified location.

before secondary eclipse (i.e. separated by multiples of the EB orbital period), which could give clues as to their origin (we discuss this further in section 4.6).

We then modelled the 2008 CoRoT light curve and simultaneously modelled the 2011/2012 CoRoT and *Spitzer* 3.6 and 4.5 μm light curves using the Affine Invariant Markov chain Monte Carlo (MCMC) method as implemented in `emcee` (Foreman-Mackey et al., 2013), stepping through the parameter space 20 000 times with each of 300 'walkers' in both cases. The first 10 000 steps were discarded as 'burn in' and parameter distributions derived from the remainder. The parameters of the fit were the size, temperature, latitude, longitude and rotational period of each spot, as well as individual zero points and jitter terms for each light curve to account for different relative offsets and the fact that the variations are more complicated than a simple two spot model, respectively. The individual 'walkers' of the MCMC were initialised uniformly from a reasonable section of the parameter space utilising a latin hypercube approach to ensure unbiased start points (e.g. McKay et al., 1979); this is a useful approach is cases where the likelihood space is complex.

Figures 4.6 and 4.7 show the results of fitting the OOE light curves with the two-spot model (cyan) in each band. Vertically offset are the individual spot models (red dashed and blue dot-dashed for spots on the primary and secondary stars, respectively) and the residuals. The masked data points, which were not used in the fit, are shown in yellow. We construct the two-spot model plotted in the figures (cyan) by marginalising over the parameters of the fit, i.e. we take the mean of 200 spot light curves drawn from the converged MCMC walkers (selected individual spot light curves are shown in grey).

The majority of the large scale structure in both CoRoT light curves can be reproduced by the constructive and destructive interference of starspot regions (Fig. 4.6 and 4.7, top plot). There are however differences: in the 2008 CoRoT light curve these are most notable in the first half of the light curve as the fit is driven by the sinusoidal modulations in the second half; some of the differences could therefore result from spot evolution, as this is not incorporated in our model. In the 2011/2012 light curves the most obvious discrepancy is seen around rHJD $\sim$ 5920-5928, but given the amplitude of the flux drop around rHJD

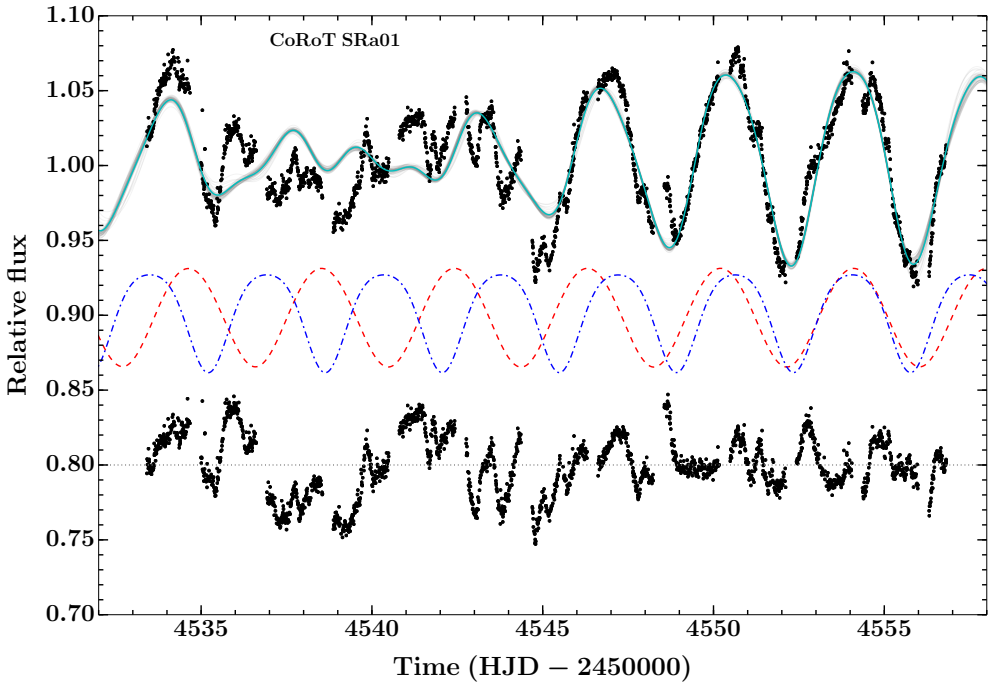

Figure 4.6: Out-of-eclipse 2008 CoRoT light curve (black) with the two-spot model (cyan) and individual light curve draws from the converged MCMC walkers (grey). Vertically offset are the individual spot models for the primary and secondary stars (red dashed and blue dot-dashed lines, respectively) and the residuals.

$\sim$ 5925 in all three bands, these variations may not be dominated by spot modulation. An alternative explanation could again be spot evolution; the CoRoT light curve spans $\sim$40 days so significant evolution is possible. A more flexible method to model the signatures of starspots would be to use Gaussian processes as these would naturally capture any starspot evolution (Rasmussen & Williams, 2006). It is important to note however that such an approach does not yield the physical parameters of the spots themselves, rather it gives an overall representation of their effect on the light curve[8].

The parameter values and uncertainties for our simple two-spot models for both the 2008 and 2011/2012 runs are given in Table 4.1. In both cases we find that the solution converges on periods of $\sim$3.8–3.9 days for one spot and $\sim$ 3.3–3.4 days for the other. Both models also favour one large and one small spot with one at high latitude and the other at mid-to-high latitude. We also see clear evidence of the well-known degeneracy between the spot size and temperature in the converged MCMC distributions and advise caution when

[8]We considered modelling each of the CoRoT and *Spitzer* light curves as the sum of two different Gaussian processes (GPs), which have different covariance properties to disentangle the spot and 'non-spot' contributions, but this did not yield immediately obvious results.

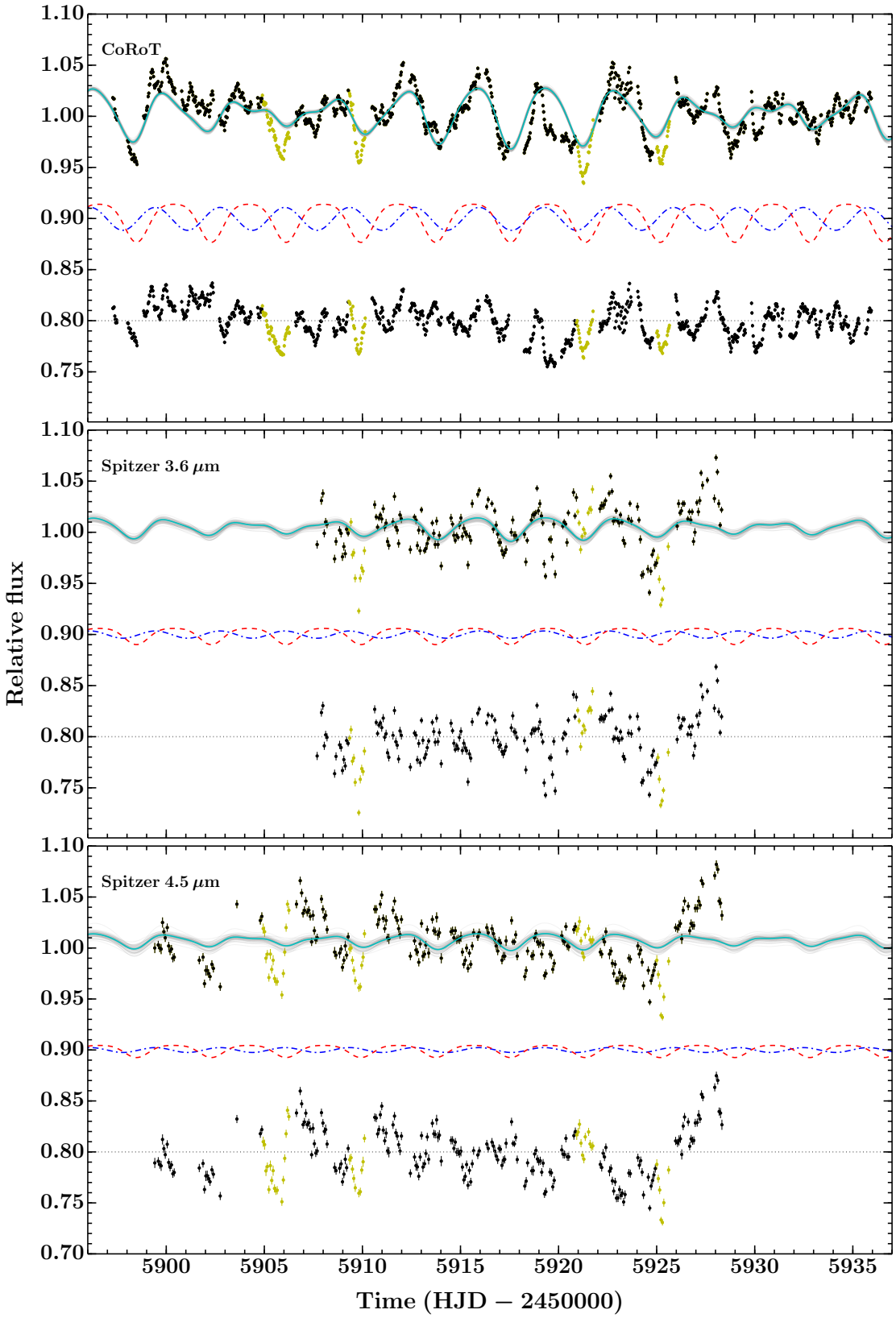

Figure 4.7: *Top*: out-of-eclipse 2011/2012 CoRoT light curve (black) with the two-spot model (cyan) and individual light curve draws from the converged MCMC walkers (grey). Data masked in in the fit are shown by yellow points. Vertically offset are the individual spot models for the primary and secondary stars (red dashed and blue dot-dashed, respectively) and the residuals. *Middle and bottom*: as above for *Spitzer* 3.6 and 4.5 μm, respectively. All plots share common axes.

interpreting the values for these parameters: while the quoted values capture something of the magnitude of the uncertainty they do not reflect the complexity of the correlation. We repeated our spot model analysis with different start points for each MCMC 'walker' to assess the sensitivity of our solution to our initial positions: the model converges on parameter values comfortably within the uncertainties quoted in Table 4.1 in all cases. In addition to our spot analysis, we also inspected the power spectra of the CoRoT SRa01 and SRa05 OOE light curves and resolve the two rotation periods in both cases, finding consistent values to our spot model.

Both the 2008 and 2011/2012 models find similar spot periods (3.9 and 3.4 days, and 3.8 and 3.3 days, respectively). If we are sensitive to spots on one star only, this suggests active latitudes that are quasi-stable over many years. However, as both stars are likely heavily spotted we are probably retrieving signatures from both (i.e. each spot in our model attempts to represent the global spot contribution to the light curves from that star). This would suggest slightly different rotation periods for the two stars: one close to or at the binary orbital period (possibly signifying synchronisation) and the other rotating slightly supersynchronous. Given the possibility of differential rotation and the simplified nature of our model we refrain from making a more quantitative statement here, but return to this point in section 4.5.

To assess the validity of our model we compute a simple statistic, namely the ratio of the root mean square of the residuals to that of the raw data: r.m.s(residuals)/r.m.s(raw data). We opted not to use a more sophisticated statistic given the simplified nature of our model. For the 2008 and 2011/2012 CoRoT light curves we find values of 0.54 and 0.70, respectively which, given the simplified nature of the model, validates the underlying prescription, i.e. the large scale structure in the optical CoRoT light curves can arise from the constructive and destructive interference of starspots at two slightly different periods. The *Spitzer* light curves, however, are significantly less well fit, having values of 0.94 and 0.98 for the 3.6 and 4.5 μm bands, respectively. The spot model is not validated in the *Spitzer* bands for three reasons: the two stars only contribute 66 and 55% of the flux in the 3.6 and 4.5 μm

Table 4.1: Parameters of the two-spot model for the 2008 CoRoT light curve (*top*) and the 2011/2012 CoRoT and *Spitzer* observations (*bottom*).

Parameter	Symbol	Unit	Value		
2008 CoRoT observations					
			Primary		*Secondary*
Radius	α	$^\circ$	$71\,^{+15}_{-20}$		$40.8\,^{+5.0}_{-2.5}$
Latitude	δ	$^\circ$	$83.98\,^{+0.70}_{-3.42}$		$65.2\,^{+2.3}_{-3.1}$
Longitude	ϕ_0	$^\circ$	$18.0\,^{+2.8}_{-4.5}$		$163.5\,^{+2.3}_{-2.7}$
Rotational period	$P_{\rm rot}$	days	$3.899\,^{+0.013}_{-0.023}$		$3.4256\,^{+0.0073}_{-0.0062}$
Temperature	$T_{\rm spot}$	K	$2222\,^{+511}_{-475}$		$2515\,^{+550}_{-660}$
Maximum flux*	$F_{\rm max}$		1.22 ± 0.11		
Jitter term	σ		0.01976 ± 0.00031		
2011 / 2012 CoRoT and Spitzer 3.6 & 4.5 μm observations					
			Primary		*Secondary*
Radius	α	$^\circ$	$25.3\,^{+2.8}_{-2.0}$		$81\,^{+13}_{-18}$
Latitude	δ	$^\circ$	70.0 ± 3.0		$84.5\,^{+1.7}_{-3.0}$
Longitude	ϕ_0	$^\circ$	195.0 ± 4.2		245.6 ± 7.3
Rotational period	$P_{\rm rot}$	days	$3.8127\,^{+0.0087}_{-0.0083}$		3.303 ± 0.011
Temperature	$T_{\rm spot}$	K	$2186\,^{+665}_{-469}$		$3131\,^{+227}_{-436}$
			CoRoT	*3.6 μm*	*4.5 μm*
Maximum flux*	$F_{\rm max}$		$1.1072\,^{+0.063}_{-0.040}$	$1.057\,^{+0.039}_{-0.020}$	$1.053\,^{+0.036}_{-0.017}$
Jitter term	σ		$0.01495\,^{+0.00038}_{-0.00034}$	0.0210 ± 0.0015	0.0240 ± 0.0017

* From an unspotted photosphere.

bands, respectively (the remaining flux comes from the dust in the cavity); starspots are expected to have a reduced effect in the IR; and extra sources of variability arising from processes near, but not at, the stellar surface are expected to significantly affect these bands (Morales-Calderón et al., 2011; Cody et al., 2014; Rebull et al., 2014). We note that the Sing (2010) LD coefficients are optimised for the CoRoT bandpass and so the validity of their use for the *Spitzer* bands is more dubious. However, given the above reasons we do not believe this effect to be significant.

4.3.2.1 Colour curves

Although the spot models appear to broadly reproduce the structure in the CoRoT light curves they are not able to reproduce the *Spitzer* bands, as expected and as discussed in section 4.3.2. To confirm the validity of our model we constructed colour vs. time

plots (colour curves) to investigate the colour signatures between the different bands in the 2011/2012 dataset. Fig. 4.8 shows the three colour curves (CoRoT – [3.6], CoRoT – [4.5] and [3.6] – [4.5]; top to bottom) with the spot model in cyan and residuals immediately below. The colours are calculated from relative magnitudes (rather than relative fluxes as used in the spot modelling) and hence we denote the *Spitzer* 3.6 and 4.5 μm bands as [3.6] and [4.5], following convention. For both CoRoT–*Spitzer* colour curves, each data point was calculated by binning the CoRoT data in a short time period around each *Spitzer* observation.

The most obvious colour signatures are seen in CoRoT – [4.5] (middle plot) as they are the most widely separated bandpasses. Between rHJD $\sim$ 5912–5920, when the LAVs dominate the CoRoT light curve, the spot model adequately reproduces the colour signatures (given the simplified nature of the model); this is also true for the corresponding CoRoT – [3.6] variations. There are two times when the spot model does not reproduce the CoRoT–[4.5] colour variations: a) at rHJD $\sim$ 5905–5907 the colour is significantly redder than the spot model predicts but this is due to an increase in the 4.5 μm flux, which is not matched in the CoRoT band, i.e. it does not appear to be due to spots, and b) at rHJDs between $\sim$ 5920–5928 when the system becomes first redder and then significantly bluer. The initial reddening is also seen in the CoRoT–[3.6] colour but not the subsequent change towards the blue; the latter appears to be due to a dip in the 4.5 μm light curve that is only partially reproduced in the CoRoT and 3.6 μm bands; again clearly not due to spots.

From the residuals of the spot model in both flux and colour spaces it is clear that there is extra variability present that is not well described by starspots, even accounting for their evolution. The question now becomes *what is the physical origin of this additional variability?*

4.3.3 Colour–magnitude space

Colour-magnitude diagrams remove the temporal element and show how the variations in the three light curves behave as complete sets. Fig. 4.9 shows colour-magnitude plots for the different 2011/2012 CoRoT and *Spitzer* combinations both before and after our spot

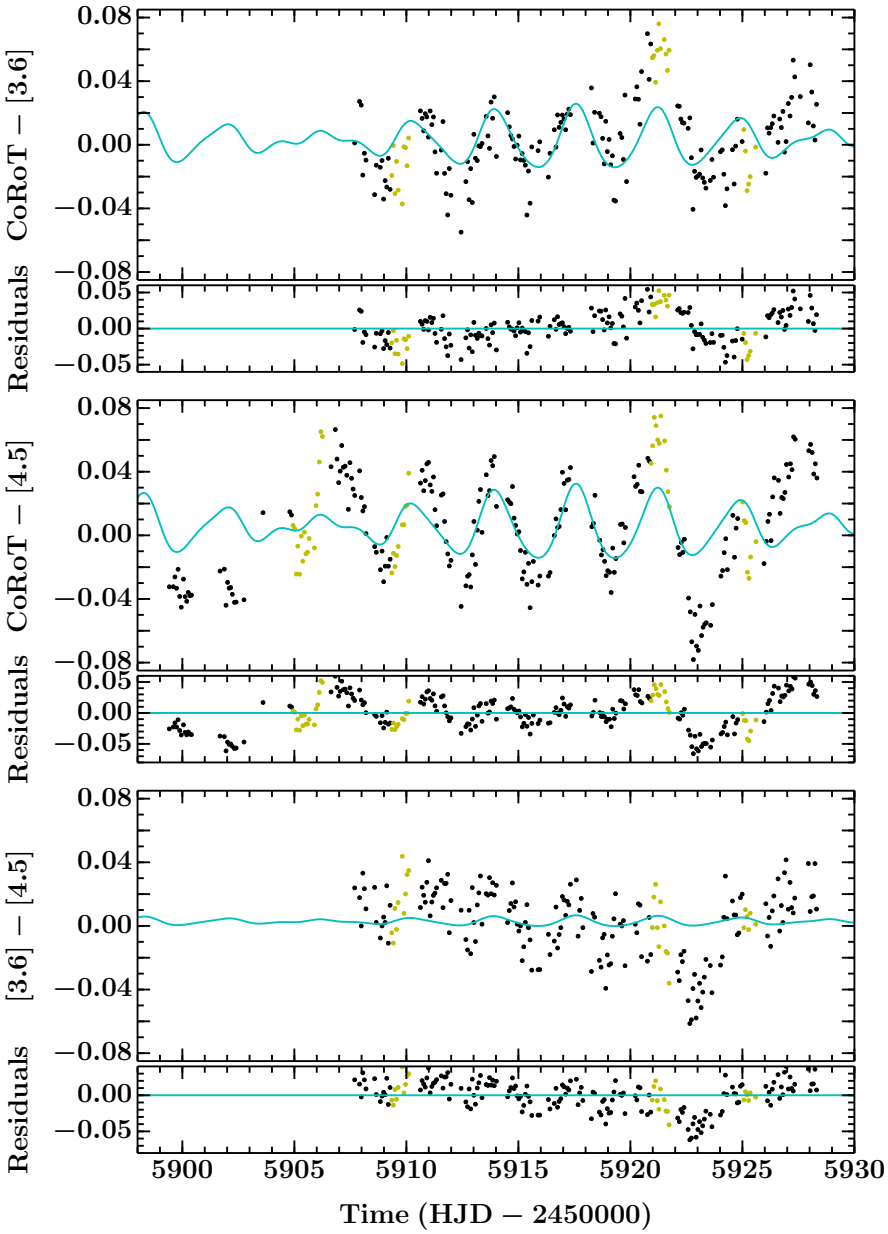

Figure 4.8: CoRoT and *Spitzer* colour vs. time relations. *Top-to-Bottom*: CoRoT–[3.6], CoRoT–[4.5] and [3.6]–[4.5]. All display quasi-sinusoidal variations, which can most clearly be seen comparing the widely separated bandpasses of the CoRoT-[4.5] colour space. All plots share common axes.

modelling (top and bottom rows, respectively)[9]. Black points indicate photometry used in the spot modelling and yellow triangles represent the masked regions. The coloured arrows indicate the directions along which the data should lie for different sources of variability. In the top plots, blue, red and green arrows represent starspots (cold spots), hot spots and dust emission, respectively.

[9]We also constructed magnitude-magnitude plots and colour-colour plots but found the colour-magnitude space to be more informative.

To calculate the cold and hot spot arrows we approximate the two stars with a single star. We use the same description for this single star as in the SED modelling, namely that it has luminosity $L_\star = L_1 + L_2$, temperature $T_\star$ such that $\sigma T_\star^4 = L_1/(4\pi R_1^2) + L_2/(4\pi R_2^2)$ and radius $R_\star$ such that $\sigma T_\star^4 = L_\star/(4\pi R_\star^2)$. As with the spot modelling, we then estimate the amount of flux in each band as the sum of the stellar and dust components and simulate the effect of cold and hot spots by substituting a fraction of the stellar flux with emission of the relevant photospheric temperature. The size and temperature of these spots were determined by fitting the amplitudes of the LAVs in the 2011/2012 CoRoT light curve (where the stars contribute all the flux). For the cold spot, we select a temperature of $T_{\rm cs} = 3000\,{\rm K}$ covering 13% of the stellar photosphere and for the hot spot, we select a temperature of $T_{\rm hs} = 5000\,{\rm K}$ covering 2% of the stellar photosphere. The exact values are unimportant as long as they are reasonable[10].

The green arrows were calculated by varying a fraction of the dust required to explain the SED. Variations in this dust emission could result from: variable amounts of dust in the cavity; variable obscuration of dust by one or both stars, or by the inner edge of the circumbinary disk; or even variable accretion, and hence variable amounts of dust at the temperatures required to strongly emit in the 3.6 and 4.5 μm bands. We require a variable dust fraction of $\lesssim 0.25$ to fit the amplitude of the variations in the *Spitzer* 4.5 μm band. This may seem high but it is important to note that this is an upper limit as it is relative to the minimum mass of dust required to fit the SED. If there is more dust in the cavity, the required variable dust fraction would decrease substantially.

The CoRoT vs. CoRoT-[3.6] and CoRoT vs. CoRoT-[4.5] raw colour-magnitude plots (top left and top middle, respectively) show that the amplitude and general direction of the variations (black points) can be explained through either cold or hot spot modulation, but that there is significant scatter above the formal uncertainties (indicated in the bottom left of each panel) that is consistent with variable dust emission. Conversely, in the [3.6] vs [3.6]-[4.5] plane, neither cold/hot spots nor dust emission can be the dominant source

[10]Changing the spot parameters by over 1000K, for example, has little effect on the direction of the arrows.

of the OOE variations. It is important to note however that these bands are very close in wavelength and hence caution should be exercised when inferring trends, unless they are caused by processes that are sensitive to this small difference, e.g. emitting at a temperature whose black-body peak occurs at a wavelength comparable to 3.6 or 4.5 μm.

Comparing the top row of plots (raw light curves) to the bottom row (residuals of the spot modelling) for CoRoT vs. CoRoT-[3.6] and CoRoT vs. CoRoT-[4.5], we see that the spread in the black points (those which could be due to spots) in the y-direction has decreased, indicating that the contribution from starspots has been substantially reduced. Note that it will not have been fully removed due to the simplified nature of our model. The colour spread is only slightly reduced, shown by a decrease in r.m.s. scatter of only 16% for both CoRoT vs. CoRoT-[3.6] and CoRoT vs. CoRoT-[4.5]) suggesting that it is not primarily caused by spots, but it is consistent with variable dust emission. However, there are significant departures from the dust emission trend below the median flux, primarily from the masked data (yellow triangles), which correspond to short, sharp flux dips. These variations are not consistent with either starspots (due to the sharpness of their features and their colours) or dust emission, but are more likely to be caused by dust obscuration.

We indicate the direction of small and large dust grain obscuration in the residual plots with the magenta and cyan arrows, respectively. For small dust grains, we assume an interstellar extinction law, following Schlegel et al. (1998) and Indebetouw et al. (2005), approximating the CoRoT bandpass with the r-band. Obscuration by large dust grains ($> 4.5\,\mu$m) show grey colour variations and are therefore vertical in all colour-magnitude planes. The amplitudes of the magenta and cyan arrows correspond to obscuring $\sim$10% of the system flux. The true dust grain size distribution in this system will undoubtedly be complex; here we simply aim to 'bracket' plausible directions for dust obscuration effects with the arrows for small and large dust grains. The spread in the residual data below the median is consistent with obscuration by any scale mixture of dust grain sizes.

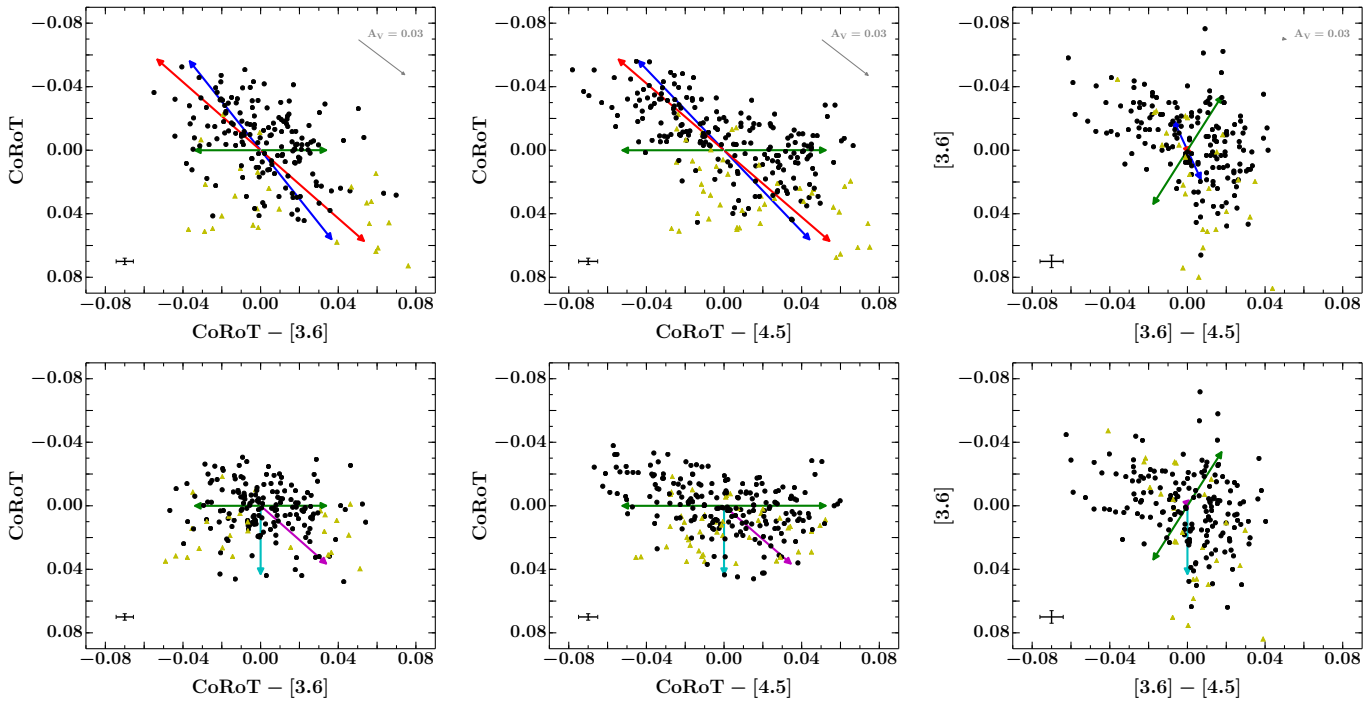

Figure 4.9: Colour-magnitude diagrams. *Top row, left to right*: raw light curve data (black points) in the CoRoT vs CoRoT–[3.6], CoRoT vs CoRoT–[4.5] and [3.6] vs [3.6]–[4.5] spaces. Data masked in the spot modelling are shown by the yellow triangles. Coloured arrows show the effects of different types of variability: cold spots (blue), hot spots (red) and dust emission (green). Grey arrows indicate the direction of interstellar dust extinction. *Bottom row, left to right*: same as for the top row but showing the residuals of the spot modelling. Magenta and cyan arrows indicate the effects of obscuration by small and large dust grains, respectively. The error bar in the bottom left corner of each subplot shows a representative uncertainty for each data point. All plots share common axes.

4.3.4 Stability of spots

To investigate the stability of the out-of-eclipse variability over an extended time period, we compared our spot model derived from the 2011/2012 CoRoT and *Spitzer* observations to data obtained with the USNO 40-inch telescope and CFHT observations (Fig. 4.10). The USNO dataset (red squares) spans 106 days (rHJD $\sim$ 5888–5994) and encompasses the dates of the 2011/2012 CoRoT observations (black points). The USNO flux measurements were obtained through relative photometry using seven non-variable, nearby stars. To vertically align the USNO and CoRoT datasets we calculated the mean offset between individual observations taken during the CoRoT run and subtracted off the mean. The USNO data is a reasonable match to the CoRoT data during the common time period, although there are some discrepancies, e.g. rHJD $\sim$ 5920, where the USNO data appears to more closely follow the *Spitzer* trend (note: the *Spitzer* light curves are not shown for

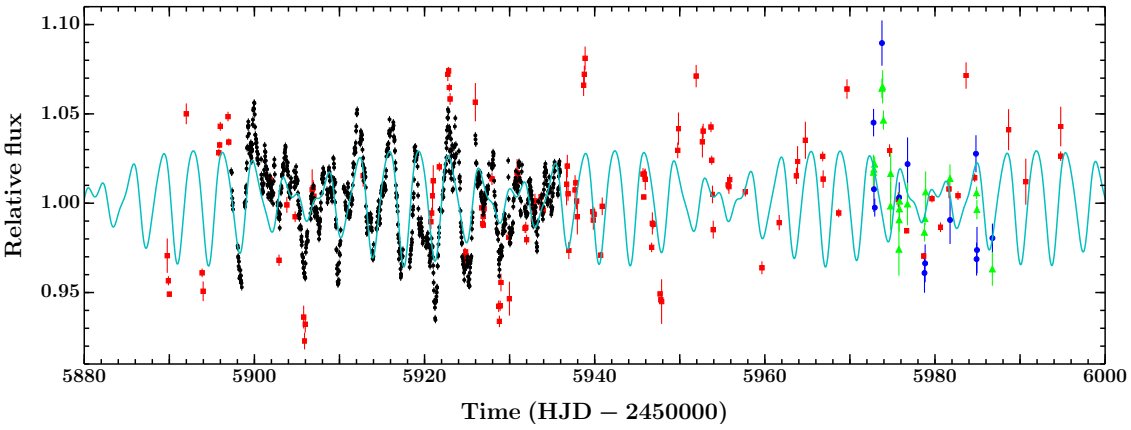

Figure 4.10: Out-of-eclipse light curves from CoRoT (2011/2012 run), USNO and CFHT (u and r-band) spanning 120 days (black points, red squares, blue circles and green triangles, respectively). For clarity, the *Spitzer* light curves are not shown. Our two-spot model, derived from fitting the simultaneous 2011/2012 CoRoT and *Sptizer* light curves, is shown in cyan and extended across the entire period of observations. For clarity, we only show USNO and CFHT data with uncertainties less than 0.015.

clarity). Beyond the CoRoT dataset the spot model does not appear to closely match the USNO or CFHT (cyan and magenta) observations. This could be due to spot evolution, which is almost certainly present to some degree given the time period covered. We note, however, that the apparent agreement of our model and the USNO and CFHT data is very sensitive to the spot periods: adjusting these slightly, yet remaining within their uncertainties, allows us to obtain a better agreement than shown here but significant discrepancies still exist, which we attribute to spot evolution and additional variability, as previously discussed.

4.4 Spectroscopic variability: emission line profiles

4.4.1 Hα

In a young stellar system the Hα profile can originate from either the star itself, i.e. from magnetically active regions in the chromosphere, or from accretion-related processes. The latter can occur through either simple or complex accretion structures.

The VLT/FLAMES Hα profiles are shown in Fig. 4.11 (ordered in binary orbital phase; indicated in the top right of each subplot). The Hα feature consists of a 3-component emission profile: a central, narrow, static, nebular component, and two components with varying width, velocity and intensity. The velocities of these two components relative to

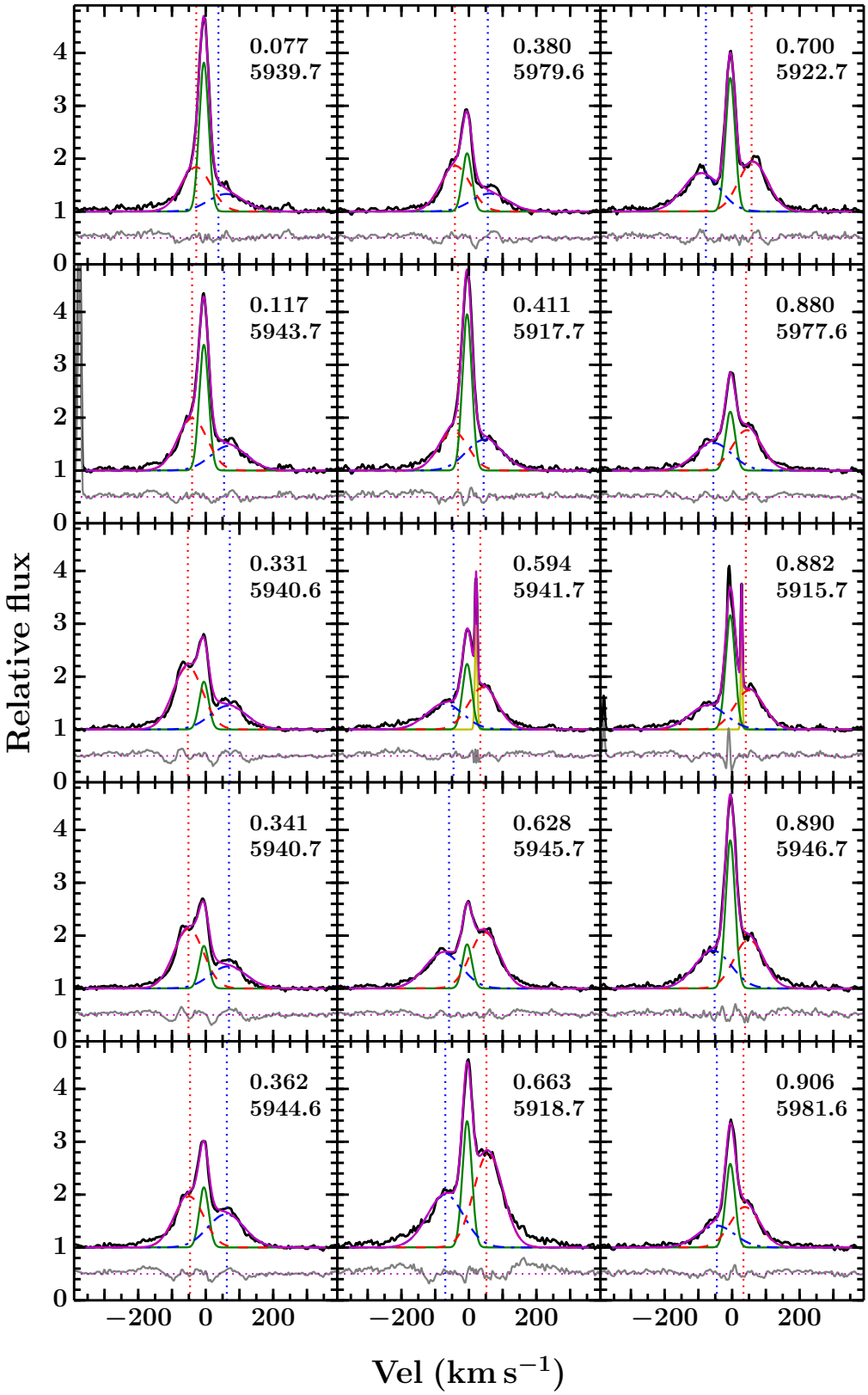

Figure 4.11: 15 VLT/FLAMES Hα profiles ordered in phase throughout the binary orbit (phase and rHJD indicated in each subplot). The spectra (black) are modelled as the sum of three Gaussians (magenta). In each case, the central, narrow, static Gaussian (green) is nebula emission and the varying red dashed and blue dot-dashed Gaussians correspond to emission associated with the primary and secondary stars, respectively. The vertical dotted red and blue lines indicate the radial velocities of the primary and secondary stars respectively, at the time of observation. All profiles have had a rotationally-broadened absorption profile subtracted. Vertically offset below are the residuals of the model in grey. In two profiles, phases 0.594 and 0.882, additional Gaussians (yellow) are present to account for spikes, which we attribute to cosmic rays.

the centre of mass of the system appear to vary in phase with the mean radial velocities of the two stars (indicated by the red and blue dashed lines for the primary and secondary, respectively), but often slightly exceed the latter.

The simplest explanation for the stellar emission components is chromospheric emission. In previous studies of single T Tauri stars where strong accretion signatures are absent, Hα emission profiles have been decomposed into narrow and broad Gaussian structures (e.g. Hatzes, 1995; Skelly et al., 2009). The narrow component is commonly attributed to the chromosphere but the broad component is the subject of more speculation: Petrov et al. (1994) suggest the broader wings could arise from the circumstellar gas environment whereas Hatzes (1995) tentatively propose large-scale mass motions or winds in the chromosphere, and both Jones et al. (1996) and Fernández et al. (2004) favour 'microflaring', i.e. small flares that cannot be individually resolved (although we note that they rule out the circumstellar gas environment hypothesis due to the absence of IR excesses in their systems).

In CoRoT 223992193, it is not obvious that the stellar emission components can be decomposed into narrow and broad structures in the majority of profiles. We therefore seek to explain the Hα feature as the sum of three Gaussians: one for the central nebula emission (green) and one each for the two stellar components (red dashed and blue dot-dashed for the primary and secondary stars, respectively). We first subtract off a rotationally broadened absorption spectrum for the two stars (e.g. Gray, 1992; Bouvier, 2013). We use solar-metallicity PHOENIX model spectra (Husser et al., 2013), selecting temperatures of 3700 and 3600 K for the primary and secondary stars, respectively, and a $\log g$ of 4.0 for both (see sections 3.4.2 and 3.3.4 for the determination of these values). The rotation periods inferred from our spot modelling imply $v \sin i$ values in the range $\sim$14–20 $\mathrm{km\,s^{-1}}$ for the two stars. In addition, the peaks in the cross-correlation functions used to derive the stellar orbits in section 3.3.2 were not obviously rotationally broadened with respect to the spectrograph's intrinsic resolution ($\sim$17 $\mathrm{km\,s^{-1}}$). We therefore set $v \sin i$ for both the primary and secondary stars to the spectrograph's resolution, i.e. 17 $\mathrm{km\,s^{-1}}$. We note that at the temperatures and surface gravities expected for CoRoT 223992193, the Hα

Table 4.2: Parameters of the three-Gaussian model used to simultaneously fit the Hα profiles. Each profile was modelled as the sum of three gaussians, which represent emission associated with the nebula, the primary star and the secondary star, respectively. The widths of each Gaussian, along with the radial velocity of the nebula component, were jointly fit for using all profiles, and are shown at the bottom of the table.

Phase	HJD	Nebula	Primary			Secondary		
		Amplitude	*Amplitude*	*RV* ($\mathrm{km\,s^{-1}}$)	Δ *RV* * ($\mathrm{km\,s^{-1}}$)	*Amplitude*	*RV* ($\mathrm{km\,s^{-1}}$)	Δ *RV* * ($\mathrm{km\,s^{-1}}$)
0.077	2455939.65778	2.821 ± 0.017	0.839 ± 0.017	-28.68 ± 0.97	-0.8	0.332 ± 0.010	60.9 ± 2.3	23.3
0.117	2455943.68750	2.382 ± 0.018	0.989 ± 0.010	-39.36 ± 0.63	1.0	0.467 ± 0.007	68.8 ± 1.2	14.4
0.331	2455940.64342	0.905 ± 0.011	1.195 ± 0.006	-53.04 ± 0.32	-0.1	0.450 ± 0.004	66.94 ± 0.84	-4.4
0.341	2455940.67976	0.805 ± 0.010	1.132 ± 0.005	-50.51 ± 0.33	0.6	0.418 ± 0.004	66.49 ± 0.85	-2.4
0.362	2455944.63515	1.139 ± 0.011	0.966 ± 0.007	-49.29 ± 0.45	-2.9	0.629 ± 0.005	60.05 ± 0.78	-2.6
0.380	2455979.57946	1.103 ± 0.011	0.863 ± 0.007	-39.53 ± 0.47	2.0	0.339 ± 0.005	61.0 ± 1.2	5.0
0.411	2455917.70423	2.960 ± 0.016	0.743 ± 0.014	-46.4 ± 1.0	-14.1	0.583 ± 0.010	45.9 ± 1.5	2.3
0.594	2455941.66163	1.242 ± 0.016	0.797 ± 0.010	41.52 ± 0.85	7.7	0.487 ± 0.006	-72.0 ± 1.2	-26.3
0.628	2455945.66720	0.836 ± 0.010	1.061 ± 0.005	47.41 ± 0.36	3.7	0.673 ± 0.004	-76.17 ± 0.59	-17.2
0.663	2455918.68222	2.393 ± 0.013	1.777 ± 0.007	57.56 ± 0.28	5.7	1.003 ± 0.005	-69.73 ± 0.63	0.3
0.700	2455922.69870	2.531 ± 0.011	0.938 ± 0.005	62.18 ± 0.40	4.5	0.726 ± 0.005	-91.66 ± 0.57	-13.9
0.880	2455977.63971	1.114 ± 0.012	0.763 ± 0.008	44.00 ± 0.57	2.7	0.523 ± 0.006	-55.6 ± 1.1	0.1
0.882	2455915.65584	2.164 ± 0.014	0.741 ± 0.007	50.66 ± 0.67	10.0	0.454 ± 0.006	-72.2 ± 1.1	-17.4
0.890	2455946.68154	2.808 ± 0.015	0.927 ± 0.010	49.24 ± 0.64	10.8	0.716 ± 0.007	-56.7 ± 1.1	-4.9
0.906	2455981.61509	1.584 ± 0.015	0.766 ± 0.014	37.72 ± 0.88	4.1	0.416 ± 0.011	-47.0 ± 2.0	-1.7
		Parameters jointly fit from all profiles						
		Nebula	Primary			Secondary		
	Width	13.978 ± 0.036	43.50 ± 0.16			53.83 ± 0.47		
	RV ($km\,s^{-1}$)	-5.371 ± 0.026						

* $\Delta\,\mathrm{RV} = \mathrm{RV}_{\mathrm{H}\alpha} - \mathrm{RV}_{\mathrm{orbit}}$ (see section 3.3.2 for details on the orbit determination).

absorption profile is very weak and so subtracting off rotationally broadened absorption lines has very little effect on the shape of the observed profile.

We modelled all Hα profiles simultaneously using `emcee`, stepping through the parameter space 20 000 times with each of 300 'walkers' (the first 10 000 steps were discarded as 'burn in' and parameter distributions derived from the remainder). Modelling all profiles simultaneously allows certain parameters to be jointly fit for: we fix the velocity and width of the nebula component across all profiles as we expect these to be constant but allow the amplitude to vary because it is dependent on the continuum stellar flux level, which changes depending on how accurate the pointing was, i.e. how much of the total system flux reached the detector through the fibre-fed spectrograph. In addition, we fix the widths of the two stellar Gaussians as it is not clear that they vary substantially between profiles

(we later relax this assumption). All other parameters were allowed to vary freely. In two profiles (phases 0.594 and 0.882) additional spikes are visible, which we attribute to cosmic rays; these were incorporated into the fit using extra Gaussians (yellow) but are not discussed further. The parameters of the fit are reported in Table 4.2.

Within our framework, we find that the model typically converges with half the stellar components best fit by Gaussians centred at velocities close to the stellar RVs and the other half at velocities $\sim$10 and 20 $\mathrm{km\,s^{-1}}$ above (i.e. outside the stellar orbits) for the primary and secondary stars, respectively (see columns 6 and 9 of Table 4.2). Given our upper limits on the $v \sin i$ of the two stars ($\sim$19 $\mathrm{km\,s^{-1}}$; see section 4.5), this is consistent with the emitting region being located on the surface of each star. Some profiles are very well explained by a simple three Gaussian model, e.g. phases 0.628 and 0.880, and the rest are reasonably well explained but some display evidence of extra emission at higher velocities than the stellar RVs, most notably at phases of 0.362 and 0.663, and occasionally non-Gaussian stellar peaks (e.g. phase = 0.700). We note that the amplitudes of the central stellar emission generally correlate with the strength of the higher velocity emission, e.g. phase = 0.331 and 0.663. Perhaps the simplest interpretation of the higher velocity emission is prominences, i.e. partially-ionised, magnetically-supported plasma structures existing above the chromospheres (e.g. Donati et al., 1999).

Given the presence of higher velocity emission, we modelled the profiles again allowing the widths of the stellar Gaussians to vary but constraining their central velocities to the stellar RVs (using Gaussian priors with standard deviations of 1 $\mathrm{km\,s^{-1}}$). This avoided some of the secondary emission being fit by the primary Gaussian and vice versa). We then determined estimates of the full widths at 10% intensity for both stellar components and find that they vary between $\sim$150 – 400 $\mathrm{km\,s^{-1}}$. Seven of the 15 profiles are best fit with secondary widths >270 $\mathrm{km\,s^{-1}}$, which is generally interpreted as indicating accretion (White & Basri, 2003). The higher velocity emission could therefore be evidence for non-steady, low-level accretion, which might be expected given the presence of dust in the central cavity and the short-lived u-band excess in the CFHT light curves. It is important

to note however that chromospheric emission would still be present in such a scenario and so each stellar component should be modelled with a narrow and broad Gaussian, rather than a single Gaussian only. The quoted full widths at 10% intensity therefore are not representative of any individual component but rather the general contribution from each star to the composite profile. We opted not to model the Hα profiles with a 5-Gaussian model as any results would still be ambiguous.

In some single T Tauri systems, such as AA Tau (Bouvier et al., 2007), the Hα profiles can be decomposed into simple Gaussian components representing different parts of the accretion flow (hot spots, accretion columns and winds). In others, such as V2129 Oph (Alencar et al., 2012), this is not possible but the profiles can be explained by emission from accreting material in the stellar magnetospheres, whose variability is driven by the rotational modulation of non-axisymmetric multipolar components of the stellar magnetic fields. In this latter scenario, the observed stellar emission profiles could be explained using radiative transfer models based on the accretion flow structure generated through three-dimensional magnetohydrodynamical (3D MHD) simulations. Such models could explain both the higher velocity emission and the variable peak shapes. However, to draw meaningful conclusions from this type of analysis one needs *a priori* knowledge of the stellar magnetic field configurations and strengths, which we do not have. We therefore see this as a potential option for future work. Given the complexity of the problem one would also certainly need multiple observational constraints, i.e. multiple emission lines observed simultaneously (particularly from different series of the same element, sharing a common upper level) to break the degeneracy between chromospheric and different accretion signatures.

We conclude that the majority of the Hα profiles are consistent with chromospheric emission. Higher velocity emission is sometimes evident, which could be due to prominences above the stellar chromospheres or, given the velocities involved, could alternatively indicate low-level, non-steady accretion. Accreting binaries typically show Hα profiles that are indistinguishable from those of single stars (see e.g. DQ Tau, Basri et al. 1997; AK Sco,

Alencar et al. 2003). By contrast, the well-separated components seen in CoRoT 223992193 could enable us to probe accretion/outflow on each star separately. However, we need higher spectral resolution data to investigate the details of the Hα profiles and make robust statements.

4.4.2 Search for other emission lines with NOT/FIES

In order to obtain more information on the origins of the emission material we obtained follow-up optical spectra taken with the Fibre-fed Echelle Spectrograph (FIES) on the 2.5m Nordic Optical Telescope (NOT), situated on La Palma. One medium resolution optical spectrum per night was obtained for three consecutive nights (4–6 January 2013; PI Gandolfi). These spectra cover the wavelength range ∼3630 – 7170 Å with a resolution R ∼ 25 000. The observations and reduction were performed by D. Gandolfi.

Due to the relative faintness of CoRoT 223992193 (R=15.8), 1-hour integration-time on the 2.5m NOT telescope– under clear and good sky conditions– only yielded a SNR of 5-15 from Hβ to Hα. This is insufficient to properly investigate the full range of emission lines in this object; we use these spectra to search for and classify additional optical emission lines. These lines were Hα, Hβ (4681 Å), HeI (5876 Å), and the forbidden emission lines OIII (4959 Å and 5007 Å), OI (6300 Å and 6364 Å), NII (6548 Å and 6584 Å) and SII (6717 Å and 6731 Å). The emission line profiles are shown in Fig. 4.12[11]. We note that the structure of the Hα profile matches the FLAMES spectra. We find tentative evidence for Hβ emission associated with the primary star, most clearly seen on the middle night (5$^{\text{th}}$ January). Higher S/N spectra are needed to make meaningful statements about the system's Hβ profile. We did not find evidence for emission associated with either star in any of the forbidden emission lines; we see only nebula emission.

[11]The OI (6300 Å and 6364 Å) emission feature is dominated by Earth airglow and is therefore not shown.

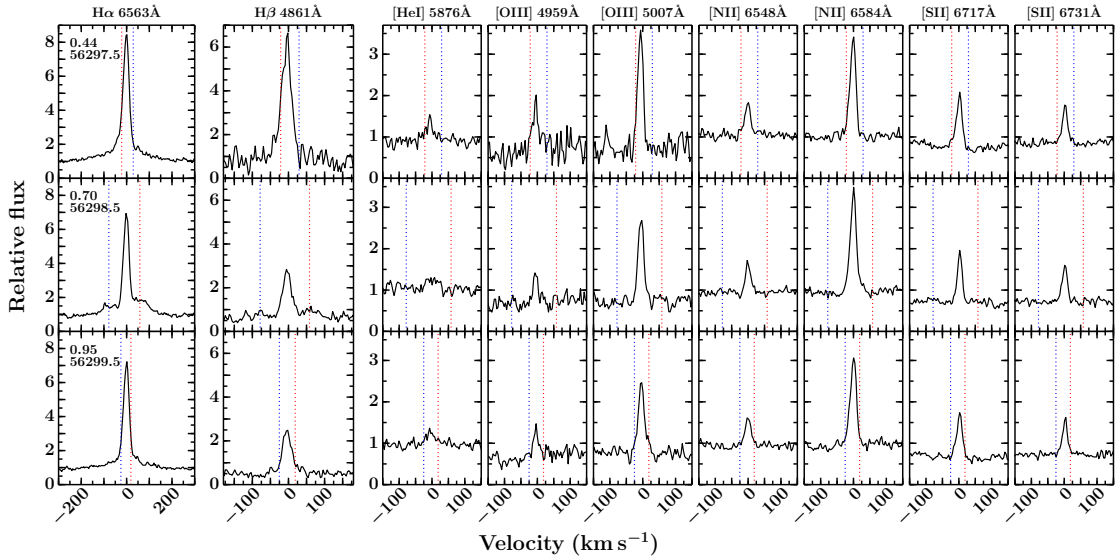

Figure 4.12: Emission line profiles observed with NOT/FIES. *Left to right*: the permitted emission lines Hα, Hβ and HeI, and the forbidden emission doublets OIII, NII and SII. *Top to bottom*: the three consecutive nights of observations.The phase and time of each observation are given in the Hα panels.

4.5 Photometric and spectroscopic consistency

4.5.1 $v \sin i$ estimation

Assuming our spot periods represent the rotation periods of the two stars implies rotational velocities of order ∼14–20 km s^{-1} for the two stars. The FLAMES resolution is ∼17 km s^{-1}, which is unlikely to be able to robustly resolve the rotational velocities of the two stars. However, FIES has a resolving power of ∼12 km s^{-1}, which is sufficient. $v \sin i$ for both stars was determined by D. Gandolfi from the three FIES spectra by cross-correlating a slowly rotating M2 spectral standard star (observed with FIES in the same setup) with each of the observed spectra for different rotational broadenings. Analysis of the height and contrast of the CCF stellar peaks implies the same $v \sin i$ for both stars of between 17–19 km s^{-1}. Taking account of the different stellar radii, this corresponds to rotation periods of 3.5–3.9 days for the primary star and 3.0–3.3 days for the secondary star, which given the $v \sin i$ uncertainties and limitations of the spot modelling, is consistent with the spot-derived periods. The primary star rotation is consistent with synchronisation and the secondary rotation is slightly supersynchronous.

4.5.2 Seeking evidence of spot modulation in VLT/FLAMES spectra

Four of the VLT/FLAMES spectra were taken simultaneous with the CoRoT/*Spitzer* observations. We sought additional evidence for the spot origin of the large scale optical photometric variability through a bisector span analysis of the Li 6708 Å absorption lines in the four simultaneous spectra. Assuming our spot periods do represent the rotation periods of the two stars, and given the combination of the FLAMES resolution being ∼17 $\mathrm{km\,s^{-1}}$ and the spectra having S/N ∼22–26, we did not expect to see unambiguous signs of the spots in the bisector spans, and indeed we do not. This does not mean that spots are not responsible for the large scale variations but simply that the FLAMES data do not possess the resolution and S/N required to unambiguously prove their presence.

4.5.3 Correlation between the photometric and spectroscopic variability

There does not appear to be a correlation between the photometric and spectroscopic variability. Four Hα profiles taken at rHJD (phase) = 5915.7 (0.882), 5917.7 (0.411), 5918.7 (0.663) and 5922.7 (0.700) were simultaneous with the 2011/2012 CoRoT and *Spitzer* photometry. The strength of the stellar component of the Hα emission does not appear to correspond to either optical or IR continuum flux levels, or variations. This lack of correlation does not appear to be an artefact, e.g. the profile at phase = 0.882 shows the smallest stellar emission amplitudes but was taken at the highest S/N (26 as opposed to 22 for the rest).

4.6 Investigating the origin of the short-duration flux dips

The model presented in this section was constructed by C. Terquem, who also provided Figure 4.13. The discussion of the model and plot are my own.

In section 4.3 we sought to understand how much of the out-of-eclipse (OOE) variability could be attributed to starspots and found that the large scale structure in the system's 2008 and 2011/2012 optical light curves are consistent with the constructive and destructive interference of active regions at two slightly different periods. However, the residuals of our

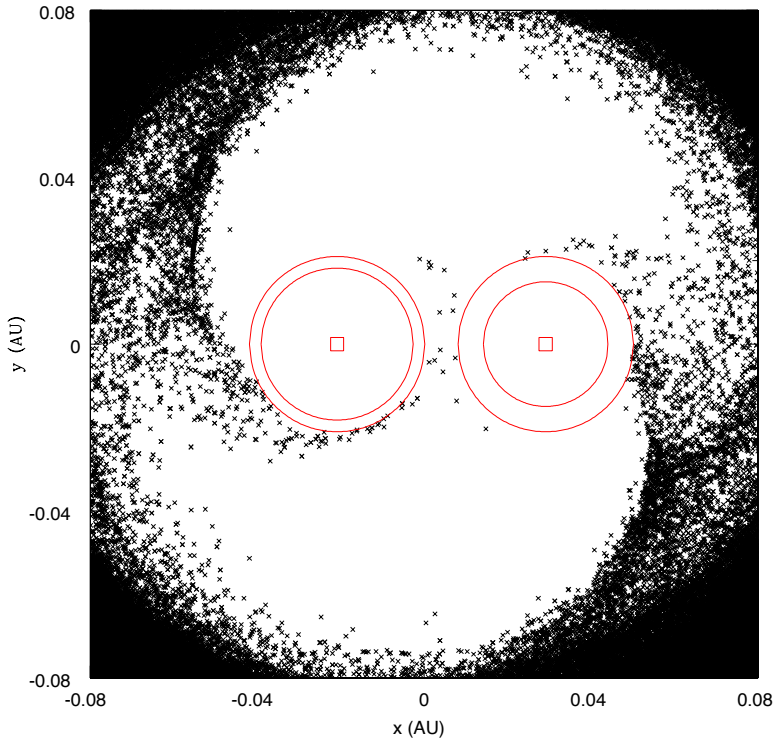

Figure 4.13: Snapshot of the accretion flow structure in the corotating frame of the binary, as output from our particle model. The red squares indicate the locations of the primary and secondary stars (left and right, respectively) and the black crosses show the locations of particles in the circumbinary disk and the accretion streams onto the two stars. The red circles delimit the inner and outer edges of where dust could reside in circumstellar disks: the inner edge represents the sublimation radius for each star and the outer edge the radius at which the disks are truncated by the other star. The binary clears out a slightly eccentric cavity of radius ∼0.08–0.1 AU (∼17–22 $R_{\odot}$).

spot models show short-timescale variations that are not consistent with spot modulation but which could arise from variable dust emission and obscuration. With respect to the latter, the 2011/2012 CoRoT, 3.6 and 4.5 μm light curves all display simultaneous, short-duration flux dips preceding secondary eclipse (yellow points, Fig. 4.7). These dips are not a permanent feature but are seen in four of the six orbital periods over which we have simultaneous photometry. There are also hints of much broader and shallower dips preceding primary eclipses, but these are harder to identify as they do not show such a disparate morphology to the large scale variations, although the dip at rHJD∼5923 clearly shows a non-spot colour signature. In this section, we seek to identify the physical origin of the short-duration flux dips.

In an accreting binary, accretion streams are thought to flow from the circumbinary disk, through the corotating Lagrangian points, and onto the stars (e.g. de Val-Borro

et al., 2011). A possible explanation for the flux dips could be that, as we are viewing the system close to edge on ($i \sim 85°$), these accretion streams partially occult one or both stars at certain phases of the binary orbit. In such a scenario, the accretion stream onto the primary could occult the binary before the primary star passes in front of the secondary, which would give dips preceding secondary eclipse, as observed. Similarly, the accretion stream onto the secondary could produce flux dips preceding primary eclipse. However, Shi et al. (2012) find that a single dominant stream develops in 3D MHD simulations of an equal-mass binary and de Val-Borro et al. (2011) find that mass is preferentially channelled towards the primary star in 2D hydrodynamic simulations for a non-equal mass system. This would cause stronger dips preceding secondary eclipse than primary eclipse, as observed.

To ascertain whether accretion streams could cause the short-duration flux dips seen in CoRoT 223992193, a simple model of the binary system was set up. The innermost regions of the circumbinary disk and the accretion flow in the central cavity were simulated with a custom-written particle code by C. Terquem. To do this, a ring of particles was set up in Keplerian rotation around the binary centre of mass at an arbitrary distance beyond the circumbinary disk's theoretical inner edge (i.e. >0.1 AU).

Each particle is then given a small radial velocity to force them to enter the cavity; this mimics turbulent processes in the disk that would cause particles to lose angular momentum and accrete onto the binary (Shi et al., 2012). Each particle is subject to the gravitational potential from the stars, but pressure effects are ignored. This is a good approximation within the cavity because the density is very low, as has been confirmed by hydrodynamical simulations, which find that the motion of particles within the cavity is essentially ballistic. However, we note that hydrodynamical effects are important in the denser circumbinary disk and that this model will not capture these details. Nonetheless, the model is valid for analysing the accretion streams, which is our aim. Once a particle enters the cavity it can either be accreted onto one of the stars or accelerated onto a trajectory that sends it back into the circumbinary disk. In the latter case, it is assumed

that the shock upon impact with the circumbinary disk circularises the particle's orbit and its velocity is therefore reset to the Keplerian value, with a small inward drift.

A snapshot of the resulting accretion flow is shown in Fig. 4.13 in a frame co-rotating with the binary and centred on its centre of mass. The black crosses represent the positions of the particles and the red squares the position of the two stars, with the primary on the left. The red circles delimit rings in which, in principle, particles could be trapped in Keplerian motion around each of the stars, forming circumstellar disks. For each ring, the inner circle lies at the sublimation radius, within which no amorphous grains of dust can exist, and the outer circle corresponds to the radius at which circumstellar disks are tidally truncated by the other star (roughly one third of the binary separation: Paczynski, 1977; Papaloizou & Pringle, 1977). Particles that reach these rings have been removed, as we expect them to be continuously channeled onto the stars by the stellar magnetic fields, but it is plausible that some material exists in these rings. In our model, the binary clears out a slightly eccentric cavity of radius ∼0.08–0.1 AU (∼17–22 $R_{\odot}$). We note that this eccentricity is consistent with 2D hydrodynamical and 3D MHD simulations (Hanawa et al., 2010; Shi et al., 2012).

The easiest way to interpret Fig. 4.13 is to move ourselves around the plot. Primary eclipse occurs when we look directly from the right hand side of the plot (i.e. the secondary star on the right lies in front of the primary star on the left) and we move clockwise around the bottom until we are looking directly from the left hand side, which corresponds to secondary eclipse. As we do so, we see that as our line of sight moves around the bottom left quadrant our view to the primary star passes through the accretion stream onto the primary. Given the inclination and system scale, simple geometry predicts that the primary accretion stream would partially occult the primary star and its surrounding material (assuming negligible scale height as expected due to the low pressure). This obscuration could persist over the $\sim 90^{\circ}$ in phase prior to secondary eclipse, which corresponds to ∼1 day and is the typical duration of the obscuration events.

Terquem et al. (2015) present 2D isothermal hydrodynamical simulations of CoRoT 223992193.

They find that the inclination and system geometry allow for the stars to be obscured by dust in the very inner regions of the system. For a given system scale, there is a fine balance between an inclination that is too high, such that the circumbinary disk obscures both stars completely, and too low, such that no obscuration occurs; CoRoT 223992193 lies between these two options, giving stars that are visible but which can be partially (and time-variably) obscured due to the non-axisymmetric nature of the binary geometry. As we showed in section 4.1, Terquem et al. find that only a very small amount of dust is required to reproduce the amplitude of the observed variations. This dust lies in the central cavity of the circumbinary disk, close to the sublimation radii around the two stars. They find that structures such as spiral arms in the circumbinary disk cannot explain the variations because, further away from the binary, less mass is intersected for a given inclination due to the rapidly decreasing density with height above the mid-plane. With material in the inner regions of the system, the general variations seen in the residuals of our 2011/2012 spot models (Figs. 4.7 and 4.9) can be understood as arising from variable obscuration and emission (the latter because this material would be close to the sublimation temperature of $T \sim 1500$ K and therefore contributing to the 3.6 and 4.5 μm bands). In some of their calculations, Terquem et al. find that a dip can be produced preceding secondary eclipse by the accretion stream onto primary partially obscuring light from the binary (their Fig. 3, phases $\sim$130–180°). However, as the model cannot capture the full complexity of the system, it is difficult to be more quantitative. Indeed, in the 3D MHD simulations of Shi & Krolik (2015), structures in the circumbinary disk appear more complicated than in hydrodynamical simulations and it is not unreasonable to expect a similar complexity within the cavity for this system.

While the above model is very simple, it shows that the expected accretion flow geometry in the cavity of the circumbinary disk can reproduce short-duration flux dips before secondary eclipse not unlike those seen in the CoRoT and *Spitzer* light curves. The accretion flow shown in Fig. 4.13 is very similar to that obtained by Hanawa et al. (2010), who perform hydrodynamical simulations of a binary with a mass ratio similar to

CoRoT 223992193. We therefore note that simple particle models, such as described here, can offer a useful alternative to computationally expensive simulations when investigating low-density phenomena, such as accretion streams in binary systems.

4.7 Conclusions and future work

Modelling of the system's broadband optical and infrared SED reveals a mid-IR excess that cannot be explained by emission from two stellar photospheres alone; additional, cool material is required. Dynamical arguments and simple disk models indicate that neither circumstellar nor circumbinary disks can solely explain this excess. We find that the excess can be reproduced by dust emission from within the inner cavity of a circumbinary disk and show that only a very small dust mass of $\sim 1 \times 10^{-13}\,M_{\odot}$ is required. It is plausible that such small amounts of dust exist in the cavity, e.g. in accretion streams from a circumbinary disk. The continued presence of dust in the cavity at 4–5 Myr implies replenishment and we thereby infer the existence of a circumbinary disk as the most natural means of doing so. This opens up the possibility that some of the OOE photometric variations could be due to obscuration of the central stars by dust located at the inner edge, or in the central cavity, of the circumbinary disk.

CoRoT 223992193 is the only known low-mass, pre-main sequence eclipsing binary to show evidence of a circumbinary disk. In seeking to understand what physical processes drive the observed photometric variability, we have shown that the large scale structure in the system's optical CoRoT light curves is broadly consistent with the constructive and destructive interference of starspot regions at two slightly different periods. Measurements of $v \sin i$ for both stars are consistent with the spot periods and suggest that the primary is synchronised and the secondary rotates slightly supersynchronous. Modelling the simultaneous 2011/2012 CoRoT and *Spitzer* 3.6 and 4.5 μm light curves indicates that additional variability is present, most notably in the *Spitzer* bands. Given that the system's SED requires the presence of dust in the central cavity of the circumbinary disk, we investigated the effect of variable dust emission as well as dust obscuration and find that the remaining variability is consistent with a combination of these two phenomena.

Analysis of 15 medium resolution Hα profiles spread throughout the binary orbit reveal an emission component associated with each star. The majority of this is consistent with chromospheric emission but some profiles also display higher velocity emission. This emission could be due to prominences, although we note that half of the secondary emission components display full widths at 10% intensity > 270 km s^{-1}, which can also be interpreted as having an accretion-related origin. Similarly, simultaneous u and r-band photometry obtained the month after the CoRoT and *Spitzer* observations reveal a short-lived u-band excess consistent with either a stellar flare or an accretion hot spot. We need simultaneous, multiple emission line observations at high resolution to break the degeneracy between chromospheric and any accretion related processes.

The 2011/2012 CoRoT and *Spitzer* light curves revealed short-duration flux dips that precede secondary eclipse (i.e. they occur broadly in phase with the binary orbit). A simple model of the binary finds that the accretion stream onto the primary star could partially obscure light from the central binary at the observed phases.

Determining the physical origins of photometric and spectroscopic variability in young binary systems is difficult due to the geometric complexity and hence many potential sources of variability. Even with high-precision photometry and medium-resolution spectroscopy we cannot unambiguously disentangle the different signals. To do so would require high-precision multi-band photometry with simultaneous high-resolution spectroscopic monitoring of multiple emission lines.

While low-mass, accreting binary systems have been the focus of much study, e.g. V4046 Sgr and DQ Tau, this is the first such system containing an eclipsing binary. The photometric and spectroscopic variations of CoRoT 223992193 are consistent with the picture of two active stars possibly undergoing non-steady, low-level accretion; the system's very high inclination provides a new view of such variability. We hope to improve our understanding of this system in the future by obtaining multi-epoch monitoring of a range of emission lines. Looking to the future, the *Kepler*/K2 mission is observing a number of nearby star forming regions and young open clusters, and could discover similar, brighter

objects that can shed further light on the processes driving variability in young binary systems.

Chapter 5

The NGC 2264 EB sample

This Chapter details the work to date on the sample of EBs discovered by CoRoT in the NGC 2264 field. We begin by giving a brief overview of the sample in section 5.1. We then apply the techniques developed in characterising CoRoT 223992193 (see Chapter 3) to the sample, which has limited success, primarily due to the one-dimensional nature of the radial velocity determination. In section 5.3 we discuss two systems solved by the applied methods, both of which are found to be main sequence field systems based on their masses, radii and systemic velocities. We then describe our efforts to characterise systems showing evidence of youth in section 5.4 before briefly discussing the remainder of the sample in section 5.5. Finally, in section 5.6 we discuss improvements to the above methods and detail new techniques to model all types of detached EB light curves and spectra.

5.1 Overview

103 eclipsing systems were discovered by CoRoT in 2008; 37 of these were classified as possible cluster members based on their colours, magnitudes and locations, as well as previous studies of the cluster (see section 2.5.1). Of these 37, certain systems were further discounted if they were likely blends or were previously solved, leaving 21 EBs in the sample. The identifiers and co-ordinates for these systems are reported in Table 5.1 and their observed characteristics are presented in Table 5.2 (the accompanying figures are discussed throughout the chapter). The spectral types, where given, were estimated via cross-correlating IDS or ISIS spectra (i.e. I-band) with the Pickles spectral library (Pickles,

Table 5.1: EB identifiers and coordinates. Throughout this chapter the EBs are referred to by their four-digit SRa01 or SRa05 Window IDs.

SRa01/SRa05 Window ID	CoRoT ID	CSI 2264 ID	RA	Dec
0091	500007022	Mon-000459	06 41 13.04	+09 27 31.90
0254	223966541	Mon-007519	06 40 5.89	+10 10 52.75
0360	223942686	Mon-007108	06 38 46.36	+10 15 55.48
0393	223946171	Mon-006951	06 38 57.65	+09 56 7.33
0445	224013042	Mon-007393	06 42 53.03	+09 54 16.02
0824	223971548	Mon-006489	06 40 24.42	+09 19 39.04
0942	223964763	Mon-006059	06 39 59.63	+09 35 11.00
1021	223955882	Mon-006079	06 39 29.10	+09 42 38.52
1113	223939728	Mon-049951	06 38 36.99	+09 06 34.96
1340	223941278	Mon-007069	06 38 41.71	+10 13 10.85
1408	224009183	Mon-015725	06 42 40.36	+10 07 18.48
1572	223998341	Mon-007360	06 42 5.04	+09 05 22.74
1625	224001237	Mon-007491	06 42 14.34	+10 06 8.50
1632	223976178	Mon-007706	06 40 42.75	+10 17 51.29
1781	223926956	Mon-006940	06 37 55.26	+09 30 56.81
2103	223951589	Mon-013490	06 39 14.82	+09 34 30.61
2677	223954720	Mon-006465	06 39 25.15	+09 32 38.15
2754	223943482	Mon-006949	06 38 48.90	+09 49 58.22
3190	224007535	Mon-007391	06 42 35.12	+09 55 56.93
3334	223979687	Mon-005706	06 40 56.65	+09 07 40.84
3602	223994191	N/A	06 41 51.13	+09 10 45.88

1998), which consists of 131 flux-calibrated spectra covering O5-M10[1] and temperatures 40 000–2500 K. Spectral types were visually estimated from the CCF contrast and should only be interpreted as suggestive. Similarly, the temperatures were determined from cross-correlation with solar-metallicity MARCS model spectra, which span 2500–8000 K and surface gravities of $\log g = 4.0$–5.0[2]. Spectral types are only quoted for some systems as the temperature estimates from the I-band spectra were found to be more instructive for prioritising follow-up.

[1] 45 spectra between O5-M6 V, 13 between B2-K3 IV, 45 between O8-M10 III, 7 between B2-M3 II and 17 between B0-M2 I.

[2] the full model library spans $\log g = 1.0$–6.0.

Table 5.2: Characteristics of EBs observed in the NGC 2264 CoRoT and *Spitzer* fields

EB	P	Eclipse depths			OOE	e [a]	V [b]	Ks [c]	SpT [d]	Temp.	no. of	evidence of	comment
		Pri	*Sec*	*Ratio*							spectra	youth [e]	
	(days)	(%)	(%)	(%)						(K)			
						Solved systems							
1781	3.1	25	25	100	flat	∼0	15.0	13.1		∼6000	8		Main sequence field system
2754	2.2	13	11	85	spots	∼0	15.7	13.2	K0V–M1V	∼6000	14		Main sequence field system
						Potential PMS EBs							
0091	5.2	3.5	0.3	9	spots	0.06	11.4	9.9			25	Hα	Likely member - P. Almeida leading
0942	11.7	21	5	24	spots	0.38	16.5	12.0	M1 [f]	4000	27	Hα	Likely member - need IR spectra
1625	3.1	13	1.5	12	spots	0.004	15.3	12.6			0	Hα	Likely member - need IR spectra
3334	14.8	13	7.5	58	∼flat	0.13	17.2	12.4		∼6000	14	weak Li	Possible member
						Remainder of the sample							
0254	14.1	21	19	90	flat	0.02	12.2	10.2			14		
0360	3.8	8.5	3.5	40	spots	0.02	12.0 (R)	10.2			16		Likely blend, possible hierarchical triple
0393	7.7	9	5	56	γ-Dor pulsations	0.01	12.7 (R)	11.2			14		Likely field system
0445	1.5	19	3	16	ellipsoidal	0.04	13.9	12.3	A2V	$\gtrsim$8000	3		Likely background object
0824	3.9	41	33	80	flat	0.47	15.2	11.8	B8V–A7V	$\gtrsim$8000	21		Likely field system
1021	0.5	23	13	57	contact EB	∼0	15.4	12.2		∼7500	2		Likely background object
1113	$\geq$22	30	22	73	flat	∼0.3	14.5	11.6		∼6500	1		No period
1340	1.3	6	4	67	spots	∼0	14.5	11.1	M0V–M2.5V	∼4000	10		Blend: cluster member with background EB
1408	3.6	19	4	21	flat	0.09	14.3	12.8		$\gtrsim$8000	2		Likely background object
1572	2.9	7.5	6	80	flat	0.11	15.8	12.0		∼6500	6		Possible blend with background EB
1632	6.6	26	13	50	flat	0.01	14.6	12.3	A5V–A7V	$\gtrsim$8000	3		Likely background object
2103	7.4	6	3	50	flat	0.03	15.4	13.8		$\gtrsim$8000	2		Likely background object
2677	2.8	20	18	90	flat	0.13	16.0	13.2	B57V–A7V	$\gtrsim$8000	4		Likely background object
3190	0.9	20	19	95	near-contact EB	∼0	16.7	14.0		∼6500	2		Likely background object
3602	3.8	12	9	75	flat	0.02	16.7	13.4		∼6500	6		Likely background object

[a] From light curve and RVs where possible, otherwise from light curve only.

[b] Sung et al. (2008) and NOMAD catalogues, Vega magnitudes. (R) indicates R band magnitude.

[c] 2MASS, Cutri et al. (2003), Vega magnitudes.

[d] Determined from cross-correlation with the Pickles spectral library (Pickles, 1998).

[e] Hα = Hα emission, Li = Li 6708 absorption and He I = He I 6678 emission.

[f] Makidon et al. (2004).

5.2 Application of the methods developed for CoRoT 223992193 to the EB sample

Having developed new techniques based on Gaussian process regression for modelling light curve variability and correlated noise in cross-correlation functions, we generalised these methods to create a framework within which to characterise the sample of EBs. Our light curve analysis consists of:

1. **OOE variability removal.** The OOE variability is modelled with Gaussian processes (optimised for the covariance properties of the light curve) and then removed, either by subtracting the GP model from the light curve or dividing it out, whichever gives the most consistent eclipse depths from one orbit to the next.

2. **Preliminary JKTEBOP modelling.** We perform a preliminary JKTEBOP run on the detrended 2008 CoRoT light curve (which executes a Levenberg-Marquardt minimisation). The limb darkening coefficients are estimated using the temperatures determined from the spectra or spectral type (see Table 5.2), eclipse ratios and assuming surface gravities of $\log g = 4.0$ and metallicity [M/H] = –0.1. The resulting fit is used to compute the reduced χ^2 for the primary, secondary and out-of eclipse data separately. The photometric uncertainties on the fluxes are then rescaled so as to give a reduced χ^2 of unity in each subset.

3. **Final JKTEBOP modelling.** JKTEBOP is re-run (with the same initial guesses) using the scaled photometric errors. All parameter distributions are derived from a Monte Carlo analysis of the 2008 light curve, except for P and $T_{\rm prim}$, which are determined from the joint 2008 + 2011/2012 datasets.

Our radial velocity determination consists of:

1. **Selecting suitable wavelength ranges.** The IDS and ISIS spectra both cover similar wavelength ranges in the near-IR: for the low-mass systems we select ranges of 8380–8392, 8455–8484, 8510–8525, 8575–8644 and 8685–8745 Å for cross correlation. These optimise the inclusion of useful lines and mask the Ca II IR triplet.

2. **Cross-correlating with MARCS spectra.** We compute CCFs for a range of MARCS models between $4000 \leqslant T \leqslant 8000$ K and $4.0 \leqslant \log g \leqslant 5.0$. The most suitable CCF is chosen based on visual inspection of the peak-to-noise contrast and the behaviour of the correlated noise around the stellar peaks.

3. **CCF modelling.** Each CCF is modelled as the sum of one or two Gaussians plus a stochastic noise component, which is described by a GP; in all cases we use the rational quadratic kernel (equation 3.3). We use a Metropolis–Hastings MCMC to obtain robust uncertainties on the parameters of the fit.

4. **RV orbit modelling.** We fit the RV measurements using Keplerian orbits with constraints on certain parameters (P, $T_{\rm prim}$, $e\cos\omega$ and $e\sin\omega$) from the light curve solution. Again, we use an MCMC to obtain robust uncertainties.

The fundamental parameters and uncertainties are then determined from propagating the distributions for the relevant parameters through equations 1.32–1.37 and using a to solve for the individual radii.

5.3 Systems solved with these techniques

Two systems were solved with these techniques, namely EBs 1781 and 2754, both of which are near-equal mass systems.

5.3.1 EB 1781

The 2008 and 2011/2012 light curves are shown in the top left and top middle plots of Figure 5.1, respectively. The system displays equal depth eclipses (∼25%) with a period of 3.15 days and low-level OOE variability. These variations modulate in phase with the binary orbit and could arise from ellipsoidal distortions, although they could also be explained as spot modulation (assuming synchronisation). The 2011/2012 light curve is noisier than in 2008, with residual systematic variations unaccounted for in the CoRoT pipeline (although in this target they are not significant). We model both OOE light curves with a Squared Exponential kernel (equation 3.2). The top right plot of Figure 5.1

shows the phase-folded, detrended 2008 light curve with the best-fit JKTEBOP model in red. Comparing the residuals of the fit to those of CoRoT 223992193 (Figure 3.5) we see less scatter during eclipse, primarily due to the lack of significant and complex variability affecting each primary and each secondary eclipse differently. The parameters of the light curve model are reported in Table 5.3.

An example WHT/ISIS spectrum is shown in the bottom left plot of Figure 5.1 (top: MARCS template, bottom: observed spectrum) with the regions used for cross-correlation shown in red. The double-lined nature of the system can clearly be seen in the Ca II triplet (the strongest three lines); these lines were not included in the cross-correlation due to their broad nature, which smears out the CCF and blends the two stellar peaks over the majority of phases (except near quadrature as evidenced here; phase = 0.30). The corresponding CCF from this spectrum is shown in the bottom middle plot and clearly displays two well-separated stellar peaks. Obtaining RVs for both stars from 8 of the 9 observed spectra (one was observed at the end of primary egress) we modelled the stellar orbits as shown in the bottom right plot. The residuals of the best-fit model are predominately within $\sim$5 $\mathrm{km\,s^{-1}}$. The systemic velocity of the system is -7.1 ± 0.6 $\mathrm{km\,s^{-1}}$, which is more than 5σ discrepant from the recessional velocity of the cluster (22 ± 3.5 $\mathrm{km\,s^{-1}}$; Fűrész et al. 2006). The parameters of the radial velocity fit along with the masses, radii and separations of both stars are reported in Table 5.3.

The masses and radii are plotted in red in Figure 5.2 and imply a main sequence system. The uncertainties on the data points are larger than neighbouring systems. For the masses this is partly due to our limited phase coverage but also to the precision of our RV determination (cf. the scatter in the residuals of the RV orbit plot). The large uncertainty on the radii is driven by the equal-brightness nature of the system, which gives rise to a degeneracy between the surface brightness and radius ratios (note the error on the latter is ~ 0.1). We lack an optical spectroscopic light ratio to break this degeneracy, as we did in CoRoT 223992193. Finally, we note that the system lies slightly above the ZAMS, like many others.

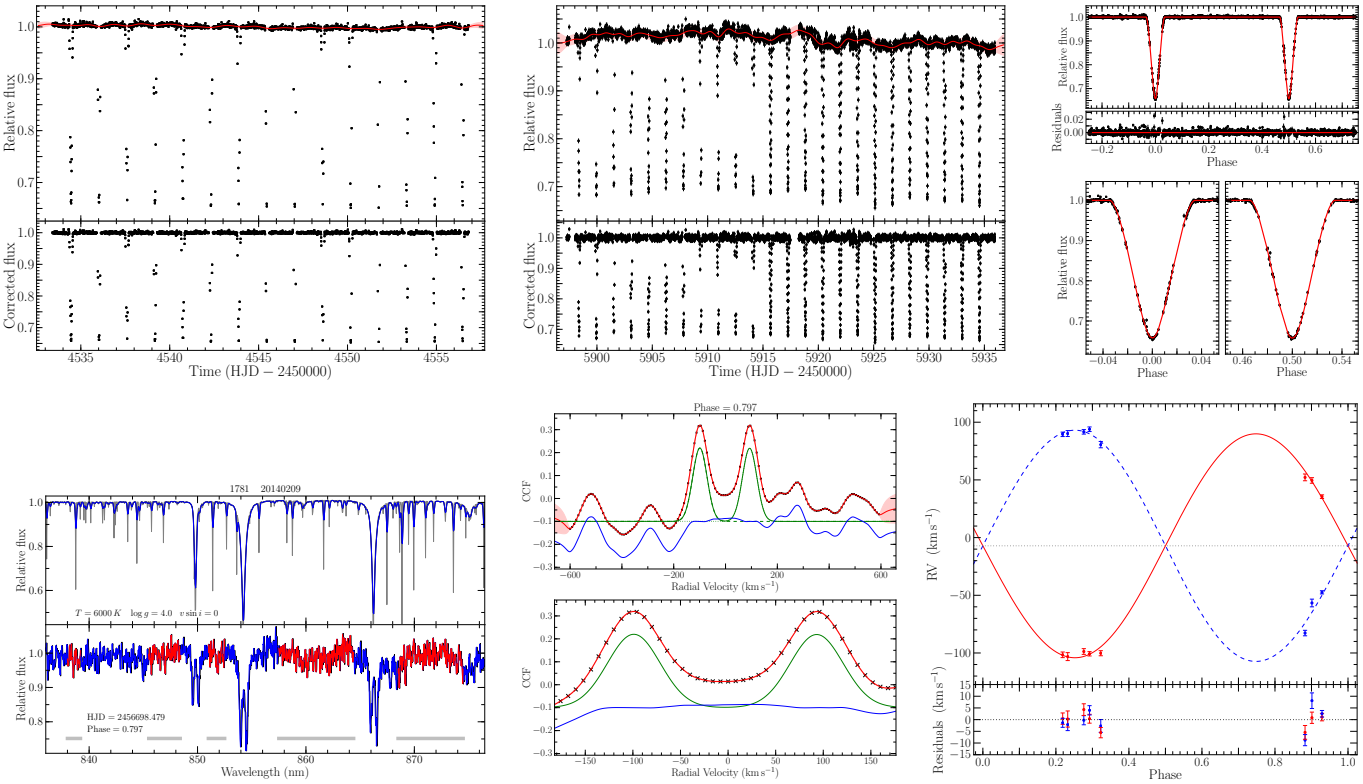

Figure 5.1: Light curves, spectra, CCFs and radial velocity orbits of EB 1781.

Top left: 2008 CoRoT light curve (black points) with the mean and 95% confidence interval of the predictive distribution of the squared exponential Gaussian Process used to model the out-of-eclipse variations (red and pink shaded region, respectively).

Top middle: same as for *top left* but for the 2011/2012 CoRoT light curve.

Top right: top panel shows the phase folded, detrended 2008 CoRoT light curve (black points) with the best-fit JKTEBOP model shown in red. The residuals of the best-fit model are also shown immediately below; phase zero marks the centre of the primary eclipse in these two plots. The bottom panels show zooms on the primary and secondary eclipses (left and right, respectively).

Bottom left: example spectrum from WHT/ISIS obtained on 9$^{\text{th}}$ February 2014. The top panel shows the MARCS template ($T = 6000$ K, $\log g = 4.0$ and $v \sin i = 0.0$ km s^{-1}); grey shows the full $R = 20\,000$ resolution spectrum and the blue shows the spectrum degraded to match the spectrograph's resolution of $R = 12\,000$. The bottom panel shows the observed spectrum in blue with the regions used in the cross-correlation indicated in red (with grey lines also indicating these regions below).

Bottom middle: CCF obtained from the ISIS spectrum taken on 9$^{\text{th}}$ February 2014 (*bottom left*), showing the best-fit model (red) together with the associated 68.5% confidence interval (pink shaded region). The Gaussian and GP terms are also shown separately by the green and blue lines respectively, with a vertical offset added for clarity. The top panel shows the full range used in the fit and the bottom panel a zoom on the region around the peaks.

Bottom right: phase-folded RV data (points with error bars) and best-fit orbital solution for the primary (red solid line) and secondary (blue dashed line). The grey horizontal dotted line indicates the systemic velocity. Bottom: residuals of the best-fit model.

5.3.2 EB 2754

The light curve, spectra, and radial velocity plots for EB 2754 are shown in Figure 5.3 and the corresponding parameters values are reported in Table 5.4. The system shows grazing eclipses with depths of ∼13 and 11% for the primary and secondary respectively,

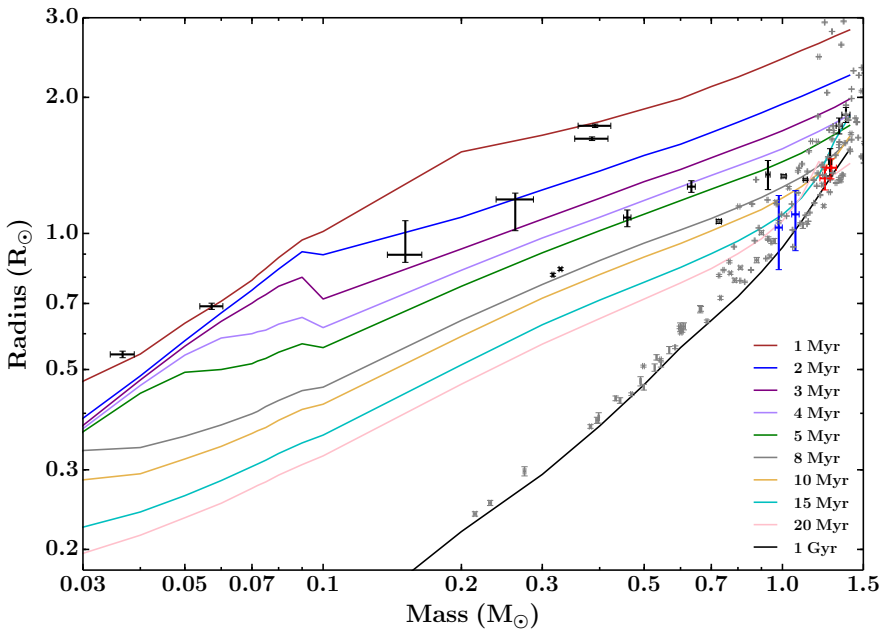

Figure 5.2: Mass-radius relation for low-mass EBs. The black and grey points show measurements for pre-main and main sequence stars with masses $< 1.5\,M_\odot$ in detached EBs[1], and the lines show, from top to bottom, the theoretical isochrones of Baraffe et al. (2015, BCAH15) for 1, 2, 3, 4, 5, 8, 10, 15, 20 Myr and 1 Gyr (brown, blue, purple, lilac, green, grey, ochre, cyan, pink and black, respectively. $Y = 0.28$ for the stellar interior, [M/H] = 0, mixing length $\alpha = 1.6$). EBs 1781 and 2754 are shown in red and blue, respectively.

and a period of 2.2 days. The OOE variations show typical evolving spot modulation patterns in the 2008 light curve with evidence for constructive and destructive interference in 2011/2012 (the former at rHJD∼5905–5917 and the latter before and after). To capture the starspot modulation and evolution, as well as the long term flux level trends, the OOE variations in the 2008 light curve were modelled using a periodic squared exponential kernel with an additional squared exponential term:

$$k(r) = A_{PSE}^2 \exp\left(-2\sin\frac{(\frac{\pi r}{P_{PSE}})^2}{S_{PSE}^2}\right) + A_{SE}^2 \exp\left(-\frac{r^2}{2\,l_{SE}^2}\right) \tag{5.1}$$

where A_{PSE}, P_{PSE} and S_{PSE} are the amplitude, period and smoothness of the periodic component, and A_{SE} and l_{SE} the amplitude and timescale of the non-periodic component. Given the presence of systematics in the 2011/2012 light curve, we opted for a rational quadratic as it allows for the necessary range of variability timescales. We note that the model used for this light curve is unimportant as we only use the data for refining the ephemeris. The residuals of the JKTEBOP fit to the 2008 eclipses are small, although some uncorrected spot signatures are still present in a fraction of the orbits.

Table 5.3: Parameter values and uncertainties for EB 1781.

Parameter	Unit	Value	
		Primary	*Secondary*
	Fitted parameters		
P	(days)	$3.14631924\,^{+0.00000045}_{-0.00000044}$	
$T_{\rm prim}$	(HJD)	$2454534.45103 \pm 0.00014$	
$e\cos\omega$		$0.000061\,^{+0.000018}_{-0.000027}$	
$e\sin\omega$		$-0.0066\,^{+0.0017}_{-0.0015}$	
J		$1.0002\,^{+0.0050}_{-0.0041}$	
$(R_{\rm pri}+R_{\rm sec})/a$		$0.22110\,^{+0.00071}_{-0.00089}$	
$R_{\rm sec}/R_{\rm pri}$		$0.949\,^{+0.111}_{-0.094}$	
i		$86.557\,^{+0.126}_{-0.043}$	
$V_{\rm sys}$	(km s^{-1})	$-7.11\,^{+0.58}_{-0.63}$	
K	(km s^{-1})	$97.0\,^{+1.1}_{-1.0}$	100.2 ± 1.1
	Derived parameters		
Mass	($M_\odot$)	$1.278\,^{+0.033}_{-0.031}$	$1.237\,^{+0.032}_{-0.031}$
Radius	($R_\odot$)	$1.397\,^{+0.065}_{-0.077}$	1.324 ± 0.077
$\log g$	(cgs)	$4.255\,^{+0.047}_{-0.040}$	$4.287\,^{+0.051}_{-0.049}$
a	($R_\odot$)	$6.047\,^{+0.067}_{-0.065}$	6.244 ± 0.066
	($R_\odot$)	$12.291\,^{+0.101}_{-0.096}$	

This system is fainter than EB 1781 giving noisier spectra (and noisier light curves) but signatures of both stars were easily extracted from 14 of the 19 spectra[3], which produce double-peaked CCFs and well-defined stellar orbits with residuals typically less than $\sim$5 km s^{-1}. We note the RVs around phase = 0.59 are significantly more scattered; these were all observed on the same night and give noisier CCFs, especially around the peak region. The systemic velocity is 37.0 ± 0.4 km s^{-1}, which is more than 4σ discrepant from the cluster value.

The masses and radii are plotted in blue in Figure 5.2 and imply a main sequence system. The uncertainties on the data points are again larger than neighbouring systems. As with EB1781, the large uncertainty on the radii is driven by the surface brightness / radius ratio degeneracy (note the error on the latter is ~ 0.3!). Again, we lack an optical spectroscopic light ratio to break this degeneracy. We note that this system also appears to lie slightly above the ZAMS. Neither EB 2754 nor EB 1781 will provide useful constraints on stellar evolution models given the more precise constraints already available in their

[3]the other five spectra were taken too close to eclipse to disentangle the primary and secondary stellar peaks.

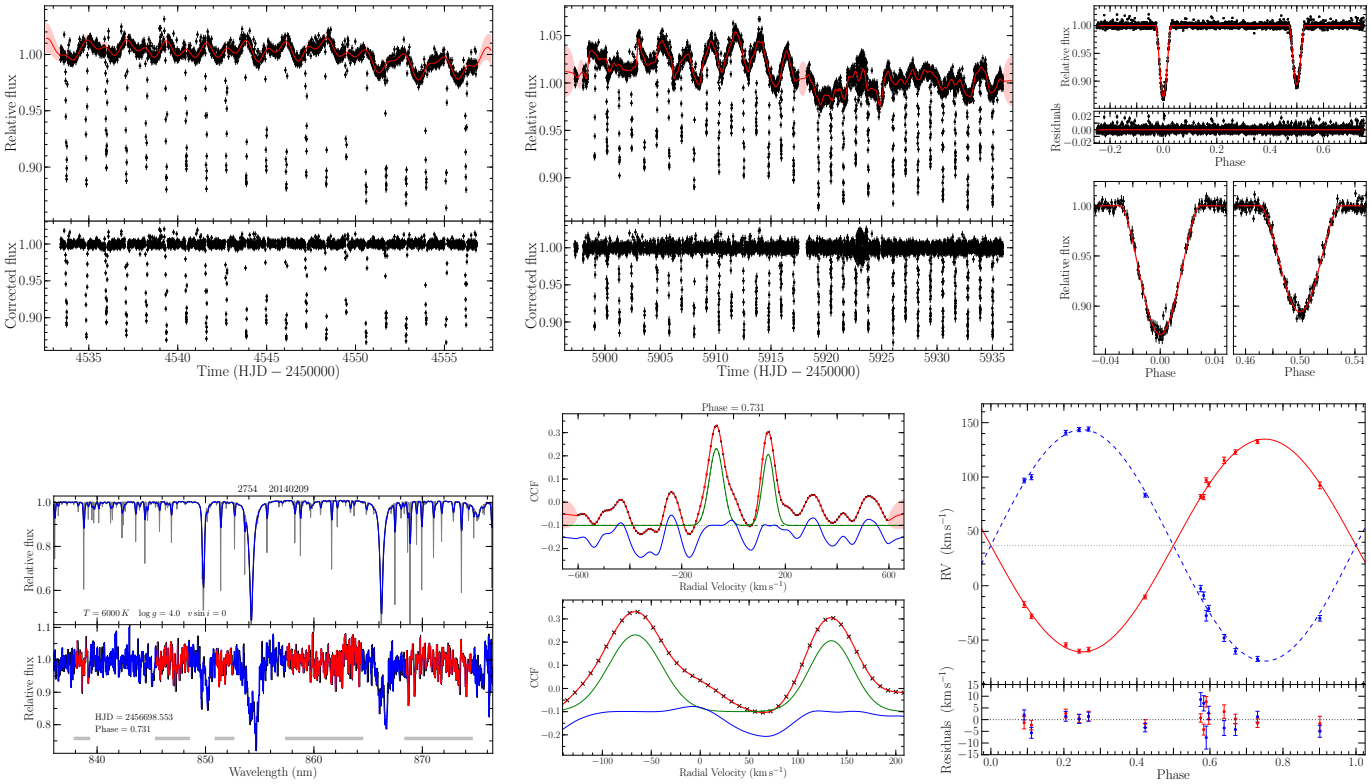

Figure 5.3: Light curves, spectra, CCFs and radial velocity orbits of EB 2754. As for Figure 5.1 except that the out-of-eclipse GP model comprises a periodic squared exponential plus a non-periodic squared exponential term for the 2008 light curve (*top left*) and a rational quadratic kernel for the 2011/2012 light curve (*top middle*). The spectra (*bottom left*) were also obtained on 9$^{\rm th}$ February 2014 and cross-correlated with a MARCS template of $T = 6000$ K, $\log g = 4.0$ and $v \sin i = 0.0$ km s^{-1}.

region of the mass, radius (and presumably age) space. We do not plan to conduct further work on these systems.

Table 5.4: Parameter values and uncertainties for EB 2754.

Parameter	Unit	Value	
		Primary	*Secondary*
	Fitted parameters		
P	(days)	$2.24744488\,^{+0.00000055}_{-0.00000053}$	
$T_{\rm prim}$	(HJD)	$2454534.86801 \pm 0.00029$	
$e\cos\omega$		$-0.0002994\,^{+0.0000099}_{-0.0000095}$	
$e\sin\omega$		$0.0004079\,^{+0.0000107}_{-0.0000057}$	
J		$0.836\,^{+0.079}_{-0.076}$	
$(R_{\rm pri}+R_{\rm sec})/a$		$0.2308\,^{+0.0024}_{-0.0059}$	
$R_{\rm sec}/R_{\rm pri}$		$0.93\,^{+0.39}_{-0.26}$	
i		$81.55\,^{+0.58}_{-0.17}$	
$V_{\rm sys}$	($\mathrm{km\,s^{-1}}$)	$37.03\,^{+0.46}_{-0.43}$	
K	($\mathrm{km\,s^{-1}}$)	$97.86\,^{+0.74}_{-0.77}$	$106.44\,^{+0.82}_{-0.85}$
	Derived parameters		
Mass	($M_\odot$)	1.067 ± 0.020	$0.982\,^{+0.017}_{-0.018}$
Radius	($R_\odot$)	$1.10\,^{+0.14}_{-0.19}$	$1.03\,^{+0.18}_{-0.20}$
$\log g$	(cgs)	$4.38\,^{+0.16}_{-0.11}$	$4.41\,^{+0.18}_{-0.14}$
a	($R_\odot$)	$4.396\,^{+0.033}_{-0.035}$	4.779 ± 0.038
	($R_\odot$)	$9.174\,^{+0.053}_{-0.054}$	

5.4 Potential PMS EBs

Although we applied the above methods to all interesting EBs in the sample, we were only able to solve the two aforementioned systems. This is primarily due to our radial velocity determination which, due to its 1D nature, is not well-suited to systems with low brightness ratios. In this section we describe four EBs that show evidence of youth but are as yet unsolved. Of these four systems, three are low-to-extreme brightness (and hence mass) ratio systems, which are particularly valuable as they will provide constraints spanning a wide range in mass and hence probe a wide range of underlying physics at the early stages of stellar evolution. The three extreme mass ratio systems (EBs 0091, 0942 and 1625) are discussed first.

5.4.1 EB 0091

EB 0091 is a likely EB cluster member, based on its position in CMDs, proper motion (Walker, 1956) and X-ray emission (Flaccomio et al., 2006; Sung et al., 2009). It was observed by CoRoT in 2008 only (see Figure 5.4, top left panel). The stars orbit in 5.2 days

and their relative eclipse depths indicate an extreme-brightness system: primary eclipse is relatively shallow at ∼3.5% but secondary is just 0.3% deep (eclipse depth ratio ∼9%). The system does not appear to be synchronised, as one might expect given its apparent youth: the OOE variations are consistent with evolving spot modulation on a shorter period than the binary orbit. The OOE variations were modelled using a quasi-periodic squared exponential kernel with an additional squared exponential kernel. This is very similar to the model used for EB 2754 but with a multiplicative squared exponential term on the periodic component to allow evolution away from strict periodicity:

$$k(r) = A_{QPSE}^2 \exp\left(-\frac{\sin^2(\frac{\pi r}{P_{QPSE}})}{2S_{QPSE}^2} - \frac{r^2}{2\,l_{QPSE}^2}\right) \; + \; A_{SE}^2 \exp\left(-\frac{r^2}{2\,l_{SE}^2}\right) \qquad (5.2)$$

where A_{QPSE}, P_{QPSE}, S_{QPSE} and l_{QPSE} are the amplitude, period, smoothness and decay time of the quasi-periodic component, and A_{SE} and l_{SE} the amplitude and timescale of the non-periodic component.

The JKTEBOP fit is shown in Figure 5.4 (top right panel). The increased residuals across primary eclipse probably result from different visible spot coverages from one eclipse to the next (especially if some spots lie under the eclipse chord).

Given the shallowness of secondary eclipse, optical spectroscopic follow-up only extracts the primary RV variations. Such extreme-brightness ratio systems are difficult to solve but are particularly valuable. We therefore obtained IR (H-band) observations with the Gemini Near Infrared Spectrograph (GNIRS) on Gemini North, Hawai'i; this program is led by Pedro Almeida. Preliminary results are shown in Figure 5.4 (bottom panel) and indicate a systemic velocity consistent with the cluster. Only 3 data points constrain the secondary orbit but at least three more have been obtained and are being analysed. Preliminary masses for the primary and secondary stars are $M_{\rm pri} \approx 0.84\,M_\odot$ and $M_{\rm sec} \approx 0.18\,M_\odot$. Subsequent analysis of high resolution images of the region revealed contamination of the CoRoT aperture by not just one faint star (as previously known) but also by another very nearby star of comparable brightness. This additional light in the CoRoT aperture needs to be included in the modelling as it will strongly affect the derived radii; this work is ongoing. Accordingly, we restrict the parameters reported in Table 5.5.

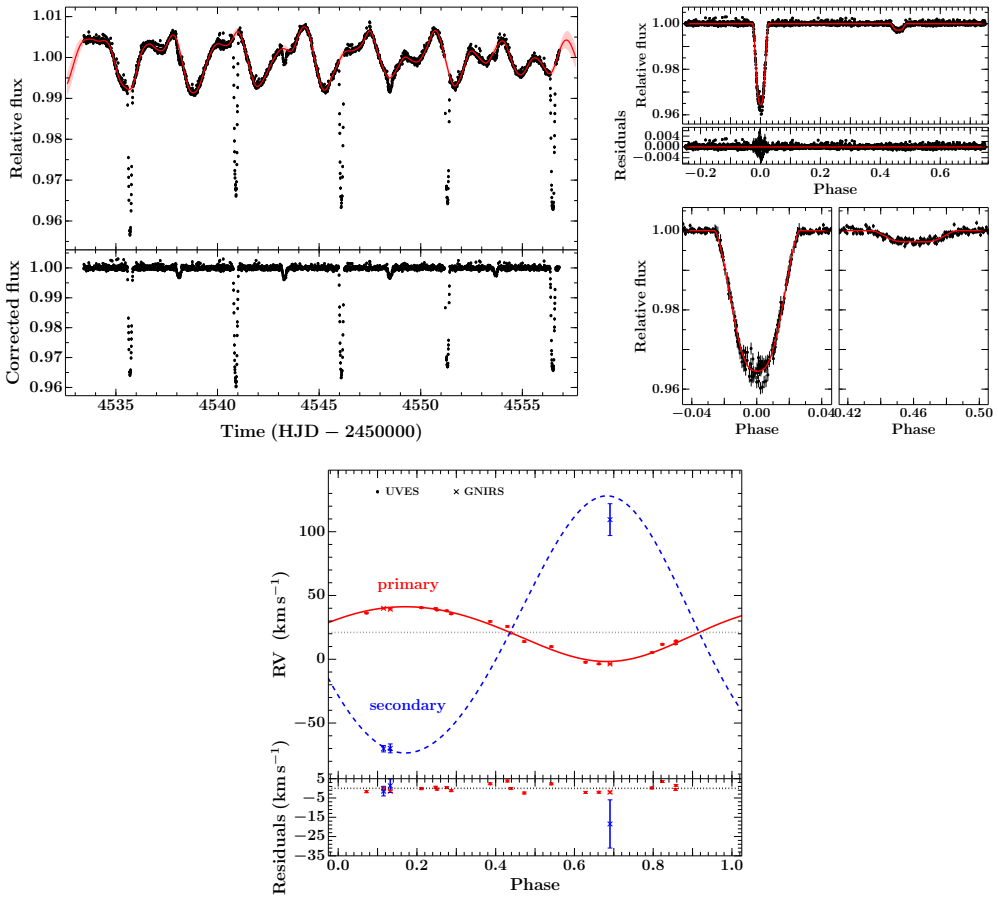

Figure 5.4: *Top left*: 2008 CoRoT light curve (black points) with the mean and 95% confidence interval of the predictive distribution of the quasi periodic squared exponential Gaussian Process used to model the out-of-eclipse variations (red and pink shaded region, respectively).

Top right: top panel shows the phase folded, detrended 2008 CoRoT light curve (black points) with the best-fit JKTEBOP model shown in red. The light curve has been divided by the OOE model. The residuals of the best-fit model are also shown immediately below; phase zero marks the centre of the primary eclipse in these two plots. The bottom panels show zooms on the primary and secondary eclipses (left and right, respectively).

Bottom: phase-folded RV data (points with error bars) and best-fit orbital solution for the primary (red solid line) and secondary (blue dashed line). The grey horizontal dotted line indicates the systemic velocity. Bottom: residuals of the best-fit model. [RVs extracted by P. Almeida]

5.4.2 EB 0942

EB 0942 is a likely young object based on its Hα emission (3.32 Å), Li 6708 Å absorption and Ca II IR triplet activity, and a potential cluster member based on its position in CMDs and M1 spectral type (Makidon et al., 2004). Rebull et al. (2002) infer a mass of 0.46 $M_{\odot}$ from spectroscopy and Makidon et al. (2004) report a rotation period of 2.98 days.

The light curve, spectra, and radial velocity plots for EB 0942 are shown in Figure 5.5 and the corresponding parameter values are reported in Table 5.6. The two stars travel on

Table 5.5: Parameter values and uncertainties for EB 0091

Parameter	Unit	Value	
		Primary	*Secondary*
	Fitted parameters		
P	(days)	$5.199760716\,^{+0.000000048}_{-0.000000037}$	
$T_{\rm prim}$	(HJD)	2454530.4985 ± 0.0011	
$e\cos\omega$		$-0.06189\,^{+0.00067}_{-0.00059}$	
$e\sin\omega$		$-0.01840\,^{+0.00098}_{-0.00057}$	
$V_{\rm sys}$	($\mathrm{km\,s^{-1}}$)	20.05 ± 0.11	
K	($\mathrm{km\,s^{-1}}$)	21.47 ± 0.16	~ 100
	Derived parameters		
Mass	($M_\odot$)	≈ 0.84	≈ 0.18

eccentric orbits ($e \sim 0.4$) with a period of 11.7 days. The light curve displays significant spot modulation (∼15% peak-to-peak amplitude) with a period of ∼3 days. The spots appear more stable than in other systems (c.f. the similar morphology in both CoRoT runs and the earlier 2.98 day period reported by Makidon et al. 2004) but still display some evolution in their shape. We model the OOE variations with a periodic squared exponential plus a non-periodic squared exponential, as with EB 2754 (equation 5.1). Secondary eclipse is shallow with respect to primary (ratio ∼21%) implying a low brightness ratio system, although not as extreme as EB 0091. In the phase-folded light curve, increased residuals are apparent across both eclipses, being larger for primary; again, due to uncorrected spot effects. Nonetheless, the JKTEBOP model is a good fit to the light curve.

The near-IR I-band spectra display activity in the Ca II triplet, common in young systems, and give strongest CCF contrast with a 4000 K template, consistent with the literature M1 spectral type. Cross correlation gives only a single stellar peak (the primary) due to the low light ratio. Preliminary analysis of the CCFs gave noisy RVs. Inspection of the spectral traces revealed hints of an additional component at certain parallactic angles, which affected clean cross-correlation. High-resolution radial and contour plots of the system confirmed the presence of a tight visual companion ∼1 arcsec to the north-east (comparable with the orientation of the spectra contaminant). At the distance of the cluster, this separation corresponds to ∼800–1000 AU, which could mean the system is a

hierarchical triple. Therefore, the spectra were re-reduced selecting only the section of the spectral trace (in the spatial direction) that was relatively unaffected by the companion star; this was only possible for a subset of the spectra (taken at suitable parallactic angles). The RVs obtained from the selected spectra trace an orbit for the primary star which is consistent with the eccentricity determined from the light curve solution[4]. Using the mass function (equation 1.39) and assuming a primary mass in the range 0.4–0.8 $M_\odot$, the primary RV orbit implies a secondary mass of $M_{\rm sec} \sim 0.09 - 0.14\,M_\odot$. This is very interesting as the secondary could be very close to the hydrogen-burning mass limit. The estimated primary mass range extends at the lower end to be below the Rebull et al. (2002) spectroscopic mass prediction and at the upper end by extrapolating from the masses of CoRoT 223992193 (0.67 and 0.50 $M_\odot$) given that it possesses an M2 spectral type. We note that the predictions of (Siess et al., 2000) for a star possessing M1 spectral type at 3 Myr, fall within this range.

EB 0942 was due to be observed by Gemini/GNIRS along with EB 0091 to extract the secondary orbit but was only observed twice in bad weather conditions. We intend to obtain further IR spectra to solve this system. Finally, we note that the presence of the faint nearby companion could slightly affect the parameters derived from the light curve analysis; this modest third light contribution will be included in future analysis.

5.4.3 EB 1625

EB 1625 is a potential young object based on its Li 6708 Å absorption and Ca II IR triplet activity. Evidence for cluster membership based on CMDs is limited, however, and Hα is in absorption. The analysis of this system has been complicated by incorrect aperture placement[5]. In 2008, CoRoT meant to observe a system designated 1959 but actually extracted an aperture around the next nearest star, 1625, upon which eclipses were detected. However, this was not realised and so the eclipses were attributed to 1959. In 2011/2012 CoRoT observed both of these systems, this time correctly: 1959 no longer showed eclipses

[4] we note that the eccentricity of the RV solution is constrained by the light curve solution so we do not draw strong conclusions from this.

[5] Aperture placement and selection of the type of mask are performed automatically on board CoRoT using an algorithm that is not optimised for crowded fields.

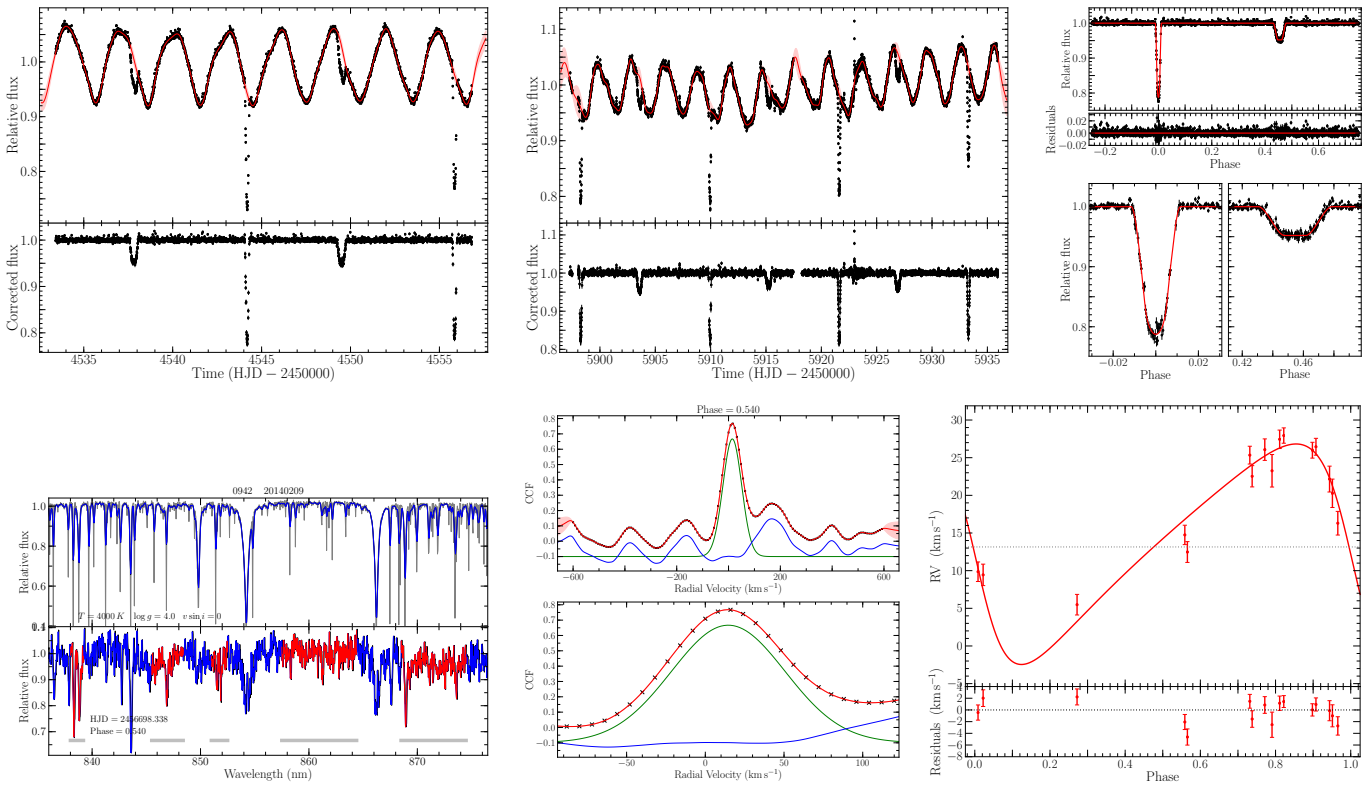

Figure 5.5: Light curves, spectra, CCFs and radial velocity orbit of EB 0942. As for Figure 5.1 except that the out-of-eclipse GP model comprises a periodic squared exponential plus a non-periodic squared exponential term for the 2008 and 2011/2012 light curves (*top left and top middle*). Note that the spectra (*bottom left*) were also obtained on 9$^{\rm th}$ February 2014 and cross-correlated with a MARCS template of $T = 4000$ K, $\log g = 4.0$ and $v \sin i = 0.0$ km s^{-1}. Only the primary star variations were extracted from the spectra (*bottom middle*) yielding a single stellar orbit (*bottom right*).

but the new system, 1625, did. That the eclipsing system was 1625 was not immediately recognised, resulting in spectra of 1959 being obtained: these did not display noticeable RV variations and the priority of the system was reduced. However, subsequent analysis of EB1625 revealed eclipse parameters comparable to those found for 1959 and a joint analysis of the light curves for both systems yielded a consistent solution. At this point, RV follow-up commenced for the true EB, EB 1625, with Keck/HIRES. This data is still under analysis but does show RV variations and evidence for youth; more observations are planned. For this work, however, we restrict ourselves to discussion of the light curves only.

The light curves are shown in Figure 5.6 and the corresponding parameter values are reported in Table 5.7. The 2008 light curve displays evolving spot modulation with ∼8% peak-to-peak amplitudes: the evolution appears to be driven by the constructive and destructive interference of starspot regions, one with a period of ∼3.5 days and the other

Table 5.6: Parameter values and uncertainties for EB 0942

Parameter	Unit	Value
P	(days)	$11.67311487 \pm 0.00000023$
$T_{\rm prim}$	(HJD)	2454544.1882 ± 0.0011
$e\cos\omega$		$-0.06624\,^{+0.00039}_{-0.00038}$
$e\sin\omega$		$0.370\,^{+0.011}_{-0.010}$
J		0.2685 ± 0.0048
$(R_{\rm pri}+R_{\rm sec})/a$		0.1064 ± 0.0016
$R_{\rm sec}/R_{\rm pri}$		0.4241 ± 0.0020
i	$^\circ$	$88.72\,^{+0.18}_{-0.16}$
$V_{\rm sys}$	($\mathrm{km\,s^{-1}}$)	13.15 ± 0.57
$K_{\rm pri}$	($\mathrm{km\,s^{-1}}$)	$14.64\,^{+0.75}_{-0.77}$

$\sim$3.3 days. By comparison, the two stars orbit in 3.1 days. As with EBs 0091 and 0942, the eclipse ratio is very low ($\sim$12%), making this an interesting system. The OOE variations in both light curves were modelled with the periodic squared exponential GP (as for EB2754, equation 5.1). The JKTEBOP model is a good fit to the detrended 2008 light curve and the residuals across the eclipses are small, being only slightly increased for primary and not visibly inflated for secondary.

5.4.4 EB 3334

EB 3334 is a 14.8 day, moderately eccentric system ($e = 0.13$) that shows some (limited) evidence for youth and cluster membership. The light curve, spectra, and radial velocity plots are shown in Figure 5.7 and the corresponding parameter values are reported in Table 5.8. CoRoT only observed EB 3334 in 2008: the light curve is relatively flat, displaying some low-level variations and a long-term trend, and is quite noisy due to the system's faintness ($R = 16.1$). Given the orbital period, only one primary and two secondary eclipses were captured; the relative eclipse depths are 13 and 7.5% for the primary and secondary, respectively (eclipse ratio $\sim$58%). The OOE flux variations were removed by dividing the full light curve by a squared exponential GP model fit to the OOE data.The JKTEBOP model is a good fit to the detrended light curve and the residuals across the eclipses are not obviously increased with respect to the OOE data.

14 ISIS spectra were obtained, which give the strongest CCF contrast with a 6000 K

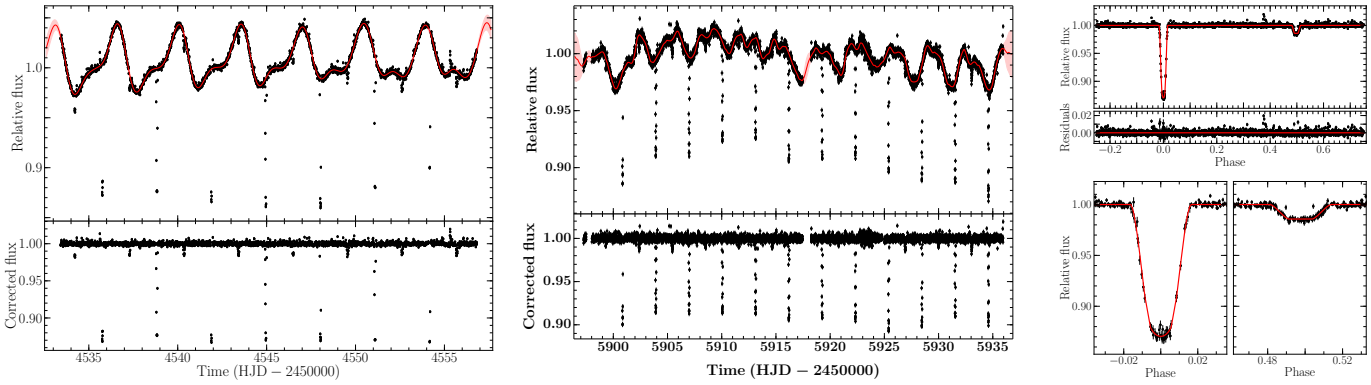

Figure 5.6: Light curves and JKTEBOP fit for EB 1625. As for the top row in Figure 5.1 except that the out-of-eclipse GP model comprises a periodic squared exponential plus a non-periodic squared exponential term for the 2008 and 2011/2012 light curves (*left and middle*).

Table 5.7: Parameter values and uncertainties for EB 1625

Parameter	Unit	Value
P	(days)	$3.06763381\,^{+0.00000081}_{-0.00000080}$
$T_{\rm prim}$	(HJD)	$2454535.75939 \pm 0.00033$
$e\cos\omega$		-0.00381 ± 0.00040
$e\sin\omega$		$-0.001\,^{+0.015}_{-0.016}$
J		$0.1040\,^{+0.0029}_{-0.0030}$
$(R_{\rm pri}+R_{\rm sec})/a$		$0.1081\,^{+0.0028}_{-0.0027}$
$R_{\rm sec}/R_{\rm pri}$		$0.3418\,^{+0.0025}_{-0.0024}$
i	$^\circ$	87.94 ± 0.23

template. Surprisingly, given the light curve parameters, cross-correlation yields only a single stellar peak (the primary). The RV variations for the primary refine the orbital period and confirm the eccentricity observed in the light curve. The systemic velocity is 13.0 ± 0.6 km s^{-1}, which is $\sim$2.5σ below the cluster value of 22 ± 3.5 km s^{-1} found by Fűrész et al. (2006). However, given that the RV distribution of cluster members is significantly non-Gaussian, and contains systems with recessional velocities comparable to EB 3334, we do not consider this significant. The lack of a second stellar peak could be due to the secondary being a rapid rotator. Further analysis is planned for this system consisting of modelling the spectra directly, as discussed in section 5.6.

Finally, we address the evidence for and against cluster membership. Recently obtained Keck/HIRES spectra display weak Li 6708 Å absorption, indicative of youth and therefore cluster membership. However, the faintness of the system and the estimated temperature

of the primary star, tentatively suggest EB 3334 lies further away than the cluster. As for CoRoT 223992193, we determine the distance using theoretical bolometric corrections of Bessell et al. (1998) in the V and K bands. As we do not know the radii of the two stars, we estimate lower limits using the theoretical predictions of Siess et al. (2000) for the ZAMS[6]. EB 3334 has V and K magnitudes of 17.1 and 12.4, which correspond to distances of $\gtrsim$3500 pc and $\gtrsim$1000 pc, respectively. As discussed for CoRoT 223992193, we take the K band as more reliable as it is less sensitive to reddening. Nonetheless, this lower limit is still at the higher end of distance estimates to the cluster. As a rudimentary proof of concept, the two K band distances for EB 1781 using its derived radii and ZAMS theoretical predictions (both using temperatures of $T = 6000$ K for the two stars, as estimated from spectra) are ∼1700–1800 pc and ∼1800–1900 pc, respectively. We note, however, that if EB 3334 is a cluster member, local extinction could redress the tentative distance discrepency.

5.4.5 Note on extreme-mass ratio PMS EBs

None of the PMS systems reported in the literature display extreme-brightness ratios, and yet half of our strong candidate PMS EBs do. It is not clear whether this is because: a) extreme-brightness ratio systems are difficult to solve and so none have been reported to date; b) previous studies, which have exclusively relied on ground-based photometry, lack the precision required to reliably detect and characterise such shallow secondary eclipses; or c) the formation and survival of such systems is a strong function of environment, and NGC 2264 is more favourable than other clusters.

Ideally, we would compare the density of NGC 2264 to other well-studied clusters, such as the ONC (which is the main source of low-mass PMS EBs in the literature). However, as these are morphologically complex associations, it is not a simple case of comparing average densities as incomplete membership and defining exactly what regions to include in such a comparison will effect the conclusions. The *Kepler*/K2 mission, which is observing a number of star forming regions and open clusters throughout the PMS phase of evolution (for ∼80 days each), should shed light on this matter. At this stage, a more detailed

[6]The ZAMS is defined as the time, after deuterium burning, when the nuclear luminosity provides at least 99% of the total stellar luminosity, i.e. when $L_{\rm nucl} \geqslant 0.99 L_{\star}$.

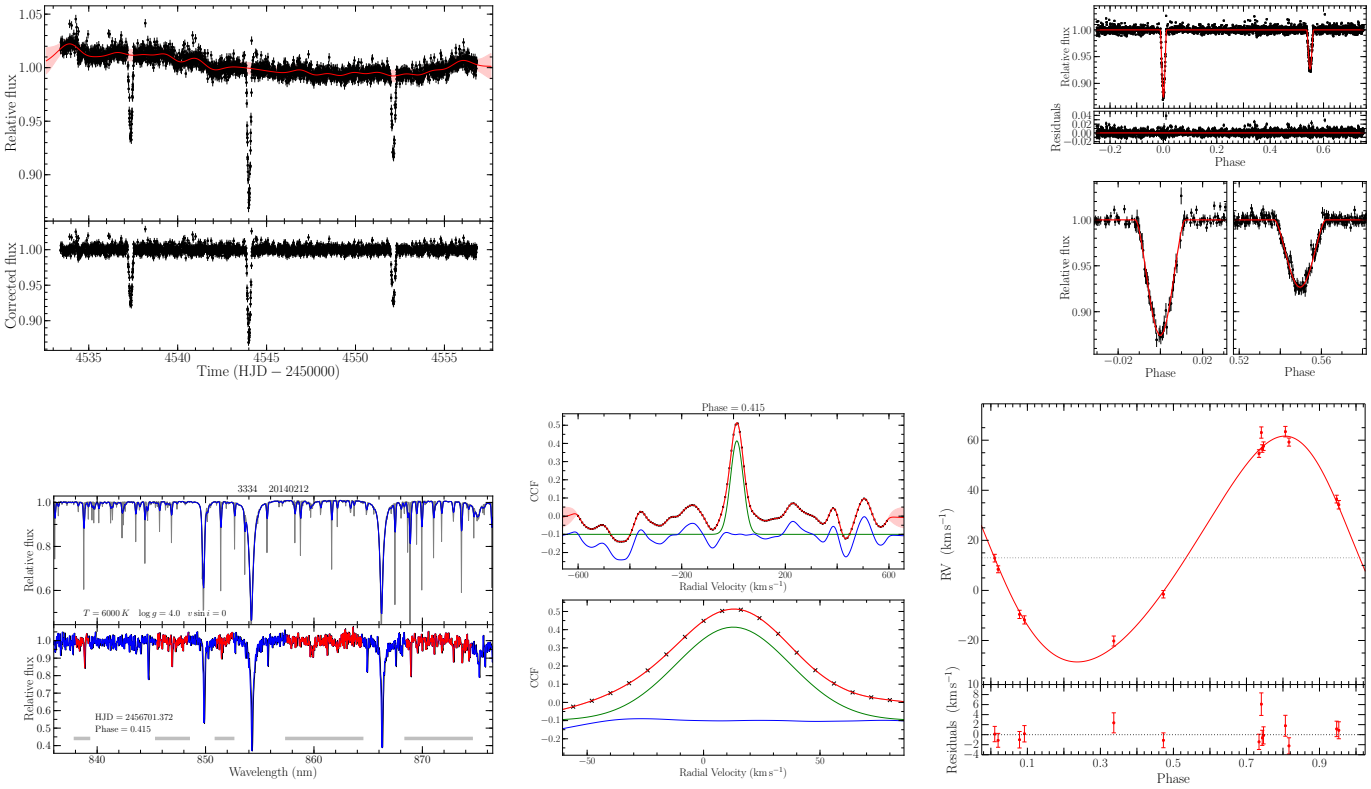

Figure 5.7: Light curves, spectra, CCFs and radial velocity orbit of EB 3334. As for Figure 5.1 except that the out-of-eclipse GP model comprises a periodic squared exponential plus a non-periodic squared exponential term for the 2008 and 2011/2012 light curves (*top left and top middle*). Note that the spectra (*bottom left*) were also obtained on 9$^{\rm th}$ February 2014 and cross-correlated with a MARCS template of $T = 4000$ K, $\log g = 4.0$ and $v \sin i = 0.0$ km s^{-1}. Only the primary star variations were extracted from the spectra (*bottom middle*) yielding a single stellar orbit (*bottom right*).

comparison between the environments of different clusters would be advisable. Another interesting point to note is that all the PMS candidates are significantly eccentric, which could be evidence of dynamical interaction with a third body.

5.5 Remainder of the sample

We now briefly discuss the remainder of the sample, detailing their photometric and spectroscopic properties and reasons for not pursuing each system further. All figures and tables for these systems are presented in Appendix A. For most of these EBs, only a preliminary analysis has been done, consisting of removing the OOE variability with cubic splines rather than GPs, performing a maximum-likelihood fit to the detrended light curves with JKTEBOP (rather than a Monte Carlo analysis), and determining CCFs from the full observed spectrum, rather than selected regions. EBs possessing this level of analysis

Table 5.8: Parameter values and uncertainties for EB 3334

Parameter	Unit	Value
P	(days)	$14.77550294\,^{+0.00000020}_{-0.00000019}$
$T_{\rm prim}$	(HJD)	2454544.0117 ± 0.0017
$e\cos\omega$		$0.07760\,^{+0.00045}_{-0.00066}$
$e\sin\omega$		$0.1081\,^{+0.0019}_{-0.0011}$
J		$1.03\,^{+0.58}_{-0.36}$
$(R_{\rm pri}+R_{\rm sec})/a$		$0.1015\,^{+0.0038}_{-0.0093}$
$R_{\rm sec}/R_{\rm pri}$		$0.56\,^{+0.20}_{-0.15}$
i	$^\circ$	$86.20\,^{+0.79}_{-0.24}$
$V_{\rm sys}$	(km s^{-1})	$13.03\,^{+0.56}_{-0.61}$
$K_{\rm pri}$	(km s^{-1})	$45.11\,^{+0.76}_{-0.70}$

typically do not have well-characterised radial velocity orbits. There are four exceptions: the first three are EBs 0254, 0360 and 0393, for which spectra were obtained by M. Lendl with the CORALIE spectrograph on the 1.2m Leonhard Euler Telescope at La Silla, Chile; these are discussed first. The fourth, EB 1340, received significant RV follow-up but was found to be a blend consisting of a cluster member and a background EB.

EB 0254 (section A.1) is a 14.1 day, circular EB, which displays negligible OOE variability in the light curve and relatively deep, near-equal eclipse depths. 14 spectra were obtained with the CORALIE spectrograph on the 1.2m Leonhard Euler Telescope at La Silla, Chile, and radial velocities extracted for the secondary star by M. Lendl. The primary's orbit was not extracted due to its early spectral type: cross-correlation and RV extraction was performed with the Geneva pipeline (e.g. Lendl et al., 2014), and only spectral templates extending as early as G2 were used. The systemic velocity of this system appears to be $\sim$20 km s^{-1}, consistent with the cluster. Extracting the primary orbit and deriving masses and radii is planned for future analysis by other members of the collaboration.

EB 0360 (section A.2) is a 3.8 day, circular EB, which displays spot-modulated OOE variability and shallow eclipse depths (8.5 and 3.5% for the primary and secondary). 16 spectra were obtained with Euler/CORALIE by M. Lendl, revealing the system to be triple lined. Relatively clean RVs for all stars were extracted (with a few exceptions; c.f. secondary RVs at phases $\sim$0.25). The velocity of the tertiary component is compatible

with the cluster ($\sim$20 km s^{-1}) but the systemic velocity of the binary appears slightly lower ($\sim$10 km s^{-1}) yet could still be a cluster member if the system is a hierarchical triple. Detailed modelling of the orbits, deriving masses and radii, and determining whether the system is a hierarchical triple, is planned for future analysis by other members of the collaboration. Both EBs 0254 and 0360 could potentially be cluster members but likely lower-mass systems were prioritised in this work.

EB 0393 (section A.3) is an 7.7 day, low-eccentricity EB, which displays γ-Dor pulsations with a period $\sim$1/4 $P_{\rm orbit}$ and shallow eclipse depths (9 and 5% for the primary and secondary). 14 spectra were obtained with Euler/CORALIE by M. Lendl, and RVs extracted for both stars. The systemic velocity is ~ -10 km s^{-1}, which is not compatible with the cluster. Detailed modelling of the orbits, and deriving masses and radii, and analysing the pulsations is planned for future analysis by other members of the collaboration.

EB 0445 (section A.4) is an 1.5 day, circular EB with low-amplitude OOE variations possibly arising from ellipsoidal deformation, and flat bottomed eclipses with depths of 19 and 3% for the primary and secondary. One IDS and two ISIS spectra were obtained showing the primary to be a hot star ($T \gtrsim 8000$ K) which, given the apparent magnitudes of the system (see Table 5.2), suggest this is a background object ($d \gtrsim 1600$ pc).

EB 0824 (section A.5) is a 3.9 day eccentric EB ($e \sim 0.47$), which displays a flat light curve containing deep 41 and 33% eclipses. One IDS and six ISIS spectra were obtained showing the primary to be a hot star ($T \gtrsim 8000$ K), which strongly suggest this is a background object ($d \gtrsim 1600$ pc). 21 VLT/FLAMES spectra also exist for this object. Given the system's eccentricity, it is an interesting object despite being a field EB, and it warrants future analysis.

EB 1021 (section A.6) is an 0.5 day, contact EB with eclipse depths of 23 and 13%. Two ISIS spectra were obtained showing the primary to be a hot star ($T \sim 7500$ K) and therefore implying this is a background object ($d \gtrsim 1500$ pc).

EB 1113 (section A.7) is a long period EB ($P \geqslant 22$ days) with eclipse depths of 30 and

22%. This system was only observed for 23 days in 2008 and hence the period remains unknown. One ISIS spectrum was obtained, which was single lined. Given the unknown period, single-lined spectrum, and lack of obvious signs of youth in the OOE light curve or activity in the Ca II triplet, this system was not observed further.

EB 1340 (section A.8) is a 1.3 day EB with shallow eclipses (6 and 4% deep for the primary and secondary). Based on its light curve variability and position in CMDs, EB 1340 was a high priority target for spectroscopic follow-up. 10 ISIS spectra were obtained, which were single-lined and whose CCF peak did not vary significantly over the orbital phase. Given the shallow eclipse depths and lack of spectroscopic variations, this system is probably a blend with the eclipsing component being a background object and the foreground single star being a cluster member (based on signs of youth in the spectra, e.g. Hα emission and activity in the Ca II triplet).

EB 1408 (section A.9) is a 3.6 day, circular EB, which displays a flat light curve and eclipse depths of 19 and 4%. Two ISIS spectra were obtained showing the primary to be a hot star ($T \gtrsim 8000$ K) and therefore implying this is a background object ($d \gtrsim 2000$ pc).

EB 1572 (section A.10) is a 2.9 day, circular EB, which displays a flat light curve and eclipse depths of 7.5 and 6%. Six ISIS spectra were obtained, which were single-lined and whose CCF peak did not vary significantly over the orbital phase (what variations are present could be attributed to varying peak shapes rather than orbital modulation). Given the shallow eclipse depths and lack of significant spectroscopic variations, this system could be a blend with the eclipsing component being a background object.

EB 1632 (section A.11) is a 6.6 day, circular EB, which displays a flat light curve and eclipse depths of 26 and 13%. One IDS and two ISIS spectra were obtained showing the primary to be a hot star ($T \gtrsim 8000$ K), which suggest this is a background object ($d \gtrsim 1700$ pc).

EB 2103 (section A.12) is a 7.4 day, circular EB, which displays a flat light curve (the variations in 2011/2012 light curve are probably systematics) and eclipse depths of 6 and

3%. Two ISIS spectra were obtained showing the primary to be a hot star ($T \gtrsim 8000$ K), which suggest this is a distant background object ($d \gtrsim 3500$ pc).

EB 2677 (section A.13) is a 2.8 day, circular EB, which displays a flat light curve (the variations in 2011/2012 light curve are probably systematics) and eclipse depths of 20 and 18%. Two IDS and two ISIS spectra were obtained showing the system to comprise at least one hot star ($T \gtrsim 8000$ K), which suggest this is a distant background object ($d \gtrsim 2700$ pc).

EB 3190 (section A.14) is an 0.9 day, near-contact EB with eclipse depths of 20 and 19%. Two ISIS spectra were obtained, which were best matched with a temperature of $T = 6500$ K; the resulting CCFs did not display large variations but showed some evidence for blended, double peaks. We attempted to model the CCFs both with one and two Gaussians, neither of which gave convincing fits. We show a CCF modelled with a double Gaussian but only show the resulting RVs for the primary, which are both of order $\sim$45 $\mathrm{km\,s^{-1}}$ (phases of $\sim$0.2 and 0.65), not consistent with the cluster. We do not report the RV semi-amplitudes or systemic velocity due to the ambiguous CCF peak shapes. Given the faintness of the system, the temperature of the spectra suggests a background object ($d \gtrsim 2600$ pc).

EB 3602 (section A.15) is a 3.8 day, circular EB, which displays a flat light curve (the apparent variations are likely systematics) and flat-bottomed eclipses that are 12 and 9% deep. Six ISIS spectra were obtained, which were best matched with a temperature of $T = 6500$ K; the resulting CCFs did not obviously show double peaks, although the one visible peak did show modulations consistent with the expected orbit for the primary. Given the faintness of the system, this spectroscopic temperature suggests a background object ($d \gtrsim 2000$ pc).

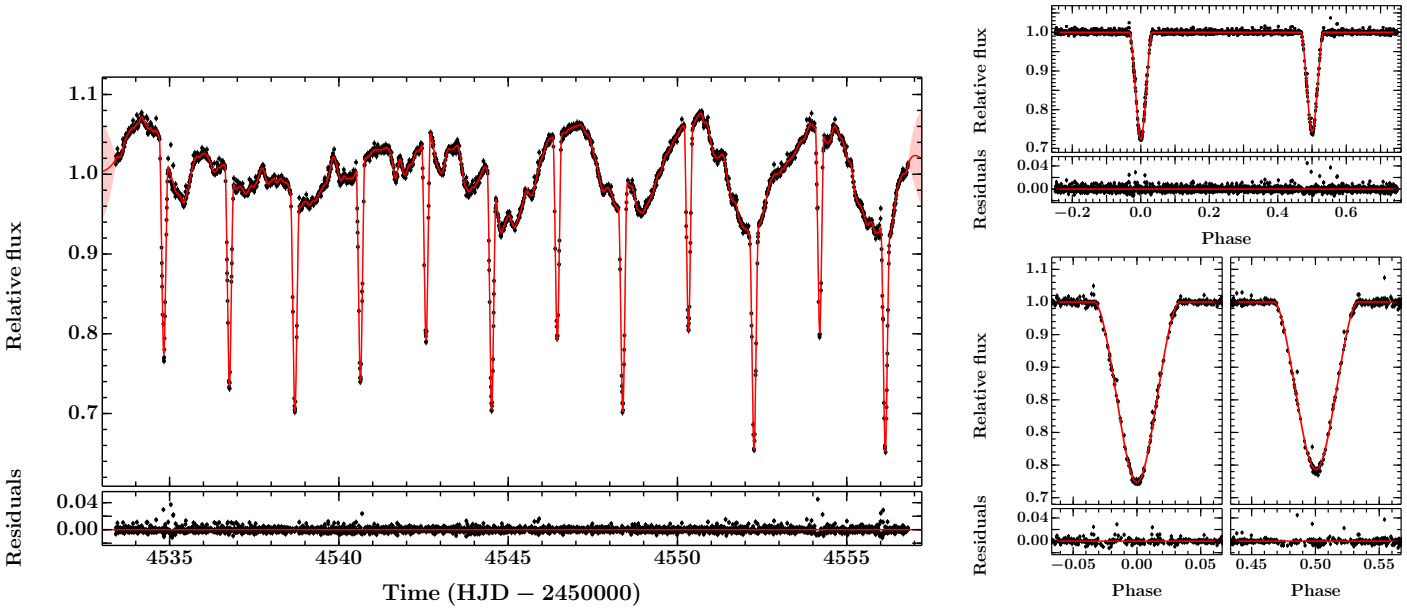

Figure 5.8: *Left*: 2008 CoRoT light curve of CoRoT 223992193 (black points) with the mean and 95% confidence interval of the predictive distribution of the eclipse + Gaussian Process model used to fit the light curve (red and pink shaded region, respectively). *Right*: phase-folded light curve with the OOE variations removed (subtracted off) and the eclipse model shown in red. Note the lack of increased scatter across the eclipses as compared to Figure 3.5.

5.6 Improving the analysis: joint MCMC modelling of light curves and spectra

As discussed, the analyses presented thus far suffered from the 1D nature of the cross-correlation performed to determine radial velocities. In addition, the precision of the light curve solutions will have been limited by our ability to precisely predict the effect of the OOE variations on each each eclipse (c.f. the increased scatter in the residuals across eclipses in many systems). We seek to address these shortcomings in this section by first presenting a slight improvement to the light curve modelling in section 5.6.1 and then presenting a new method for determining RVs directly from the observed spectra in section 5.6.2. The methods presented are a work in progress and have yet to be applied to the sample.

5.6.1 Light curves: modelling the out-of-eclipse and eclipse data simultaneously

In the light curve analyses presented thus far, the OOE data has been modelled and removed, and the eclipses subsequently fit. However, such a process is reliant on the

robustness of the initial detrending in much the same way as standard Monte Carlo methods are reliant on the goodness of fit of the initial model. Gaussian processes provide a means of interpolating across eclipses based on the covariance properties of the entire light curve but will predict the simplest model possible across each eclipse, as should be the case given the lack of data (we mask the regions containing eclipses when modelling the OOE variability). This means we lose some information contained within the light curve, namely the form of the variations across each eclipse. An alternative approach is to model the OOE data at the same time as fitting the eclipses, which has the added benefit of using all the light curve data at each stage of the modelling. We note, however, that any differential effects across an eclipse, such as from spots on the background star being tracked by the foreground star will not necessarily be accounted for in a principled way, but they will be incorporated in as far as the flexibility of the chosen GP kernel allows.

We model the light curve as the sum of an eclipsing binary model and a Gaussian process model. We use the basic EBOP model presented in Irwin et al. (2011), which is a modified version of the subroutine "light" in JKTEBOP. As with JKTEBOP this model uses spheres for the eclipse shapes and biaxial spheroids for reflection and ellipsoidal effects. It uses the analytic method of Mandel & Agol (2002) for the quadratic limb darkening law. Performing regression with GPs requires an inversion of the covariance matrix as well as the evaluation of its determinant, which typically scale poorly with the number of data points ($\mathcal{O}(n^3)$). Therefore, when detrending the light curves previously we subsampled the OOE data for computational tractability. However, we do not want to subsample the eclipses as each data point is valuable. We tested the effect of subsampling the OOE data and not the eclipse data, but found that the GP model has difficulty reconciling the different noise levels in the two subsets; therefore, we do not subsample the light curve data. Given the number of data points (3936 and 6528 for the 2008 and 2011/2012 CoRoT light curves, respectively) this would require a prohibitive amount of computing time using traditional Cholesky decomposition for the matrix inversion. Instead, we use `george`[7], a GP library where the covariance matrix is hierarchically factored it into a product of block low-rank

[7] http://dan.iel.fm/george

updates of the identity matrix, which gives an $\mathcal{O}(n \log^2 n)$ inversion (Ambikasaran et al., 2014). We apply our light curve model using the Affine Invariant Markov chain Monte Carlo (MCMC) method as implemented in `emcee` (Foreman-Mackey et al., 2013). The parameters of the fit are the those for the eclipses (P, $T_{\rm prim}$, $(R_{\rm pri} + R_{\rm sec})/a$, $R_{\rm sec}/R_{\rm pri}$, J, $\cos i$, $e\cos\omega$, $e\sin\omega$, and the quadratic limb darkening parameters for both stars: $u_{\rm pri}$, $u'_{\rm pri}$, $u_{\rm sec}$ and $u'_{\rm sec}$) and the GP hyperparameters (chosen to match the covariance properties of the OOE light curve). All the parameters of the fit are allowed to vary freely, except for the limb darkening parameters which are constrained with a Gaussian prior whose mean is set to the quadratic limb darkening estimates of Claret et al. (2012, 2013) for the estimated stellar temperatures and whose standard deviation is derived from a plausible range of temperatures (nominally ±200–500 K). In practice, we do not expect the limb darkening parameters to affect the fit significantly, as we showed in Chapter 3.

We show this model applied to the 2008 light curve of CoRoT 223992193 in Figure 5.8. We use the same OOE model (a Matérn-3/2 kernel) and initial guesses for all parameters as in Chapter 3 to allow for direct comparison. The left hand plot shows the full light curve with our GP + eclipse model in red, with the residuals directly below indicating a good fit to the data. The right hand plot shows the phase-folded light curve with the OOE model subtracted off and our eclipse model in red. The parameters of the fit are reported in Table 5.9 and are very similar to those presented in Chapter 3 for the eclipse parameters but we find a shorter characteristic timescale for the OOE variations, presumably due to modelling the all the data rather than subsampling.

5.6.2 Spectra: modelling the data directly

As we have seen, 1D cross-correlation is not well suited to systems with low brightness ratios and it is unable to extract precise RVs close to eclipses when the two stellar peaks are blended. These issues are well known and motivated the development of other techniques such as TODCOR (TwO-Dimensional CORrelation; Zucker & Mazeh 1994), which is able to overcome the shortcomings of the single dimension. TODCOR has been developed over the last two decades in a series of papers that have incrementally incorporated the ability

Table 5.9: Parameters of the EB model applied to the full light curve of CoRoT 223992193. Presented are the eclipse parameters and GP hyperparameters.

Parameter	Symbol	Unit	Value
	Eclipse parameters		
Central surface brightness ratio	J		$0.837\,^{+0.066}_{-0.060}$
Sum of radii	$(R_{\rm pri} + R_{\rm sec})/a$		0.2213 ± 0.0020
Radius ratio	$R_{\rm sec}/R_{\rm pri}$		$0.816\,^{+0.044}_{-0.042}$
Orbital inclination	i	(°)	$85.18\,^{+0.15}_{-0.13}$
Orbital period	P	(days)	3.87463 ± 0.00016
Time of primary eclipse centre	$T_{\rm prim}$	(HJD)	$2454536.76329 \pm 0.00053$
	$e\cos\omega$		0.00055 ± 0.00022
	$e\sin\omega$		-0.0017 ± 0.0010
eccentricity	e		0.0172 ± 0.0097
omega	ω	(°)	$271.85\,^{+2.7}_{-0.92}$
Linear LD coefficient for primary	$u_{\rm pri}$		0.70 ± 0.10
Non-linear LD coefficient for primary	$u'_{\rm pri}$		0.12 ± 0.10
Linear LD coefficient for secondary	$u_{\rm sec}$		0.46 ± 0.13
Non-linear LD coefficient for secondary	$u'_{\rm sec}$		0.18 ± 0.11
	OOE variability parameters		
Amplitude	A	(%)	$0.0370\,^{+0.0049}_{-0.0038}$
Timescale	l	(days)	$0.206\,^{+0.045}_{-0.033}$
White noise	σ	(mmag)	$0.003953\,^{+0.000064}_{-0.000062}$

* LD = limb darkening

to model triple and quadruple systems, and multi-order échelle spectra (Mazeh et al., 1995; Zucker et al., 1995, 2003; Torres et al., 2007). However, several studies imply that residual systematics may be present in the TODCOR RVs and efforts have been made to estimate the effect of these (e.g. Torres et al., 2009; Zucker, 2012). In addition, TODCOR still does not provide a principled way to extract robust uncertainties on the RVs. One could model the 2D CCF as the sum of two Gaussians with a GP noise term in much the same way as we did in the 1D case, but this would be computationally expensive as GPs do not scale well with the number of input dimensions. Furthermore, as CCFs are simply maximum likelihood representations of the data, they do not capture the full range of parameters able to adequately explain the data, and no amount of subsequent modelling can recover this information.

An alternative to the cross-correlation approach is the spectral deconvolution method,

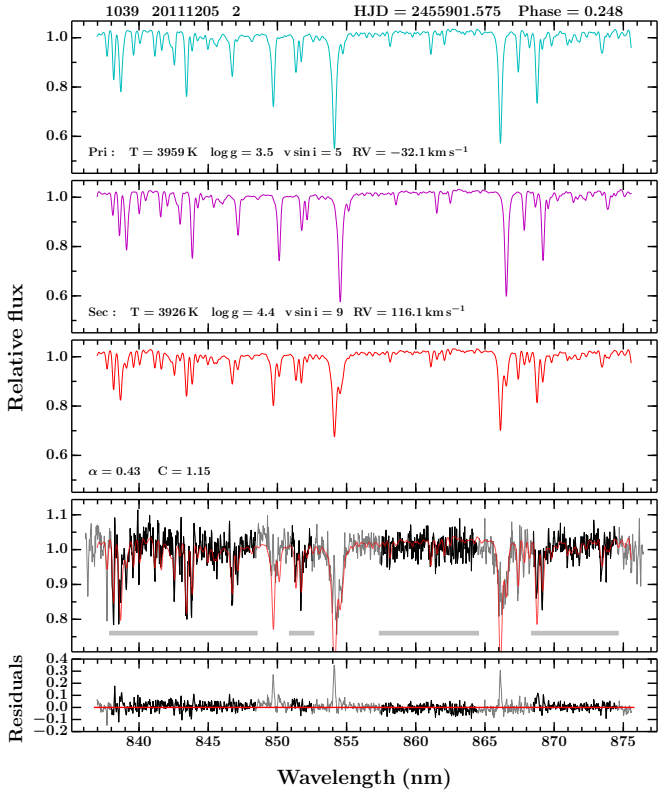

Figure 5.9: The top two panels show the model spectra for the primary and secondary stars shifted by their respective RVs (cyan and magenta), and the third panel shows their joint spectrum (red). The fourth panel shows the observed data in grey with the selected regions used in the fitting shown in black, and the model spectrum in red. The regions used in the fit are the same as those for cross-correlation; they simply mask the Ca II triplet because it is broad and displays activity not captured in the model. The residuals of the fit are shown in the bottom panel.

which analyses the spectra directly (Donati et al., 1997). This method assumes the observed spectra are the sum of two varying components, and reconstructs each component spectrum from the relative displacement of spectral lines from one spectrum to the next. While very powerful, it requires high S/N spectra and a relatively complete phase coverage, i.e. it is not suitable for analysis based on a small number of spectra with $S/N \sim 30$.

An alternative to the cross-correlation and spectral disentangling approaches is to model the spectra directly with either observed or model templates. This has a number of benefits: it yields robust uncertainties on the RVs, and also for the temperatures, surface gravities and $v \sin i$s of the two stars, as well as their light ratio in the spectroscopic band[8]. In addition, regions of the spectra can be selected without impunity as "edge effects", which can introduce correlated noise into CCFs, do not have any effect on modelling the

[8]Note, the $v \sin i$s are only retrievable if they are larger than the resolution of the spectrograph.

spectra directly.[9] However, despite significant benefits it is computationally expensive. With very high S/N spectra and a perfect template, CCFs and modelling the spectra directly will give the same results. In practice, however, this is rarely the case and so we investigated the potential for modelling the spectra directly.

Each observed spectrum is modelled as the sum of two model spectra. The parameters of the fit are the temperature, surface gravity, $v \sin i$ and radial velocity of each star, as well as the light ratio between the two components, a multiplicative scale factor to enhance or mute spectral features in the model spectra, and a white noise term. All spectra are modelled simultaneously, which allows the temperatures, surface gravities and $v \sin i$s to be jointly fit for, along with the light ratio in each band. We use PHOENIX model spectra (Husser et al., 2013) as these spectra incorporate Li and an improved prescription for Ti O, which provide a better fit to the FLAMES spectra than the MARCS models.

Figure 5.9 shows an example ISIS spectrum of CoRoT 223992193 fit with this model. The top two panels show the model spectra for the primary and secondary stars shifted by their respective RVs (cyan and magenta), and the third panel shows their joint spectrum (red). The fourth panel shows the model spectrum (red) fit to the observed data (full spectrum in grey and the selected regions used in the fitting in black). The regions used in the fit are chosen to mask the Ca II triplet but include as much of the remaining spectrum as possible. The residuals of the fit are shown in the bottom panel. We can see from the residuals that some absorption lines in the model do not have the correct strength, i.e. the residuals do not look like pure white noise. An option for future work could be to include a GP with which to down-weight regions of the spectra that are not well described by the model due to incomplete line lists or abundance ratios (e.g. Czekala et al., 2014). This is important to ensure convergence on the 'correct' region of parameter space.

5.6.3 The final model: joint light curve and spectra analyses

In future, the light curve and spectra models will be joined into a single comprehensive model. This will allow the RVs of the two stars to be predicted from the orbital parameters

[9] However, while edge effects can be troublesome for transiting planets, they tend not to be an issue for EBs given the typical magnitude of the RV variations.

rather than explicitly fitting for them in the spectra model. With parameter distributions derived from all data simultaneously, this work promises to yield robust uncertainties on the stellar fundamental parameters and hence provide reliable constraints for stellar evolution models when applied to the whole PMS sample. While these methods have not yet been applied to the whole sample, the light curve model is applied to a visual multiple system in Chapter 6.

5.7 Conclusions and further work

The techniques developed for characterising CoRoT 223992193 were applied to the EB sample. These techniques work well for near equal-mass systems and two main sequence EBs were solved. However, primarily due to the one-dimensional nature of the radial velocity determination, the majority of the sample remains unsolved. Four low-mass EBs show evidence for youth, with three of these displaying low-to-extreme brightness (and hence mass) ratios. Interestingly, no such PMS systems have been reported in the literature. This could be due to a number of factors, including their difficulty to solve, the photometric precision of previous studies, or a more favourable environment in NGC 2264 for the survival of close, low-mass-ratio binaries. *Kepler*/K2 should shed light on this matter over the next few years.

As the applied methods were not able to solve some of the PMS candidate EBs, alternative methods were developed. For the light curve analysis, a slight improvement can be made by modelling the OOE variability simultaneously with the eclipses to provide a more robust treatment for the OOE variations across eclipses. For the RV determination, a new method was presented based on direct modelling of the spectra rather than on cross-correlation. While promising, these new methods have not yet been applied to the sample but will be in future work. They are, however, applied to components of a visual multiple system in Chapter 6.

Chapter 6

A visual multiple containing three eclipsing binaries spanning B – M spectral types

In this chapter we present a visual multiple in the NGC 2264 star forming region, STF 951, which comprises three high-mass sources. One of these objects is a previously known eclipsing binary and we report the discovery of eclipses on another component from the 2008 CoRoT observations. In 2011/2012, Spitzer detected eclipses on an M3 star lying between the two eclipsing components of STF 951. That three nearest neighbour stars all display eclipses pointed towards the possibility that they could be members of the same multiple (formed from a single parent molecular cloud) and, given that one component is a likely cluster member, that all are members of NGC 2264; this motivated a detailed characterisation.

We begin with a brief overview of STF 951, before discussing the CoRoT observations, where we focus on the aperture placement and resulting light curves as evidence for which systems are responsible for the eclipses. We then present our analysis of the new eclipsing system detected by CoRoT, using the 2008 CoRoT light curve and VLT/FLAMES spectra. We find that the observations require similar radii for the two stars but also an extreme brightness ratio. We propose two scenarios: an evolved system containing a small, hot subdwarf primary or a young system containing a large, cool PMS secondary. The spectra and spectral energy distribution (SED) cannot conclusively differentiate between these two scenarios. Finally, we discuss the Spitzer-detected EB, detailing our analysis of the 3.6 and

4.5 μm light curves (follow-up spectroscopy is currently being obtained) and preliminary analysis on the system's SED.

Two of the three eclipsing binaries show strong evidence for youth (as well as evidence for cluster membership). With the current data, the third EB is slightly harder to characterise. However, given its location along the line-of-sight to NGC 2264, close proximity to two other young EBs, and plausible scenario for youth, we tentatively favour the hypothesis of a young system rather than an evolved object. If correct, and all three systems are associated, this would be the first triply-eclipsing multiple system discovered, and would offer an important test-bed for models of star formation and stellar evolution in cluster environments.

6.1 Components of the visual multiple

Approximately 8 arcminutes to the southwest of S Mon, in the heart of the NGC 2264 reflection nebula, lies a visual multiple system, designated STF 951. The components of STF 951 reported in the literature are V684 Mon (a well-known B5V-B5V eclipsing binary), NGC 2264 67 (a B2 star) and V780 Mon (reportedly an A0 star) (Walker, 1956; Koch et al., 1986; Pribulla et al., 2010; Zasche, 2012). All three systems display X-ray emission (Sung et al., 2008) and extensive studies of V684 Mon strongly suggest youth and cluster membership (e.g. Bradstreet et al., 2007).

The left panel of Fig. 6.1 shows *ugri* CFHT images of the region containing STF 951 (top left, top right, bottom left and bottom right, respectively; the CFHT observations are detailed in section 2.3). The u, g and r band images are plotted in linear brightness and show V684 Mon, which is the brightest source lying to the south east, NGC 2264 67, the next brightest to the north and V780 Mon, the faintest of the three and the easternmost. Radial and contour plots of V780 Mon in each band reveal the source to be a tight visual binary with components aligned roughly northwest to southeast. The i band image is shown in the natural logarithm of the brightness to draw out the fainter sources, Mon-1411 and Mon-7898 (both circled). Mon-1411 lies slightly to the southwest of the chord joining V684 and V780 Mon, and Mon-7898 lies roughly a quarter of the distance between NGC 2264 67

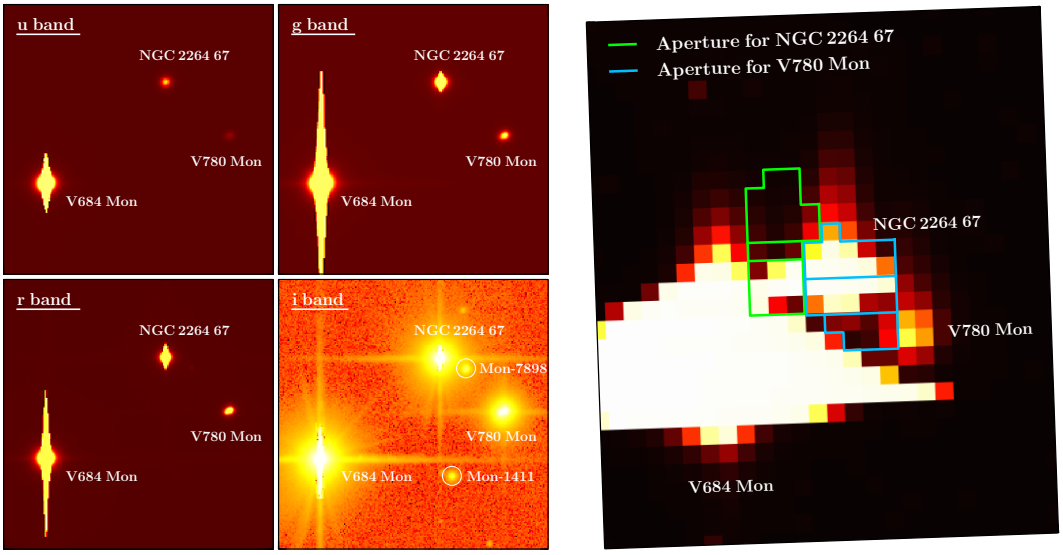

Figure 6.1: *Left:* Region of NGC 2264 hosting components of STF 951 as observed by CFHT in February 2011. The four subplots show SDSS u, g, r and i band images (top left, top right, bottom left and bottom right, respectively) orientated with North up and East left. The u, g and r band images are plotted on a linear brightness scale and the i band image in the natural logarithm of the brightness to bring out the fainter sources, Mon-1411 and Mon-7898, both of which are circled.

Right: CoRoT image showing a similar region to the CFHT images, rotated to have the same orientation, and showing V684 Mon, NGC 2264 67 and V780 Mon. The CoRoT apertures for NGC 2264 67 and V780 Mon are shown in light green and sky blue, respectively; both are misplaced with respect to their target stars. White light observed by CoRoT is dispersed by a prism onto the CCD so that blue, green and red wavelengths from a given source fall onto adjacent pixels. The CoRoT aperture is correspondingly split into blue, green and red sections (top, middle and bottom, respectively, for both apertures) which result in three colour light curves for a given source.

and V780 Mon. The optical and infrared magnitudes of V684 Mon, NGC 2264 67, V780 Mon and Mon-1411 are listed in Table 6.1[1].

6.2 CoRoT apertures and light curves

The 2008 CoRoT observations included NGC 2264 67 and V780 Mon (V684 Mon was not observed as it saturates the CoRoT detector, although MOST did observe it). The aperture placement for both NGC 2264 67 and V780 Mon was not accurate resulting in contaminated photometry. The right panel of Fig. 6.1 displays a similar region to the CFHT images adjacent (with the same orientation), and shows V684 Mon, NGC 2264 67 and V780 Mon. The CoRoT apertures for NGC 2264 67 and V780 Mon are shown in light green and sky blue, respectively; both of which are misplaced with respect to their target stars.

[1]The magnitudes for Mon-7898 are not listed as they are not relevant to the work presented in this chapter

Table 6.1: Coordinates and photometric properties of the components of the potential multiple. Note that the photometric uncertainties, where given, are formal measurement errors; they do not account for intrinsic variability in the systems.

	V864 Mon	NGC 2264 67	V780 Mon	Mon-1411	(refs.)
RA	06 40 38.36	06 40 37.27	06 40 36.66	06 40 37.17	
Dec	+09 47 16.10	+09 47 29.58	+09 47 22.31	+09 47 13.77	
U	7.71	11.119 ± 0.020			^{a} ^{b} – –
B	8.31	11.509 ± 0.024	13.226 ± 0.051		^{a} ^{c} ^{c} –
V	8.44	10.98 ± 0.04	12.528 ± 0.051	19.718 ± 0.005	^{a} ^{c} ^{c} ^{c}
R	8.475 ± 0.018	10.39 ± 0.04	11.825 ± 0.039	18.13 ± 0.06	^{c} ^{c} ^{c} ^{c}
I	8.518 ± 0.028	9.658 ± 0.02	10.992 ± 0.013	16.43 ± 0.06	^{c} ^{c} ^{c} ^{c}
J	8.635 ± 0.032	8.409 ± 0.030	9.647 ± 0.029	14.689 ± 0.038	^{d} ^{d} ^{d} ^{d}
H	8.623 ± 0.034	7.843 ± 0.040	9.001 ± 0.027	13.820 ± 0.051	^{d} ^{d} ^{d} ^{d}
K	8.696 ± 0.021	7.495 ± 0.021	8.593 ± 0.021	13.125 ± 0.054	^{d} ^{d} ^{d} ^{d}
[3.6]	8.785 ± 0.063	7.366 ± 0.019	8.362 ± 0.021	12.456 ± 0.033	^{e} ^{e} ^{e} ^{f}
[4.5]	8.736 ± 0.027	7.344 ± 0.020	8.404 ± 0.041	12.154 ± 0.034	^{e} ^{e} ^{e} ^{f}
[5.8]	8.725 ± 0.016	7.300 ± 0.013	8.263 ± 0.035	11.769 ± 0.099	^{e} ^{e} ^{e} ^{f}
[8.0]	8.805 ± 0.024	7.312 ± 0.017	8.222 ± 0.030	10.769 ± 0.184	^{e} ^{e} ^{e} ^{f}

^{a} Ducati 2002; ^{b} Sung et al. 1997; ^{c} Sung et al. 2008; ^{d} Cutri et al. 2003; ^{e} Sung et al. 2009; ^{f} Cody et al. 2014 (all in Vega magnitudes)

Prisms in front of CoRoT's Planet Finder CCDs disperse the observed 300–1000 nm broadband flux from each source onto the detector giving a small spectrum (Auvergne et al., 2009). Each CoRoT aperture consists of three individual apertures that extract the red, green and blue light separately. These three 'colour' light curves are combined onboard the spacecraft to produce 'white' light curves. For stars brighter than $R < 15$ the individual 'colour' light curves are downloaded along with the combined 'white' light curve; both NGC 2264 67 and V780 Mon satisfy this brightness criterion.

In the following two subsections we detail how the red, green and blue apertures, and resulting light curves, were used to determine whether a source displayed eclipses.

6.2.1 Colour light curves of NGC 2264 67

The right panel of Fig. 6.1 shows that both V684 Mon and NGC 2264 67 contribute light to the CoRoT aperture intended for the latter (light green). The light curves extracted from this aperture are shown in the left four panels of Fig. 6.2 (white, red, green and blue; top to bottom). Eclipses are visible in all colour channels with different depths, being

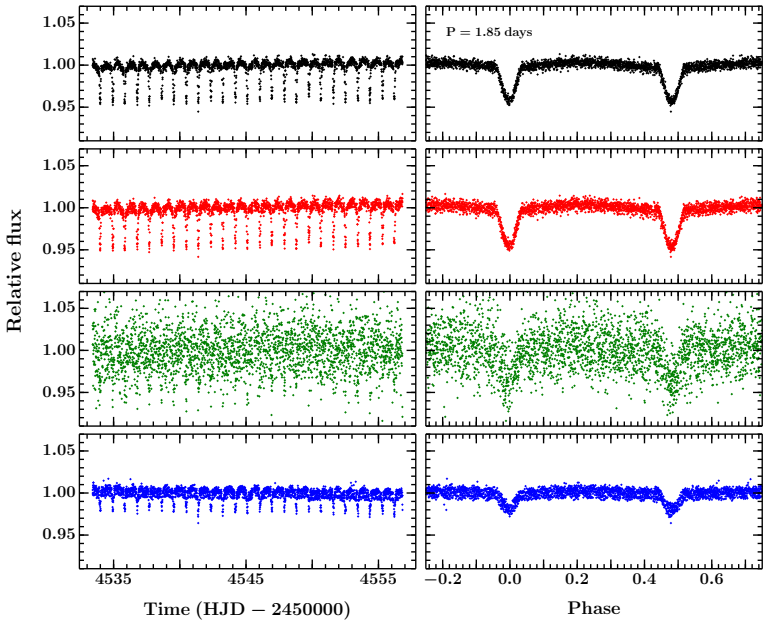

Figure 6.2: *Left:* the three colour light curves extracted from the aperture intended for NGC 2264 67 (red, green and blue; bottom three panels) along with the combined 'white' light curve (top). *Right*: light curves phase folded on the $P = 1.85$ day period of V684 Mon. Note that secondary eclipse corresponds to the more massive component being occulted (Bradstreet et al., 2007; Pribulla et al., 2010).

shallowest in blue. Preliminary modelling of the light curves with JKTEBOP (Southworth et al., 2004) yielded a period of 1.85 days; the right four panels show the light curves folded on this period. Both the period of 1.85 days and the light curve morphology are consistent with literature estimates for V684 Mon (Pribulla et al. 2010; Table 2 and Figure 2) and we therefore conclude that the eclipses are due to this system rather than NGC 2264 67. We note that although the CoRoT aperture is split into red, green and blue sections, all the apertures extract 'blue' light of V684 Mon because of the aperture mis-placement.

6.2.2 Colour light curves of V780 Mon

The CoRoT aperture extracted for V780 Mon (sky blue) predominately extracts light from NGC 2264 67. The three individual apertures extract, from top to bottom, blue, green and red light. The corresponding light curves are shown in the left four panels of Fig. 6.3 (white, red, green and blue; top to bottom). Both the blue and green channels, which almost exclusively contain light from NGC 2264 67, display flat light curves, which confirms our earlier determination that this system does not show eclipses. Eclipses are visible in

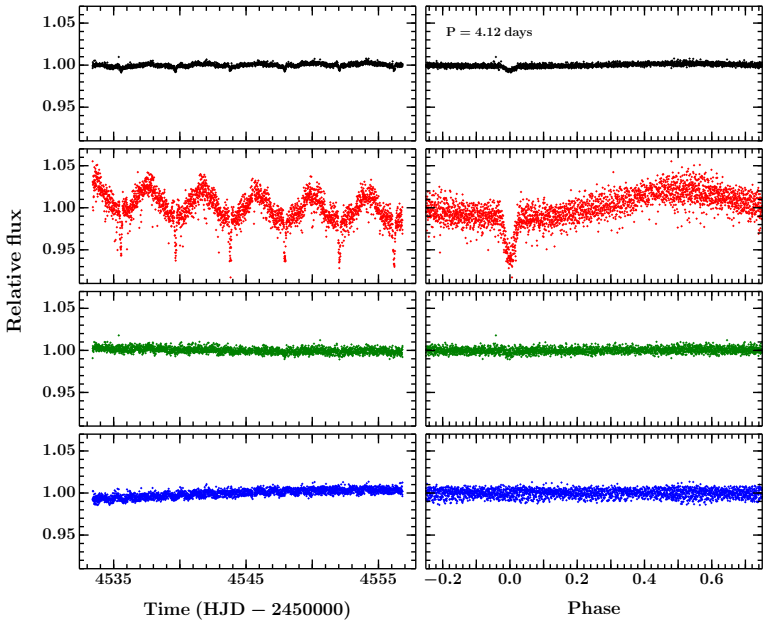

Figure 6.3: *Left:* the three colour light curves extracted from the aperture intended for V780 Mon (red, green and blue; bottom three panels) along with the combined 'white' light curve (top). *Right*: light curves phase folded on a period of 4.125 days, which corresponds to a scenario where only eclipses on one star are observed.

the red channel, however, which also captures light from V780 Mon (and perhaps also Mon-7898; see Fig. 6.1, i band). Preliminary modelling of the red channel light curve yielded a period of either 4.125 days (assuming we only see eclipses on one star) or 8.25 days (corresponding to an equal-brightness system).

Lamm et al. (2004) report a rotation period of 4.12 days for V780 Mon, which is consistent with the period of the out-of-eclipse modulation in the red channel. We therefore consider the eclipses to be on V780 Mon rather than Mon-7898 (no photometry was reported for this system in the Lamm et al. study). The CFHT images revealed V780 Mon to be a tight visual binary star; with the present data it is not possible to discern which component is responsible for the eclipses. In the right four panels of Fig. 6.3 we fold the light curves assuming the Lamm et al. (2004) period, i.e. only eclipses on one star are visible. We perform a more detailed analysis, with the inclusion of spectra, in section 6.3, and confirm this period.

6.3 Analysis of V780 Mon: photometry and spectroscopy

20 VLT/FLAMES spectra covering the wavelength range 644 – 682 nm, and spanning ∼2 months, show only two strong absorption lines (Hα and He I 667.8 nm; see Fig. 6.4). Initial analysis of the Hα and He I lines showed variations on a 4.12 day period confirming that the eclipses in the light curve are on one star only. The system is therefore either an extreme mass or brightness ratio system, or the orbit is eccentric (such that eclipses are only visible on one star).

In Fig. 6.4 the spectra are ordered in binary orbital phase (phase = 0/1 corresponds to primary eclipse) and the He I line variations can clearly be seen. Modelling the He I line as a single Gaussian traces out a clean orbit for the primary star. Attempts to model the He I line as the sum of two varying Gaussians and, given that the EB is part of a visual double system, as the sum of one varying and one stationary Gaussian (for the primary and tertiary, respectively) did not yield convincing orbits, unlike the single Gaussian model. Therefore, in the following analysis we model the light curve assuming the eclipses are on one star only (the primary) and the variations in the He I line arise from the motion of the primary around the EB centre of mass.

The full light curve (i.e. eclipses and out-of-eclipse variability) and the He I line in all spectra were simultaneously modelled using the Affine Invariant Markov chain Monte Carlo (MCMC) method as implemented in `emcee`, stepping through the parameter space 50 000 times with each of 300 'walkers'. The first 25 000 steps were discarded as 'burn in' and parameter values and uncertainties derived from the remainder. The parameters of the fit are those to explain the light curve (eclipses and OOE variability) and the He I line variations in the spectra. The He I lines in all spectra are modelled with Gaussians, whose RVs are predicted from the model parameters, and which share a common width but have individual amplitudes[2]. We apply two types of model to the OOE variations in the light curve:

[2]We allow the amplitude to vary because it is dependent on the continuum stellar flux level, which changes depending on how accurate the pointing was, i.e. how much of the total system flux reached the detector through the fibre-fed spectrograph.

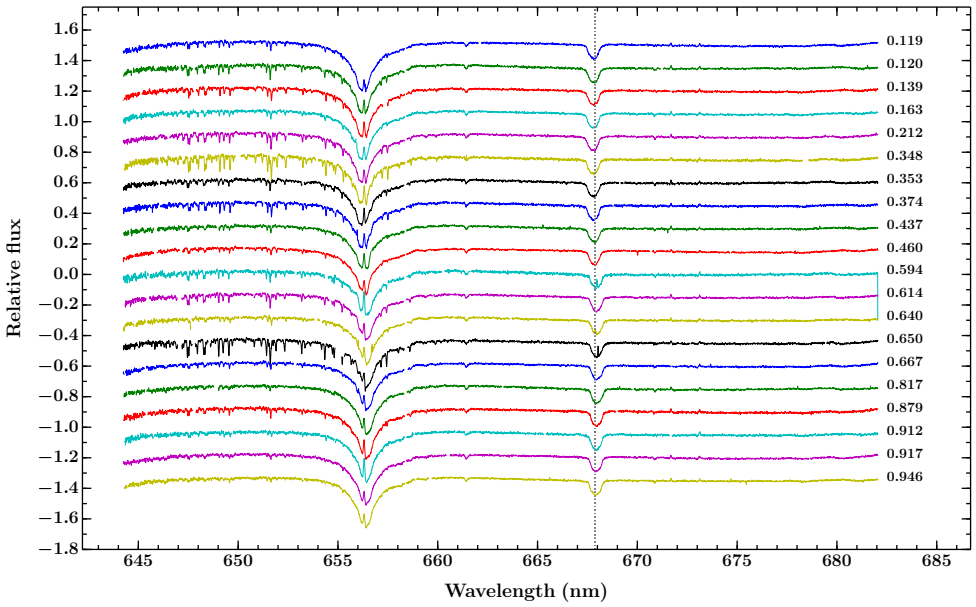

Figure 6.4: Optical spectra of V780 Mon obtained by the FLAMES spectrograph on the Very Large Telescope (VLT). The 20 medium resolution spectra cover the wavelength range 644–682 nm with a spectral resolution of $R \sim 17\,000$ and were obtained over a ∼2 month period (20 Dec 2011 – 29 Feb 2012) with both densely and sparsely sampled time intervals. The spectra are vertically offset for clarity and ordered by binary orbital phase (indicated by the numbers on the right hand side). Two strong absorption lines are present, namely Hα and He I 667.8 nm; the vertical grey dashed line indicates the He I line's rest wavelength (in the system's frame). Note, the narrow lines blueward of Hα are tellurics, and the emission in the core of the Hα line is from the nebula.

1. The OOE variability is modelled as the sum of two Gaussian process (GPs) whose covariance properties are chosen to explain the periodic peaks between eclipses and the long term downwards trend, respectively (see section 6.3.1). We test two models within this framework and refer to these as Models A and B.

2. The periodic flux peaks between eclipses are modelled as reflected primary light from the inwards facing hemisphere of the secondary. We keep the same GP used in the first analysis to explain the long term downwards trend (see section 6.3.2). We refer to this as Model C.

6.3.1 GP OOE Models

We model the OOE variability as the sum of two GPs: an exponential sine squared kernel (ESS) to explain the periodic peaks in flux and a squared exponential kernel (SE) to explain the long term downwards trend; this is Model A. The ESS kernel is a periodic kernel

defined as

$$k_{\mathrm{ESS}}(r) = A^2 \exp\left(-\Gamma \sin^2\left[\frac{\pi}{P} r\right]\right) \tag{6.1}$$

where $r = |t - t'|$ is the time-interval between the observations, A is the amplitude, Γ represents the scale of the correlations and P denotes the period. The SE kernel is introduced in section 3.3.2. Modelling the light curve with an eclipse model plus two GPs, and the He I line in each spectrum with a Gaussian, we find that the data is best fit by a system comprising a large primary and small secondary, which orbit with low eccentricity (e$\sim$0.015). The light curves, spectra and RVs of Model A, along with representations of the system geometry along the line of sight at primary and secondary eclipse, are shown in Figure 6.5 with selected parameters reported in Table 6.2.

The model gives a reasonable fit to the light curve and fits the spectra well. The low eccentricity is driven by the spectra: the lack of obvious secondary eclipse means the light curve model is probably unable to constrain the eccentricity precisely. The reason we do not clearly observe a secondary eclipse is due to the faintness of the secondary, i.e. the eclipse is there (given the low eccentricity) but is lost in the noise. The model does find a very shallow secondary eclipse (see Fig 6.5, top and bottom left panels), although given that there are significant correlations in the residuals, and the secondary eclipse appears (at times) to fall in the troughs of these, it is difficult to asses the significance of this result. At this stage we opted not to fit the additional (apparently periodic) variations in the light curve for model tractability but we relax this constraint in subsequent analysis (see Model C in section 6.3.2).

6.3.1.1 Model B: assessing the plausibility of a bright secondary on an eccentric orbit

To asses whether this solution is unique, we re-modelled the data, placing a constraint on the surface brightness ratio between the two stars ($J\sim$0.5); this is Model B. The aim of this model was to explore the range of eccentricities needed to have a bright secondary that does not get eclipsed. As expected, the model is unable to explain both the light curve and RVs: most notably, the secondary eclipse is too deep. To reduce the depth of

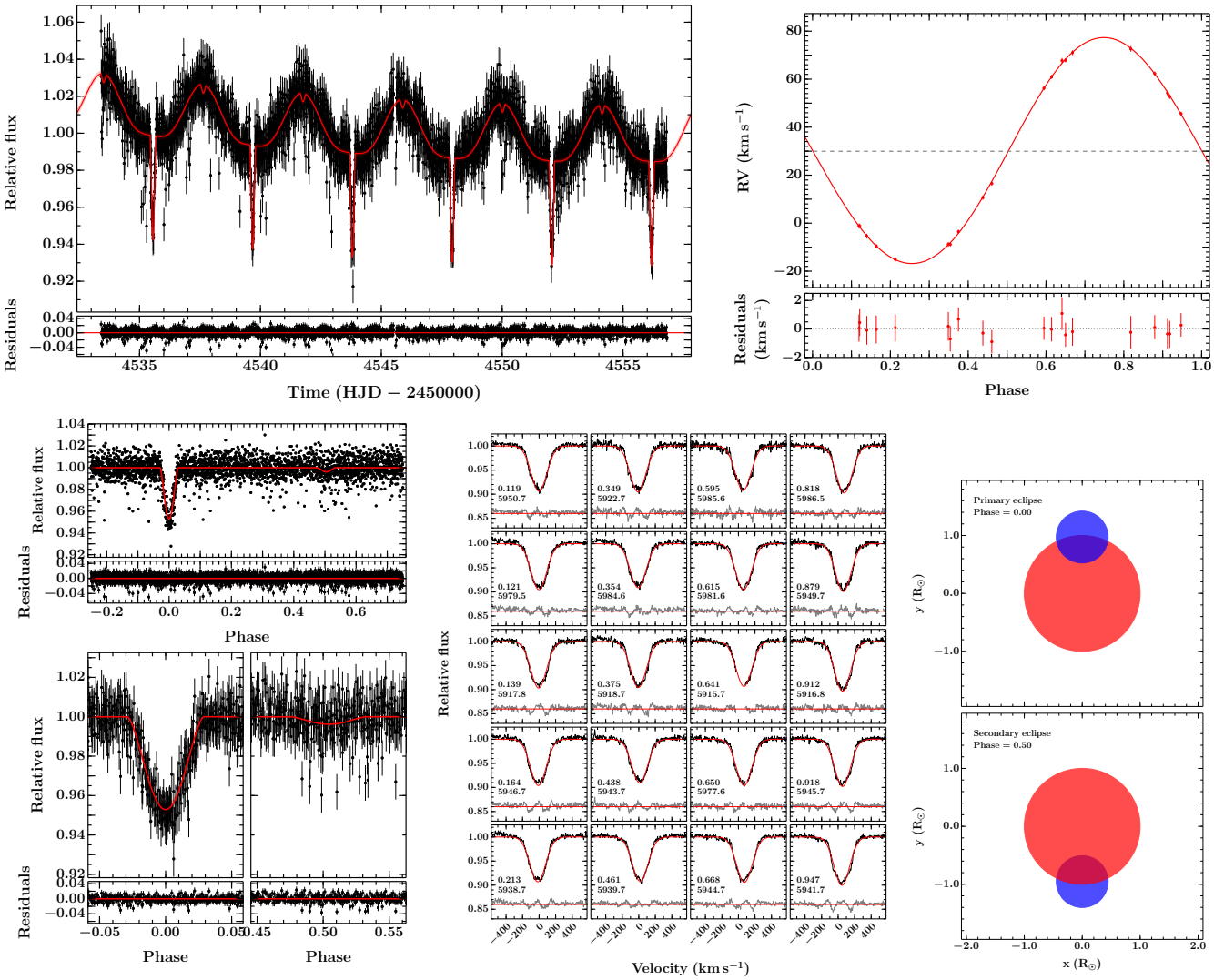

Figure 6.5: Results for Model A. *Top left*: CoRoT light curve (black points) with the GP + eclipse model in red and residuals below.

Bottom left: Upper panel shows the phase folded, detrended CoRoT light curve (black points) with the median model shown in red. The residuals of the median model are also shown immediately below; phase zero marks the centre of the primary eclipse in these two plots. The lower panels show zooms on the primary and secondary eclipses (left and right, respectively) along with their residuals below.

Bottom middle: Zooms on the HeI 667.8 nm line in the 20 VLT/FLAMES spectra (black) with the best-fit Gaussian model in red and residuals vertically offset below in grey. The panels are ordered in phase (indicated in each subplot along with rHJD). The width of the Gaussian was jointly fit for using all spectra.

Top right: phase folded RV curve for the primary star (red line) derived from our model. Also plotted, but not used in the fit, are the RVs determined from modelling the spectra directly and alone, i.e. independent of any light curve constraints (these measurements are included to asses the goodness of fit of the model-predicted RVs to the spectra).

Bottom right: inferred system geometry at primary and secondary eclipse given the stellar and orbital parameters derived from the model. The primary star is shown in red and the secondary in blue. The primary star radius is set to 1 $R_\odot$: only the radius ratio is relevant, not the absolute sizes of the two stars, which are arbitrary. The projected separation of the two stars was calculated using equation 1.43.

Table 6.2: Parameters of Model A, i.e. using two Gaussian processes to model the out-of-eclipse (OOE) variability. The GP component comprises an exponential sine squared kernel (ESS) to explain the periodic peaks in flux and a squared exponential kernel (SE) to explain the long term downwards trend. The amplitudes of the Gaussians used to model the 20 VLT/FLAMES spectra are omitted for clarity but all have well-characterised values in the range 0.09–0.10 (in relative flux units).

Parameter	Symbol	Unit	Value
	Eclipse parameters		
Central surface brightness ratio	J		$0.074\,^{+0.030}_{-0.028}$
Sum of radii	$(R_{\rm pri} + R_{\rm sec})/a$		0.242 ± 0.39
Radius ratio	$R_{\rm sec}/R_{\rm pri}$		$0.44\,^{+0.24}_{-0.18}$
Orbital inclination	i	(°)	$80.7\,^{+2.9}_{-3.2}$
Orbital period	P	(days)	$4.124234\,^{+0.000025}_{-0.000035}$
Time of primary eclipse centre	$T_{\rm prim}$	(HJD)	2454539.6818 ± 0.0017
	$e\cos\omega$		$0.0062\,^{+0.0080}_{-0.0046}$
	$e\sin\omega$		$-0.010\,^{+0.078}_{-0.069}$
eccentricity	e		$0.0146^{+0.0068}_{-0.0059}$
omega	ω	(°)	-57^{+43}_{-25}
Linear LD coefficient for primary	$u_{\rm pri}$		0.23 ± 0.13
Non-linear LD coefficient for primary	$u'_{\rm pri}$		0.34 ± 0.27
Linear limb LD for secondary	$u_{\rm sec}$		0.24 ± 0.13
Non-linear LD coefficient for secondary	$u'_{\rm sec}$		0.39 ± 0.26
Third light	L_3		0.38 ± 0.26
	OOE variability parameters		
Amplitude of SE term	$A_{\rm SE}$	(%)	$0.21\,^{+0.18}_{-0.11}$
Timescale of SE term	$l_{\rm SE}$	(days)	$60\,^{+8}_{-14}$
Amplitude of ESS term	$A_{\rm ESS}$	(%)	$0.142\,^{+0.143}_{-0.093}$
Scale factor of ESS term	$\Gamma_{\rm ESS}$		$0.090\,^{+0.143}_{-0.060}$
Period of ESS term	$P_{\rm ESS}$	(days)	$4.1289\,^{+4.0922}_{-0.0074}$
White noise	σ	(mmag)	0.00903 ± 0.00015
	Spectra / RV parameters		
Gaussian width	σ	($\rm km\,s^{-1}$)	94.93 ± 0.25
Systemic velocity	$V_{\rm sys}$	($\rm km\,s^{-1}$)	$29.96^{+0.37}_{-0.31}$
Primary semi-amplitude	$K_{\rm pri}$	($\rm km\,s^{-1}$)	47.07 ± 0.42

* LD = limb darkening

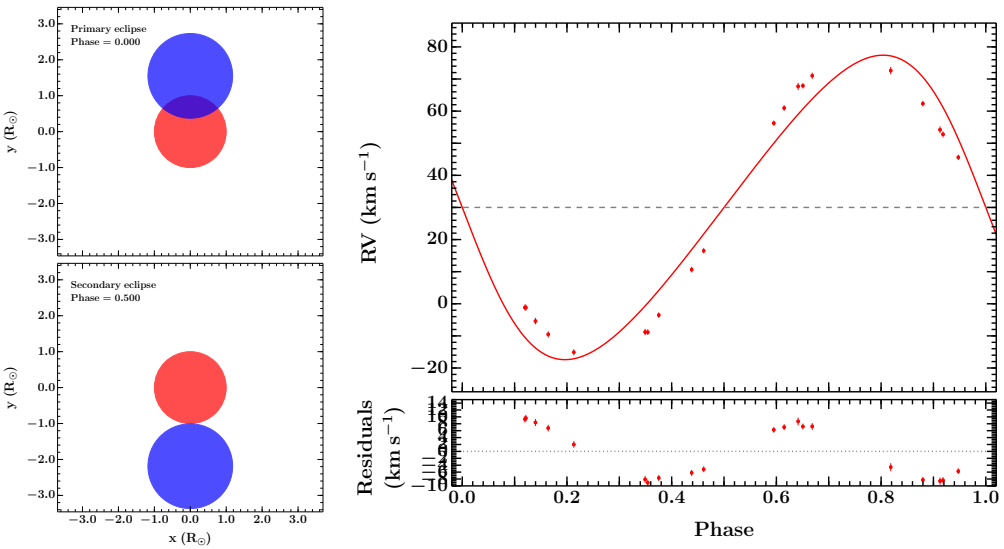

Figure 6.6: Model B. *Left*: system geometry required to yield a primary but no secondary eclipse (top and bottom panels, respectively), given the stellar parameters derived from the model, i.e. only varying the eccentricity and longitude of periastron. *Right*: Resulting RV orbit for the eccentricity required to yield no secondary eclipse. The individual RVs (red points) are determined from modelling the spectra directly and alone, i.e. independent of the model; they are plotted for comparison. Note, in the model with a bright secondary, the model favours a secondary that is larger than the primary, presumably required to reproduce the shape of the primary eclipse given the surface brightness ratio enforced. Even were the secondary smaller the required eccentricity would still not be compatible with the RVs.

secondary eclipse the model attempts to increase the eccentricity, but this is countered by the spectra/RVs: the result of the compromise is an eccentricity that is slightly too high for the RVs but not high enough to reduce the secondary eclipse depth to become consistent with the light curve. We do not show plots or report system parameters but simply note the result; a model containing a bright secondary is not validated.

To confirm this conclusion we explored the eccentricity required to not yield a secondary eclipse for this model. We use the combination terms, $e\cos\omega$ and $e\sin\omega$, instead of e and ω themselves, as they are more instructive. In such an assessment, $e\cos\omega$ and $e\sin\omega$ counter each other: larger absolute $e\cos\omega$ values increase the area under the eclipse chord and higher absolute $e\sin\omega$ values decrease it. Therefore, the smallest eccentricity required to not see secondary eclipse corresponds to $e\sin\omega = \pm 0.17$ and $e\cos\omega = 0.0$ (see Fig. 6.6, left panel). The corresponding RV orbit is not a good match to the data (Fig. 6.6, right panel). We note that the plotted model RV orbit is for $e\sin\omega$=0.17 but the fit is equally poor in the opposite sense if $e\sin\omega$=–0.17. In addition, varying $e\cos\omega$ away from 0 deteriorates the fit further. We conclude that a model with a bright secondary is not consistent with

both the observed light curve and RVs; a low-eccentricity, and hence very low brightness ratio, is required.

From the above analysis it would appear as though the only consistent model is model A, i.e. one comprising a large primary and small secondary orbiting with low eccentricity. However, this is the favoured scenario only if we do not interpret a physical origin for the OOE variations. In the present case, it is possible that the periodic peaks in the light curve are due to light from the primary star reflected off the inward-facing hemisphere of the secondary. In section 6.3.2 we attempt to determine whether such a scenario is plausible (Model C), but first we determine the origin of the correlated variations in the residuals of the light curve (see Figure 6.5, top left plot).

6.3.1.2 Origin of the correlated variations in the residuals

We perform a least squares fitting of sine curves to the residual time-series, finding that they are best fit with a period $P = 0.996$ days and amplitude $A = 0.32\%$. The variations appear to display a relatively constant base level with periodic increases in dispersion toward higher fluxes. The period of the variations is consistent with the sidereal day and therefore, remembering the misplaced CoRoT aperture, we interpret them as arising from variable scattered light entering the telescope as it orbits Earth (i.e. dependent on the position of the spacecraft in its orbit), which is not fully corrected for in the background subtraction. We use the determined period and amplitude as initial guesses for our model including reflection, in which we treat the scattered light variations with an additional periodic GP (see below).

6.3.2 Reflection + GP OOE Models

We include a simple reflection model (c.f. Milne 1926; Russell 1939) in place of our periodic GP to explain the recurring peaks in the OOE light curve; this is Model C. The reflected primary light from the secondary is given by

$$L_{\rm sec}^{\rm refl} \;=\; \frac{1}{2}\; L_{\rm pri}^{\rm direct} \left(\frac{R_{\rm sec}}{a}\right)^2 (1 + 2\cos\psi)^2 \tag{6.2}$$

Table 6.3: Parameters of Model C, i.e. using a simple reflection model, along with squared exponential (SE) and exponential sine squared (ESS) GPs to explain the OOE variations (the periodic peaks, long term downwards trend and periodic variations on the sidereal day, respectively). The amplitudes of the Gaussians used to model the 20 spectra are omitted for clarity but all have well-characterised values in the range 0.09–0.10 (in relative flux units).

Parameter	Symbol	Unit	Value
	Eclipse parameters		
Central surface brightness ratio	J		0.063 ± 0.37
Sum of radii	$(R_{\rm pri} + R_{\rm sec})/a$		$0.330\,^{+0.014}_{-0.010}$
Radius ratio	$R_{\rm sec}/R_{\rm pri}$		$0.93\,^{+0.23}_{-0.16}$
Orbital inclination	i	(°)	$73.92\,^{+0.69}_{-0.97}$
Orbital period	P	(days)	$4.124248\,^{+0.000021}_{-0.000026}$
Time of primary eclipse centre	$T_{\rm prim}$	(HJD)	2454539.6811 ± 0.0019
	$e\cos\omega$		$0.0039\,^{+0.0045}_{-0.0031}$
	$e\sin\omega$		$-0.0016\,^{+0.0060}_{-0.0071}$
eccentricity	e		$0.0072\,^{+0.0056}_{-0.0036}$
omega	ω	(°)	$343\,^{+79}_{-52}$
Linear LD coefficient for primary	$u_{\rm pri}$		$0.24\,^{+0.14}_{-0.12}$
Non-linear LD coefficient for primary	$u'_{\rm pri}$		0.32 ± 0.26
Linear LD coefficient for secondary	$u_{\rm sec}$		0.26 ± 0.13
Non-linear LD coefficient for secondary	$u'_{\rm sec}$		0.37 ± 0.27
Third light	L_3		$0.118\,^{+0.0135}_{-0.080}$
Albedo of secondary	$A_{\rm sec}$		$0.83\,^{+0.12}_{-0.16}$
	OOE variability parameters		
Amplitude of SE term	$A_{\rm SE}$	(%)	$0.061\,^{+0.111}_{-0.029}$
Timescale of SE term	$l_{\rm SE}$	(days)	32 ± 2
Amplitude of Cosine term	$A_{\rm cos}$	(%)	$0.073\,^{+0.311}_{-0.066}$
Period of Cosine term	$P_{\rm cos}$	(days)	$0.9975\,^{+0.0055}_{-0.0034}$
White noise	σ	(mmag)	0.00877 ± 0.00019
	Spectra / RV parameters		
Gaussian width	σ	($\rm km\,s^{-1}$)	$94.94\,^{+0.27}_{-0.24}$
Systemic velocity	$V_{\rm sys}$	($\rm km\,s^{-1}$)	29.91 ± 0.27
Primary semi-amplitude	$K_{\rm pri}$	($\rm km\,s^{-1}$)	$47.14^{+0.48}_{-0.44}$

* LD = limb darkening

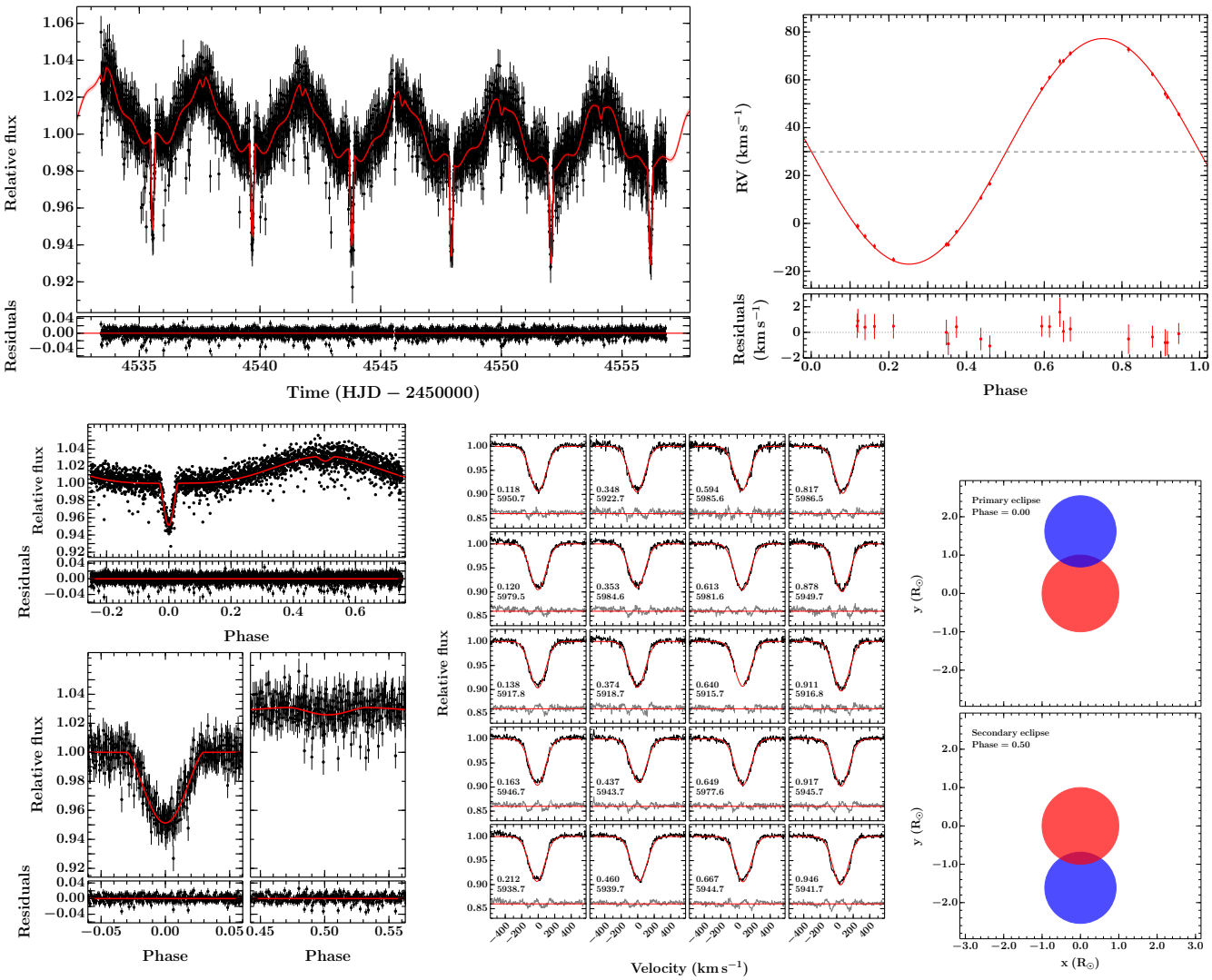

Figure 6.7: Model C. As for Fig 6.5 except that the *bottom left* plot shows the phase folded CoRoT light curve (black points), which has been detrended with respect to the GP model but not the reflection model. The median model is shown in red.

where $L_{\rm pri}^{\rm direct} = L_{\rm pri}/4$ is the direct light from the primary to the observer, $R_{\rm sec}/a$ is the secondary radius relative to the semi-major axis, and ψ is the angle between the line of sight and the line joining the two stars. In addition to our reflection model and a GP to explain the long-term downwards trend we include a second GP to account for the variable scattered light. We tested both the exponential sine squared (ESS) and cosine kernels, finding each gave comparable results, and opted for the latter due to its simplicity. The cosine kernel is given by

$$k_{\rm cos}(r) = A^2 \cos\left(\frac{2\pi}{P} r\right) \ . \tag{6.3}$$

The final light curve model therefore comprises a reflection term for the periodic peaks

and two GPs, one for the long term downwards trend and one for the low-level periodic scattered-light variations. We note that the scatted light variations are not strictly speaking sinusoidal, but rather result from a periodic increase in flux spread towards brighter values, whilst maintaining a quasi-constant base flux level. Therefore, the model currently used may not be the most appropriate. Nonetheless, including our model for the periodic variations does provide an explanation for the apparent deviations in the light curve away from smooth variability and ably reproduces the light curve morphology, most notably around secondary eclipse, as well as resulting in less-correlated residuals. The light curves, spectra and RVs, along with the system geometry are shown in Fig 6.7 and selected parameters are reported in Table 6.3. The model requires a large secondary (relative to primary) to explain the amplitude of the reflection peak in the light curve. However, the secondary is still required to be faint as the spectra/RVs constrain the model to low eccentricities meaning the secondary is eclipsed. There are two plausible options for such a scenario:

1. The primary is small and hot, e.g. a hot subdwarf, and the secondary is a low-mass main sequence star.

2. The secondary is large and cool, e.g. a PMS star, and the primary has already evolved onto the main sequence.

Both of these scenarios are interesting. The former would represent an evolved system where the primary has undergone mass loss from its outer layers during its red giant phase. The latter is very interesting indeed, as it would constitute the first such system discovered in our galaxy. Recently, Moe & Di Stefano (2015) reported the discovery of a new class of nascent EB, comprising early main sequence B-type primaries and lower-mass PMS secondaries, which show significant reflection effects. The 22 systems in this new class were discovered in the Large Magellanic Cloud (LMC) and are found to be associated with HII regions, as expected given their youth. As V780 Mon lies along the line of sight to the NGC 2264 star forming region, one might argue that the second scenario is the more likely. Nonetheless, we consider both options in the following discussion.

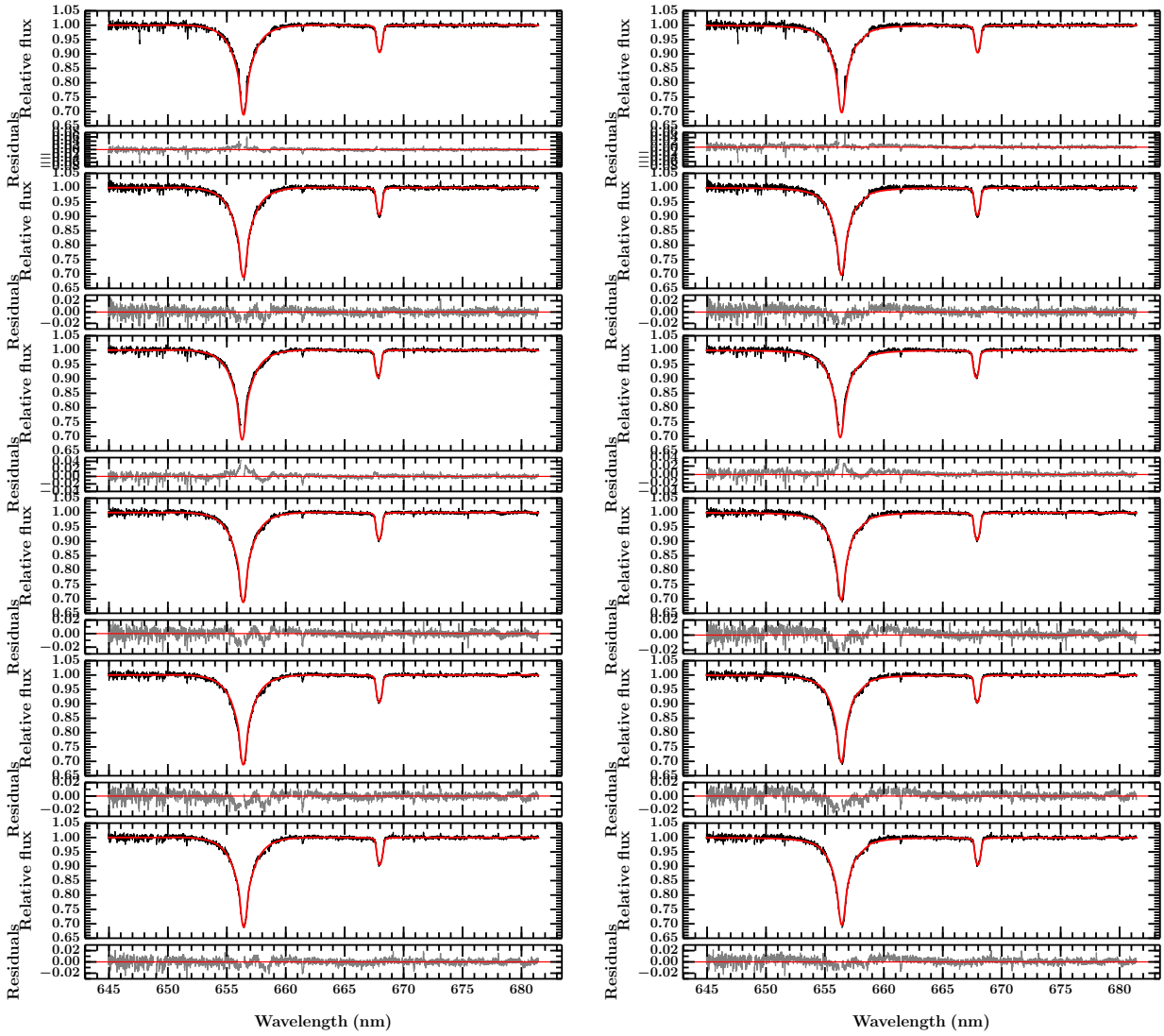

Figure 6.8: Nemeth hot subdwarf and ATLAS main sequence model fits to six selected FLAMES spectra (left and right columns, respectively). The plot for each spectrum consists of the model fit with residuals immediately below: the observed spectra are plotted in black, best-fit model in red and residuals in grey. The parameters of the best-fit models are, for the hot subdwarf: $T \sim 30\,800$ K, $\log g \sim 5.61$ and [He/H] ~ 0.07, and for the ATLAS main sequence star: $T \sim 24\,200$ K, $\log g \sim 4.85$ and [M/H] ~ -1.56.

6.3.2.1 Subdwarf vs. main sequence primary: modelling the FLAMES spectra

We selected the six highest quality FLAMES spectra (see Figure 6.4; phases 0.460, 0.640, 0.817, 0.912, 0.917 and 0.946) and simultaneously fit them using a least-squares approach with model spectra from the Nemeth subdwarf and ATLAS BLUERED libraries (Nemeth et al. 2014 and Bertone et al. 2004, respectively). Given our earlier analysis, we assume only the primary star significantly contributes to the spectra. The parameters of the fit are the temperature, surface gravity, element ratios ($[M/H]$ for ATLAS and [He/H] for the

Nemeth models) and $v \sin i$, as well as the RV offset of each spectrum. The temperature, surface gravity and element ratios were determined from the model grids using trilinear interpolation.

The best-fit models for a hot subdwarf and a main sequence star are shown in Figure 6.8 (left and right columns, respectively). Both sets of models are able to adequately reproduce the observed spectra. The parameters of the best-fit hot subdwarf model are $T \sim 30\,800$ K, $\log g \sim 5.61$ and [He/H] ~ 0.07, and those for the ATLAS main sequence model are $T \sim 24\,200$ K, $\log g \sim 4.85$ and [M/H] ~ -1.56. Both models find $v \sin i \sim 150$ km s^{-1}, however they each favour slightly different RVs. The ATLAS models find RVs that are broadly consistent with the joint light curve and He I line modelling but the subdwarf models find RVs consistently 2–3 km s^{-1} lower. The subdwarf models achieve a slightly lower χ^2 than the ATLAS models but the difference is not significant given: the simplicity of the model; trilinear interpolation within a grid; and the limitations of direct spectral fitting using a χ^2 statistic without weighting the spectral features to account for missing elements or incorrect abundances in the models. We note, for example, that the subdwarf models only contain H and He, whereas there is evidence of CNO elements in the spectra, specifically OII 6571.6 Å and CII 6578.1 and 6582.9 Å absorption features in the red wing of Hα; these features are better fit by the ATLAS models, which do include the relevant transitions. It is important to note that the lack of these elements in the Nemeth models does not necessarily represent a lack of those elements in truth, e.g. He-rich sdO subdwarfs show CNO elements (Stroeer et al., 2007).

6.3.2.2 SED analysis

As the spectra are unable to distinguish between a hot subdwarf and a main sequence primary, we sought an alternative approach. For the system to be young (i.e. MS primary and PMS secondary) then, given that the system is viewed along the line-of-sight to NGC 2264, it is reasonable to assume the system must be a cluster member. This allows us to place constraints on the young system hypothesis.

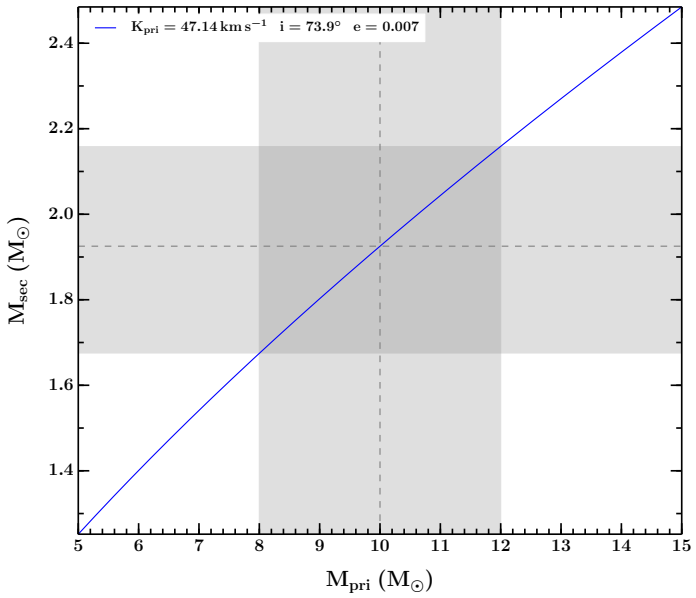

Figure 6.9: Mass function of V780 Mon computed from equation 1.39 using the results of the light curve and He I line modelling presented in Table 6.3. A primary mass of $M_{\rm pri} = 10 \pm 2\,M_{\odot}$ is indicated by the vertical dotted grey line and grey shaded region, which corresponds to a secondary mass of $M_{\rm sec} \sim 1.9 \pm 0.3\,M_{\odot}$ (indicated by the horizontal dotted grey line and grey shaded region).

A primary temperature of $T_{\rm pri} \sim 24\,000$ K implies a spectral type $\sim$B1.5 and primary mass of $M_{\rm pri} \sim 10\,M_{\odot}$ (Hohle et al., 2010). The system's mass function (equation 1.39), shown in Figure 6.9, constrains the mass ratio: a primary mass of $M_{\rm pri} = 10 \pm 2\,M_{\odot}$ is indicated by the dotted grey line and grey shaded region, which implies a secondary mass of $M_{\rm sec} \sim 1.9 \pm 0.3\,M_{\odot}$. The error on the primary mass was estimated from the range of temperatures able to provide an adequate fit to the spectra: an error of $\sim$ 2000 K was determined, which corresponds to spectral class uncertainty of $\pm$0.5 and $\pm 2\,M_{\odot}$. We opted not to propagate the errors on the orbital elements through into this uncertainty as the error budget is dominated by the temperature uncertainty. Comparing to Bressan et al. (2012) stellar evolution models[3] we note that a $\sim$2 $M_{\odot}$ star has a comparable size to a $\sim$10 $M_{\odot}$ star at an age of $\sim$1 Myr, consistent with the age of the cluster ($\sim 3 \pm 5$ Myr, with ongoing star formation). The model-predicted radii at 0.8 Myr are 3.8 and 3.5 $R_{\odot}$ for the primary and secondary stars, which is consistent with the light curve radius ratio.

Assuming cluster membership, we can place the following constraints on the SED analysis:

[3]The only PMS models, known to the author, that span the required mass range.

1. The distance to the system is $d = 760$ pc.

2. The primary temperature is $T_{\rm pri} \sim 24\,000$ K.

3. The individual radii are $R_{\rm pri} \sim R_{\rm sec} \sim 3 - 4\,R_{\odot}$ and their ratio is $R_{\rm sec}/R_{\rm pri} \sim 0.93$.

Before analysing the SED we note that the binary is a member of a tight visual double and therefore it is possible that three stars in fact contribute to the observed SED. As we do not have reliable constraints on the third star we do not include it in the following analysis. Accordingly, we restrict the goal of the SED modelling to simply answer the question, *are the observed broadband magnitudes incompatible with V780 Mon being a cluster member, given the temperature and radius constraints?*

We modelled the SED as the sum of two stellar photospheres, interpolating in temperature between ATLAS model grids (Castelli & Kurucz, 2003), and placing Gaussian priors on the radius ratio and primary radius. The distance was fixed at $d = 760$ pc. The observed SED (Figure 6.10, cyan points) does not, upon initial inspection, appear to be consistent with a primary temperature of $T_{\rm pri} \sim 24\,000$ K (dotted red SED). However, it is possible that the system is highly extincted, either due to dust in the system or in the local molecular cloud, or both. We find that the SED can be explained with V780 Mon as a cluster member. However, significant reddening is required. The best-fit temperatures and radii are $T_{\rm pri} = 24\,000$ K and $T_{\rm sec} = 6000$ K, and $R_{\rm pri} = 3.78\,R_{\odot}$ and $R_{\rm sec} = 3.82\,R_{\odot}$. The best-fit model requires $A_{\rm V} = 5.2$ which, while high, is within a plausible range given the location of the system within the cluster and comparing to the Ophiuchus and Perseus molecular clouds (Ridge et al., 2006). As extinction within clusters is not restricted to a standard interstellar extinction law, we allow $R_{\rm V}$ to be fit for following the prescription of Cardelli et al. (1989) and find the slope of the optical and near-IR magnitudes is best described with $R_{\rm V} = 7.7$. We note that $\log g$ was fixed to 4.5 and 4.0 for the primary and secondary stars, which is acceptable as the surface gravity should not affect the broadband magnitudes appreciably and certainly not affect the conclusions.

The key point is that the optical and IR magnitudes are consistent with a cluster member comprising a hot main sequence primary and a cool PMS secondary. The required

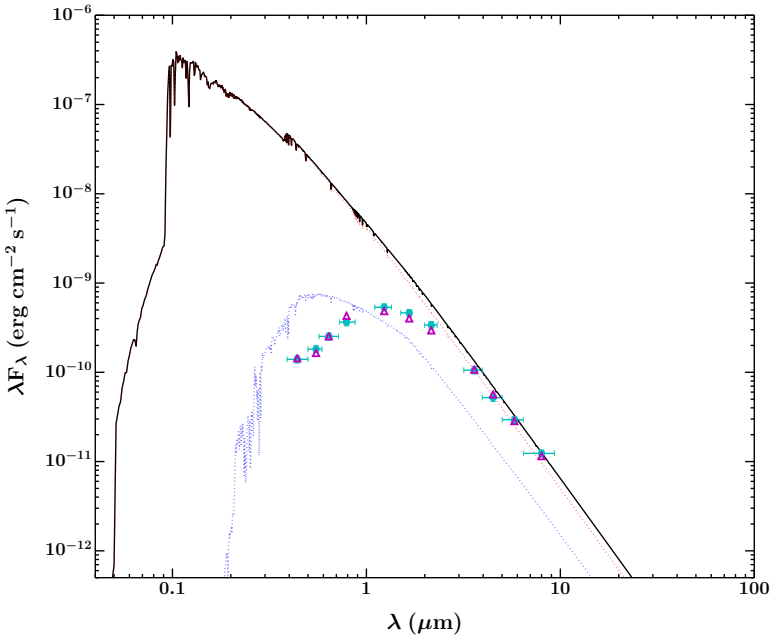

Figure 6.10: Spectral energy distribution of Mon-1411 (cyan points) based on the magnitudes listed in Table 6.1 but with errors inflated to 0.1 mag to account for the intrinsic variability in the system. The red and blue dotted lines show the *unreddened* emission from the primary and secondary stars, with black indicating their combined flux. The magenta triangles show the best-fit two naked photospheres model (black curve) reddened to match the observed SED (cyan points).

reddening is significant but is within plausible bounds for dense molecular clouds, especially considering the very young age suggested by the radii constraints and hence possibility of dust in the system. We therefore cannot rule out this scenario for V780 Mon.

Finally, we note that the temperature estimate for the primary star in the hot subdwarf scenario is $T \sim 31\,000$ K, and hence would require at least as much reddening as the above model, but this could be explained through dust in the system.

6.3.3 Conclusions and further work

If we do not ascribe a physical origin to the OOE variability in the light curve, the data is best fit by a model comprising a large primary and small, faint secondary, which orbit with low eccentricity ($R_{\rm sec}/R_{\rm pri} = 0.44$, $J = 0.074$ and $e = 0.015$). However, if we interpret the periodic increases in flux as arising from reflected primary light (from the inwards facing hemisphere of the secondary), then the aforementioned model cannot explain the light curve: the secondary is too small to reflect the amount of light required to match the amplitude of the OOE variations. The data is, however, consistent with a model comprising

a comparatively large secondary star ($R_{\rm sec}/R_{\rm pri} = 0.93$), but where the secondary is much fainter ($J = 0.063$), contributing only $\sim$5 % of the system light in the CoRoT bandpass (ignoring limb darkening). Due to the physical explanation for the OOE variability, we favour this latter model.

Therefore, there are two plausible scenarios to explain the light curve and RV variations: a hot subdwarf primary and low-mass MS secondary, and a massive MS primary and low-mass PMS secondary. Analysis of the VLT/FLAMES spectra is unable to distinguish between the two models, and a preliminary SED analysis is unable to rule out the young system hypothesis. As a final comment, however, we note that the properties of the Moe & Di Stefano (2015) class are well-matched to V780 Mon: early B-type primaries ($M_{\rm pri} = 5 - 16\,M_{\odot}$), short orbital periods $P = 3.0 - 8.5$ days, young ages $\tau \approx 0.6 - 8$ Myr, and small secondary masses $M_{\rm sec} \approx 0.8 - 2.4\,M_{\odot}$ ($q \approx 0.07 - 0.36$). Given the location of the source, broad consistency with cluster membership, and similar light curve morphology and system parameters to a well-defined class of young extreme-mass-ratio binaries, we tentatively favour this hypothesis. However, we stress the uncertainty in such a conclusion.

As the primary dominates the optical photometric and spectroscopic light, high cadence observations in the infrared could prove fruitful for detecting the secondary eclipse, characterising the secondary's orbit and solving the system. Finally, we note that low cadence *Spitzer* observations of the system ($\sim$2 hours; obtained as part of CSI 2264) display a similar light curve morphology to that seen in CoRoT but do not sample any eclipses sufficiently to model.

6.4 Mon-1411

Mon-1411 (aka CXORRS J064037.2+094713) is a previously identified source with strong X-ray emission and M3 spectral type (Sung et al., 2004; Ramírez et al., 2004). Simultaneous 3.6 and 4.5 μm light curves were obtained by *Spitzer* in 2011/2012. We model the light curves in section 6.4.1 and present a preliminary analysis of the system's SED in section 6.4.2.

6.4.1 Joint modelling of *Spitzer* 3.6 and 4.5 μm light curves

We simultaneously model the *Spitzer* 3.6 and 4.5 μm light curves with the Gaussian process + eclipse model presented in section 5.6.1. The light curves are presented in Fig. 6.11 along with our joint solution (3.6 and 4.5 μm are top left and top right, respectively). Both light curves display a systematic ramp in flux with evidence of additional, coarse variations on ∼day-long timescales. We therefore choose a Matérn-3/2 kernel for the OOE GP model in each band, which is appropriate for data displaying a relatively rough behaviour. The residuals at the bottom of each panel are predominately 'white' but do show correlations at certain times, e.g. around rHJD = 5900 and 5927, which suggest additional variability not captured by our GP model. We therefore tested a more sophisticated OOE model, comprising the sum of two GPs (we tried both two Matérn-3/2 kernels and one Matérn-3/2 and one squared exponential), with one GP initially set to a short timescale and the other to a long timescale, to try and capture the different forms of variability present. However, these models repeatedly favoured solutions with both GPs varying on long timescales, implying that the information content of the *Spitzer* light curves is insufficient to support the more sophisticated treatment. In the following analysis therefore, we use only a single Matérn-3/2 kernel to explain the OOE variations in each band, but note its limitations.

The parameters of the joint light curve model are reported in Table 6.4. We caution that the relatively sparse time sampling and presence of complex systematics and variability (which are not fully accounted for) in the *Spitzer* light curves could mean the solution is not robustly constrained to the 'correct' region of parameter space. The model converges on a slightly eccentric solution, driven primarily by the apparent longer duration of primary eclipse compared to secondary. This can be seen in the bottom two plots of Fig. 6.11, which show the phase-folded light curves for 3.6 μm and 4.5 μm (left and right, respectively). Inspection of the residuals at phases 0.03–0.1 in the 4.5 μm band reveals a systematic trend of faint measurements (present from one orbit to the next) that would act to increase the duration of primary eclipse. Indeed, the model under predicts the expected flux during primary egress (phases 0.0-0.03), as would be expected if this were the case.

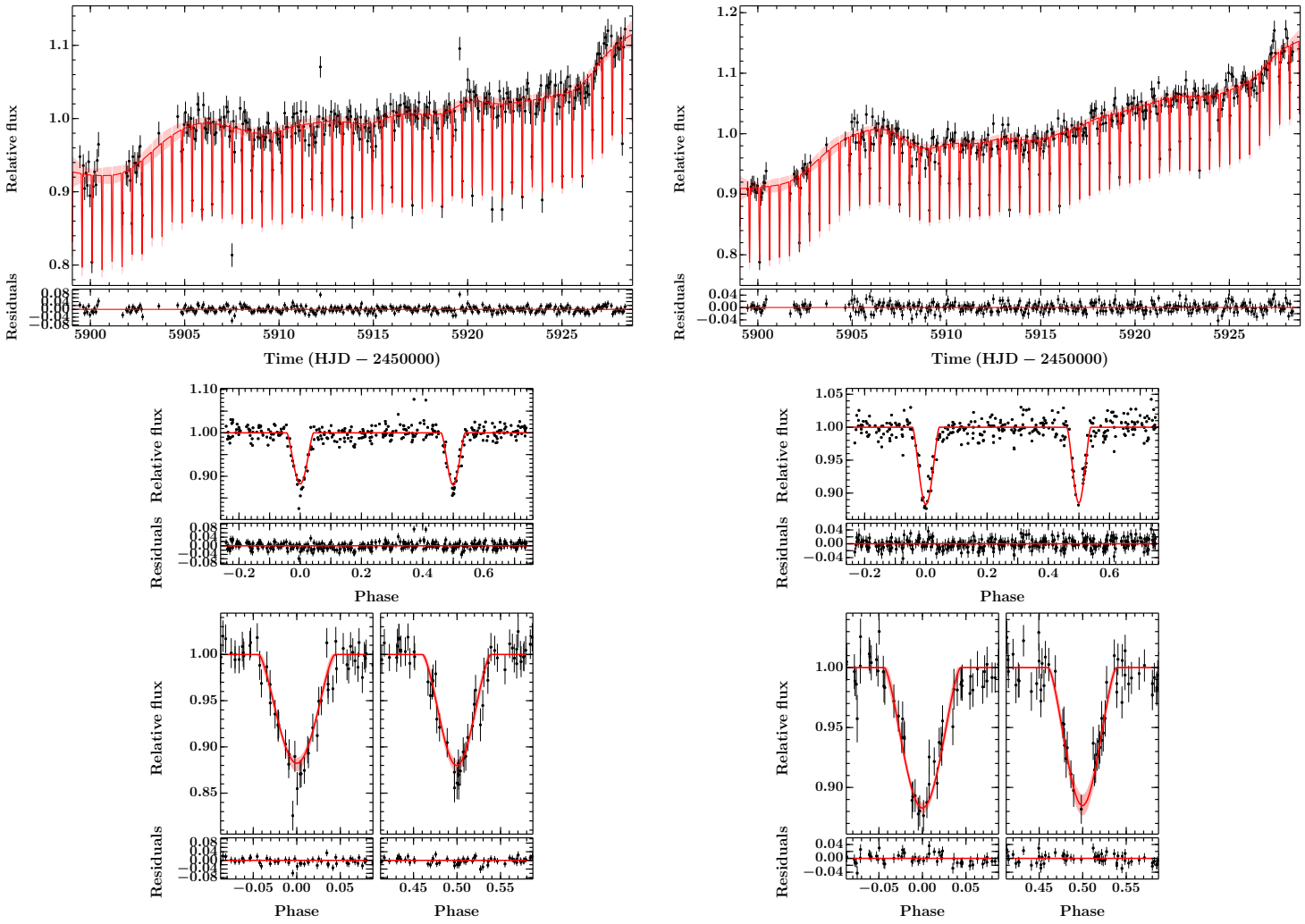

Figure 6.11: Light curve model for Mon-1411. *Top left and top right*: *Spitzer* 3.6 and 4.5 μm light curves (black points) with the GP + eclipse model in red and residuals below.

Bottom left and bottom right: Top panels show the phase-folded, detrended *Spitzer* light curves (black points) in the 3.6 and 4.5 μm bands (left and right, respectively), with the median model shown in red and residuals immediately below; phase zero marks the centre of the primary eclipse in these two plots. The bottom panels show zooms on the primary and secondary eclipses (left and right, respectively) along with their residuals below.

Primary eclipse is found to be shallower than secondary eclipse at 3.6 μm, yet of comparable depth at 4.5 μm[4]. This could be partially due to the eccentricity driven by the 4.5 μm data around primary egress, which drives the primary eclipse shape towards a broader "V" and would explain the shallower primary eclipse depth at 3.6 μm in the model than the data in that band alone might suggest. This effect results in surface

[4]We note that the system was modelled both ways, i.e. with each star defined as primary and the other as secondary. We define primary and secondary from the configuration that yielded surface brightness ratios $J < 1$.

Table 6.4: Parameters of the light curve model for Mon-1411.

Parameter	Symbol	Unit	Value	
			Spitzer 3.6 μm	Spitzer 4.5 μm
Eclipse parameters				
Central surface brightness ratio	J		0.63 ± 0.15	$0.59^{+0.15}_{-0.12}$
Sum of radii	$(R_{\rm pri} + R_{\rm sec})/a$		0.317 ± 0.013	
Radius ratio	$R_{\rm sec}/R_{\rm pri}$		$0.76^{+1.04}_{-0.24}$	
Orbital inclination	i	(°)	$79.10\ ^{+1.10}_{-0.86}$	
Orbital period	P	(days)	1.060582 ± 0.000080	
Time of primary eclipse centre	$T_{\rm prim}$	(HJD)	5915.99984 ± 0.00082	
	$e\cos\omega$		-0.0006 ± 0.0016	
	$e\sin\omega$		$-0.124^{+0.061}_{-0.056}$	
eccentricity	e		$0.124^{+0.056}_{-0.061}$	
omega	ω	(°)	-90.25 ± 0.80	
Linear LD coeff. for primary	$u_{\rm pri}$		0.078 ± 0.018	0.064 ± 0.021
Non-linear LD coeff. for primary	$u'_{\rm pri}$		0.201 ± 0.059	0.192 ± 0.061
Linear LD coeff. for secondary	$u_{\rm sec}$		0.083 ± 0.017	0.059 ± 0.021
Non-linear LD coeff. for secondary	$u'_{\rm sec}$		0.205 ± 0.070	0.189 ± 0.069
Gaussian process hyperparameters				
Amplitude of Matérn-3/2 kernel	A	(%)	$0.178^{+0.104}_{-0.081}$	$0.204^{+0.096}_{-0.083}$
Timescale of Matérn-3/2 kernel	l	(days)	248^{+167}_{-157}	265^{+159}_{-149}
White noise	σ	(mmag)	0.01155 ± 0.00093	$0.000000^{+0.000019}_{-0.000000}$

* LD = limb darkening

brightness ratios that tentatively hint at the secondary being comparatively brighter at the bluer 3.6 μm wavelength, whereas the opposite is generally expected. However, given that the values are consistent to within error, and that this effect might be caused by residual variability presently unaccounted for, we do not consider it significant. Further work involving modelling each band separately and comparing results could prove fruitful for testing the validity of the presented solution but, given the systematics present and intrinsic noise level of the 3.6 μm light curve, robust conclusions may be difficult. We believe the most promising step forward will come from the inclusion of radial velocity data into our solution, but this is beyond the scope of the present work.

6.4.2 Evidence for youth: SED

Without spectroscopic observations the fundamental parameters of the two stars, and hence evidence for youth and cluster membership, cannot be determined directly. However,

analysis of the spectral energy distribution (SED) offers an alternative approach. The SED of Mon-1411 is shown in Fig. 6.12 and displays an IR excess, which is commonly attributed to circumstellar/circumbinary dust and hence youth. Following Allen et al. (2004), the IRAC colours imply a Class II SED, which suggests a system that has dispersed most of its envelope but still possesses a non-truncated disk. We note that the system lies towards the centre of the NGC 2264 reflection nebula, whose reflected light and emission from polycyclic aromatic hydrocarbons (PAHs) could effect the precise values of the IRAC magnitudes, but we consider the IR excess to be a robust detection. We inflate the uncertainties presented in Table 6.1 to 0.1 mag to account for the intrinsic variability in the system and further increase the uncertainty to 0.2 mag for the 3.6, 4.5 and 5.8 μm bands, and to 0.3 mag for the 8.0 μm band, in light of the potential nebula contribution at these wavelengths.

Given the unsolved nature of the system, the SED modelling presented here relies on three assumptions, which we subsequently argue are validated for the purposes of analysing the SED to provide evidence of cluster membership. The assumptions are:

1. The system is a cluster member (distance = 760 pc and age = 3 Myr).

2. The reddening to the system is $A_v = 0.45$ (following Rebull et al. 2002).

3. The parameters determined from the light curve modelling are correct.

Following our SED analysis of CoRoT 223992193 we fit the VRI and JHK bands with the emission from two naked MARCS model photospheres, assuming a distance of 760 pc and reddening of $A_v = 0.45$, and placing a Gaussian prior on the radius ratio as determined from the light curve modelling. We find that the best fit is obtained with temperatures of $T_{\rm pri} = 3200$ K and $T_{\rm sec} = 2800$ K, and radii of $R_{\rm pri} = 1.04\ R_{\odot}$ and $R_{\rm sec} = 0.77\ R_{\odot}$, which are consistent with the temperature and radius ratios inferred from the light curve modelling. We further note that the temperature and radius pairs agree with the predictions of the Baraffe et al. (2015) stellar evolution models for stars younger than 5 Myr. The key point is that the optical and near-IR magnitudes are consistent with a low mass cluster member of ∼M3 spectral type (as observed), which we believe

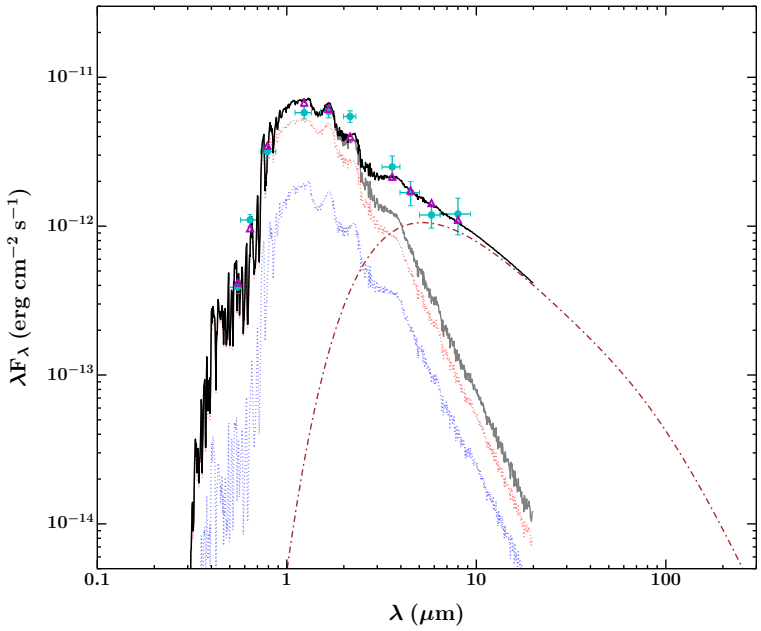

Figure 6.12: Spectral energy distribution of Mon-1411 (cyan points) based on the magnitudes listed in Table 6.1 but with errors inflated to 0.1 mag to account for the intrinsic variability in the system. The red and blue dotted lines show the emission from the primary and secondary stars, with grey indicating their combined flux. The black line and magenta triangles show the best-fit two naked photospheres model (grey curve) plus the expected emission from a razor-thin circumbinary disk extending down to twice the binary separation of $\sim$11 $R_\odot$ (brown dot-dashed line), which is illuminated by the central star and heated by the gravitational potential energy released from accretion with $\dot{M} = 3 \times 10^{-7}$ $M_\odot$ yr^{-1}.

validates our initial assumption of cluster membership. We note that the reddening (within reasonable limits) has little effect on the conclusions, acting only to find a slightly higher primary temperature, and the constraint placed on the radius ratio from the light curve solution helped only to differentiate between groups of plausible models, each of which had comparable χ^2 values. The primary and secondary star SEDs are shown in Fig. 6.12 by the dotted red and blue curves respectively, with their combined flux shown in grey. The two stars alone cannot explain the IRAC data points[5]; additional emission at cooler temperatures than the stars (including starspots) is required.

In CoRoT 223992193 we found that emission from a circumbinary disk could not explain the modest IR excess (given constraints on the mass accretion rate) but that it was consistent with emission from a small amount of optically thin dust in the central cavity of such a disk. We do not have a similar constraint on the mass accretion rate in Mon-1411

[5]We also tried fitting the whole SED with two stellar photospheres but could still not reproduce the IRAC fluxes

but given its Class II nature one might argue that it could be substantially higher. Typical mass accretion rates for classical T Tauri stars (which usually display Class II SEDs) are of order $10^{-7} - 10^{-8}$ $M_\odot$ yr^{-1} (e.g. Valenti et al., 1993; Hartigan et al., 1995; Gullbring et al., 1998). Following our analysis of CoRoT 223992193 we approximate the two stars with a single star (using the temperatures and radii determined above, and inferring masses from the Baraffe et al. (2015) models at 3 Myr), and refit the whole SED as the sum of our stellar model plus the expected emission from a razor-thin circumbinary disk extending down to twice the binary separation[6]. In such a model, the IR excess is best explained with a mass accretion rate of $\dot{M} \sim 3 \times 10^{-7}$ $M_\odot$ yr^{-1}, consistent with the vales given above. The result is the black curve in Fig. 6.12, which is able to broadly reproduce the main features of the SED. Shi & Krolik (2015) have shown that the mass accretion rate within the circumbinary disk equals the rate onto the stars and so we expect material to stream through the inner cavity and onto the binary. This material would have temperatures ranging up to the dust sublimation temperature of $T \sim 1500$ K and would therefore contribute emission to the K and 3.6 μm bands, which are under predicted by the current model.

If we had precise constraints on the temperatures and radii of the two stars we could perform a more sophisticated modelling of the SED. Such an effort should include a more realistic circumbinary disk model, which possesses vertical extent, and include emission from optically thin dust in the cavity. Accurately estimating the nebula contribution in the IRAC bands from higher resolution images would also be beneficial.

6.5 Conclusions

We set out to characterise the new eclipsing systems in STF 951, namely V780 Mon and Mon-1411, to determine evidence for youth and cluster membership, and hence ascertain whether the three eclipsing systems (including V684 Mon) might be associated and furthermore, infer whether they could have formed from the same parent molecular cloud.

V780 Mon is revealed to be a tight visual binary. Joint analysis of the light curve and spectra suggests the eclipsing component is either a hot subdwarf primary and low-mass

[6]The theoretical limit on the inner edge of such a disk (Lin & Papaloizou, 1979)

MS secondary, or a massive MS primary and low-mass PMS secondary. We tentatively favour the latter hypothesis given the system's location. The light curves and SED of Mon-1411 are consistent with a low-mass member of NGC 2264.

It is possible that the eclipsing binaries V684 Mon, V780 Mon and Mon-1411 are members of a multiple that formed from the same parent molecular cloud. Assuming all stars form as binaries with random inclinations, and given the parameters found for V780 Mon and Mon-1411, and literature values for V684 Mon, the probability of the three systems being unassociated, yet all displaying eclipses, is of order $\sim$4 %. Although this is not conclusive, it is arguably suggestive that the most likely interpretation for the three eclipsing systems is that they are associated and hence all young members of NGC 2264. Further observations, specifically spectroscopy of V780 Mon and Mon-1411 are needed to confirm this tentative interpretation.

An interesting avenue to pursue in future would be to study archival photometric plates of the region which, if the time coverage is sufficient, could provide evidence for kinematic association, not only between V684 Mon, V780 Mon and Mon-1411, but also for NGC 2264 67 and the tertiary component of V780 Mon. Furthermore, the ongoing GAIA mission should also shed light on their potential association.

Chapter 7

Conclusions

This thesis presented a study of eclipsing binaries discovered in the ∼3 Myr NGC 2264 star forming region by the CoRoT and *Spitzer* space missions. A sample of EBs in a young open cluster such as this, constitutes a particularly strong test of stellar evolution models because the EBs share the same age and composition, yet span a wide range of masses. Furthermore, young binary star systems are complex objects, which display significant photometric and spectroscopic variability over a range of timescales and wavelengths. With known stellar parameters, eclipsing binaries offer powerful test-beds for characterising variability in young binary systems.

Accurate characterisation of the fundamental stellar parameters in PMS EBs requires robust treatment of sources of uncertainties. Innovative methods, based on Gaussian process regression, were applied to areas of the light curve modelling and radial velocity determination where standard approaches are arguably unsatisfactory: namely, the OOE removal process and the extraction of RVs from cross-correlation functions.

CoRoT 223992193 is arguably the most interesting system presented as it displays complex photometric and spectroscopic variability and is the first low-mass PMS EB to show evidence of a circumbinary disk. Another potentially significant discovery was found in a visual multiple system, which contains three EBs spanning B–M spectral types. If these are confirmed to be members of the same multiple, they could provide a powerful test of star formation and stellar evolution models. Several other potential cluster members have been discovered and are in various stages of characterisation. Once complete the full

NGC 2264 sample will form one of the most stringent tests of PMS stellar evolution models to date.

In the following sections we briefly detail the important results of each chapter, before giving a final concluding remark.

Chapter 2. Improving the CoRoT background correction

Chapter 2 presented attempts to improve the CoRoT background correction after noting that eclipses in SRa05 were shallower than SRa01 (the 2011/2012 and 2008 CoRoT observations, respectively). The eclipse discrepancies arose from a higher and more spatially variable background in SRa05, which was not fully accounted for by CoRoT's median correction. We attempted to improve the background correction by applying a spatially dependent correction to account for nebula emission and systematics. While a slight improvement over the nominal CoRoT background correction was achieved in both runs, the model failed to rectify the difference in eclipse depths. In the following chapters therefore, we focussed on the SRa01 light curves for determining the eclipse parameters, using the SRa05 data to constrain the system ephemerides only.

Chapter 3. Fundamental parameters of CoRoT 223992193

Chapter 3 presented the initial characterisation of CoRoT 223992193: a detached, double-lined eclipsing binary, comprising two pre-main sequence M dwarfs. Using multi-epoch optical and near-IR follow-up spectroscopy with VLT/FLAMES and WHT/ISIS we obtained a full orbital solution and derived the fundamental parameters of both stars by modelling the light curve and radial velocity data. The orbit is circular with a period of 3.8745745 ± 0.0000014 days. The masses and radii of the two stars are 0.67 ± 0.01 and 0.495 ± 0.007 $M_{\odot}$ and 1.30 ± 0.04 and $1.11\ ^{+0.04}_{-0.05}$ $R_{\odot}$, respectively. The systemic velocity is within 1σ of the cluster value which, along with the presence of lithium absorption, strongly indicates cluster membership.

At the time of discovery this was only the ninth PMS EB system with component

masses below 1.5 $M_{\odot}$. It is a useful test of evolutionary models of young low-mass stars, as it lies in a region of parameter space where observational constraints are scarce. Within the current uncertainties, the parameters of the two stars are essentially consistent with the predictions of PMS stellar evolution models for ages of ∼3.5–6 Myr. Although we broke the degeneracy between the radius and surface brightness ratios, which can be a severe limitation in grazing EB systems, the final uncertainties on the component masses and radii are still a few percent. As highlighted by Torres et al. (2010), sub-percent accuracies are needed to place truly significant constraints on evolutionary models.

Chapter 4. CoRoT 223992193: environment and variability

Chapter 4 presented analysis of CoRoT 223992193's spectral energy distribution (SED) and investigated the system's photometric and spectroscopic variability. The SED revealed a mid-infrared excess, which was modelled as thermal emission from a small amount of dust located in the inner cavity of a circumbinary disk. The presence of dust in the cavity at ∼4–5 Myr implies the presence of a circumbinary disk as the most natural means of replenishment.

CoRoT 223992193 displays complex photometric and spectroscopic variability over a range of timescales and wavelengths. The large scale structure in both CoRoT light curves is consistent with the constructive and destructive interference of starspot signals at two slightly different periods. The $v \sin i$ of both stars imply the two stars have slightly different rotation periods: the primary is consistent with synchronisation and the secondary rotates slightly supersynchronously. Comparison of the raw 2011/2012 CoRoT and *Spitzer* light curves to the residuals of the spot model in colour-magnitude space indicated additional contributions consistent with a combination of variable dust emission and obscuration. For the latter, short-duration flux dips preceding secondary eclipse were identified in all three CoRoT and Spitzer bands. A model of the inner regions of the binary was used to propose that these dips could be caused by partial occultation of the central binary by the accretion stream onto the primary star.

The VLT/FLAMES Hα profiles revealed an emission profile associated with each star. The majority of this is consistent with chromospheric emission but the presence of additional, higher velocity emission could be due to prominences, or alternatively interpreted as having an accretion-related origin. In addition, the simultaneous u and r-band CFHT/MegaCam observations revealed a short-lived u-band excess consistent with either a stellar flare or an accretion hot spot.

The photometric and spectroscopic variations are consistent with the picture of two active stars possibly undergoing non-steady, low-level accretion; the system's very high inclination provides a new view of such variability.

Chapter 5. The NGC 2264 EB sample

Chapter 5 presented the current work to date on the NGC 2264 EB sample. The techniques developed to characterise CoRoT 223992193 were applied to the sample. These work well for near equal-mass systems and two main sequence EBs were solved. However, primarily due to the one-dimensional nature of the radial velocity determination, the majority of the sample remains unsolved. Four low-mass EBs show evidence for youth, with three of these displaying low-to-extreme brightness (and hence mass) ratios. Interestingly, no such PMS systems have been reported in the literature. This could be due to a number of factors, including their difficulty to solve, the photometric precision of previous studies, or a more favourable environment in NGC 2264 for the survival of close, low-mass-ratio binaries. *Kepler*/K2 should shed light on this matter over the next few years.

As the applied methods did not work well on all candidate PMS EBs, an alternative method for the radial velocity determination was presented, based on direct modelling of the spectra rather than cross-correlation. The development of this technique is still ongoing, but it will be applied to the sample in future work. A slight improvement to the light curve analysis was also presented, in which the OOE variability is simultaneously modelled with the eclipses to provide a more robust treatment for the OOE variations across eclipse. This model was applied to the components of the visual multiple discussed

in Chapter 6.

Chapter 6. A visual multiple containing three EBs

Chapter 6 presented a visual multiple containing three EBs spanning B–M spectral types. One of the EBs, V684 Mon, was previously known. In addition, eclipses were detected on V780 Mon and Mon-1411. We investigated the possibility that these three nearest neighbour stars could be members of the same multiple, having formed from the same parent molecular cloud, especially given that V684 Mon is a known likely cluster member.

The light curves of Mon-1411 suffer from systematic effects, which inhibited clear inference about the stellar properties. However, the SED revealed a mid-IR excess; this was found to be consistent with a low-mass cluster member possessing a circumbinary disk. Spectroscopic observations of this system are required to solve for the fundamental parameters and confirm membership.

V780 Mon is interesting system in its own right. Joint analysis of the CoRoT light curve and VLT/FLAMES spectra implied similar radii for the two stars but an extreme brightness ratio. Such a scenario is consistent with either an evolved system comprising a hot subdwarf primary and a low-mass main sequence secondary, or a young system comprising a massive main sequence primary and a lower-mass PMS secondary. The Hα and He I 667.8 nm profiles are consistent with either scenario. Arguably, the young system scenario is more appealing due to the system's apparent proximity to two other likely young EBs in NGC 2264. In an attempt to rule out this scenario, the system's SED was analysed but was found to be consistent with cluster membership, given the temperature and radii constraints, although a significant amount of extinction is required.

Future work on Mon-1411 and V780 Mon is required but, if they are found to be likely cluster members, it is possible that all three EBs are members of the same multiple. They would then constitute the first triply-eclipsing multiple system discovered, and provide a powerful test of star formation and stellar evolution models in dense cluster environments.

Final remark

The characterisation of young eclipsing binaries is a difficult task: it is both time and resource intensive, and can suffer from many potential complications owing to the youth of the systems and their natal environment. However, the systems we do find are all interesting in their own rights, from circumbinary disks and complex variability to extreme mass ratios and multiplicity. The importance of such systems for furthering our understanding of the formation and early evolution of stars and clusters will no doubt ensure continued effort to characterise more PMS EBs across as wide a range of mass, age and metallicity as possible.

Appendix A

Additional EBs in the NGC 2264 sample

A.1 EB 0254 (CoRoT 223966541)

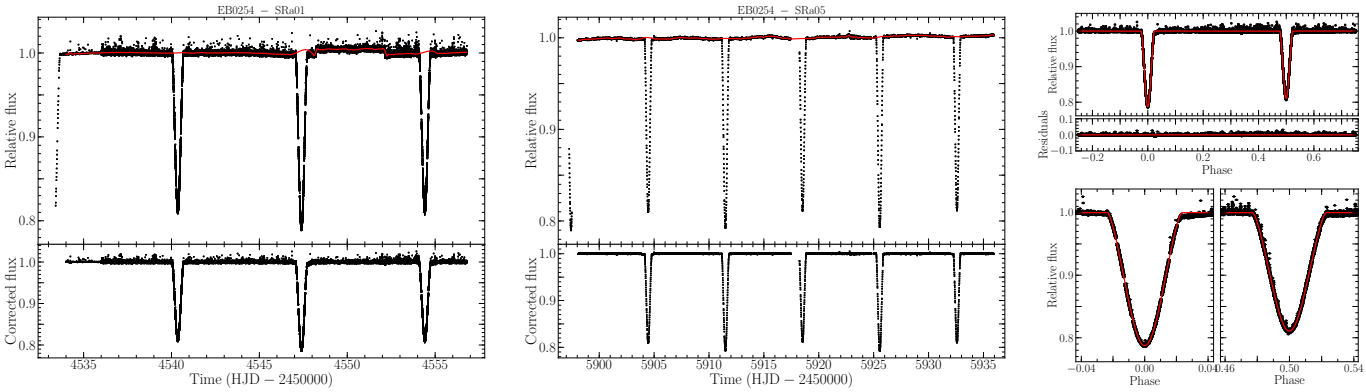

Figure A.1: SRa01 (left) and SRa05 (middle) light curves, and JKTEBOP phase folded fit (right).

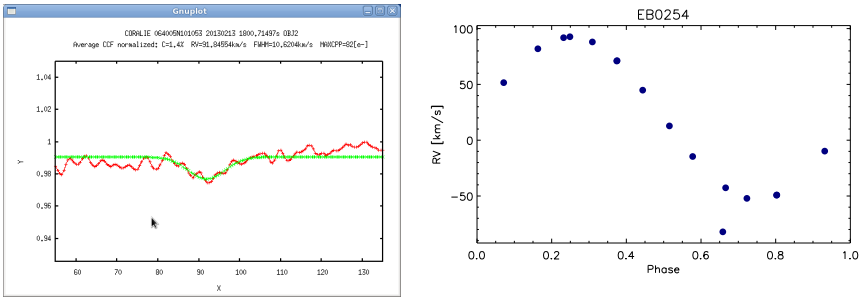

Figure A.2: CORALIE CCF (zoomed in; middle) and RV orbit (right).

Table A.1: Fundamental parameters

P	(days)	$14.06287760 \pm 0.00000087$
$T_{\rm prim}$	(HJD)	$2454533.331860 \pm 0.000085$
$e \cos \omega$		-0.0000966 ± 0.0000088
$e \sin \omega$		-0.02004 ± 0.00066
J		0.8490 ± 0.0062
$(R_{\rm pri} + R_{\rm sec})/a$		0.1631 ± 0.0022
$R_{\rm sec}/R_{\rm pri}$		0.75 ± 0.12
i	(°)	85.66 ± 0.27

A.2 EB 0360 (CoRoT 223942686)

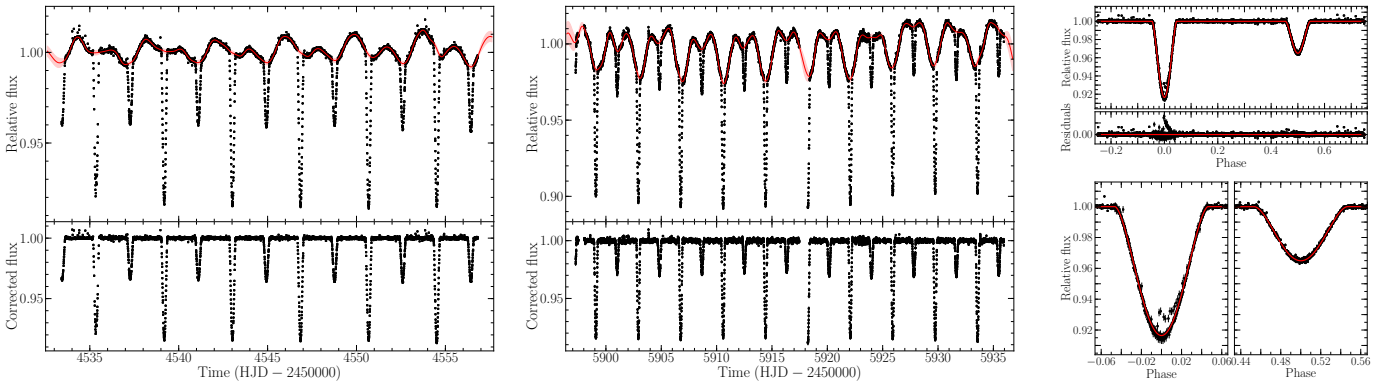

Figure A.3: SRa01 (left) and SRa05 (middle) light curves, and JKTEBOP phase folded fit (right).

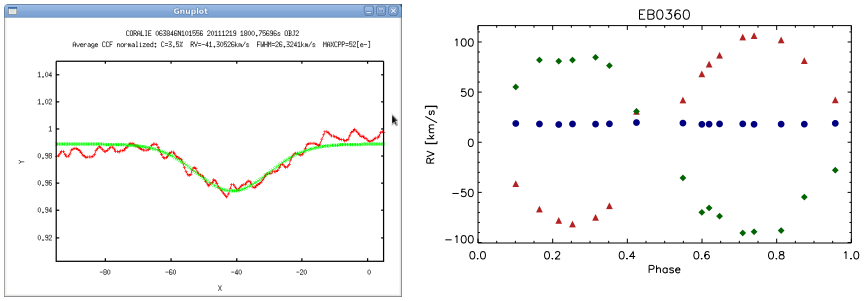

Figure A.4: CORALIE CCF (zoomed in; middle) and RV orbit (right).

Table A.2: Fundamental parameters

P	(days)	3.8 ± 0.0
$T_{\rm prim}$	(HJD)	2454535.4 ± 0.0
$e \cos \omega$		0.00016 ± 0.00013
$e \sin \omega$		-0.0220 ± 0.0067
J		0.352 ± 0.013
$(R_{\rm pri} + R_{\rm sec})/a$		0.3773 ± 0.0065
$R_{\rm sec}/R_{\rm pri}$		0.486 ± 0.043
i	($^\circ$)	75.29 ± 0.60

A.3 EB 0393 (CoRoT 223946171)

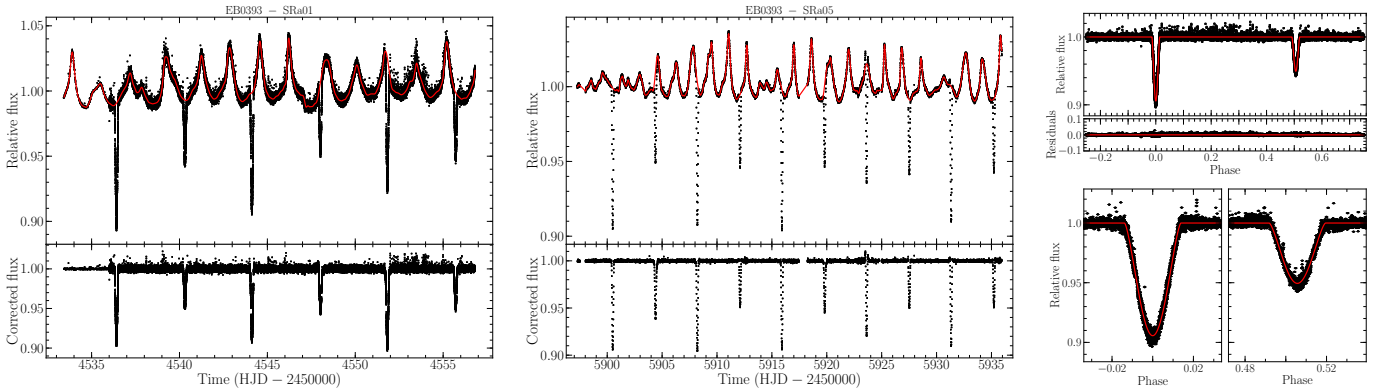

Figure A.5: SRa01 (left) and SRa05 (middle) light curves, and JKTEBOP phase folded fit (right).

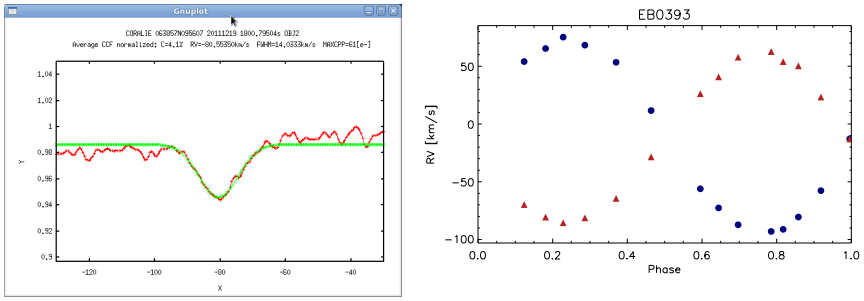

Figure A.6: CORALIE CCF (zoomed in; middle) and RV orbit (right).

Table A.3: Fundamental parameters

P	(days)	$7.70670904 \pm 0.00000039$
$T_{\rm prim}$	(HJD)	$2454536.416874 \pm 0.000059$
$e \cos \omega$		0.008894 ± 0.000029
$e \sin \omega$		-0.010 ± 0.019
J		0.503 ± 0.070
$(R_{\rm pri} + R_{\rm sec})/a$		0.120 ± 0.010
$R_{\rm sec}/R_{\rm pri}$		0.57 ± 0.29
i	(°)	85.24 ± 0.84

A.4 EB 0445 (CoRoT 224013042)

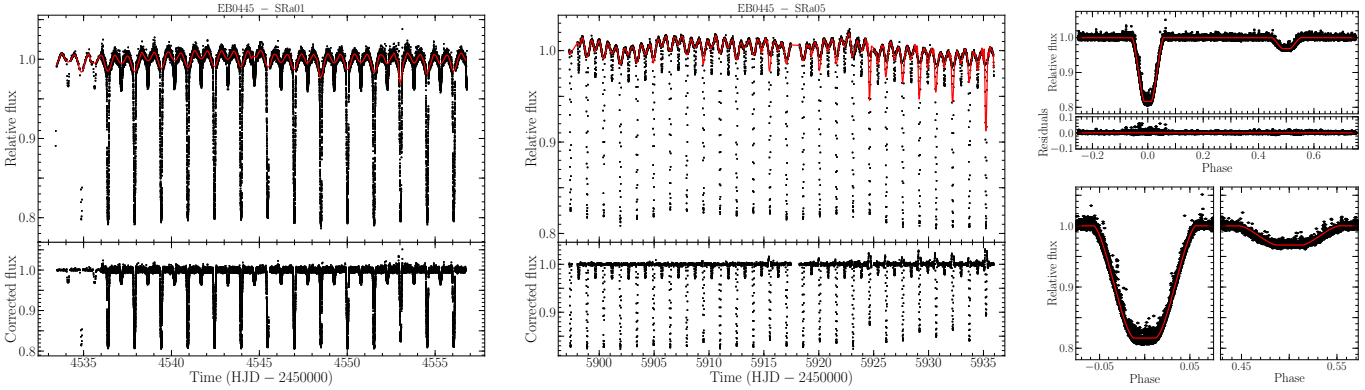

Figure A.7: SRa01 (left) and SRa05 (middle) light curves, and JKTEBOP phase folded fit (right).

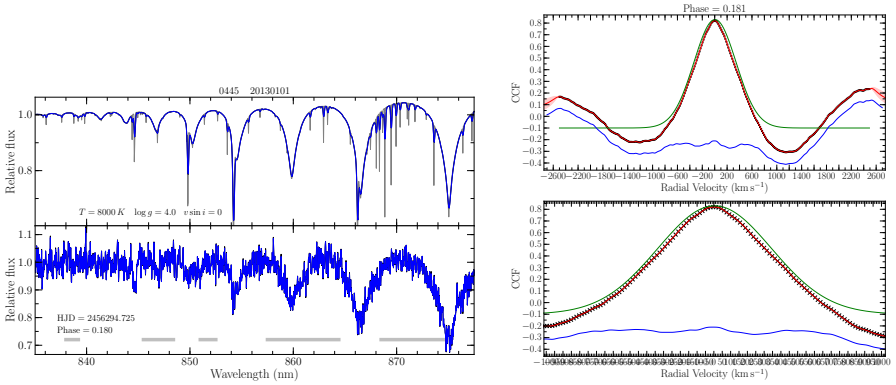

Figure A.8: ISIS spectra (left), CCF (modelled with Gaussian(s) and a GP; middle) and RV orbit (right).

Table A.4: Fundamental parameters

P	(days)	$1.51559534 \pm 0.00000016$
$T_{\rm prim}$	(HJD)	$2454533.32994 \pm 0.00061$
$e \cos \omega$		0.00025 ± 0.00011
$e \sin \omega$		-0.04341 ± 0.00097
J		0.17134 ± 0.00041
$(R_{\rm pri} + R_{\rm sec})/a$		0.35120 ± 0.00019
$R_{\rm sec}/R_{\rm pri}$		0.435145 ± 0.000097
i	(°)	$83.47494713 \pm 0.00000045$

A.5 EB 0824 (CoRoT 223971548)

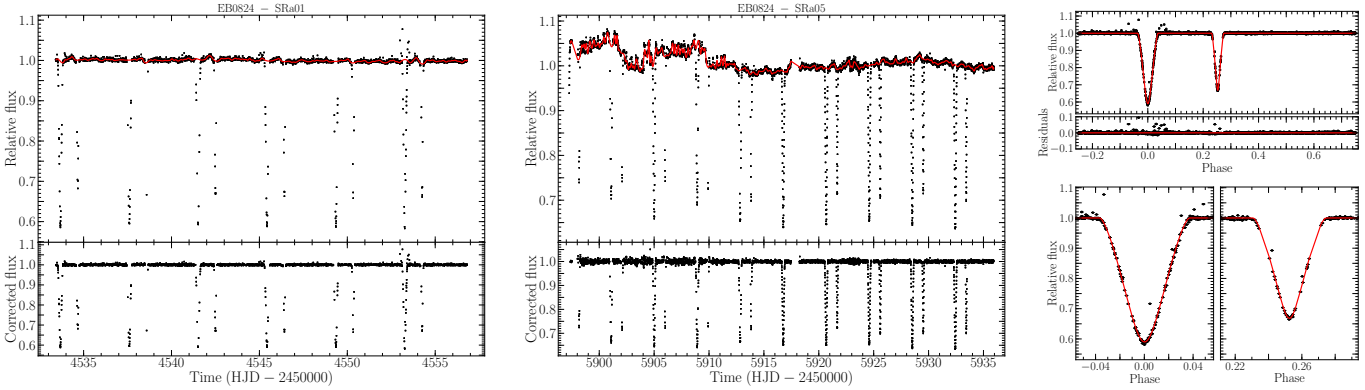

Figure A.9: SRa01 (left) and SRa05 (middle) light curves, and JKTEBOP phase folded fit (right).

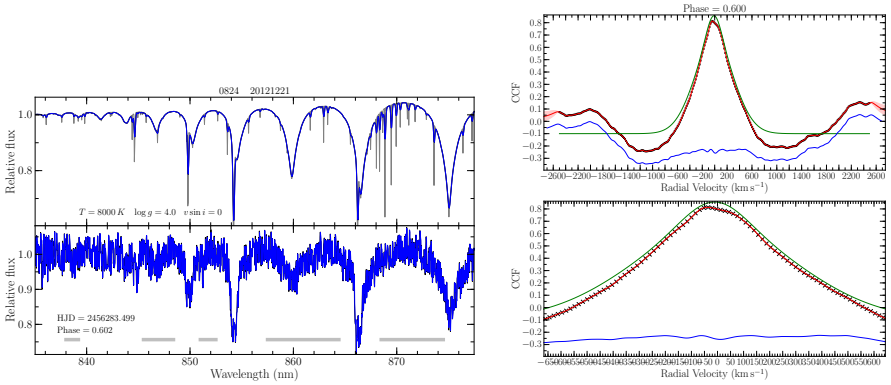

Figure A.10: ISIS spectra (left), CCF (modelled with Gaussian(s) and a GP; middle) and RV orbit (right).

Table A.5: Fundamental parameters

P	(days)	$3.91809328 \pm 0.00000062$
$T_{\rm prim}$	(HJD)	$2454533.67241 \pm 0.00022$
$e \cos \omega$		-0.38491 ± 0.00042
$e \sin \omega$		-0.2677 ± 0.0038
J		0.6914 ± 0.0088
$(R_{\rm pri} + R_{\rm sec})/a$		0.1954 ± 0.0011
$R_{\rm sec}/R_{\rm pri}$		1.186 ± 0.055
i	(°)	87.406 ± 0.088

A.6 EB 1021 (CoRoT 223955882)

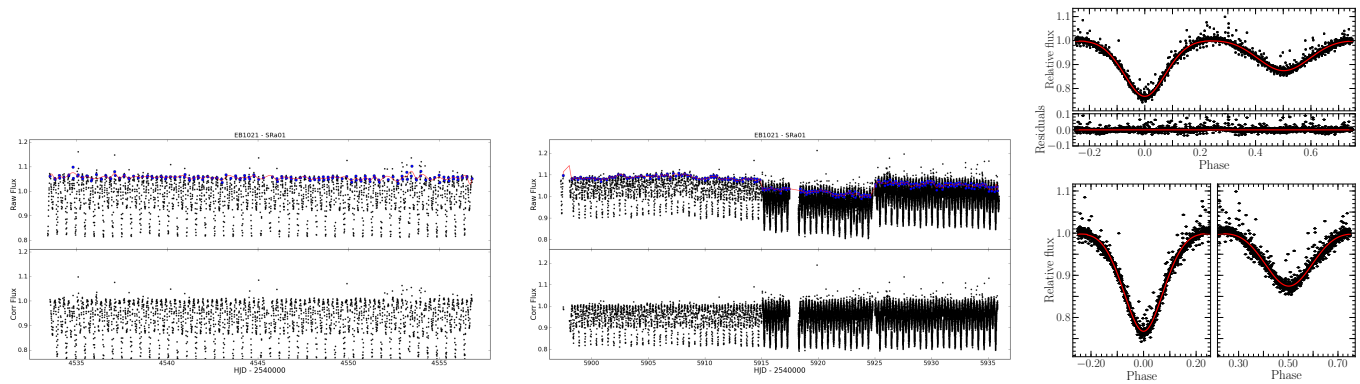

Figure A.11: SRa01 (left) and SRa05 (middle) light curves, and JKTEBOP phase folded fit (right).

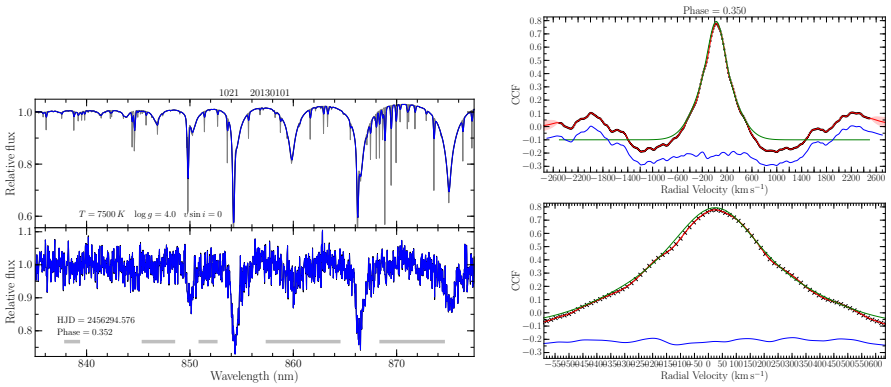

Figure A.12: ISIS spectra (left), CCF (modelled with Gaussian(s) and a GP; middle) and RV orbit (right).

Table A.6: Fundamental parameters

P	(days)	$0.51102265 \pm 0.00000022$
$T_{\rm prim}$	(HJD)	$2454533.92314 \pm 0.00066$
$e \cos \omega$		0.00267 ± 0.00078
$e \sin \omega$		0.1102 ± 0.0061
J		0.74 ± 0.13
$(R_{\rm pri} + R_{\rm sec})/a$		1.0216 ± 0.0052
$R_{\rm sec}/R_{\rm pri}$		0.74 ± 0.40
i	(°)	58.8 ± 6.6

A.7 EB 1113 (CoRoT 223939728)

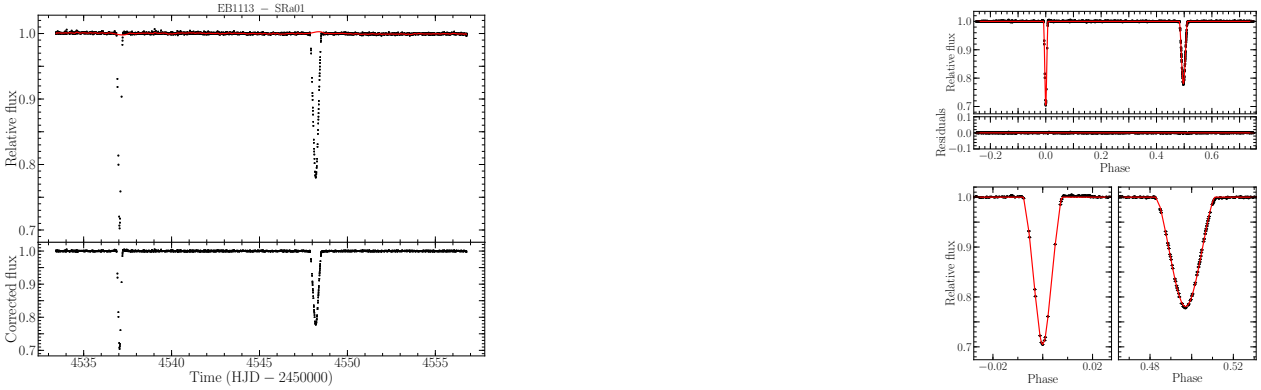

Figure A.13: SRa01 (left) and SRa05 (middle) light curves, and JKTEBOP phase folded fit (right).

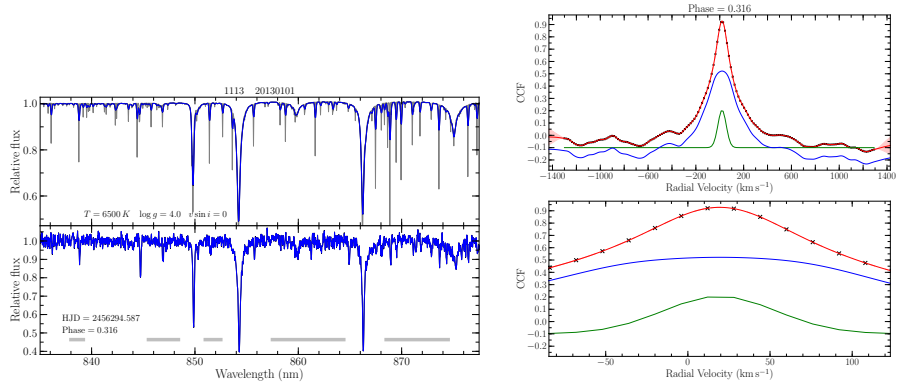

Figure A.14: ISIS spectra (left), CCF (modelled with Gaussian(s) and a GP; middle) and RV orbit (right).

Table A.7: Fundamental parameters

P	(days)	22.442 ± 0.011
$T_{\rm prim}$	(HJD)	$2454537.04509 \pm 0.00014$
$e \cos \omega$		-0.00434 ± 0.00037
$e \sin \omega$		0.33076 ± 0.00095
J		1.188 ± 0.017
$(R_{\rm pri} + R_{\rm sec})/a$		0.07099 ± 0.00020
$R_{\rm sec}/R_{\rm pri}$		1.305 ± 0.033
i	(°)	88.577 ± 0.021

A.8 EB 1340 (CoRoT 223941278)

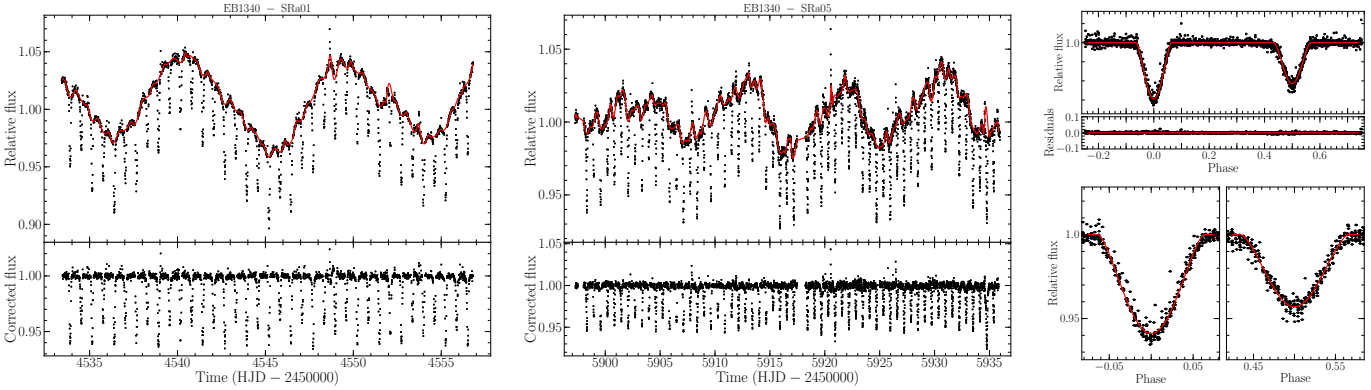

Figure A.15: SRa01 (left) and SRa05 (middle) light curves, and JKTEBOP phase folded fit (right).

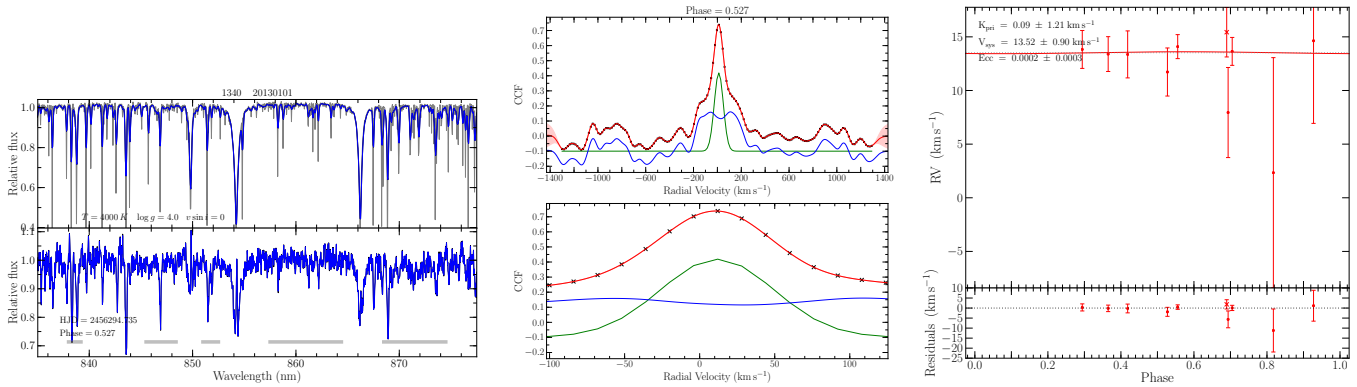

Figure A.16: ISIS spectra (left), CCF (modelled with Gaussian(s) and a GP; middle) and RV orbit (right).

Table A.8: Fundamental parameters

P	(days)	$1.25638613 \pm 0.00000087$
$T_{\rm prim}$	(HJD)	2454533.875 ± 0.016
$e \cos \omega$		0.00018 ± 0.00039
$e \sin \omega$		-0.098 ± 0.051
J		0.33 ± 0.13
$(R_{\rm pri} + R_{\rm sec})/a$		0.5384 ± 0.0059
$R_{\rm sec}/R_{\rm pri}$		0.67 ± 0.15
i	(°)	66.70 ± 0.46

A.9 EB 1408 (CoRoT 224009183)

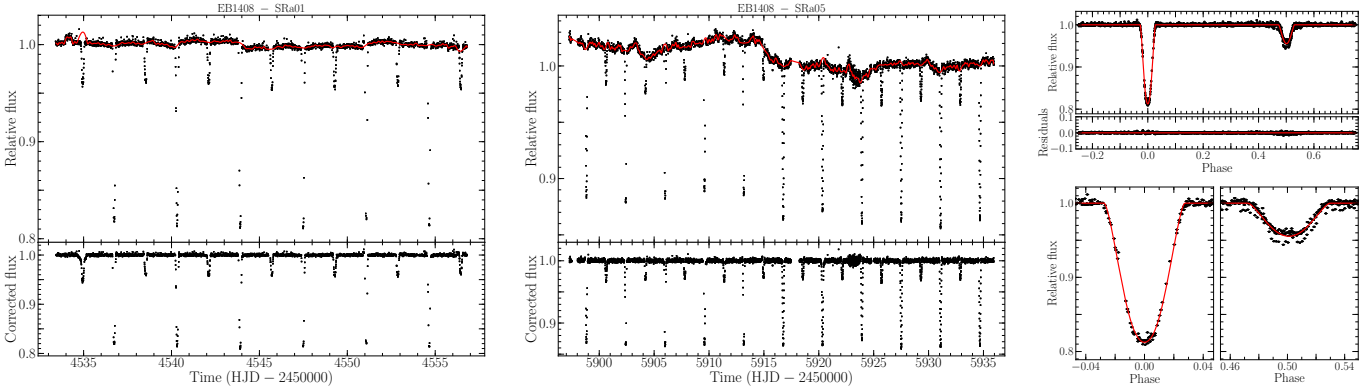

Figure A.17: SRa01 (left) and SRa05 (middle) light curves, and JKTEBOP phase folded fit (right).

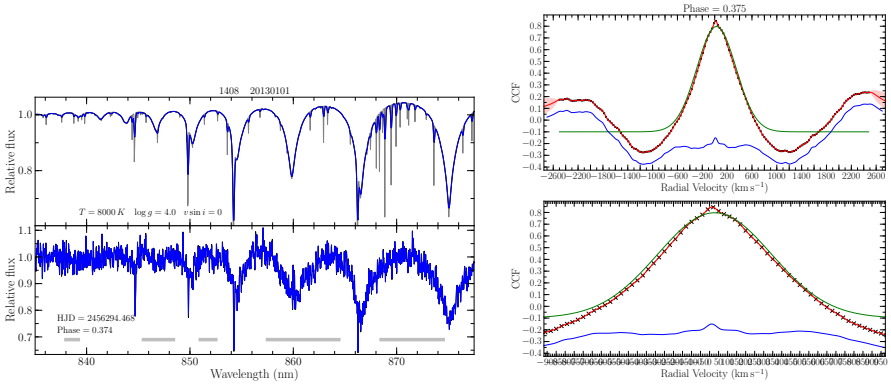

Figure A.18: ISIS spectra (left), CCF (modelled with Gaussian(s) and a GP; middle) and RV orbit (right).

Table A.9: Fundamental parameters

P	(days)	3.5844638 ± 0.0000010
$T_{\rm prim}$	(HJD)	$2454536.73808 \pm 0.00040$
$e \cos \omega$		0.00165 ± 0.00019
$e \sin \omega$		0.091 ± 0.013
J		0.350 ± 0.019
$(R_{\rm pri} + R_{\rm sec})/a$		0.2300 ± 0.0013
$R_{\rm sec}/R_{\rm pri}$		3.359 ± 0.092
i	(°)	81.371 ± 0.071

A.10 EB 1572 (CoRoT 223998341)

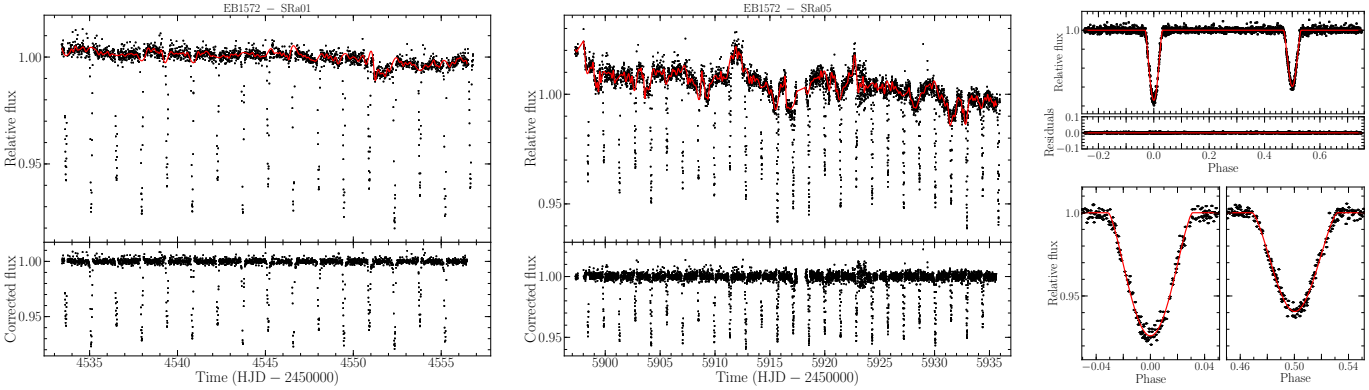

Figure A.19: SRa01 (left) and SRa05 (middle) light curves, and JKTEBOP phase folded fit (right).

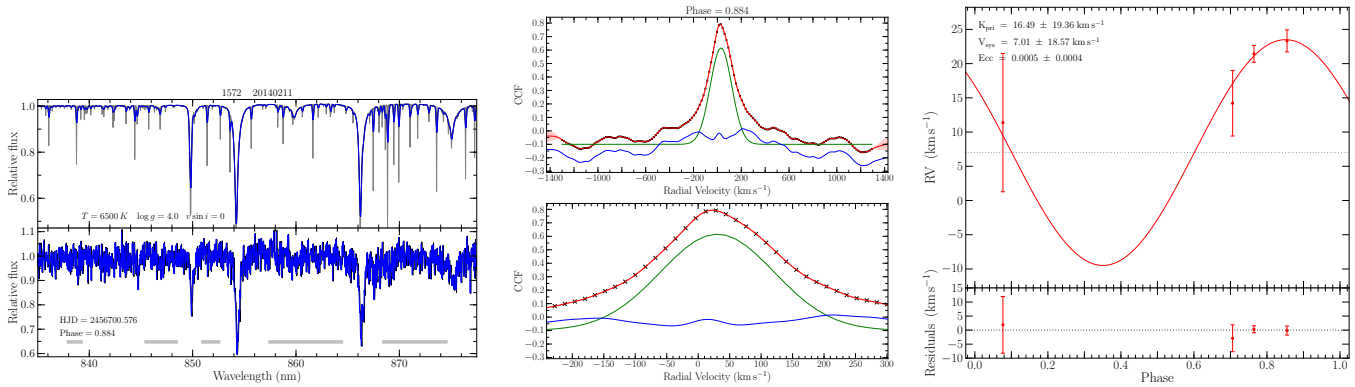

Figure A.20: ISIS spectra (left), CCF (modelled with Gaussian(s) and a GP; middle) and RV orbit (right).

Table A.10: Fundamental parameters

P	(days)	2.8762672 ± 0.0000017
$T_{\rm prim}$	(HJD)	$2454535.08003 \pm 0.00084$
$e \cos \omega$		0.00051 ± 0.00018
$e \sin \omega$		-0.115 ± 0.053
J		0.35 ± 0.14
$(R_{\rm pri} + R_{\rm sec})/a$		0.2779 ± 0.0059
$R_{\rm sec}/R_{\rm pri}$		0.84 ± 0.26
i	(°)	78.60 ± 0.27

A.11 EB 1632 (CoRoT 223976178)

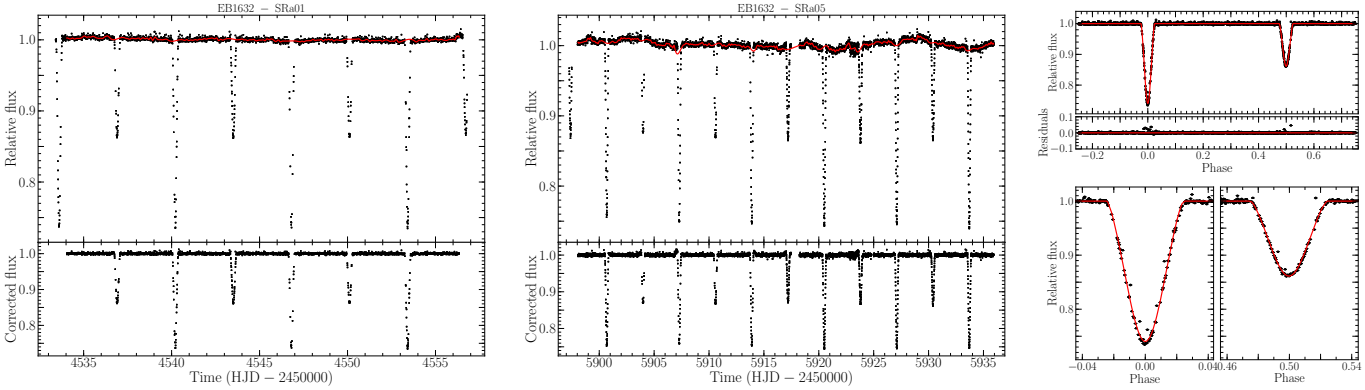

Figure A.21: SRa01 (left) and SRa05 (middle) light curves, and JKTEBOP phase folded fit (right).

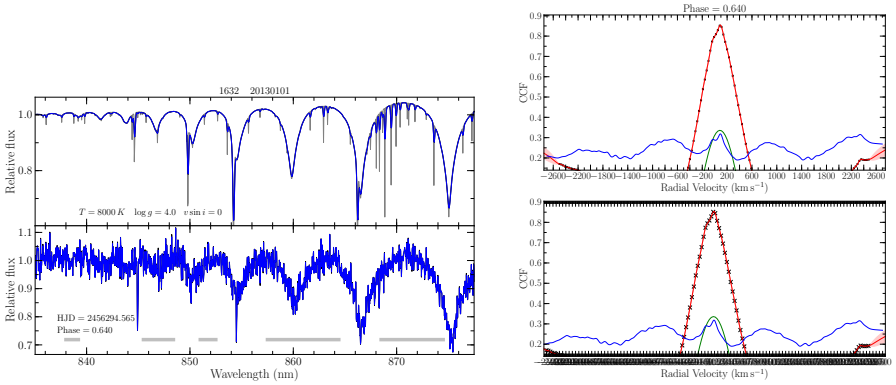

Figure A.22: ISIS spectra (left), CCF (modelled with Gaussian(s) and a GP; middle) and RV orbit (right).

Table A.11: Fundamental parameters

P	(days)	6.6041871 ± 0.0000046
$T_{\rm prim}$	(HJD)	$2454540.22548 \pm 0.00095$
$e \cos \omega$		-0.000498 ± 0.000088
$e \sin \omega$		0.0061 ± 0.0028
J		0.5404 ± 0.0066
$(R_{\rm pri} + R_{\rm sec})/a$		0.169 ± 0.012
$R_{\rm sec}/R_{\rm pri}$		0.67 ± 0.31
i	(°)	86.0 ± 1.7

A.12 EB 2103 (CoRoT 223951589)

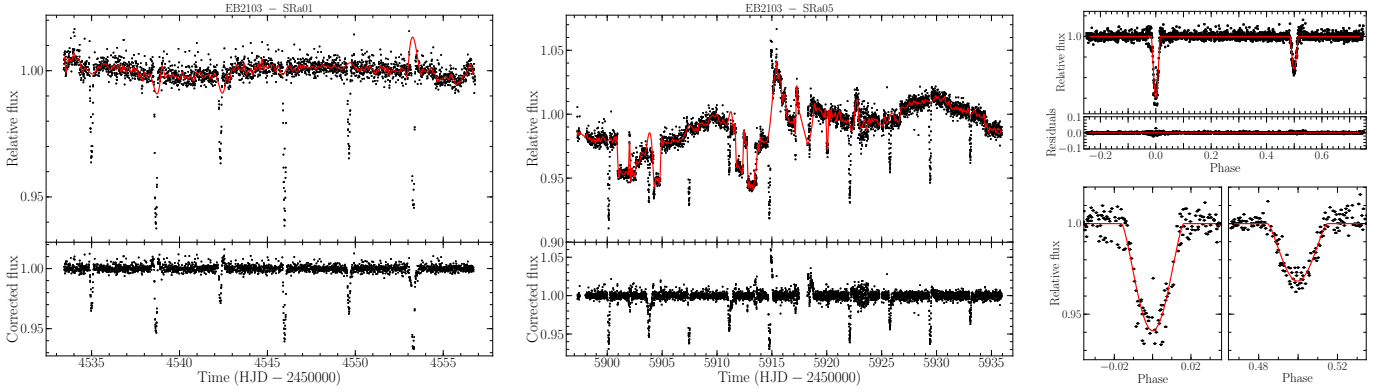

Figure A.23: SRa01 (left) and SRa05 (middle) light curves, and JKTEBOP phase folded fit (right).

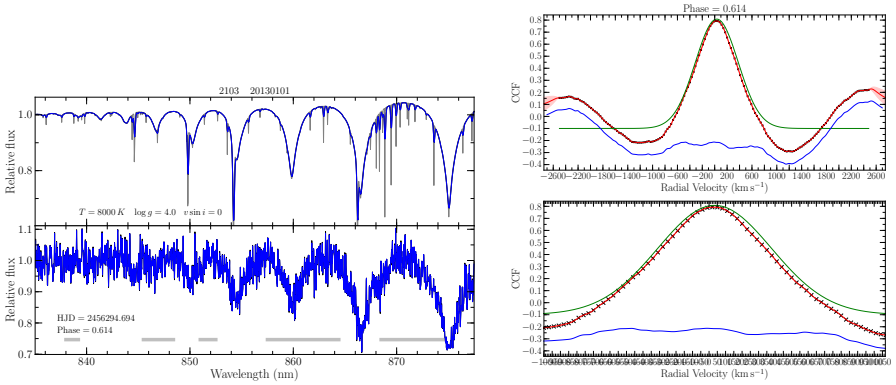

Figure A.24: ISIS spectra (left), CCF (modelled with Gaussian(s) and a GP; middle) and RV orbit (right).

Table A.12: Fundamental parameters

P	(days)	$7.35945658 \pm 0.00000069$
$T_{\rm prim}$	(HJD)	$2454538.62377 \pm 0.00045$
$e \cos \omega$		-0.00050 ± 0.00029
$e \sin \omega$		0.032 ± 0.056
J		0.82 ± 0.31
$(R_{\rm pri} + R_{\rm sec})/a$		0.171 ± 0.050
$R_{\rm sec}/R_{\rm pri}$		1.3 ± 8.9
i	(°)	81.9 ± 3.6

A.13 EB 2677 (CoRoT 223954720)

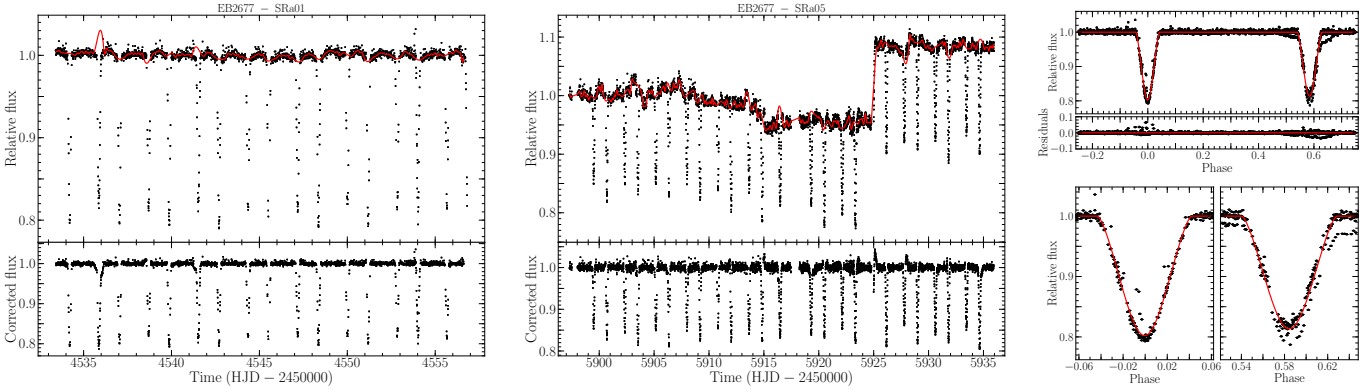

Figure A.25: SRa01 (left) and SRa05 (middle) light curves, and JKTEBOP phase folded fit (right).

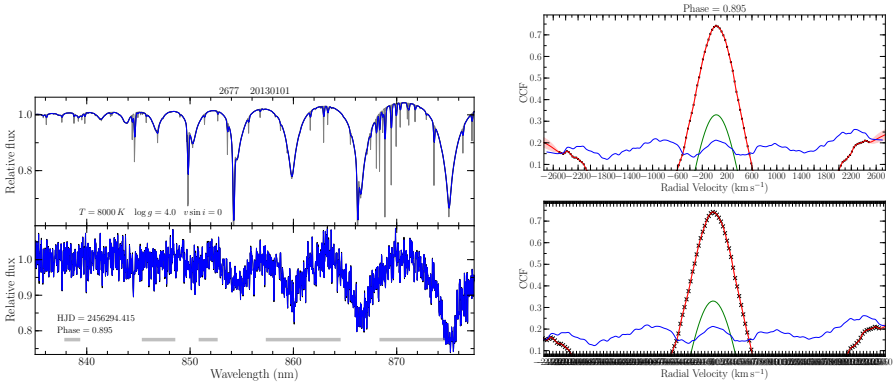

Figure A.26: ISIS spectra (left), CCF (modelled with Gaussian(s) and a GP; middle) and RV orbit (right).

Table A.13: Fundamental parameters

P	(days)	2.8349540 ± 0.0000012
$T_{\rm prim}$	(HJD)	2454534.2053 ± 0.0010
$e \cos \omega$		0.1320 ± 0.0019
$e \sin \omega$		0.0247 ± 0.0093
J		1.01 ± 0.10
$(R_{\rm pri} + R_{\rm sec})/a$		0.310 ± 0.041
$R_{\rm sec}/R_{\rm pri}$		0.9 ± 5.6
i	(°)	80.8 ± 5.1

A.14 EB 3190 (CoRoT 224007535)

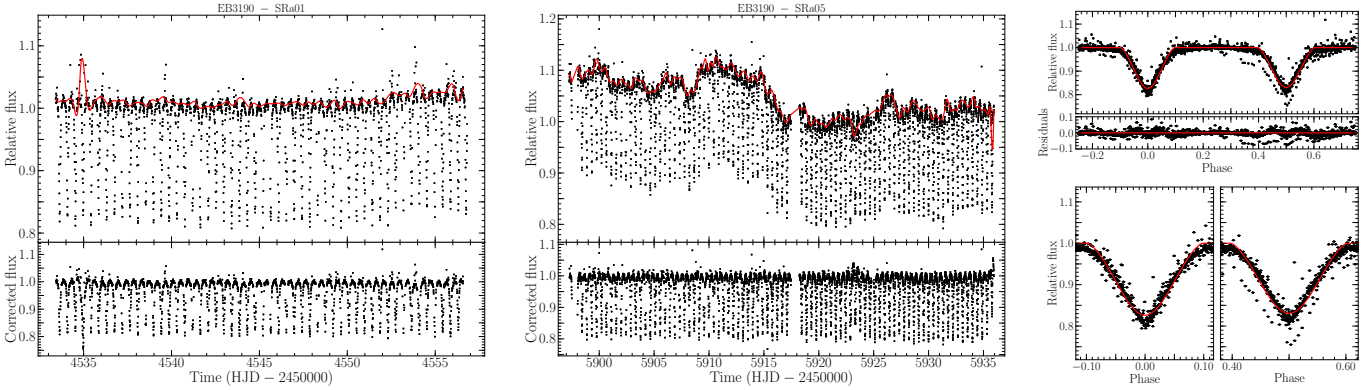

Figure A.27: SRa01 (left) and SRa05 (middle) light curves, and JKTEBOP phase folded fit (right).

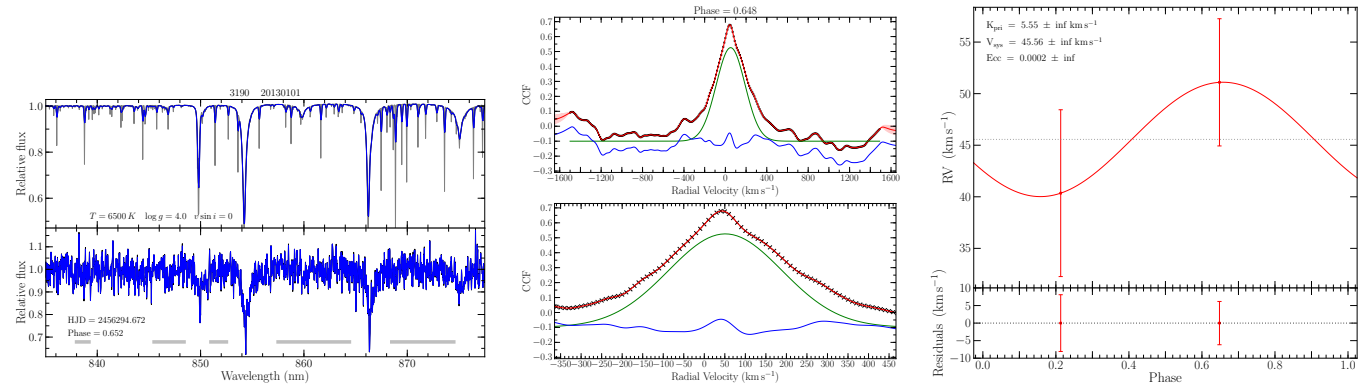

Figure A.28: ISIS spectra (left), CCF (modelled with Gaussian(s) and a GP; middle) and RV orbit (right).

Table A.14: Fundamental parameters

P	(days)	$0.88911725 \pm 0.00000019$
$T_{\rm prim}$	(HJD)	$2454533.64026 \pm 0.00030$
$e \cos \omega$		-0.00014 ± 0.00072
$e \sin \omega$		0.034 ± 0.019
J		1.09 ± 0.23
$(R_{\rm pri} + R_{\rm sec})/a$		0.652 ± 0.076
$R_{\rm sec}/R_{\rm pri}$		1.3 ± 3.9
i	(°)	69.7 ± 3.4

A.15 EB 3602 (CoRoT 223994191)

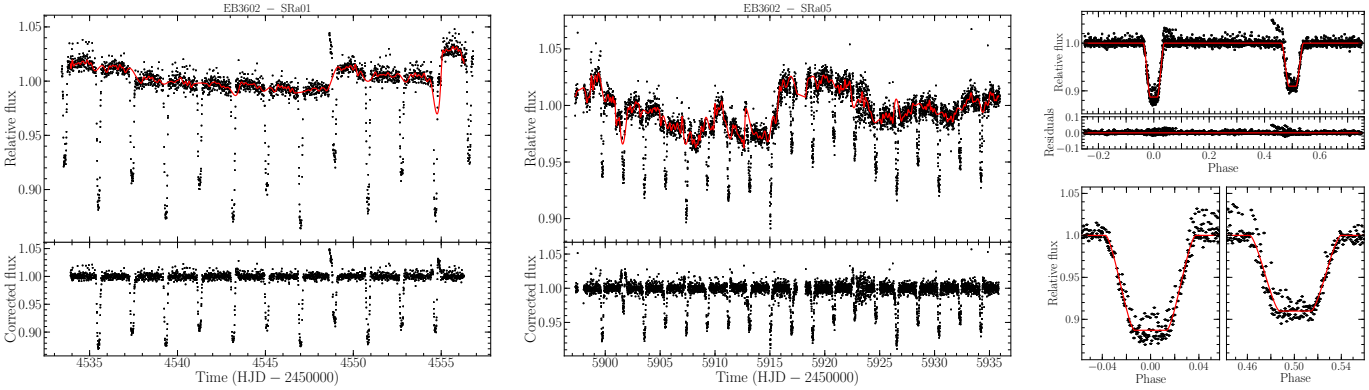

Figure A.29: SRa01 (left) and SRa05 (middle) light curves, and JKTEBOP phase folded fit (right).

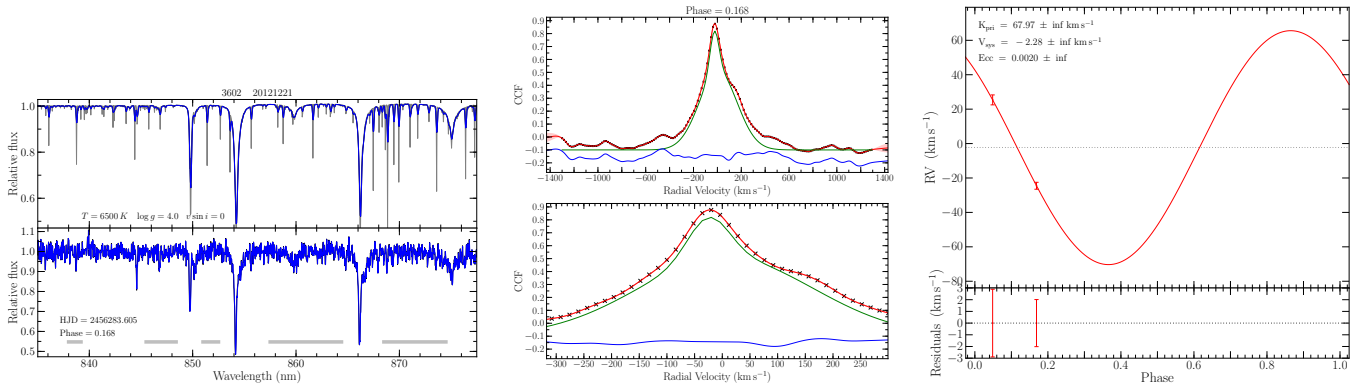

Figure A.30: ISIS spectra (left), CCF (modelled with Gaussian(s) and a GP; middle) and RV orbit (right).

Table A.15: Fundamental parameters

P	(days)	3.8321405 ± 0.0000055
$T_{\rm prim}$	(HJD)	2454535.5035 ± 0.0020
$e \cos \omega$		0.00139 ± 0.00036
$e \sin \omega$		0.0234 ± 0.0064
J		0.7979 ± 0.0078
$(R_{\rm pri} + R_{\rm sec})/a$		0.2501 ± 0.0025
$R_{\rm sec}/R_{\rm pri}$		0.3525 ± 0.0012
i	(°)	85.11 ± 0.22

References

Abazajian, K. N., et al. (2009). The Seventh Data Release of the Sloan Digital Sky Survey. ApJS, *182*, 543–558.

Adams, M. T., Strom, K. M., and Strom, S. E. (1983). The star-forming history of the young cluster NGC 2264. ApJS, *53*, 893–936.

Adelman-McCarthy, J. K. and et al. (2009). The SDSS Photometric Catalog, Release 7 (Adelman-McCarthy+, 2009). *VizieR Online Data Catalog*, *2294*, 0.

Affer, L., Micela, G., Favata, F., Flaccomio, E., and Bouvier, J. (2013). Rotation in NGC 2264: a study based on CoRoT photometric observations. MNRAS, *430*, 1433–1446.

Aigrain, S., Barge, P., Deleuil, M., Fressin, F., Moutou, C., Queloz, D., Auvergne, M., and Baglin, A. (2008). The CoRoT Exoplanet Programme: Exploring the Gas-Giant/Terrestrial Planet Transition. In G. van Belle (Ed.) *14th Cambridge Workshop on Cool Stars, Stellar Systems, and the Sun*, vol. 384 of *Astronomical Society of the Pacific Conference Series*, (p. 270).

Aigrain, S., Hodgkin, S., Irwin, J., Hebb, L., Irwin, M., Favata, F., Moraux, E., and Pont, F. (2007). The Monitor project: searching for occultations in young open clusters. MNRAS, *375*, 29–52.

Aigrain, S. and Irwin, M. (2004). Practical planet prospecting. MNRAS, *350*, 331–345.

Aigrain, S., Pont, F., and Zucker, S. (2012). A simple method to estimate radial velocity variations due to stellar activity using photometry. MNRAS, *419*, 3147–3158.

Alencar, S. H. P., et al. (2012). Accretion dynamics in the classical T Tauri star V2129 Ophiuchi. A&A, *541*, A116.

Alencar, S. H. P., Melo, C. H. F., Dullemond, C. P., Andersen, J., Batalha, C., Vaz, L. P. R., and Mathieu, R. D. (2003). The pre-main sequence spectroscopic binary AK Scorpii revisited. A&A, *409*, 1037–1053.

Alencar, S. H. P., Teixeira, P. S., Guimarães, M. M., McGinnis, P. T., Gameiro, J. F., Bouvier, J., Aigrain, S., Flaccomio, E., and Favata, F. (2010). Accretion dynamics and disk evolution in NGC 2264: a study based on CoRoT photometric observations. A&A, *519*, A88.

Alencar, S. H. P. and Vaz, L. P. R. (1997). The gravity-brightening effect and stellar atmospheres. I. Results for models with 3700K ¡ T_eff ¡ 7000K. A&A, *326*, 257–262.

Alexander, D. R. and Ferguson, J. W. (1994). Low-temperature Rosseland opacities. ApJ, *437*, 879–891.

Alexander, R. (2008). From discs to planetesimals: Evolution of gas and dust discs. New A Rev., *52*, 60–77.

Alexander, R. (2012). The Dispersal of Protoplanetary Disks around Binary Stars. ApJ, *757*, L29.

Allard, F., Homeier, D., and Freytag, B. (2011). Model Atmospheres From Very Low Mass Stars to Brown Dwarfs. In C. Johns-Krull, M. K. Browning, & A. A. West (Eds.) *16th Cambridge Workshop on Cool Stars, Stellar Systems, and the Sun*, vol. 448 of *Astronomical Society of the Pacific Conference Series*, (p. 91).

Allen, D. A. (1972). Infrared Objects in H II Regions. ApJ, *172*, L55.

Allen, L. E., et al. (2004). Infrared Array Camera (IRAC) Colors of Young Stellar Objects. ApJS, *154*, 363–366.

Alves de Oliveira, C., Moraux, E., Bouvier, J., and Bouy, H. (2012). Spectroscopy of new brown dwarf members of ρ Ophiuchi and an updated initial mass function. A&A, *539*, A151.

Ambikasaran, S., Foreman-Mackey, D., Greengard, L., Hogg, D. W., and O'Neil, M. (2014). Fast Direct Methods for Gaussian Processes. *ArXiv e-prints*.

Andersen, J. (1991). Accurate masses and radii of normal stars. A&A Rev., *3*, 91–126.

Andersen, J., Clausen, J. V., and Gimenez, A. (1993). Absolute Dimensions of Eclipsing Binaries - Part Twenty - Gg-Lupi - Young Metal Deficient B-Stars. A&A, *277*, 439.

Andersen, J., Clausen, J. V., and Nordstrom, B. (1984). Absolute dimensions of eclipsing binaries. V - VV Pyxidis, a detached early A-type system with equal components. A&A, *134*, 147–157.

Andersen, J., Nordstrom, B., and Clausen, J. V. (1990). Absolute dimensions of eclipsing binaries. XVI - V 1031 Orionis. A&A, *228*, 365–378.

Andre, P., Ward-Thompson, D., and Barsony, M. (1993). Submillimeter continuum observations of Rho Ophiuchi A - The candidate protostar VLA 1623 and prestellar clumps. ApJ, *406*, 122–141.

Armitage, P. J. (2010). *Astrophysics of Planet Formation*.

Artymowicz, P. and Lubow, S. H. (1994). Dynamics of binary-disk interaction. 1: Resonances and disk gap sizes. ApJ, *421*, 651–667.

Artymowicz, P. and Lubow, S. H. (1996). Mass Flow through Gaps in Circumbinary Disks. ApJ, *467*, L77.

Auvergne, M., et al. (2009). The CoRoT satellite in flight: description and performance. A&A, *506*, 411–424.

Baglin, A. (2003). COROT: A minisat for pionnier science, asteroseismology and planets finding. *Advances in Space Research*, *31*, 345–349.

Bakos, G., Noyes, R. W., Kovács, G., Stanek, K. Z., Sasselov, D. D., and Domsa, I. (2004). Wide-Field Millimagnitude Photometry with the HAT: A Tool for Extrasolar Planet Detection. PASP, *116*, 266–277.

Baraffe, I. and Chabrier, G. (2010). Effect of episodic accretion on the structure and the lithium depletion of low-mass stars and planet-hosting stars. A&A, *521*, A44.

Baraffe, I., Chabrier, G., Allard, F., and Hauschildt, P. H. (1998). Evolutionary models for solar metallicity low-mass stars: mass-magnitude relationships and color-magnitude diagrams. A&A, *337*, 403–412.

Baraffe, I., Chabrier, G., Allard, F., and Hauschildt, P. H. (2002). Evolutionary models for low-mass stars and brown dwarfs: Uncertainties and limits at very young ages. A&A, *382*, 563–572.

Baraffe, I., Chabrier, G., and Gallardo, J. (2009). Episodic Accretion at Early Stages of Evolution of Low-Mass Stars and Brown Dwarfs: A Solution for the Observed Luminosity Spread in H-R Diagrams? ApJ, *702*, L27–L31.

Baraffe, I., Homeier, D., Allard, F., and Chabrier, G. (2015). New evolutionary models for pre-main sequence and main sequence low-mass stars down to the hydrogen-burning limit. A&A, *577*, A42.

Baraffe, I., Vorobyov, E., and Chabrier, G. (2012). Observed Luminosity Spread in Young Clusters and FU Ori Stars: A Unified Picture. ApJ, *756*, 118.

Barnes, J. W., van Eyken, J. C., Jackson, B. K., Ciardi, D. R., and Fortney, J. J. (2013). Measurement of Spin-orbit Misalignment and Nodal Precession for the Planet around Pre-main-sequence Star PTFO 8-8695 from Gravity Darkening. ApJ, *774*, 53.

Basri, G., Johns-Krull, C. M., and Mathieu, R. D. (1997). The Classical T Tauri Spectroscopic Binary DQ Tau. II. Emission Line Variations with Orbital Phase. AJ, *114*, 781–792.

Bass, G., Orosz, J. A., Welsh, W. F., Windmiller, G., Ames Gregg, T., Fetherolf, T., Wade, R. A., and Quinn, S. N. (2012). Kepler Studies of Low-mass Eclipsing Binaries. I. Parameters of the Long-period Binary KIC 6131659. ApJ, *761*, 157.

Bate, M. R. (1998). Collapse of a Molecular Cloud Core to Stellar Densities: The First Three-dimensional Calculations. ApJ, *508*, L95–L98.

Bate, M. R. (2011). Collapse of a molecular cloud core to stellar densities: the formation and evolution of pre-stellar discs. MNRAS, *417*, 2036–2056.

Bate, M. R. (2015). Origins of the Statistical Properties of Binary Systems. In S. M. Rucinski, G. Torres, & M. Zejda (Eds.) *Astronomical Society of the Pacific Conference Series*, vol. 496 of *Astronomical Society of the Pacific Conference Series*, (p. 37).

Bate, M. R., Bonnell, I. A., and Bromm, V. (2002). The formation of close binary systems by dynamical interactions and orbital decay. MNRAS, *336*, 705–713.

Baxter, E. J., Covey, K. R., Muench, A. A., Fűrész, G., Rebull, L., and Szentgyorgyi, A. H. (2009). The Distance to NGC 2264. AJ, *138*, 963–974.

Benacquista, M. (2013). *An Introduction to the Evolution of Single and Binary Stars*.

Bertone, E., Buzzoni, A., Chávez, M., and Rodríguez-Merino, L. H. (2004). ATLAS Versus NextGen Model Atmospheres: A Combined Analysis of Synthetic Spectral Energy Distributions. AJ, *128*, 829–841.

Bessell, M. S., Castelli, F., and Plez, B. (1998). Model atmospheres broad-band colors, bolometric corrections and temperature calibrations for O - M stars. A&A, *333*, 231–250.

Bildsten, L., Brown, E. F., Matzner, C. D., and Ushomirsky, G. (1997). Lithium Depletion in Fully Convective Pre-Main-Sequence Stars. ApJ, *482*, 442–447.

Billot, N., Morales-Calderón, M., Stauffer, J. R., Megeath, S. T., and Whitney, B. (2012). Herschel Far-infrared Photometric Monitoring of Protostars in the Orion Nebula Cluster. ApJ, *753*, L35.

Borucki, W. J., Koch, D., Basri, G., Batalha, N., Brown, T., Caldwell, D., Caldwell, J., Christensen-Dalsgaard, J., Cochran, W. D., and et al. (2010). Kepler Planet-Detection Mission: Introduction and First Results. *Science*, *327*, 977–.

Boss, A. P. (1986). Protostellar formation in rotating interstellar clouds. V - Non-isothermal collapse and fragmentation. ApJS, *62*, 519–552.

Boss, A. P. and Bodenheimer, P. (1979). Fragmentation in a rotating protostar - A comparison of two three-dimensional computer codes. ApJ, *234*, 289–295.

Bouchy, F., Pont, F., Melo, C., Santos, N. C., Mayor, M., Queloz, D., and Udry, S. (2005). Doppler follow-up of OGLE transiting companions in the Galactic bulge. A&A, *431*, 1105–1121.

Bouvier, J. (2013). Observational studies of stellar rotation. In P. Hennebelle, & C. Charbonnel (Eds.) *EAS Publications Series*, vol. 62 of *EAS Publications Series*, (pp. 143–168).

Bouvier, J., et al. (2007). Magnetospheric accretion-ejection processes in the classical T Tauri star AA Tauri. A&A, *463*, 1017–1028.

Bouvier, J., Cabrit, S., Fernandez, M., Martin, E. L., and Matthews, J. M. (1993). Coyotes-I - the Photometric Variability and Rotational Evolution of T-Tauri Stars. A&A, *272*, 176.

Bouvier, J., et al. (1999). Magnetospheric accretion onto the T Tauri star AA Tauri. I. Constraints from multisite spectrophotometric monitoring. A&A, *349*, 619–635.

Bouvier, J., et al. (2003). Eclipses by circumstellar material in the T Tauri star AA Tau. II. Evidence for non-stationary magnetospheric accretion. A&A, *409*, 169–192.

Boyajian, T., et al. (2015). Stellar diameters and temperatures - VI. High angular resolution measurements of the transiting exoplanet host stars HD 189733 and HD 209458 and implications for models of cool dwarfs. MNRAS, *447*, 846–857.

Boyajian, T. S., et al. (2012a). Stellar Diameters and Temperatures. I. Main-sequence A, F, and G Stars. ApJ, *746*, 101.

Boyajian, T. S., et al. (2013). Stellar Diameters and Temperatures. III. Main-sequence A, F, G, and K Stars: Additional High-precision Measurements and Empirical Relations. ApJ, *771*, 40.

Boyajian, T. S., et al. (2012b). Stellar Diameters and Temperatures. II. Main-sequence K- and M-stars. ApJ, *757*, 112.

Bradstreet, D. H., Hargis, J. R., Sanders, S. J., and Etzel, P. B. (2007). Absolute Parameters for the Very Young, Hot Eclipsing Binary V684 Mon in NGC 2264. In *American Astronomical Society Meeting Abstracts #210*, vol. 39 of *Bulletin of the American Astronomical Society*, (p. 98).

Bressan, A., Marigo, P., Girardi, L., Salasnich, B., Dal Cero, C., Rubele, S., and Nanni, A. (2012). PARSEC: stellar tracks and isochrones with the PAdova and TRieste Stellar Evolution Code. MNRAS, *427*, 127–145.

Bressert, E., et al. (2010). The spatial distribution of star formation in the solar neighbourhood: do all stars form in dense clusters? MNRAS, *409*, L54–L58.

Burke, C. J., Pinsonneault, M. H., and Sills, A. (2004). Theoretical Examination of the Lithium Depletion Boundary. ApJ, *604*, 272–283.

Cardelli, J. A., Clayton, G. C., and Mathis, J. S. (1989). The relationship between infrared, optical, and ultraviolet extinction. ApJ, *345*, 245–256.

Cargile, P. A., Stassun, K. G., and Mathieu, R. D. (2008). Discovery of Par 1802 as a Low-Mass, Pre-Main-Sequence Eclipsing Binary in the Orion Star-Forming Region. ApJ, *674*, 329–335.

Castelli, F. and Kurucz, R. L. (2003). New Grids of ATLAS9 Model Atmospheres. In N. Piskunov, W. W. Weiss, & D. F. Gray (Eds.) *Modelling of Stellar Atmospheres*, vol. 210 of *IAU Symposium*, (p. 20P).

Chabrier, G. and Baraffe, I. (1997). Structure and evolution of low-mass stars. A&A, *327*, 1039–1053.

Chabrier, G., Gallardo, J., and Baraffe, I. (2007). Evolution of low-mass star and brown dwarf eclipsing binaries. A&A, *472*, L17–L20.

Charbonneau, D., Brown, T. M., Latham, D. W., and Mayor, M. (2000). Detection of Planetary Transits Across a Sun-like Star. ApJ, *529*, L45–L48.

Claret, A. (2000). A new non-linear limb-darkening law for LTE stellar atmosphere models. Calculations for -5.0 ¡= log[M/H] ¡= +1, 2000 K ¡= T_{eff} ¡= 50000 K at several surface gravities. A&A, *363*, 1081–1190.

Claret, A. (2004). On the irradiated stellar atmospheres in close binary systems: Improvements and uncertainties. A&A, *422*, 665–673.

Claret, A. (2007). An approach to the limb darkening of irradiated stellar atmospheres. A&A, *470*, 1099–1103.

Claret, A. and Gimenez, A. (1990). Limb-darkening for cool stars - Standard and irradiated models. Ap&SS, *169*, 223–225.

Claret, A., Hauschildt, P. H., and Witte, S. (2012). New limb-darkening coefficients for PHOENIX/1D model atmospheres. I. Calculations for 1500 K $\leq$ T_{eff} $\leq$ 4800 K Kepler, CoRot, Spitzer, uvby, UBVRIJHK, Sloan, and 2MASS photometric systems. A&A, *546*, A14.

Claret, A., Hauschildt, P. H., and Witte, S. (2013). New limb-darkening coefficients for Phoenix/1d model atmospheres. II. Calculations for 5000 K $\leq$ T_{eff} $\leq$ 10 000 K Kepler, CoRot, Spitzer, uvby, UBVRIJHK, Sloan, and 2MASS photometric systems. A&A, *552*, A16.

Clarke, C. and Carswell, B. (2014). *Principles of Astrophysical Fluid Dynamics*.

Clausen, J. V., Torres, G., Bruntt, H., Andersen, J., Nordström, B., Stefanik, R. P., Latham, D. W., and Southworth, J. (2008). Absolute dimensions of eclipsing binaries. XXVI.. Setting a new standard: Masses, radii, and abundances for the F-type systems AD Bootis VZ Hydrae, and WZ Ophiuchi. A&A, *487*, 1095–1117.

Cody, A. M., et al. (2014). CSI 2264: Simultaneous Optical and Infrared Light Curves of Young Disk-bearing Stars in NGC 2264 with CoRoT and Spitzer - Evidence for Multiple Origins of Variability. AJ, *147*, 82.

Commerçon, B., Hennebelle, P., Audit, E., Chabrier, G., and Teyssier, R. (2010). Protostellar collapse: radiative and magnetic feedbacks on small-scale fragmentation. A&A, *510*, L3.

Coughlin, J. L., López-Morales, M., Harrison, T. E., Ule, N., and Hoffman, D. I. (2011). Low-mass Eclipsing Binaries in the Initial Kepler Data Release. AJ, *141*, 78.

Covino, E., Catalano, S., Frasca, A., Marilli, E., Fernández, M., Alcalá, J. M., Melo, C., Paladino, R., Sterzik, M. F., and Stelzer, B. (2000). RXJ 0529.4+0041: a low-mass pre-main sequence eclipsing-spectroscopic binary. A&A, *361*, L49–L52.

Covino, E., Frasca, A., Alcalá, J. M., Paladino, R., and Sterzik, M. F. (2004). Improved fundamental parameters for the low-mass pre-main sequence eclipsing system ¡ASTROBJ¿RX J0529.4+0041¡/ASTROBJ¿. A&A, *427*, 637–649.

Covino, E., Melo, C., Alcalá, J. M., Torres, G., Fernández, M., Frasca, A., and Paladino, R. (2001). New low-mass pre-main sequence spectroscopic binaries in Orion. A&A, *375*, 130–144.

Crutcher, R. M., Hartkopf, W. I., and Giguere, P. T. (1978). The NGC 2264 molecular cloud - CO observations. ApJ, *226*, 839–850.

Cutri, R. M., et al. (2003). *2MASS All Sky Catalog of point sources.*.

Czekala, I., Andrews, S. M., Mandel, K. S., Hogg, D. W., and Green, G. M. (2014). Constructing A Flexible Likelihood Function For Spectroscopic Inference. *ArXiv e-prints*.

Dahm, S. E. (2008). *The Young Cluster and Star Forming Region NGC 2264*, (p. 966). ASP Monograph Publications, "The Handbook of Star Forming Regions, Volume I" ed.

Dahm, S. E. and Simon, T. (2005). The T Tauri Star Population of the Young Cluster NGC 2264. AJ, *129*, 829–855.

Dahm, S. E., Simon, T., Proszkow, E. M., and Patten, B. M. (2007). X-Ray Observations of the Young Cluster NGC 2264. AJ, *134*, 999–1018.

D'Antona, F. and Mazzitelli, I. (1998). A Role for Superadiabatic Convection in Low Mass Structures? In R. Rebolo, E. L. Martin, & M. R. Zapatero Osorio (Eds.) *Brown Dwarfs and Extrasolar Planets*, vol. 134 of *Astronomical Society of the Pacific Conference Series*, (p. 442).

de Val-Borro, M., Gahm, G. F., Stempels, H. C., and Pepliński, A. (2011). Modelling circumbinary gas flows in close T Tauri binaries. MNRAS, *413*, 2679–2688.

Diaz-Cordoves, J. and Gimenez, A. (1992). A new nonlinear approximation to the limb-darkening of hot stars. A&A, *259*, 227–231.

Donati, J.-F., Collier Cameron, A., Hussain, G. A. J., and Semel, M. (1999). Magnetic topology and prominence patterns on AB Doradus. MNRAS, *302*, 437–456.

Donati, J.-F., et al. (2008). Magnetospheric accretion on the T Tauri star BP Tauri. MNRAS, *386*, 1234–1251.

Donati, J.-F., Mengel, M., Carter, B. D., Marsden, S., Collier Cameron, A., and Wichmann, R. (2000). Surface differential rotation and prominences of the Lupus post T Tauri star RX J1508.6-4423. MNRAS, *316*, 699–715.

Donati, J.-F., Semel, M., Carter, B. D., Rees, D. E., and Collier Cameron, A. (1997). Spectropolarimetric observations of active stars. MNRAS, *291*, 658.

Dorren, J. D. (1987). A new formulation of the starspot model, and the consequences of starspot structure. ApJ, *320*, 756–767.

Dotter, A., Chaboyer, B., Jevremović, D., Kostov, V., Baron, E., and Ferguson, J. W. (2008). The Dartmouth Stellar Evolution Database. ApJS, *178*, 89–101.

Doyle, L. R., et al. (2011). Kepler-16: A Transiting Circumbinary Planet. *Science*, *333*, 1602–.

Drummond, R., Lapeyrere, V., Auvergne, M., Vandenbussche, B., Aerts, C., Samadi, R., and Costa, J. E. S. (2008). Correcting for background changes in CoRoT exoplanet data. A&A, *487*, 1209–1220.

Ducati, J. R. (2002). VizieR Online Data Catalog: Catalogue of Stellar Photometry in Johnson's 11-color system. *VizieR Online Data Catalog*, *2237*, 0.

Duchêne, G. and Kraus, A. (2013). Stellar Multiplicity. ARA&A, *51*, 269–310.

Dzib, S. A., Loinard, L., Rodríguez, L. F., and Galli, P. (2014). Deep VLA Images of the HH 124 IRS Radio Cluster and Its Surroundings, and a New Determination of the Distance to NGC 2264. ApJ, *788*, 162.

Errmann, R., Raetz, S., Kitze, M., Neuhäuser, R., and YETI Team (2014). The search for transiting planets using the YETI network. *Contributions of the Astronomical Observatory Skalnate Pleso*, *43*, 513–517.

Espaillat, C., Furlan, E., D'Alessio, P., Sargent, B., Nagel, E., Calvet, N., Watson, D. M., and Muzerolle, J. (2011). A Spitzer IRS Study of Infrared Variability in Transitional and Pre-transitional Disks Around T Tauri Stars. ApJ, *728*, 49.

Etzel, P. B. (1980). EBOP users guide.

Etzel, P. B. (1981). A Simple Synthesis Method for Solving the Elements of Well-Detached Eclipsing Systems. In E. B. Carling, & Z. Kopal (Eds.) *Photometric and Spectroscopic Binary Systems*, (p. 111).

Etzel, P. B. (1993). Light curve modelling of eclipsing binary stars. *Springer-Verlag, Milone E. F., ed.*, (p. 113).

Fabrycky, D. and Tremaine, S. (2007). Shrinking Binary and Planetary Orbits by Kozai Cycles with Tidal Friction. ApJ, *669*, 1298–1315.

Fang, M., van Boekel, R., Wang, W., Carmona, A., Sicilia-Aguilar, A., and Henning, T. (2009). Star and protoplanetary disk properties in Orion's suburbs. A&A, *504*, 461–489.

Favata, F., Micela, G., Alencar, S., Aigrain, S., and Zwintz, K. (2010). Stellar rotation at young ages: new results from Corot's monitoring NGC 2264. *Highlights of Astronomy*, *15*, 752–752.

Feiden, G. A. (2015a). Eclipsing Binary Systems as Tests of Low-Mass Stellar Evolution Theory. In S. M. Rucinski, G. Torres, & M. Zejda (Eds.) *Astronomical Society of the Pacific Conference Series*, vol. 496 of *Astronomical Society of the Pacific Conference Series*, (p. 137).

Feiden, G. A. (2015b). Stellar Evolution Models of Young Stars: Progress and Limitations. *ArXiv e-prints*.

Feiden, G. A. and Chaboyer, B. (2012a). Reevaluating the Mass-Radius Relation for Low-mass, Main-sequence Stars. ApJ, *757*, 42.

Feiden, G. A. and Chaboyer, B. (2012b). Self-consistent Magnetic Stellar Evolution Models of the Detached, Solar-type Eclipsing Binary EF Aquarii. ApJ, *761*, 30.

Feiden, G. A. and Chaboyer, B. (2013). Magnetic Inhibition of Convection and the Fundamental Properties of Low-mass Stars. I. Stars with a Radiative Core. ApJ, *779*, 183.

Feigelson, E. D., et al. (2013). Overview of the Massive Young Star-Forming Complex Study in Infrared and X-Ray (MYStIX) Project. ApJS, *209*, 26.

Fernández, M., Stelzer, B., Henden, A., Grankin, K., Gameiro, J. F., Costa, V. M., Guenther, E., Amado, P. J., and Rodriguez, E. (2004). The weak-line T Tauri star V410 Tau. II. A flaring star. A&A, *427*, 263–278.

Fűrész, G., Hartmann, L. W., Szentgyorgyi, A. H., Ridge, N. A., Rebull, L., Stauffer, J., Latham, D. W., Conroy, M. A., Fabricant, D. G., and Roll, J. (2006). Kinematics of NGC 2264: Signs of Cluster Formation. ApJ, *648*, 1090–1098.

Flaccomio, E., Micela, G., and Sciortino, S. (2006). ACIS-I observations of NGC 2264. Membership and X-ray properties of PMS stars. A&A, *455*, 903–921.

Flaccomio, E., Micela, G., Sciortino, S., Damiani, F., Favata, F., Harnden, F. R., Jr., and Schachter, J. (2000). HRI observations of PMS stars in NGC 2264. A&A, *355*, 651–667.

Flaccomio, E., Sciortino, S., Micela, G., Damiani, F., Favata, F., Corbally, C., Tomaney, A., Harnden, F. R., Jr., and Schachter, J. (1997). X-Ray and optical observations of the star forming region NGC 2264. Mem. Soc. Astron. Italiana, *68*, 1073.

Flaherty, K. M. and Muzerolle, J. (2010). Modeling Mid-infrared Variability of Circumstellar Disks with Non-axisymmetric Structure. ApJ, *719*, 1733–1749.

Fonseca, N. N. J., Alencar, S. H. P., Bouvier, J., Favata, F., and Flaccomio, E. (2014). Dynamical star-disk interaction in the young stellar system V354 Monocerotis. A&A, *567*, A39.

Foreman-Mackey, D., Hogg, D. W., Lang, D., and Goodman, J. (2013). emcee: The MCMC Hammer. PASP, *125*, 306–312.

Gibson, N. P., Aigrain, S., Roberts, S., Evans, T. M., Osborne, M., and Pont, F. (2012). A Gaussian process framework for modelling instrumental systematics: application to transmission spectroscopy. MNRAS, *419*, 2683–2694.

Gillen, E., et al. (2014). CoRoT 223992193: A new, low-mass, pre-main sequence eclipsing binary with evidence of a circumbinary disk. A&A, *562*, A50.

Gómez Maqueo Chew, Y., Stassun, K. G., Prša, A., Stempels, E., Hebb, L., Barnes, R., Heller, R., and Mathieu, R. D. (2012). Luminosity Discrepancy in the Equal-mass, Pre-main-sequence Eclipsing Binary Par 1802: Non-coevality or Tidal Heating? ApJ, *745*, 58.

Grankin, K. N., Bouvier, J., Herbst, W., and Melnikov, S. Y. (2008). Results of the ROTOR-program. II. The long-term photometric variability of weak-line T Tauri stars. A&A, *479*, 827–843.

Grankin, K. N., Melnikov, S. Y., Bouvier, J., Herbst, W., and Shevchenko, V. S. (2007). Results of the ROTOR-program. I. The long-term photometric variability of classical T Tauri stars. A&A, *461*, 183–195.

Gray, D. F. (1992). *The observation and analysis of stellar photospheres.*.

Greene, T. P., Wilking, B. A., Andre, P., Young, E. T., and Lada, C. J. (1994). Further mid-infrared study of the rho Ophiuchi cloud young stellar population: Luminosities and masses of pre-main-sequence stars. ApJ, *434*, 614–626.

Gullbring, E., Hartmann, L., Briceño, C., and Calvet, N. (1998). Disk Accretion Rates for T Tauri Stars. ApJ, *492*, 323–341.

Günther, R. and Kley, W. (2002). Circumbinary disk evolution. A&A, *387*, 550–559.

Gustafsson, B., Edvardsson, B., Eriksson, K., Jørgensen, U. G., Nordlund, Å., and Plez, B. (2008). A grid of MARCS model atmospheres for late-type stars. I. Methods and general properties. A&A, *486*, 951–970.

Hanawa, T., Ochi, Y., and Ando, K. (2010). Gas Accretion from a Circumbinary Disk. ApJ, *708*, 485–497.

Hartigan, P., Edwards, S., and Ghandour, L. (1995). Disk Accretion and Mass Loss from Young Stars. ApJ, *452*, 736.

Hatzes, A. P. (1995). SPOT and chromospheric activity on the RS CVN star DM Ursae Majoris. AJ, *109*, 350–358.

Hebb, L., Cegla, H. M., Stassun, K. G., Stempels, H. C., Cargile, P. A., and Palladino, L. E. (2011). Precise orbit solution of MML 53, a low-mass, pre-main sequence eclipsing binary in Upper Centaurus Lupus. A&A, *531*, A61.

Hebb, L., et al. (2010). MML 53: a new low-mass, pre-main sequence eclipsing binary in the Upper Centaurus-Lupus region discovered by SuperWASP. A&A, *522*, A37.

Herbst, W., Herbst, D. K., Grossman, E. J., and Weinstein, D. (1994). Catalogue of UBVRI photometry of T Tauri stars and analysis of the causes of their variability. AJ, *108*, 1906–1923.

Hillenbrand, L. A. and White, R. J. (2004). An Assessment of Dynamical Mass Constraints on Pre-Main-Sequence Evolutionary Tracks. ApJ, *604*, 741–757.

Hohle, M. M., Neuhäuser, R., and Schutz, B. F. (2010). Masses and luminosities of O- and B-type stars and red supergiants. *Astronomische Nachrichten*, *331*, 349.

Hopkinson, G. R., Dale, C. J., and Marshall, P. W. (1996). Proton effects in charge-coupled devices. *IEEE Transactions on Nuclear Science*, *43*, 614–627.

Howell, S. B., et al. (2014). The K2 Mission: Characterization and Early Results. PASP, *126*, 398–408.

Hoxie, D. T. (1973). The low-mass main-sequence: the comparison between theory and observation. A&A, *26*, 437–441.

Huber, D., et al. (2013). Fundamental Properties of Kepler Planet-candidate Host Stars using Asteroseismology. ApJ, *767*, 127.

Husser, T.-O., Wende-von Berg, S., Dreizler, S., Homeier, D., Reiners, A., Barman, T., and Hauschildt, P. H. (2013). A new extensive library of PHOENIX stellar atmospheres and synthetic spectra. A&A, *553*, A6.

Indebetouw, R., et al. (2005). The Wavelength Dependence of Interstellar Extinction from 1.25 to 8.0 μm Using GLIMPSE Data. ApJ, *619*, 931–938.

Irwin, J. (2007). Observational constraints on pre-main sequence stellar evolution from time- series analysis of open cluster stars. *Thesis*.

Irwin, J., et al. (2007). The Monitor project: JW 380 - a 0.26-, 0.15-M_{solar}, pre-main-sequence eclipsing binary in the Orion nebula cluster. MNRAS, *380*, 541–550.

Irwin, J. and Bouvier, J. (2009). The rotational evolution of low-mass stars. In E. E. Mamajek, D. R. Soderblom, & R. F. G. Wyse (Eds.) *IAU Symposium*, vol. 258 of *IAU Symposium*, (pp. 363–374).

Irwin, J., Charbonneau, D., Nutzman, P., and Falco, E. (2009). The MEarth project: searching for transiting habitable super-Earths around nearby M dwarfs. In F. Pont, D. Sasselov, & M. J. Holman (Eds.) *IAU Symposium*, vol. 253 of *IAU Symposium*, (pp. 37–43).

Irwin, J. M., et al. (2011). LSPM J1112+7626: Detection of a 41 Day M-dwarf Eclipsing Binary from the MEarth Transit Survey. ApJ, *742*, 123.

Jackson, R. J. and Jeffries, R. D. (2014). The effect of starspots on the radii of low-mass pre-main-sequence stars. MNRAS, *441*, 2111–2123.

Jeans, J. H. (1902). The Stability of a Spherical Nebula. *Royal Society of London Philosophical Transactions Series A*, *199*, 1–53.

Jeffries, R. D. (2004). Pre-main-sequence Lithium Depletion. *ArXiv Astrophysics e-prints*.

Jensen, E. L. N. and Mathieu, R. D. (1997). Evidence for Cleared Regions in the Disks Around Pre-Main-Sequence Spectroscopic Binaries. AJ, *114*, 301–316.

Jester, S., et al. (2005). The Sloan Digital Sky Survey View of the Palomar-Green Bright Quasar Survey. AJ, *130*, 873–895.

Jones, B. F., Fischer, D. A., and Stauffer, J. R. (1996). Keck Rotational Velocities of the Faintest Pleiades and Hyades Members. AJ, *112*, 1562.

Joy, A. H. (1945). T Tauri Variable Stars. ApJ, *102*, 168.

Kaas, A. A., et al. (2004). The young stellar population in the Serpens Cloud Core: An ISOCAM survey. A&A, *421*, 623–642.

Kallrath, J. and Milone, E. F. (2009). *Eclipsing Binary Stars: Modeling and Analysis*.

Kervella, P., Thévenin, F., Di Folco, E., and Ségransan, D. (2004). The angular sizes of dwarf stars and subgiants. Surface brightness relations calibrated by interferometry. A&A, *426*, 297–307.

King, J. R., Soderblom, D. R., Fischer, D., and Jones, B. F. (2000). Spectroscopic Abundances in Cool Pleiades Dwarfs and NGC 2264 Stars. ApJ, *533*, 944–958.

Klinglesmith, D. A. and Sobieski, S. (1970). Nonlinear Limb Darkening for Early-Type Stars. AJ, *75*, 175.

Koch, R. H., Bradstreet, D. H., Hrivnak, B. J., Pfeiffer, R. J., and Perry, P. M. (1986). HD 47755, a new eclipsing binary. AJ, *91*, 590–597.

Koch, R. H. and Perry, P. M. (1974). Photographic photometry in the field of NGC 2264. AJ, *79*, 379–386.

Kopal, Z. (1950). Detailed effects of limb darkening upon light and velocity curves of close binary systems. *Harvard College Observatory Circular*, *454*, 1–12.

Kraus, A. L., Cody, A. M., Covey, K. R., Rizzuto, A. C., Mann, A. W., and Ireland, M. J. (2015). The Mass-Radius Relation of Young Stars, I: UScoCTIO 5, An M4.5 Eclipsing Binary in Upper Scorpius Observed By K2. *ArXiv e-prints*.

Kraus, A. L. and Hillenbrand, L. A. (2009). The Coevality of Young Binary Systems. ApJ, *704*, 531–547.

LaCourse, D. M., et al. (2015). Kepler eclipsing binary stars - VI. Identification of eclipsing binaries in the K2 Campaign 0 data set. MNRAS, *452*, 3561–3592.

Lacy, C. H. S., Torres, G., Claret, A., and Vaz, L. P. R. (2005). Absolute Properties of the Eclipsing Binary Star RW Lacertae. AJ, *130*, 2838–2846.

Lamm, M. H., Bailer-Jones, C. A. L., Mundt, R., Herbst, W., and Scholz, A. (2004). A rotational and variability study of a large sample of PMS stars in ¡ASTROBJ¿NGC 2264¡/ASTROBJ¿. A&A, *417*, 557–581.

Lapeyrere, V., Bernardi, P., Buey, J.-T., Auvergne, M., and Tiphène, D. (2006). Calibration of flight model CCDs for CoRoT mission. MNRAS, *365*, 1171–1179.

Lendl, M., et al. (2014). WASP-117b: a 10-day-period Saturn in an eccentric and misaligned orbit. A&A, *568*, A81.

Lin, D. N. C. and Papaloizou, J. (1979). On the structure of circumbinary accretion disks and the tidal evolution of commensurable satellites. MNRAS, *188*, 191–201.

Lindegren, L., et al. (2008). The Gaia mission: science, organization and present status. In W. J. Jin, I. Platais, & M. A. C. Perryman (Eds.) *A Giant Step: from Milli- to Micro-arcsecond Astrometry*, vol. 248 of *IAU Symposium*, (pp. 217–223).

Long, M., Romanova, M. M., and Lovelace, R. V. E. (2007). Accretion to stars with non-dipole magnetic fields. MNRAS, *374*, 436–444.

Long, M., Romanova, M. M., and Lovelace, R. V. E. (2008). Three-dimensional simulations of accretion to stars with complex magnetic fields. MNRAS, *386*, 1274–1284.

López-Morales, M. (2007). On the Correlation between the Magnetic Activity Levels, Metallicities, and Radii of Low-Mass Stars. ApJ, *660*, 732–739.

López-Morales, M. and Ribas, I. (2005). GU Bootis: A New 0.6 M_{solar} Detached Eclipsing Binary. ApJ, *631*, 1120–1133.

Lucy, L. B. (1967). Gravity-Darkening for Stars with Convective Envelopes. ZAp, *65*, 89.

Macdonald, J. and Mullan, D. J. (2010). Magneto-convection and Lithium Age Estimates of the β Pictoris Moving Group. ApJ, *723*, 1599–1606.

MacDonald, J. and Mullan, D. J. (2014). Surface Magnetic Field Strengths: New Tests of Magnetoconvective Models of M Dwarfs. ApJ, *787*, 70.

Makidon, R. B., Rebull, L. M., Strom, S. E., Adams, M. T., and Patten, B. M. (2004). Periodic Variability of Pre-Main-Sequence Stars in the NGC 2264 OB Association. AJ, *127*, 2228–2245.

Malo, L., Doyon, R., Feiden, G. A., Albert, L., Lafrenière, D., Artigau, É., Gagné, J., and Riedel, A. (2014). BANYAN. IV. Fundamental Parameters of Low-mass Star Candidates in Nearby Young Stellar Kinematic Groups - Isochronal Age Determination using Magnetic Evolutionary Models. ApJ, *792*, 37.

Mandel, K. and Agol, E. (2002). Analytic Light Curves for Planetary Transit Searches. ApJ, *580*, L171–L175.

Mathieu, R. D. (1994). Pre-Main-Sequence Binary Stars. ARA&A, *32*, 465–530.

Mathieu, R. D., Baraffe, I., Simon, M., Stassun, K. G., and White, R. (2007). Dynamical Mass Measurements of Pre-Main-Sequence Stars: Fundamental Tests of the Physics of Young Stars. *Protostars and Planets V*, (pp. 411–425).

Maxted, P. F. L., Hutcheon, R. J., Torres, G., Lacy, C. H. S., Southworth, J., Smalley, B., Pavlovski, K., Marschall, L. A., and Clausen, J. V. (2015). Precise mass and radius measurements for the components of the bright solar-type eclipsing binary star V1094 Tauri. A&A, *578*, A25.

Mayne, N. J. and Naylor, T. (2008). Fitting the young main-sequence: distances, ages and age spreads. MNRAS, *386*, 261–277.

Mayor, M. and Queloz, D. (1995). A Jupiter-mass companion to a solar-type star. Nature, *378*, 355–359.

Mazeh, T., Zucker, S., Goldberg, D., Latham, D. W., Stefanik, R. P., and Carney, B. W. (1995). Study of Spectroscopic Binaries with TODCOR. II. The Highly Eccentric Binary HD 2909. ApJ, *449*, 909.

McGinnis, P. T., et al. (2015). CSI 2264: Probing the inner disks of AA Tauri-like systems in NGC 2264. A&A, *577*, A11.

McKay, M. D., Beckman, R. J., and Conover, W. J. (1979). A Comparison of Three Methods for Selecting Values of Input Variables in the Analysis of Output from a Computer Code. *Technometrics*, *21*(2), 239–245.

Meisenheimer, K. (1994). Cafos 2.2 - Der Fokalreduktor des 2.2-m-Teleskops auf dem Calar-Alto. *Sterne und Weltraum*, *33*, 516–522.

Milne, E. A. (1926). The reflection effect in eclipsing binaries. MNRAS, *87*, 43–55.

Moe, M. and Di Stefano, R. (2015). A New Class of Nascent Eclipsing Binaries with Extreme Mass Ratios. ApJ, *801*, 113.

Morales, J. C., Gallardo, J., Ribas, I., Jordi, C., Baraffe, I., and Chabrier, G. (2010). The Effect of Magnetic Activity on Low-Mass Stars in Eclipsing Binaries. ApJ, *718*, 502–512.

Morales-Calderón, M., et al. (2011). Ysovar: The First Sensitive, Wide-area, Mid-infrared Photometric Monitoring of the Orion Nebula Cluster. ApJ, *733*, 50.

Morales-Calderón, M., et al. (2012). YSOVAR: Six Pre-main-sequence Eclipsing Binaries in the Orion Nebula Cluster. ApJ, *753*, 149.

Morgan, W. W., Hiltner, W. A., Neff, J. S., Garrison, R., and Osterbrock, D. E. (1965). Studies in Spectral Classification. III. The H-R Diagrams of NGC 2244 and NGC 2264. ApJ, *142*, 974.

Mullan, D. J. and MacDonald, J. (2001). Are Magnetically Active Low-Mass M Dwarfs Completely Convective? ApJ, *559*, 353–371.

Naylor, T. (2009). Are pre-main-sequence stars older than we thought? MNRAS, *399*, 432–442.

Nelson, B. and Davis, W. D. (1972). Eclipsing-Binary Solutions by Sequential Optimization of the Parameters. ApJ, *174*, 617.

Nemeth, P., Östensen, R., Tremblay, P., and Hubeny, I. (2014). Synthetic Spectra for O and B Type Subdwarf Stars. In V. van Grootel, E. Green, G. Fontaine, & S. Charpinet (Eds.) *6th Meeting on Hot Subdwarf Stars and Related Objects*, vol. 481 of *Astronomical Society of the Pacific Conference Series*, (p. 95).

Neuhäuser, R., et al. (2011). The Young Exoplanet Transit Initiative (YETI). *Astronomische Nachrichten*, *332*, 547.

Nguyen, D. C., Brandeker, A., van Kerkwijk, M. H., and Jayawardhana, R. (2012). Close Companions to Young Stars. I. A Large Spectroscopic Survey in Chamaeleon I and Taurus-Auriga. ApJ, *745*, 119.

Nordlund, A. and Vaz, L. P. R. (1990). The reflection effect in model stellar atmospheres. II - The bolometric reflection albedo in non-grey atmospheres with convection. A&A, *228*, 231–237.

Offner, S. S. R., Klein, R. I., McKee, C. F., and Krumholz, M. R. (2009). The Effects of Radiative Transfer on Low-Mass Star Formation. ApJ, *703*, 131–149.

Orosz, J. A. and Hauschildt, P. H. (2000). The use of the NextGen model atmospheres for cool giants in a light curve synthesis code. A&A, *364*, 265–281.

Orosz, J. A., et al. (2012a). The Neptune-sized Circumbinary Planet Kepler-38b. ApJ, *758*, 87.

Orosz, J. A., et al. (2012b). Kepler-47: A Transiting Circumbinary Multiplanet System. *Science*, *337*, 1511–.

Paczynski, B. (1977). A model of accretion disks in close binaries. ApJ, *216*, 822–826.

Pallé, P. L. and Esteban, C. (2014). *Asteroseismology*.

Papaloizou, J. and Pringle, J. E. (1977). Tidal torques on accretion discs in close binary systems. MNRAS, *181*, 441–454.

Park, B.-G., Sung, H., Bessell, M. S., and Kang, Y. H. (2000). The Pre-Main-Sequence Stars and Initial Mass Function of NGC 2264. AJ, *120*, 894–908.

Parks, J. R., Plavchan, P., White, R. J., and Gee, A. H. (2014). Periodic and Aperiodic Variability in the Molecular Cloud ρ Ophiuchus. ApJS, *211*, 3.

Perez, M. R., The, P. S., and Westerlund, B. E. (1987). On the distances to the young open clusters NGC 2244 and NGC 2264. PASP, *99*, 1050–1066.

Petrov, P. P., Shcherbakov, V. A., Berdyugina, S. V., Shevchenko, V. S., Grankin, K. N., and Melnikov, S. Y. (1994). Photometric and spectroscopic observations of the spotted T Tauri star V410 Tauri. A&AS, *107*, 9–22.

Pickles, A. J. (1998). A Stellar Spectral Flux Library: 1150-25000 Å. PASP, *110*, 863–878.

Pollacco, D. L., et al. (2006). The WASP Project and the SuperWASP Cameras. PASP, *118*, 1407–1418.

Popper, D. M. (1984). Error analysis of light curves of detached eclipsing binary systems. AJ, *89*, 132–144.

Popper, D. M. and Etzel, P. B. (1981). Photometric orbits of seven detached eclipsing binaries. AJ, *86*, 102–120.

Pribulla, T., et al. (2010). Eclipsing binaries in the MOST satellite fields. *Astronomische Nachrichten*, *331*, 397.

Prša, A., et al. (2011). Kepler Eclipsing Binary Stars. I. Catalog and Principal Characterization of 1879 Eclipsing Binaries in the First Data Release. AJ, *141*, 83.

Prša, A. and Zwitter, T. (2005). A Computational Guide to Physics of Eclipsing Binaries. I. Demonstrations and Perspectives. ApJ, *628*, 426–438.

Ramírez, S. V., Rebull, L., Stauffer, J., Hearty, T., Hillenbrand, L., Jones, B., Makidon, R., Pravdo, S., Strom, S., and Werner, M. (2004). Chandra X-Ray Observations of Young Clusters. I. NGC 2264 Data. AJ, *127*, 2659–2673.

Rasmussen, C. E. and Williams, C. K. I. (2006). Gaussian processes for machine learning. *MIT Press*.

Rebull, L. M., et al. (2014). Young Stellar Object Variability (YSOVAR): Long Timescale Variations in the Mid-Infrared. *ArXiv e-prints*.

Rebull, L. M., Makidon, R. B., Strom, S. E., Hillenbrand, L. A., Birmingham, A., Patten, B. M., Jones, B. F., Yagi, H., and Adams, M. T. (2002). Circumstellar Disk Candidates Identified in NGC 2264. AJ, *123*, 1528–1547.

Reiners, A. (2012). Observations of Cool-Star Magnetic Fields. *Living Reviews in Solar Physics*, *9*, 1.

Reipurth, B. and Mikkola, S. (2012). Formation of the widest binary stars from dynamical unfolding of triple systems. Nature, *492*, 221–224.

Reipurth, B., Pettersson, B., Armond, T., Bally, J., and Vaz, L. P. R. (2004). Hα Emission-Line Stars in Molecular Clouds. I. The NGC 2264 Region. AJ, *127*, 1117–1130.

Ribas, I. (2003). The 0.4-M_{sun} eclipsing binary CU Cancri. Absolute dimensions, comparison with evolutionary models and possible evidence for a circumstellar dust disk. A&A, *398*, 239–251.

Ribas, I. (2006). Masses and Radii of Low-Mass Stars: Theory Versus Observations. Ap&SS, *304*, 89–92.

Ridge, N. A., et al. (2006). The COMPLETE Survey of Star-Forming Regions: Phase I Data. AJ, *131*, 2921–2933.

Robitaille, T. P., Whitney, B. A., Indebetouw, R., and Wood, K. (2007). Interpreting Spectral Energy Distributions from Young Stellar Objects. II. Fitting Observed SEDs Using a Large Grid of Precomputed Models. ApJ, *169*, 328–352.

Roettenbacher, R. M., Monnier, J. D., Harmon, R. O., Barclay, T., and Still, M. (2013). Imaging Starspot Evolution on Kepler Target KIC 5110407 Using Light-Curve Inversion. ApJ, *767*, 60.

Román-Zúñiga, C. G. and Lada, E. A. (2008). *Star Formation in the Rosette Complex*, (p. 928). Handbook of Star Forming Regions, Volume I. ASP Monograph Publications.

Romanova, M. M., Kulkarni, A. K., and Lovelace, R. V. E. (2008). Unstable Disk Accretion onto Magnetized Stars: First Global Three-dimensional Magnetohydrodynamic Simulations. ApJ, *673*, L171–L174.

Romanova, M. M., Ustyugova, G. V., Koldoba, A. V., and Lovelace, R. V. E. (2011). MRI-driven accretion on to magnetized stars: axisymmetric MHD simulations. MNRAS, *416*, 416–438.

Romanova, M. M., Ustyugova, G. V., Koldoba, A. V., and Lovelace, R. V. E. (2013). Warps, bending and density waves excited by rotating magnetized stars: results of global 3D MHD simulations. MNRAS, *430*, 699–724.

Romanova, M. M., Ustyugova, G. V., Koldoba, A. V., Wick, J. V., and Lovelace, R. V. E. (2003). Three-dimensional Simulations of Disk Accretion to an Inclined Dipole. I. Magnetospheric Flows at Different Θ. ApJ, *595*, 1009–1031.

Rucinski, S. M. (2002). Radial Velocity Studies of Close Binary Stars. VII. Methods and Uncertainties. AJ, *124*, 1746–1756.

Russell, H. N. (1912a). On the Determination of the Orbital Elements of Eclipsing Variable Stars. I. ApJ, *35*, 315.

Russell, H. N. (1912b). On the Determination of the Orbital Elements of Eclipsing Variable Stars. II. ApJ, *36*, 54.

Russell, H. N. (1939). Notes on Ellipticity in Eclipsing Binaries. ApJ, *90*, 641.

Russell, H. N. and Shapley, H. (1914). Elements of the eclipsing variable stars Z Draconis and RT Persei. ApJ, *39*, 405–427.

Samadi, R., Fialho, F., Costa, J. E. S., Drummond, R., Pinheiro da Silva, L., Baudin, F., Boumier, P., and Jorda, L. (2006). Extraction of the Photometric Information: Corrections. In M. Fridlund, A. Baglin, J. Lochard, & L. Conroy (Eds.) *ESA Special Publication*, vol. 1306 of *ESA Special Publication*, (p. 317).

Samadi, R., Georgobiani, D., Trampedach, R., Goupil, M. J., Stein, R. F., and Nordlund, Å. (2007). Excitation of solar-like oscillations across the HR diagram. A&A, *463*, 297–308.

Schlegel, D. J., Finkbeiner, D. P., and Davis, M. (1998). Maps of Dust Infrared Emission for Use in Estimation of Reddening and Cosmic Microwave Background Radiation Foregrounds. ApJ, *500*, 525.

Schwamb, M. E., et al. (2013). Planet Hunters: A Transiting Circumbinary Planet in a Quadruple Star System. ApJ, *768*, 127.

Schwartz, P. R. (1987). Star-forming loops in the IRAS sky images. ApJ, *320*, 258–265.

Schwartz, P. R., Thronson, H. A., Jr., Odenwald, S. F., Glaccum, W., Loewenstein, R. F., and Wolf, G. (1985). Active star formation in NGC 2264. ApJ, *292*, 231–237.

Sergison, D. J., Mayne, N. J., Naylor, T., Jeffries, R. D., and Bell, C. P. M. (2013). No evidence for intense, cold accretion on to YSOs from measurements of Li in T-Tauri stars. MNRAS, *434*, 966–977.

Shang, H., Glassgold, A. E., Shu, F. H., and Lizano, S. (2002). Heating and Ionization of X-Winds. ApJ, *564*, 853–876.

Shi, J.-M. and Krolik, J. H. (2015). Three-dimensional MHD Simulation of Circumbinary Accretion Disks. II. Net Accretion Rate. ApJ, *807*, 131.

Shi, J.-M., Krolik, J. H., Lubow, S. H., and Hawley, J. F. (2012). Three-dimensional Magnetohydrodynamic Simulations of Circumbinary Accretion Disks: Disk Structures and Angular Momentum Transport. ApJ, *749*, 118.

Siess, L., Dufour, E., and Forestini, M. (2000). An internet server for pre-main sequence tracks of low- and intermediate-mass stars. A&A, *358*, 593–599.

Simkin, S. M. (1974). Measurements of Velocity Dispersions and Doppler Shifts from Digitized Optical Spectra. A&A, *31*, 129.

Sing, D. K. (2010). Stellar limb-darkening coefficients for CoRot and Kepler. A&A, *510*, A21.

Skelly, M. B., Unruh, Y. C., Barnes, J. R., Lawson, W. A., Donati, J.-F., and Collier Cameron, A. (2009). Doppler images and chromospheric variability of TWA 17. MNRAS, *399*, 1829–1838.

Skiff, B. A. (2013). VizieR Online Data Catalog: General Catalogue of Stellar Spectral Classifications. *VizieR Online Data Catalog*, *1*, 2023.

Southworth, J. (2012). Eclipsing Binary Stars: the Royal Road to Stellar Astrophysics. *ArXiv e-prints*.

Southworth, J. (2013). The solar-type eclipsing binary system LL Aquarii. *ArXiv e-prints*.

Southworth, J., Bruntt, H., and Buzasi, D. L. (2007). Eclipsing binaries observed with the WIRE satellite. II. β Aurigae and non-linear limb darkening in light curves. A&A, *467*, 1215–1226.

Southworth, J., Maxted, P. F. L., and Smalley, B. (2004). Eclipsing binaries in open clusters - II. V453 Cyg in NGC 6871. MNRAS, *351*, 1277–1289.

Southworth, J., Maxted, P. F. L., and Smalley, B. (2005). Eclipsing binaries as standard candles. HD 23642 and the distance to the Pleiades. A&A, *429*, 645–655.

Srour, J. R., Marshall, C. J., and Marshall, P. W. (2003). Review of displacement damage effects in silicon devices. *IEEE Transactions on Nuclear Science*, *50*, 653–670.

Stassun, K. G., Feiden, G. A., and Torres, G. (2014). Empirical Tests of Pre-Main-Sequence Stellar Evolution Models with Eclipsing Binaries. *ArXiv e-prints*.

Stassun, K. G., Mathieu, R. D., Cargile, P. A., Aarnio, A. N., Stempels, E., and Geller, A. (2008). Surprising dissimilarities in a newly formed pair of 'identical twin' stars. Nature, *453*, 1079–1082.

Stassun, K. G., Mathieu, R. D., and Valenti, J. A. (2006). Discovery of two young brown dwarfs in an eclipsing binary system. Nature, *440*, 311–314.

Stassun, K. G., Mathieu, R. D., and Valenti, J. A. (2007). A Surprising Reversal of Temperatures in the Brown Dwarf Eclipsing Binary 2MASS J05352184-0546085. ApJ, *664*, 1154–1166.

Stassun, K. G., Mathieu, R. D., Vaz, L. P. R., Stroud, N., and Vrba, F. J. (2004). Dynamical Mass Constraints on Low-Mass Pre-Main-Sequence Stellar Evolutionary Tracks: An Eclipsing Binary in Orion with a 1.0 M_{solar} Primary and a 0.7 M_{solar} Secondary. ApJS, *151*, 357–385.

Stauffer, J., et al. (2014). CSI 2264: Characterizing Accretion-burst Dominated Light Curves for Young Stars in NGC 2264. AJ, *147*, 83.

Stauffer, J., et al. (2015). CSI 2264: Characterizing Young Stars in NGC 2264 With Short-Duration Periodic Flux Dips in Their Light Curves. AJ, *149*, 130.

Stempels, H. C., Hebb, L., Stassun, K. G., Holtzman, J., Dunstone, N., Glowienka, L., and Frandsen, S. (2008). The pre-main-sequence eclipsing binary ASAS J052821+0338.5. A&A, *481*, 747–755.

Stroeer, A., Heber, U., Lisker, T., Napiwotzki, R., Dreizler, S., Christlieb, N., and Reimers, D. (2007). Hot subdwarfs from the ESO supernova Ia progenitor survey. II. Atmospheric parameters of subdwarf O stars. A&A, *462*, 269–280.

Strom, K. M., Strom, S. E., and Merrill, K. M. (1993). Infrared luminosity functions for the young stellar population associated with the L1641 molecular cloud. ApJ, *412*, 233–253.

Sung, H. and Bessell, M. S. (2010). The Initial Mass Function and Young Brown Dwarf Candidates in NGC 2264. IV. The Initial Mass Function and Star Formation History. AJ, *140*, 2070–2085.

Sung, H., Bessell, M. S., and Chun, M.-Y. (2004). The Initial Mass Function and Young Brown Dwarf Candidates in NGC 2264. I. The Initial Mass Function around S Monocerotis. AJ, *128*, 1684–1693.

Sung, H., Bessell, M. S., Chun, M.-Y., Karimov, R., and Ibrahimov, M. (2008). The Initial Mass Function and Young Brown Dwarf Candidates in NGC 2264. III. Photometric Data. AJ, *135*, 441–466.

Sung, H., Bessell, M. S., and Lee, S.-W. (1997). UBVRI H(alpha) Photometry of the Young Open Cluster NGC 2264. AJ, *114*, 2644.

Sung, H., Stauffer, J. R., and Bessell, M. S. (2009). A Spitzer View of the Young Open Cluster NGC 2264. AJ, *138*, 1116–1136.

Swenson, F. J., Faulkner, J., Rogers, F. J., and Iglesias, C. A. (1994). The Hyades lithium problem revisited. ApJ, *425*, 286–302.

Symington, N. H., Harries, T. J., Kurosawa, R., and Naylor, T. (2005). T Tauri stellar magnetic fields: HeI measurements. MNRAS, *358*, 977–984.

Teixeira, P. S., et al. (2006). Identifying Primordial Substructure in NGC 2264. ApJ, *636*, L45–L48.

Terquem, C., Sørensen–Clark, P. M., and Bouvier, J. (2015). Circumbinary discs and variability of eclipsing binary light curves with application to corot 223992193. *MNRAS*, *submitted*.

Tobin, J. J., Hartmann, L., Fűrész, G., Hsu, W.-H., and Mateo, M. (2015). Kinematic and Spatial Substructure in NGC 2264. AJ, *149*, 119.

Tody, D. (1993). IRAF in the Nineties. In R. J. Hanisch, R. J. V. Brissenden, & J. Barnes (Eds.) *Astronomical Data Analysis Software and Systems II*, vol. 52 of *Astronomical Society of the Pacific Conference Series*, (p. 173).

Tognelli, E., Prada Moroni, P. G., and Degl'Innocenti, S. (2011). The Pisa pre-main sequence tracks and isochrones. A database covering a wide range of Z, Y, mass, and age values. A&A, *533*, A109.

Tognelli, E., Prada Moroni, P. G., and Degl'Innocenti, S. (2013). The PISA Pre-Main Sequence accreting models. In *Protostars and Planets VI Posters*, (p. 101).

Tokovinin, A. (2014a). From Binaries to Multiples. I. Data on F and G Dwarfs within 67 pc of the Sun. AJ, *147*, 86.

Tokovinin, A. (2014b). From Binaries to Multiples. II. Hierarchical Multiplicity of F and G Dwarfs. AJ, *147*, 87.

Tokovinin, A., Thomas, S., Sterzik, M., and Udry, S. (2006). Tertiary companions to close spectroscopic binaries. A&A, *450*, 681–693.

Tonry, J. and Davis, M. (1979). A survey of galaxy redshifts. I - Data reduction techniques. AJ, *84*, 1511–1525.

Torres, G., Andersen, J., and Giménez, A. (2010). Accurate masses and radii of normal stars: modern results and applications. A&A Rev., *18*, 67–126.

Torres, G., Claret, A., and Young, P. A. (2009). Binary Orbit, Physical Properties, and Evolutionary State of Capella (α Aurigae). ApJ, *700*, 1349–1381.

Torres, G., Latham, D. W., and Stefanik, R. P. (2007). Cross-Correlation in Four Dimensions: Application to the Quadruple-lined Spectroscopic System HD 110555. ApJ, *662*, 602–612.

Torres, G. and Ribas, I. (2002). Absolute Dimensions of the M-Type Eclipsing Binary YY Geminorum (Castor C): A Challenge to Evolutionary Models in the Lower Main Sequence. ApJ, *567*, 1140–1165.

Valenti, J. A., Basri, G., and Johns, C. M. (1993). T Tauri stars in blue. AJ, *106*, 2024–2050.

van Eyken, J. C., et al. (2011). The Palomar Transient Factory Orion Project: Eclipsing Binaries and Young Stellar Objects. AJ, *142*, 60.

van Eyken, J. C., et al. (2012). The PTF Orion Project: A Possible Planet Transiting a T-Tauri Star. ApJ, *755*, 42.

Vaz, L. P. R. (1984). Ph.D. thesis, Ph. D. Thesis, Copenhagen University Observatory, (1984).

Vaz, L. P. R. (1986). Corrections and improvements in the effectiveness and extension of the applicability range of the WINK model of eclipsing binaries. Rev. Mexicana Astron. Astrofis., *12*, 177–183.

Vaz, L. P. R. and Nordlund, A. (1985). The reflection effect in model stellar atmospheres. I - Grey atmospheres with convection. A&A, *147*, 281–299.

Venuti, L., et al. (2014). Mapping accretion and its variability in the young open cluster NGC 2264: a study based on u-band photometry. *ArXiv e-prints*.

Venuti, L., et al. (2015). UV variability and accretion dynamics in the young open cluster NGC 2264. A&A, *581*, A66.

von Braun, K., et al. (2011). 55 Cancri: Stellar Astrophysical Parameters, a Planet in the Habitable Zone, and Implications for the Radius of a Transiting Super-Earth. ApJ, *740*, 49.

von Braun, K., et al. (2014). Stellar diameters and temperatures - V. 11 newly characterized exoplanet host stars. MNRAS, *438*, 2413–2425.

von Zeipel, H. (1924). The radiative equilibrium of a slightly oblate rotating star. MNRAS, *84*, 684–701.

Walker, M. F. (1956). Studies of Extremely Young CLUSTERS.I.NGC 2264. ApJS, *2*, 365.

Welsh, W. F., et al. (2012). Transiting circumbinary planets Kepler-34 b and Kepler-35 b. Nature, *481*, 475–479.

White, R. J. and Basri, G. (2003). Very Low Mass Stars and Brown Dwarfs in Taurus-Auriga. ApJ, *582*, 1109–1122.

Wilking, B. A. (1989). The formation of low-mass stars. PASP, *101*, 229–243.

Williams, J. P. and Cieza, L. A. (2011). Protoplanetary Disks and Their Evolution. ARA&A, *49*, 67–117.

Wilson, R. E. (1993). Computation Methods and Organization for Close Binary Observables. In K.-C. Leung, & I.-S. Nha (Eds.) *New Frontiers in Binary Star Research*, vol. 38 of *Astronomical Society of the Pacific Conference Series*, (p. 91).

Wilson, R. E. and Devinney, E. J. (1971). Realization of Accurate Close-Binary Light Curves: Application to MR Cygni. ApJ, *166*, 605.

Windmiller, G., Orosz, J. A., and Etzel, P. B. (2010). The Effect of Starspots on Accurate Radius Determination of the Low-Mass Double-Lined Eclipsing Binary Gu Boo. ApJ, *712*, 1003–1009.

Wood, D. B. (1973). A Computer Program for Modeling Nonspherical Eclipsing Binary Star Systems. PASP, *85*, 253.

Young, A. (1978). Differential Reddening in the Young Cluster NGC 2264. PASP, *90*, 144.

Young, E. T., Teixeira, P. S., Lada, C. J., Muzerolle, J., Persson, S. E., Murphy, D. C., Siegler, N., Marengo, M., Krause, O., and Mainzer, A. K. (2006). Spitzer and Magellan Observations of NGC 2264: A Remarkable Star-forming Core near IRS 2. ApJ, *642*, 972–978.

Zasche, P. (2012). On the Apsidal Motion of Thirteen Eclipsing Binaries. Acta Astron., *62*, 97–111.

Zucker, S. (2012). TODCOR - Two-Dimensional Correlation. In M. T. Richards, & I. Hubeny (Eds.) *IAU Symposium*, vol. 282 of *IAU Symposium*, (pp. 371–378).

Zucker, S. and Mazeh, T. (1994). Study of spectroscopic binaries with TODCOR. 1: A new two-dimensional correlation algorithm to derive the radial velocities of the two components. ApJ, *420*, 806–810.

Zucker, S., Mazeh, T., Santos, N. C., Udry, S., and Mayor, M. (2003). Multi-order TODCOR: Application to observations taken with the CORALIE echelle spectrograph. I. The system ¡ASTROBJ¿HD 41004¡/ASTROBJ¿. A&A, *404*, 775–781.

Zucker, S., Torres, G., and Mazeh, T. (1995). Study of Spectroscopic Binaries with TODCOR. III. Application to Triple-lined Systems. ApJ, *452*, 863.

Zwintz, K., et al. (2011). Pulsational Analysis of V 588 Mon and V 589 Mon Observed with the MOST and CoRoT Satellites. ApJ, *729*, 20.